INFORMATION TO USERS

This manuscript has been reproduced from the microfilm master. UMI films the text directly from the original or copy submitted. Thus, some thesis and dissertation copies are in typewriter face, while others may be from any type of computer printer.

The quality of this reproduction is dependent upon the quality of the copy submitted. Broken or indistinct print, colored or poor quality illustrations and photographs, print bleedthrough, substandard margins, and improper alignment can adversely affect reproduction.

In the unlikely event that the author did not send UMI a complete manuscript and there are missing pages, these will be noted. Also, if unauthorized copyright material had to be removed, a note will indicate the deletion.

Oversize materials (e.g., maps, drawings, charts) are reproduced by sectioning the original, beginning at the upper left-hand corner and continuing from left to right in equal sections with small overlaps. Each original is also photographed in one exposure and is included in reduced form at the back of the book.

Photographs included in the original manuscript have been reproduced xerographically in this copy. Higher quality 6" x 9" black and white photographic prints are available for any photographs or illustrations appearing in this copy for an additional charge. Contact UMI directly to order.

UMI

A Bell & Howell Information Company
300 North Zeeb Road, Ann Arbor MI 48106-1346 USA
313/761-4700 800/521-0600

Downloaded from SHAREOK. Persistent Handle URL: https://hdl.handle.net/11244/5806

UNIVERSITY OF OKLAHOMA

GRADUATE COLLEGE

MOISTURE AND DIABATIC INITIALIZATION BASED ON RADAR AND SATELLITE OBSERVATIONS

A Dissertation

SUBMITTED TO THE GRADUATE FACULTY

in partial fulfillment of the requirements for the degree of

Doctor of Philosophy

By
JIAN ZHANG
Norman, Oklahoma
1999

UMI Number: 9929559

UMI Microform 9929559
Copyright 1999, by UMI Company. All rights reserved.

This microform edition is protected against unauthorized copying under Title 17, United States Code.

UMI
300 North Zeeb Road
Ann Arbor, MI 48103

© Copyright by Jian Zhang 1999
All Rights Reserved

MOISTURE AND DIABATIC INITIALIZATION BASED ON RADAR AND SATELLITE OBSERVATIONS

A DISSERTATION APPROVED FOR

THE SCHOOL OF METEOROLOGY

BY

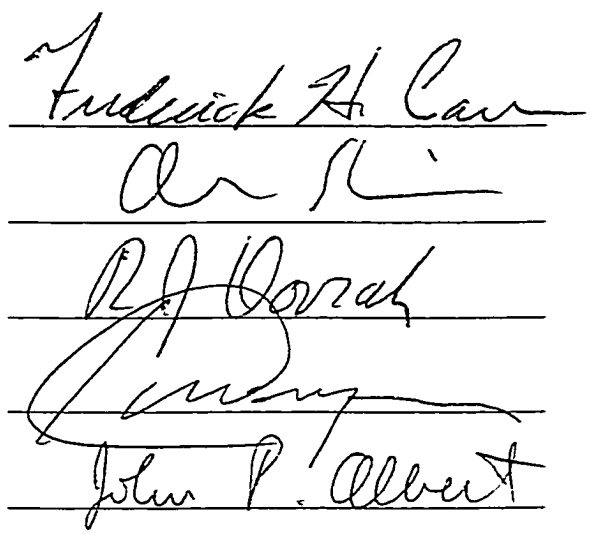

ACKNOWLEDGMENTS

I would like to express my deep appreciation to Dr. Frederick H. Carr, my major supervisor, for his insightful and patient guidance during the last five years. I have greatly benefited from his solid scientific background and comprehensive knowledge of data assimilation and numerical weather prediction. Without his persistent guidance and help, this dissertation would not have been possible.

I am very grateful to Dr. Kelvin Droegemeier for many of his inspirational ideas that greatly helped this work. Dr. Alan Shapiro has provided many helpful discussions and suggestions not only for this dissertation, but also for other research projects that I have involved in. I thank Dr. Richard Doviak, my very first advisor in the United States and long time mentor, for his kindness and for his helpfulness during my years at OU as graduate students. I would also like to thank Dr. John Albert for serving on my doctoral committee. His time and efforts are greatly appreciated.

A special thanks goes to Dr. Tzvi Gal-Chen, my late major advisor, who provided me invaluable advises. I admired him not only as a great scientist, but also as a great philosopher.

Keith Brewster, Drs. Donghai Wang, and Ming Xue are acknowledged for their help in many ways on the data and the model that are used in the work. Dr. Richard Carpenter is thanked for his comments and suggestions on the cloud analysis. I am grateful to my friends, Yong Zheng, Yuan Ho, Dr. Chia-Rong Chen, Dr. Steve Lazarus, Mike Splitt, Dr. Steve Weygandt and Sue Weygandt for their friendship. This friendship has helped me in ways they don't realize.

I thank my husband and my daughter for their love and patience. I am deeply thankful to my parents for their love, understanding, and encouragement. This dissertation could never have been possible without their love and support.

This research was supported by the Center for Analysis and Prediction of Storms (CAPS) at the University of Oklahoma, which is funded by Grant ATM 91-20009 from the National Science Foundation (NSF) and a supplemental grant through the NSF from the Federal Aviation Administration.

TABLE OF CONTENTS

ACKNOWLEDGMENTS IV
TABLE OF CONTENTS V
LIST OF TABLES VII
LIST OF FIGURES VIII
LIST OF ACRONYMS XIII
ABSTRACT XIV

CHAPTER 1 INTRODUCTION 1

1.1 MOTIVATION FOR THE RESEARCH 1
1.2 REVIEW OF PREVIOUS STUDIES 4
1.2.1 Estimation of precipitation rate 6
1.2.2 Latent heating profile 7
1.2.3 Diabatic initialization 8
1.2.4 Moisture adjustment/initialization 11
1.2.5 Newtonian-relaxation (nudging) 13
1.2.6 Cloud water initialization 15
1.2.7 Adjoint initializations 16
1.2.8 OSSEs on cloud-scale numerical weather predictions 18
1.3 OUTLINE OF THE PRESENT STUDY 19

CHAPTER 2 ADAS CLOUD ANALYSIS 25

2.1 INTRODUCTION 25
2.2 THREE-DIMENSIONAL VOLUMETRIC CLOUD FRACTION (VCF) ANALYSIS 27
2.2.1 Background volumetric cloud fraction field 27
2.2.2 Insertion of the cloud reports from METARs 30
2.2.3 Insertion of satellite infrared (IR) imagery data 32
2.2.4 Insertion of radar reflectivity data 35
2.2.5 Insertion of satellite visible imagery data 37
2.3 CLOUD LIQUID- AND ICE-WATER MIXING RATIO ANALYSIS 41
2.4 CLOUD TYPE AND IN-CLOUD VERTICAL VELOCITY ANALYSIS 44
2.5 PRECIPITATE TYPE AND MIXING RATIO ANALYSIS 49
2.6 SUMMARY 51

CHAPTER 3 MOISTURE AND DIABATIC INITIALIZATION 54

3.1 INTRODUCTION 54
3.2 INITIALIZATION OF THE ARPS CLOUD AND PRECIPITATION FIELDS 55
3.3 A DIABATIC INITIALIZATION 57
3.4 MOISTURE ADJUSTMENT 74
3.5 SUMMARY 78

CHAPTER 4 SENSITIVITY OF CONVECTIVE-SCALE NUMERICAL SIMULATIONS TO MOISTURE /DIABATIC INITIALIZATION 80

4.1 INTRODUCTION 80
4.2 THE MODEL 82
4.3 THE CONTROL RUN 83

4.4. EXPERIMENTAL DESIGN 87
4.5 CRITERIA FOR VERIFICATION AND COMPARISONS 92
4.6 RESULTS AND DISCUSSION 95
4.6.1 Conventional wind experiments without diabatic initialization 95
4.6.2 Retrieved wind experiments without diabatic initialization 101
4.6.3 Conventional wind experiments with diabatic initialization 103
4.6.4 Retrieved wind experiments with diabatic initialization 118
4.7 SUMMARY 123

CHAPTER 5 A CASE STUDY 126

5.1 INTRODUCTION 126
5.2 THE CASE 127
5.3 THE MODEL CONFIGURATIONS 133
5.4 EXPERIMENTAL DESIGN 135
5.5 RESULTS 146
5.5.1 Verification 146
5.5.2 Conventional data analysis experiments 146
5.5.2 ADAS analysis experiment 149
5.5.3 Diabatic initialization experiments 154
5.6 SUMMARY 162

CHAPTER 6 SUMMARY AND CONCLUSIONS 166

6.1 SUMMARY 166
6.2 CONCLUSIONS AND FUTURE WORK 171

APPENDIX A REVERSE-KESSLER SCHEME 174

A.1 INTRODUCTION 174
A.2 REVERSE-KESSLER SCHEME 175
A.3 OBSERVATIONAL SYSTEM SIMULATION EXPERIMENTS (OSSEs) 178
A.3.1 The Control Run 178
A.3.2 Experimental Design 179
A.3.3 Results 180
A.4. SUMMARY 182

REFERENCES 184

LIST OF TABLES

TABLE 1.1 LIST OF A FEW COMMONLY USED WEATHER OBSERVING SYSTEMS 2
TABLE 1.2. LIST OF THE MODELS AND THE GRID RESOLUTIONS USED IN SOME OF THE PREVIOUS STUDIES. 5
TABLE 2.1 VOLUMETRIC CLOUD FRACTIONS ASSOCIATED WITH THE METAR CLOUD REPORTS. 32
TABLE 2.2 CLOUD TYPES AS A FUNCTION OF CLOUD DEPTH H (KM) AND STABILITY σ (K/KM) FOR TEMPERATURES WARMER THAN -10°C (A), FOR TEMPERATURES BETWEEN -20°C AND -10°C (B), AND FOR TEMPERATURES COLDER THAN -20°C (C). 45
TABLE 4.1 LIST OF THE MOISTURE AND DIABATIC INITIALIZATION EXPERIMENTS. 91
TABLE 5.1 LIST OF THE REAL DATA MOISTURE AND DIABATIC INITIALIZATION EXPERIMENTS. 138
TABLE 5.2 MAXIMUM HOURLY RAINFALL VALUES AT DIFFERENT TIMES IN THE ABRFC RAINFALL ANALYSIS AND IN EXPS. DIA, DIB, AND DIC. 156
TABLE 5.3 MAXIMUM HOURLY RAINFALL VALUES AT DIFFERENT TIMES IN THE ABRFC RAINFALL ANALYSIS AND IN THE PREDICTIONS OF DIWA, DIWB, AND DIWC. 159
TABLE A.1 LIST OF THE OSSES 180
TABLE A.2 THE ERROR STATISTICS OF THE RETRIEVED FIELDS 181

LIST OF FIGURES

FIG. 2.1 SCHEMATIC DIAGRAM OF THE ADAS CLOUD ANALYSIS SYSTEM. 26
FIG. 2.2 FLOWCHART OF THE ADAS VOLUMETRIC CLOUD FRACTION ANALYSIS. 28
FIG. 2.3 RELATIONSHIPS BETWEEN VOLUMETRIC CLOUD FRACTION AND RELATIVE HUMIDITY AT DIFFERENT HEIGHT LEVELS [SEE EQ. (2.1) IN THE TEXT] 29
FIG. 2.4 CLOUD COVER DERIVED FROM THE ADAS RELATIVE HUMIDITY ANALYSIS AT 18Z MAY 7, 1995. 30
FIG. 2.5 SATELLITE VISIBLE IMAGE AT 1745Z MAY 7, 1995. THE LINE AB INDICATES THE LOCATION WHERE VERTICAL CROSS SECTIONS OF VARIOUS FIELDS ARE TAKEN 31
FIG. 2.6 ILLUSTRATION OF A CONCEPTUAL MODEL FOR DETERMING THE CLOUD TOP HEIGHT FOR STRATOCUMULUS. THE THICK SOLID LINE REPRESENTS THE REAL ATMOSPHERIC TEMPERATURE PROFILE, AND THE LONG DASHED-LINE REPRESENTS THE TEMPERATURE PROFILE RESOLVED BY THE MODEL GRID. T_S, T_D, AND T_I ARE THE SURFACE TEMPERATURE, SURFACE DEWPOINT, AND THE CLOUD TOP TEMPERATURE, RESPECTIVELY. THE DOT-DASHED LINES INDICATE THE DRY- AND MOIST-ADIABATIC TEMPERATURE LAPSE RATES. POINTS A, B, AND C REPRESENT THE CLOUD TOP HEIGHT OF THE REAL CLOUD, AND THAT DERIVED FROM THE SCAN-AND-MATCHING METHOD AND FROM THE CONCEPTUAL MODEL, RESPECTIVELY. 34
FIG. 2.7 VERTICAL CROSS SECTIONS OF THE ADAS VCF ANALYSIS AT 18Z MAY 7, 1995 AFTER INSERTING THE METARS (A) AND THE SATELLITE IR IMAGERY DATA (B). THE LOCATION OF THE CROSS SECTIONS IS INDICATED BY THE LINE AB IN FIG. 2.5. 36
FIG. 2.8 SAME CROSS SECTIONS AS IN FIG. 2.7 EXCEPT FOR THE OBSERVED RADAR REFLECTIVITY (A) AND THE VCF ANALYSIS AFTER INSERTING THE REFLECTIVITY (B). 38
FIG. 2.9 SAME CROSS SECTION AS IN FIG. 2.7 EXCEPT FOR THE VCF ANALYSIS AFTER INSERTING THE SATELLITE VISIBLE IMAGERY DATA. 39
FIG. 2.10 COLUMN TOTAL CLOUD COVER BEFORE (A) AND AFTER (B) INSERTING THE SATELLITE VISIBLE DATA 40
FIG. 2.11 FLOWCHART OF THE ADAS CLOUD LIQUID/ICE WATER CONTENT ANALYSIS 41
FIG. 2.12 ENTRAINMENT REDUCTION CURVE. 42
FIG. 2.13 VERTICAL CROSS SECTIONS OF THE TEMPERATURE ANALYSES AT 18Z MAY 7, 1995. THE CROSS SECTIONS ARE TAKEN ALONG THE LINE AB AS INDICATED IN FIG. 2.5. 43
FIG. 2.14 SAME CROSS SECTION AS IN FIG. 2.13 EXCEPT FOR THE CLOUD LIQUID (SOLID LINE) AND CLOUD ICE (DASHED LINE) WATER MIXING RATIO (UNIT: G/KG) ANALYSES AT 18Z MAY 7, 1995. THE CROSS SECTIONS ARE TAKEN ALONG THE LINE AB AS INDICATED IN FIG. 2.5. THE CONTOUR INTERVAL IS 0.25G/KG. 43
FIG. 2.15 VERTICAL CROSS SECTIONS OF THE CLOUD TYPE FIELD AT 18Z MAY 7, 1995 BEFORE (A) AND AFTER (B) THE QUALITY CHECK. THE CROSS SECTIONS ARE TAKEN ALONG THE LINE AB AS INDICATED IN FIG. 2.5 46
FIG. 2.16 PROFILES OF THE IN-CLOUD VERTICAL VELOCITY IN THE LAPS CLOUD ANALYSIS (DASHED LINE) AND IN THE ADAS CLOUD ANALYSIS (SOLID LINE). 49
FIG. 2.17 SAME CROSS SECTION AS IN FIG. 2.14 EXCEPT FOR THE ANALYZED IN-CLOUD VERTICAL VELOCITY FIELD AT 18Z MAY 7, 1995 50
FIG. 2.18 SAME CROSS SECTION AS IN FIG. 2.16 EXCEPT FOR THE ANALYZED RAINWATER (SOLID LINE) AND SNOW (DASH LINE) MIXING RATIOS (UNIT: G/KG) AT 18Z MAY 7, 1995. THE CONTOUR INTERVAL IS 0.1 G/KG. 52
FIG. 3.1 AN EXAMPLE OF THE BUOYANCY ADJUSTMENT. PANEL A SHOWS THE BACKGROUND θ'-FIELD (UNIT: K) AND THE θ'-FIELD AFTER THE BUOYANCY ADJUSTMENT (B). THE DIFFERENCE

BETWEEN (A) AND (B) IS SHOWN IN PANEL C. THE CONTOUR INTERVALS ARE 1K IN PANELS A AND B, AND 0.5K IN PANEL C. 60
FIG. 3.2 CONTROL LATENT HEATING RATE FIELDS (UNIT: K/S) PRODUCED BY THE CONTROL SIMULATION AT 25 (A), 30 (B), 60 (C) AND 90 MINUTES (D) OF THE SIMULATION TIME. THE VERTICAL CROSS SECTIONS WERE TAKEN THROUGH THE CORES OF THE SIMULATED STORMS. 63
FIG. 3.3 THE SIMULATED PERTURBATION POTENTIAL TEMPERATURE FIELDS (UNIT: K) IN THE SAME CROSS SECTIONS AS IN FIG. 3.2 AT 25 (A), 30 (B), 60 (C), AND 90 MINUTES (D) OF THE SIMULATION TIME. 64
FIG. 3.4 THE PRECIPITATION-DERIVED LATENT HEATING RATE FIELDS (UNIT: K/S) IN THE SAME CROSS SECTIONS AS IN FIG. 3.2 AT 25 (A), 30 (B), 60 (C), AND 90 MINUTES (D) OF THE SIMULATION TIME. HALF-HOUR PRECIPITATION FIELDS IN THE CONTROL RUN AND PARABOLIC PROFILES ARE USED TO DERIVED THE LATENT HEATING RATES. 67
FIG. 3.5 CONTROL Q_R FIELDS (UNIT: G/KG) IN THE SAME CROSS SECTIONS AS IN FIG. 3.2 AT 25 (A), 30 (B), 60 (C), AND 90 MINUTES (D) OF THE SIMULATION TIME. 68
FIG. 3.6 CONTROL Q_C FIELDS (UNIT: G/KG) IN THE SAME CROSS SECTIONS AS IN FIG. 3.2 AT 25 (A), 30 (B), 60 (C), AND 90 MINUTES (D) OF THE SIMULATION TIME. 70
FIG. 3.7 TEMPERATURE ADJUSTMENT FIELDS (UNIT: K) BASED ON LATENT HEAT RELEASE IN THE SAME CROSS SECTIONS AS IN FIG. 3.2 AT 25 (A), 30 (B), 60 (C), AND 90 MINUTES (D) OF THE SIMULATION TIME. THE AMOUNT OF THE LATENT HEAT IS RELATED TO THE Q_C-FIELD THAT IS DERIVED USING THE SMITH-FEDDES MODEL. 72
FIG. 3.8 SMITH-FEDDES MODEL-DERIVED Q_C FIELDS (UNIT: G/KG) IN THE SAME CROSS SECTIONS AS IN FIG. 3.2 AT 25 (A), 30 (B), 60 (C), AND 90 MINUTES (D) OF THE SIMULATION TIME. 73
FIG. 3.9 RELATIONSHIP BETWEEN THE MINIMUM RELATIVE HUMIDITY AND CLOUD COVER. 75
FIG. 3.10 RELATIVE HUMIDITY FIELDS BEFORE (A) AND AFTER (B) THE MOISTURE ADJUSTMENT. 76
FIG. 3.11 PRECIPITABLE WATER BEFORE (A) AND AFTER (B) THE MOISTURE ADJUSTMENT. 77
FIG. 4.1 THE SOUNDING THAT WAS USED TO CREATE THE BASE STATE MODEL FIELDS IN THE CONTROL RUN. 84
FIG. 4.2 X-Y (A) AND X-Z (B) CROSS SECTIONS OF THE WARM BUBBLE THAT WAS USED TO CREATE THE INITIAL PERTURBATION TEMPERATURE FIELD IN THE CONTROL RUN. THE CROSS SECTIONS ARE THROUGH THE CENTER OF THE BUBBLE. 86
FIG. 4.3 TIME SERIES OF THE DOMAIN MAXIMUM QC AND QR IN THE CONTROL RUN. 87
FIG. 4.4 THE ACCUMULATED RAINFALL (MM) AT 30 (A), 60 (B), 90 (C), AND 120 (D) MINUTES IN THE CONTROL RUN. THE ACCUMULATION PERIODS WERE 30 MIN EXCEPT FOR THAT IN PANEL (A), WHICH WAS ACCUMULATED FROM 25 TO 30 MINUTES. THE CONTOUR VALUES ARE 1 MM, 5 MM, 10 MM, 30 MM, AND 50 MM, RESPECTIVELLY. 88
FIG. 4.5 TIME SERIES OF THE BIAS (A) AND THREAT SCORES (B) FOR EXPS. 1A, 1B, AND 1C. 96
FIG. 4.6 THE 5 MIN ACCUMULATED RAINFALL VALID AT 30 MIN (A) AND THE HALF-HOUR ACCUMULATED RAINFALL VALID AT 60 MIN (B), 90 MIN (C), AND 120 MIN (D) IN EXP. 1C. THE CONTOUR VALUES ARE 1 MM, 5 MM, AND 10 MM, RESPECTIVELLY. 97
FIG. 4.7 THE SURFACE POTENTIAL TEMPERATURE PERTURBATION (K, CONTOUR) AND THE WIND VECTOR (M/S) FIELDS AT 30MIN (A), 60 MIN (B), 90 MIN (C), AND 120 MIN (D) IN EXP. 1C. THE CONTOUR INTERVAL IS 0.5K. 98
FIG. 4.8 X-Z CROSS SECTION OF THE PERTURBATION POTENTIAL TEMPERATURE FIELD (UNIT: K) THROUGH Y = 22 KM AT 25 MIN IN THE CONTROL RUN. THE CONTOUR INTERVAL IS 2K. 99
FIG. 4.9 THE PRECIPITABLE WATER FIELDS (UNIT: CM) AT 25 MIN IN THE CONTROL RUN (A), IN THE EXPS. 1A, 1B, AND 1C (B), AND THE DIFFERENCE BETWEEN THE TWO (C). THE CONTOUR INTERVALS ARE 0.2 CM IN PANELS A AND B, AND 0.1 CM IN PANEL C. 100
FIG. 4.10 TIME SERIES OF THE BIAS (A) AND THREAT SCORES (B) FOR EXPS. 2A, 2B, AND 2C. 101
FIG. 4.11 TIME SERIES OF THE DOMAIN MAXIMUM UPDRAFT (UNIT: M/S) IN THE CONTROL RUN AND IN EXPS. 2A, 2B, AND 2C. 102
FIG. 4.12 TIME SERIES OF THE BIAS (A) AND THREAT SCORES (B) FOR EXPS. 3A, 3B, AND 3C. 104

FIG. 4.13 THE 30 MIN ACCUMULATED RAINFALL VALID AT 60 MIN (LEFT PANELS) AND 120MIN (RIGHT PANELS) IN THE CONTROL RUN (PANELS A AND B) AND IN EXPS. 3A (PANELS C AND D), 3B (PANELS E AND F), AND 3C (PANELS G AND H). THE UNIT IS MM, AND THE CONTOUR VALUES ARE 1 MM, 5 MM, 10 MM, 30 MM, AND 50 MM. 105
FIG. 4.14 THE PRECIPITABLE WATER FIELDS (UNIT: CM) AT 25 MIN IN THE CONTROL RUN (A), IN THE EXPS. 3A, 3B, AND 3C (B), AND THE DIFFERENCE BETWEEN THE TWO (C). THE CONTOUR INTERVALS ARE 0.2 CM IN PANELS A AND B, AND 0.1 CM IN PANEL C. 108
FIG. 4.15 TIME SERIES OF BIAS SCORES FOR THE 5 MINUTE-ACCUMULATED RAINFALL IN EXPS. 3A, 3B, AND 3C. 109
FIG. 4.16 TIME SERIES OF THE MAXIMUM THREAT SCORE WITH SHIFTING (MTSS, PANEL A) AND THE SHIFTING DISTANCE CORRESPONDING TO THE MAXIMUM THREAT SCORE (D_MTSS, PANEL B) FOR EXPS. 3A, 3B, AND 3C. 111
FIG. 4.17 THE HALF-HOUR ACCUMULATED RAINFALL VALID AT 90 MIN IN THE CONTROL RUN (A) AND IN EXPS. 3A (B), 3B (C), AND 3C (D). THE UNIT IS MM, AND THE CONTOUR VALUES ARE 1 MM, 5 MM, 10 MM, 30 MM, AND 50 MM. 112
FIG. 4.18 LOW-LEVEL (0-2 KM) CONVERGENCE (CONTOURS IN LEFT PANELS, UNIT: $10^{-3}s^{-1}$) AND THE SURFACE PERTURBATION POTENTIAL TEMPERATURE (CONTOURS IN RIGHT PANELS, UNIT: K) OVERLAPPED WITH THE SURFACE WIND VECTOR FIELDS AT 30 MIN (PANELS A, AND B), 60 MIN (PANELS C AND D), 90 MIN (PANELS E AND F), AND 120 MIN (PANELS G AND H) IN THE CONTROL RUN. THE CONTOUR INTERVALS FOR THE LOW-LEVEL CONVERGENCE AND PERTURBATION POTENTIAL TEMPERATURE FIELDS ARE $0.5x10^{-3}s^{-1}$ AND 0.5 K, RESPECTIVELY. 114
FIG. 4.19 LOW-LEVEL (0-2 KM) CONVERGENCE (CONTOURS IN UNIT OF $10^{-3}s^{-1}$) AND THE SURFACE WIND VECTOR FIELDS AT 30 MIN (A), 60 MIN (B), 90 MIN (C), AND 120 MIN (D) IN EXP. 3A. THE CONTOUR INTERVAL IS $0.5x10^{-3}s^{-1}$. 116
FIG. 4.20 LOW-LEVEL (0-2 KM) CONVERGENCE (CONTOURS IN UNIT OF $10^{-3}s^{-1}$) AND THE SURFACE WIND VECTOR FIELDS AT 30 MIN (A), 60 MIN (B), 90 MIN (C), AND 120 MIN (D) IN EXP. 3C. THE CONTOUR INTERVAL IS $0.5x10^{-3}s^{-1}$. 117
FIG. 4.21 TIME SERIES OF THE BIAS (A) AND THREAT SCORES (B) FOR EXPS. 4A, 4B, AND 4C. ... 119
FIG. 4.22 TIME SERIES OF THE MAXIMUM THREAT SCORE WITH SHIFTING (MTSS, PANEL A) AND THE SHIFTING DISTANCE CORRESPONDING TO THE MAXIMUM THREAT SCORE (D_MTSS, PANEL B) FOR EXPS. 4A, 4B, AND 4C. 120
FIG. 4.23 X-Z CROSS SECTION OF THE VERTICAL VELOCITY FIELD (UNIT: M/S) THROUGH Y = 22 KM AT 25 MIN IN EXP. 4C. THE CONTOUR INTERVAL IS 5 M/S. 121
FIG. 4.24 LOW-LEVEL (0-2 KM) CONVERGENCE (CONTOURS IN UNIT OF $10^{-3}s^{-1}$) AND THE SURFACE WIND VECTOR FIELDS AT 30 MIN (A), 60 MIN (B), 90 MIN (C), AND 120 MIN (D) IN EXP. 4C. THE CONTOUR INTERVAL IS $0.5x10^{-3}s^{-1}$. 122
FIG. 5.1 RUC ANALYSIS OF THE 500 MB GEOPOTENTIAL HEIGHT (UNIT: 10 M) AND WIND FIELDS AT 1200 (A) AND 1800 Z (B) ON 7 MAY AND 0000 Z (C) ON 8 MAY, 1995. THE CONTOUR INTERVALS ARE 25 M. 128
FIG. 5.2 RUC ANALYSIS OF THE SURFACE DEWPOINT (UNIT: °C) AND WIND VECTOR (UNIT: M/S) FIELDS VALID AT 1200 (A) AND 1800 (B) Z ON 7 MAY AND 0000 (C) Z ON 8 MAY, 1995. THE CONTOUR INTERVALS ARE 2.5 °C. 129
FIG. 5.3 RUC ANALYSIS OF THE 850 MB WATER VAPOR MIXING RATIO (UNIT: G/KG) AND WIND VECTOR (UNIT: M/S) FIELDS VALID AT 1200 (A) AND 1800 Z (B) ON 7 MAY AND 0000 Z (C) ON 8 MAY, 1995. NOTE THAT THE DATA NEAR THE WEST BOUNDARY OF THE MODEL DOMAIN WERE MISSING BECAUSE THE 850 MB LEVEL WAS BELOW THE SURFACE. THE CONTOUR INTERVALS ARE 1G/KG. 130
FIG. 5.4 COMPOSITE REFLECTIVITIES VALID AT 1200 (A), 1430 (B), 1600 (C), 1800 (D), 2000 (E), AND 2200 (F) Z 7 MAY, 1995. 131

FIG. 5.5 A MAP OF THE MODEL DOMAIN AND THE TOPOGRAPHY HEIGHT FIELD (UNIT: M) IN THE DOMAIN. 134
FIG. 5.6 DISTRIBUTION OF THE OKLAHOMA MESONET STATIONS (CIRCLES), SURFACE AVIATION OBSERVATIONS (TRIANGLES), WIND PROFILERS (SQUARES), WSR-88D RADARS (FILLED TRIANGLES), AND RADIOSONDE STATIONS (FILLED CIRCLES) 136
FIG. 5.7 RUC ANALYSIS OF THE TEMPERATURE (T, UNIT: °C, LEFT COLUMN) AND THE DEWPOINT (T_D, UNIT: °C, RIGHT COLUMN) FIELDS ON THE SURFACE (TOP ROW), 850 MB (MIDDLE ROW), AND 500 MB (BOTTOM ROW) LEVELS VALID AT 1800 Z ON 7 MAY 1995. THE CONTOUR INTERVALS ARE 1 °C 139
FIG. 5.8 ADAS ANALYSIS OF THE TEMPERATURE (T, UNIT: °C, LEFT COLUMN) AND THE DEWPOINT (T_D, UNIT: °C, RIGHT COLUMN) FIELDS ON THE SURFACE (TOP ROW), 850 MB (MIDDLE ROW), AND 500 MB (BOTTOM ROW) LEVELS VALID AT 1800 Z ON 7 MAY 1995. THE CONTOUR INTERVALS ARE 1 °C 140
FIG. 5.9 A VERTICAL CROSS SECTION OF THE CLOUD LIQUID (SOLID LINE, UNIT: G/KG) AND ICE (DASH LINE, UNIT: G/KG) MIXING RATIO FIELDS FROM THE ADAS CLOUD ANALYSIS VALID AT 1800 Z ON 7 MAY 1995. THE CROSS SECTION WAS EAST-WEST THROUGH OKLAHOMA CITY. THE CONTOUR INTERVALS ARE 0.25G/KG. 141
FIG. 5.10 A VERTICAL CROSS SECTION OF THE RAINWATER (SOLID LINE, UNIT: G/KG) AND SNOW (DASH LINE, UNIT: G/KG) MIXING RATIO FIELDS FROM THE ADAS CLOUD ANALYSIS VALID AT 1800 Z ON 7 MAY 1995. THE CROSS SECTION WAS EAST-WEST THROUGH OKLAHOMA CITY. THE CONTOUR INTERVALS ARE 0.1G/KG. 142
FIG. 5.11 VERTICAL CROSS SECTIONS OF THE INITIAL RELATIVE HUMIDITY FIELDS IN EXP. CNVN (A), MESO (B), AND DIB (C). THE CROSS SECTIONS ARE THE SAME AS IN FIG. 5.10. THE CONTOUR INTERVALS ARE 0.1 143
FIG. 5.12 VERTICAL CROSS SECTIONS OF THE INITIAL PERTURBATION POTENTIAL TEMPERATURE FIELDS IN EXPS. CNVN (A), MESO (B), DIB (C) AND DIWB (D). THE CROSS SECTIONS WERE THE SAME AS IN FIG. 5.10. THE CONTOUR INTERVALS ARE 0.5 K FOR PANEL *A* AND 1 K FOR PANELS *B*, *C*, AND *D* 145
FIG. 5.13 HOURLY PRECIPITATION (UNIT: MM) ANALYSES FROM THE ABRFC VALID AT 1900 (A), 2000 (B), 2100 (C), 2200 (D), AND 2300 Z (E) ON 7 MAY AND 0000 (F) Z ON 8 MAY, 1995. THE BOX INDICATES THE MODEL DOMAIN FOR THE NUMERICAL PREDICTION EXPERIMENTS. 147
FIG. 5.14 THE BIAS (A) AND THREAT SCORES (B) FOR THE HOURLY PRECIPITATION FIELDS IN THE EXPERIMENTS CNVN AND MESO 148
FIG. 5.15 THE HOURLY PRECIPITATION (UNIT: MM) FIELDS FROM EXP. CNVN VALID AT 1900 (A), 2000 (B), 2100 (C), 2200 (D), AND 2300 Z (E) ON 7 MAY AND 0000 (F) Z ON 8 MAY, 1995. 150
FIG. 5.16 THE HOURLY PRECIPITATION (UNIT: MM) FIELDS FROM EXP. MESO VALID AT 1900 (A), 2000 (B), 2100 (C), 2200 (D), AND 2300 Z (E) ON 7 MAY AND 0000 (F) Z ON 8 MAY, 1995. 152
FIG. 5.17 THE RUC ANALYSIS OF THE SURFACE CAPE (PANEL A, UNIT: J/KG) AND CIN (PANEL B, UNIT: J/KG) FIELDS AT 1800 Z ON 7 MAY, 1995 153
FIG. 5.18 THE ADAS ANALYSIS OF THE SURFACE CAPE (PANEL A, UNIT: J/KG) AND CIN (PANEL B, UNIT: J/KG) FIELDS AT 1800 Z ON 7 MAY, 1995 153
FIG. 5.19 THE BIAS (A) AND THREAT SCORES (B) FOR THE HOURLY PRECIPITATION FIELDS IN EXPS. CNVN, MESO, DIA, DIB, AND DIC. 155
FIG. 5.20 THE HOURLY PRECIPITATION (UNIT: MM) FIELDS FROM EXP. DIB VALID AT 1900 (A), 2000 (B), 2100 (C), 2200 (D), AND 2300 Z (E) ON 7 MAY AND 0000 (F) Z ON 8 MAY, 1995. 157
FIG. 5.21 THE BIAS (A) AND THREAT (B) SCORES FOR THE HOURLY PRECIPITATION FIELDS IN EXPS. DIA, DIB, DIC, DIWA, DIWB, AND DIWC. 160

FIG. 5.22 THE HOURLY PRECIPITATION FIELDS FROM EXP. DIWB VALID AT 1900 (A), 2000 (B), 2100 (C), 2200 (D), AND 2300 Z (E) ON 7 MAY AND 0000 (F) Z ON 8 MAY, 1995..... 161
FIG. 5.23 THE BIAS (A) AND THREAT SCORES (B) FOR THE HOURLY PRECIPITATION FIELDS IN EXPS. CNVN, MESO, DIB, AND DIWB..... 163

LIST OF ACRONYMS

ABRFC: Arkansas-red Basin River Forecast Center
ADAS: ARPS Data Analysis System
AMSU: the Advanced Microwave Sounding Unit
ARPS: Advanced Regional Prediction System
BMRC: Bureau of Meteorology Research Center (Australia)
CAPE: Convective Available Potential Energy
CAPS: Center for Analysis and Prediction of Storms
CCM1: Community Climate Model-1 (at NCAR)
CIMSS: Cooperative Institute for Meteorological Satellite Studies
CIN: Convective INhibition
CRAS: CIMSS Regional Assimilation System
CST: Central Standard Time
d_MTSS: distance associated with the MTSS
DMSP: the Defense Meteorological Satellite Program
ECMWF: European Center for Medium-range Weather Forecasting
FSU: Florida State University
GASP: Global Assimilation Prediction System (at BMRC, Australia)
GMASS: Goddard Mesoscale Atmospheric Simulation System
GMS: Geostationary Meteorological Satellite (Japan)
GOES: Geostationary Operational Environmental Satellite (the U.S.A.)
JMA: Japan Meteorological Agency
JSM: Japan Spectral Model (at JMA)
LAPS: Local Analysis and Prediction System
METARs: (French) Aviation Routine Weather Reports
MTSS: Maximum Threat Score with Shifting
NCAR: National Center for Atmospheric Research
NCEP: National Center for Environmental Prediction
NEXRAD: NEXt generation weather RADar
NNMI: Nonlinear Normal Mode Initialization
NOAA: National Oceanic and Atmospheric Administration
OLR: Outgoing Long-wave Radiation
OSSE: Observing System Simulation Experiments
RH: Relative Humidity
RUC: the Rapid Update Cycle
SSM: Subsynoptic-Scale Model (at CIMSS)
SSM/I: the Special Sensor Microwave/Imager
TKE: Turbulent Kinetic Energy
TRMM: Tropical Rainfall Measuring Mission
WMO: World Meteorological Organization

ABSTRACT

The "spinup" problem is one of the most serious problems for short-range precipitation forecasting. It is known to be related to the deficiencies in the initial moisture, latent heating and divergent circulations. The motivation for this research is to mitigate the spinup problem by providing better initial conditions using radar and satellite data.

Most of the previous real-data diabatic initialization studies have used two-dimensional surface precipitation data to derive and adjust the initial latent heating and moisture fields in order to alleviate the spinup problem. The deployment of high resolution meteorological radar and satellite observation systems has provided new resources for diabatic initialization. A cloud analysis system was developed to synthesize these data sources and to construct three-dimensional cloud and precipitation fields. The system is based on the LAPS cloud analysis, with several modifications. Based on the three-dimensional cloud and precipitation analyses, a moisture and diabatic initialization scheme was developed. In the initialization scheme, the initial thermal field is adjusted to account for the latent heating due to cloud condensation. The relative humidity field in the analyzed cloudy regions is adjusted to alleviate deficiencies in conventional moisture observations. The initialization scheme was tested using both simulated storms and real data cases.

The results show that this new moisture and diabatic initialization can provide significant improvement in convective-scale precipitation forecasts with the aid of radar and satellite observations over a conventional data initialization. It is found that the moisture adjustment is very important for compensating deficiencies in conventional radiosonde observations. Without the moisture adjustment, cloud condensation and, in turn, precipitation are significantly underestimated. The thermal adjustment is important in data sparse regions for improving the initial thermal field as well as the initial moisture field. Without the thermal adjustment, the moisture adjustment can be insufficient in those regions. The results show that inserting a cloud or rainwater field at the initial time can help produce cold outflows at the surface and generate new storms. However, if the initial water load is not balanced by consistent updrafts, it could be detrimental to the development of the existing storms at the initial time. It is also found that an accurate initial wind field in the rain region has a significant positive impact on reducing phase errors in precipitation simulations.

Chapter 1
Introduction

1.1 Motivation for the research

Precipitation is one of the meteorological factors that constantly affect human life. It is one of the most important prognostic variables for numerical weather predictions.

Numerical weather predictions are made by numerical models. In each of the models there is a set of time derivative equations that represent the evolution of the earth's atmospheric system. The equations are discretized for running on computers. Given a state of the atmospheric system at any given time, the equations are integrated from this state forward in time and the future atmospheric state can be obtained, or, "predicted", or, "forecasted". That given time is known as the "initial time", and the given state is known as the "initial condition" for numerical weather prediction models.

Initial conditions for numerical weather predictions are obtained from various atmospheric observation systems. A perfect observation system would be

the one that measures the atmospheric state continuously in time and space, which is completely impossible. The currently deployed weather observation systems are limited in space and in time and in the physical quantities that the systems are able to measure (Table 1.1). Due to distribution and accuracy limitations, the initial conditions we have at present are only approximations of the real atmospheric system. How good the approximations are depends on the spatial and temporal scales of the atmospheric systems under investigation. It is recognized that at least 5 data samples are needed to resolve a wave well. In the earth's atmosphere, synoptic-scale phenomena have spatial scales on the order of 1000 km and time scales of 3 ~ 5 days. These phenomena can be measured well

Table 1.1 List of a few commonly used weather observing systems

Source	Spatial resolution	Temporal resolution	Measurements
Radiosonde	~ 350km, multi-levels	12 hour	T, u, v, p, q_v
Local Mesonet	~ 40km, sfc	15 min.	T, u, v, p, q_v
Wind Profiler	~ 350 km, multi-levels	1 hour	u, v
GOES VIS imagery	2 km, cloud top envelop	15 min.	Cloud albedo
GOES IR imagery	8 km, cloud top envelop	15 min.	Cloud top temp.
NEXRAD	~ 1km, multi-levels	5 min.	Z, Vr

Note: **T:** temperature,
u,v,w: the three dimensional Cartesian components of wind vector,
p: pressure,
q_v: water vapor mixing ratio,
Z: radar reflectivity,
Vr: Doppler radial velocity

by the current weather observation systems in space and time (Table 1.1), and "good" initial conditions can be obtained for the numerical prediction of these

phenomena. But the current observation systems (with the exception of radar) are very deficient to accurately measuring convective-scales (on the order of 10 km) phenomena in the atmosphere (Table 1.1).

To make best possible numerical weather forecast, a perfect model is needed in addition to the accurate initial conditions. However, the evolution of the earth's atmospheric system involves many physical processes that are highly nonlinear and complicated. The equations in numerical weather models can only approximate these processes. It has become more and more recognized that anthropomorphic effects also have an impact on the earth's climate and weather systems. This makes it even more difficult to develop a set of model equations that can precisely represent the real atmosphere.

Owing to deficiencies in initial conditions and defects in numerical weather prediction models, there are inaccuracies in the models' forecasts. To reduce the inaccuracies, improvements need to be made in both initial conditions and numerical models. This is the general motivation for our research. The focus of our research is on the initial condition problem. Improvement of the formulation of numerical models is beyond the scope of this research.

We further focus our research on one of the problems related to the deficiencies in initial conditions, the so-called "spinup" problem. The term is generally used for the underestimation of the appropriate amount and areal coverage of precipitation during the early stages of numerical weather forecasts.

The spinup problem appears in nearly all forecast models, both in mid-latitude and tropics (Kasahara et al., 1988). It is one of the most serious problems for short-range forecasting and constitutes a fundamental issue in data assimilation. By solving the spinup problem, short-range forecasting can be improved, thereby improving hazardous weather warnings. Better warnings of thunderstorms, winter storms, flash floods, hurricanes, and other severe weather help to save lives, preserve property, and benefit commercial interests.

1.2 Review of previous studies

The causes of the spinup problem and the techniques to alleviate it have been studied since the late 1970's. A major class of the techniques is generally known as "diabatic" initialization. Diabatic initialization uses precipitation and other observations to estimate the diabatic forcing associated with condensation processes. The diabatic forcing is then used to induce the divergent circulations that are needed for models to correctly forecast the subsequent precipitation processes.

Most of the previous real-data diabatic initialization studies were carried out using meso- or larger- scale numerical models with grid resolutions ranging from 30 km to several hundreds of kilometers (Table 1.2). The techniques used in these studies can be summarized into three categories: 1) estimation of precipitation rate P_{obs} from observations; 2) determination of the latent heating

associated with the estimated precipitation rate and the vertical distribution of the latent heating; 3) adjustment of initial temperature and moisture fields. A review of these techniques will be given in the early parts of this section (sections *1.2.1*, *1.2.2*, *1.2.3*, *1.2.4*, and *1.2.5*).

Table 1.2. List of the models and the grid resolutions used in some of the previous studies.

Paper	Model	Grid resolution
Wang & Warner 1988	Penn State/NCAR Mesoscale model	30km
Krishnamurti 1988, 1991	Global spectral model/FSU	T42, T106
Turpeinen 1990; Turpeinen et al. 1990	Canadian regional finite-element model	140km
Puri & Miller 1990	ECMWF	T106
Kasahara et al. 1992	CCM1/NCAR	T42
Puri & Davidson 1992	BMRC/GASP	T31, ~350km
Zhao 1993	Eta/NCEP	80km
Takano & Segami 1993	JSM/JMA	40km
Aonashi 1993	JSM/JMA	40km
Manobianco et al. 1994	GMASS	40-80km
Krishnamurti et al. 1995	Global model	T213, ~55km
Raymond et al. 1995	CRAS	40-150km
Wu et al. 1995	SSM/CIMSS	80km
Aonashi & Shibata 1996	JSM/JMA	40km

Along with the deployment of new meteorological radar and satellite observation systems and the improvement in various physical parameterizations in numerical weather prediction models, new areas have been explored in recent diabatic initialization studies. Zhao (1993), Wu et al. (1995) and Raymond et al (1995) have tested the idea of reducing precipitation spinup in numerical weather

models by initializing cloud water and/or rainwater fields. The possibility of initializing diabatic processes during adjoint data assimilations has been explored in recent years (e.g., Verlinde and Cotton 1993; Zou et al. 1993; Vukicevic and Errico 1993; Zupanski and Mesinger 1995). Studies on the initialization of convective-scale weather prediction models have been undertaken at the Center for Analysis and Prediction of Storms (CAPS) at the University of Oklahoma, either through observing system simulation experiments (OSSEs) (Weygandt et al. 1990, 1993; Park 1996; Lazarus 1996) or through real data case studies (Xue et al. 1998). Brief introductions about these efforts will be given in the later parts of this section (*1.2.6, 1.2.7,* and *1.2.8*).

1.2.1 Estimation of precipitation rate

There have been three major observation sources for estimations of precipitation rate in the previous studies: raingages (Wang and Warner 1988; Carr and Baldwin 1991a, b; Aonashi 1993; Zhao and Carr 1997), radar (Molinari 1982; Wang and Warner 1988; Aonashi 1993;), and satellite data (Danard 1985; Turpeinen et al. 1990; Chang and Holt 1993; Manobianco et al. 1994; Wu et al. 1995). Raingage observations provide direct rain rate data, although the horizontal resolution of the data is poor. Radar reflectivities can provide precipitation rate estimation through empirical Z-R relationships (Z: reflectivity factor; R: rainfall rate). While there have been variations in techniques for deriving precipitation rates from satellite data, all of them are

based on the assumption that deep clouds produce more precipitation. Regression relationships were developed between precipitation rate and various satellite observations based on raingage or radar data collocated with the satellite imageries. The satellite observations used in previous studies include Outgoing Long-wave Radiation (OLR) data observed by the polar-orbiting satellite NOAA-9 (Puri and Miller 1990), GOES (Geostationary Operational Environmental Satellite) satellite IR (Infrared)/VIS (visible) imagery data (Turpeinen et al. 1990; Manobianco et al. 1994), the microwave brightness temperature observations from the Special Sensor Microwave/Imager (SSM/I) on board the Defense Meteorological Satellite Program (DMSP) (Chang and Holt 1994; Manobianco et al. 1994), and imagery data from the Japanese Geostationary Meteorological Satellite (GMS) (Puri and Davidson 1992).

1.2.2 Latent heating profile

Based on the estimated precipitation rate (R), the associated latent heating rate ($\dot{Q}_T$) is determined simply by:

$$\dot{Q}_T = L_v \rho_w R dx dy \tag{1.1}$$

where L_v is the latent heat of evaporation/condensation for water, ρ_w is the air density, and dx and dy are the size of a model grid box. This latent heating rate is an approximation of the vertically integrated rate at a particular location. For application in numerical weather prediction models, certain assumptions

concerning the vertical structure of the latent heating field are required. There have been three kinds of vertical distributions used in previous studies. 1) climatological profiles in similar situations (Puri and Miller 1990), 2) analytic profiles such as parabolic (Carr 1977; Wang and Warner 1988; Takano and Segami 1993; Wu et al. 1995), and 3) model-generated profiles (Turpeinen et al. 1990; Manobianco et al. 1994; Raymond et al. 1995). Using fixed profiles as in 1) and 2) throughout a particular domain is unsatisfactory because in real clouds latent heating distributions can vary with the locations and life cycle of a convective system. The specified profiles may also not be consistent with the model. Approach 3) will generate a heating rate that is consistent with the model and rainfall data. However, potential problems can arise in areas where there is observed precipitation when the model produces none. It is noteworthy, though, that some studies found relatively low sensitivities of their results to the shape of vertical latent heating profiles (Wang and Warner 1988; Puri and Miller 1990; Turpeinen 1990).

1.2.3 Diabatic initialization

The purpose of diabatic initialization is to force vertical circulations and the associated divergence that will most likely induce realistic precipitation distributions. To achieve this goal, latent heating rates derived from observed precipitation rates are incorporated into a model's thermodynamic equations, either by incorporating the latent heating rate into a nonlinear normal mode

initialization (NNMI) (e.g., Mohanty et al. 1986; Puri 1987; Errico and Rasch 1988; Puri and Miller 1990; Turpeinen et al. 1990; Takano and Segami 1993; Wu et al. 1995; Raymond et al. 1995) or by intermittent insertion of latent heating rates into the thermodynamic equation during a data assimilation period (Wang and Warner 1988; Manobianco et al. 1994).

Nonlinear Normal Mode Initialization (NNMI) is an initialization technique for suppressing high-frequency oscillations and obtaining balanced initial conditions in large-scale numerical models. Since it was introduced by Machenhauer (1977) and Baer and Tribbia (1977), NNMI techniques have been widely used in global (Andersen 1977; Daley 1979; Temperton and Williamson 1981) as well as regional (e.g., Brière, 1982; Bourke and McGregor, 1983) numerical weather prediction models. The dynamic balance in NNMI is determined essentially by a system of nonlinear equations resembling a quasi-geostrophic (QG) ω-equation coupled with a nonlinear balance equation and a potential vorticity tendency constraint (Errico and Bates 1988). Wind, temperature and surface pressure fields are initialized during NNMI, but not the moisture field. In diabatic NNMI the prescribed latent heating rate is incorporated as a forcing term in the QG ω-equation. This forcing is then kept constant to prevent producing time-variant divergence fields that can induce gravity waves early in the forecast. Note that the assumptions (e.g., quasi-geostrophic balance) made in NNMI make it an inappropriate initialization scheme for convective-scale numerical prediction models.

The intermittent insertion method is relatively simple and straightforward. By inserting the latent heating rate in the diabatic forcing term in a model's thermodynamic equation, a positive buoyancy component is produced in regions of the heating and vertical circulations can be induced. The insertions are usually done during a pre-forecast model integration period, which is often the data assimilation period as well. The length of the assimilation period was 1-h and 2-h in Wang and Warner (1988) and 9.5 hours in Manobianco et al. (1994). The diabatic forcing can vary in time and space for the intermittent insertion method, which is an advantage over the diabatic NNMI. A drawback of this approach is that a possible imbalance can exist between the prescribed latent heating distribution and the one that the physical parameterization in the model would produce. Note that both Wang and Warner (1988) and Manobianco et al. (1994) found that such imbalance was not significant and the diabatic forcing did not introduce noise into the simulations during or after the data assimilation period.

An alternative class of diabatic initialization is the time-filtering type of technique (Huang and Lynch 1993; Fox-Rabinovitz 1996; Lynch et al. 1997). In a diabatic digital-filtering initialization proposed by Huang and Lynch (1993), the model was adiabatically integrated backward in time for N time steps to produce a model state at $t = -N\Delta t$ (Δt is the time step for model integration). Then a diabatic forward integration was carried out in time to $+N\Delta t$. A time filter was applied to the time series of the model variables produced by the diabatic integration (total

time span of $T_S = 2N\Delta t$). The high frequencies in the data were removed, and an initial condition is obtained for the time in the middle of the time span. Using this scheme all the model variables are initialized, and consistency between the initialized fields and the model is ensured since all fields are produced by the model itself. But the computational expense may become very large for slow-spinup models, because the forward time span must be long enough to reach the time when the model has developed the diabatic processes. So the digital filtering technique can be used as a scheme to reduce high frequency oscillations in model fields rather than to speed up the process of model precipitation. A comparison between the digital filtering initialization and NNMI (Huang et al. 1994) suggested that both schemes are found to produce well-balanced model states and the changes to the initial conditions made by the two schemes are similar.

1.2.4 Moisture adjustment/initialization

Diabatic initialization can produce significant divergence in the initial state. But as mentioned above, NNMI does not initialize the moisture field. If the environment is not humid enough, the upward motion associated with the initialized divergence field will not be sustained by latent heat release (Wolcott and Warner, 1981). Turpeinen (1990) indicated that diabatic NNMI had little effect on the duration of the spinup time unless the humidity field was enhanced. Thus it is important that adjustment of the humidity accompany diabatic initialization.

Moisture adjustments in most of the previous studies were carried out by setting a model's water vapor field to saturation or increasing relative humidity to a threshold so that condensation could be triggered in regions where precipitation was observed. Wolcott and Warner (1981) could produce realistic rainfall only by enhancing the moisture to 100% based on analogue IR satellite data and the reported weather from synoptic stations. Turpeinen et al. (1990) enhanced the initial relative humidity field to 95% between sigma level 0.875 and the cloud top wherever the probability of precipitation, derived from satellite imagery data, was larger than 40%. The same technique was used in Takano and Segami (1993) with different vertical levels (between σ=0.9 and σ=0.345).

Krishnamurti et al. (1984) and Krishnamurti (1985) introduced the concept of "physical initialization", an approach in which the initial moisture fields are adjusted based on a model's cumulus parameterization scheme so that the rainfall rate in the early stages of model integration is close to the observed rate. This concept has been widely used in subsequent moisture and diabatic initialization studies (e.g., Donner 1988; Krishnamurti et al. 1988, 1991, 1995; Puri and Miller 1990; Puri and Davidson 1992; Aonashi 1993; Zhao 1993). Physical initialization usually involves the "inversion" of the relevant physical processes in a model. Since the representation of the physical processes can be different from model to model, a physical initialization scheme for one model may not be applicable to another. Another disadvantage with physical initialization is that most of the microphysical processes are not reversible and an inverse scheme is

not assured, especially for those explicit microphysical schemes that include one or more ice categories.

It is noteworthy that there are studies in which the temperature adjustment is based on the moisture adjustment by preserving some specific thermal characteristics in the background field, e.g., buoyancy (Xue et al. 1998a) or virtual temperature (Aonashi 1993). In regions where the model underestimated precipitation, the water vapor field was moistened and the initial temperature was decreased to keep the virtual temperature unchanged (Aonashi 1993). On the other hand, the initial temperature was increased to keep the buoyancy unchanged in regions where the cloud water and rainwater were inserted. Moisture adjustment has also been carried out through nudging (Ramamurthy and Carr 1988).

1.2.5 Newtonian-relaxation (nudging)

The Newtonian-relaxation, or nudging, technique (e.g., Hoke and Anthes 1976; Davies and Turner 1977; Kuo and Guo 1989; Brill et al. 1991) has been widely used for dynamic initialization of numerical weather prediction models. In this procedure, one or more of the prognostic model variables are relaxed toward observations or analyses valid during or at the end of the pre-forecast period. An artificial tendency term is added to the forecast equation for a model variable α^m, of the form

$$\frac{\partial \alpha^m}{\partial t} = F(\alpha^m, \mathbf{x}, t) + G_\alpha \cdot W(\mathbf{x}, t)\varepsilon(\mathbf{x}) \cdot (\alpha^t - \alpha^m) \tag{1.2}$$

where F represents all of the model's physical forcing terms, x represents independent spatial variables, t is time, G_α is a positive relaxation coefficient that determines the relative weight of the relaxation term to F, α^t (where the superscript "t" stands for "target") is the observed α-field analyzed to the model grid and interpolated linearly in time to t, W is a four-dimensional weighting function, and ε is the analysis quality factor which has a value between 0 and 1 based on the quality and distribution of the data used to produce the gridded analysis.

The Newtonian-relaxation technique is used mainly for temperature, wind and surface pressure fields. This has been used in conjunction with diabatic initialization in many studies (e.g., Ramamurthy and Carr 1988; Wang and Warner 1988; Zhao 1993; Krishnamurti et al. 1991, 1995; Jones and Macpherson 1997). In Wang and Warner (1988), temperature is nudged as well as diabatically forced during the pre-forecast period. The combined data assimilation was shown to be beneficial because only synoptic-scale wind and temperature field features were resolved in the analyses used in the nudging terms whereas the diabatic forcing was on the mesoscale. In Zhao (1993) and Krishnamurti et al (1991, 1993) the model's temperature and wind fields are nudged while the moisture field is adjusted every time step based on the physical

initialization. Via this approach, condensation can evolve in the model and a divergence field that is consistent with the observed precipitation can be obtained at the end of the data assimilation period.

1.2.6 Cloud water initialization

Since many models now have grid scale microphysical processes in which cloud hydrometers (e.g. rain, snow, hail, etc) are explicitly predicted, initializing cloud water and rainwater fields is now necessary. Satellite and radar data are the most useful sources for this task. Zhao (1993) used the three-dimensional cloud cover fields from an operational nephanalysis and 24 hour accumulated precipitation data to initialize the cloud water field for the NCEP (National Center for Environmental Predictions) Eta model. At the beginning of the data assimilation period, the vertical profile of cloud water was specified by the cloud cover field determined from the nephanalysis, and the values of cloud water mixing ratio are scaled by the observed precipitation data. During the assimilation period, the model-produced cloud water content profile was adjusted according to the difference between the observed and model-produced rainfall. In Wu et al. (1995) the cloud water distribution was prescribed by using simulated satellite total cloud water and cloud height information while assuming a parabolic profile. Another cloud initialization study involving satellite data has been done by Kristjansson (1991). Xue et al. (1998) utilized WSR-88D radar reflectivity values to estimate cloud water content and to moisten the water vapor

field. The adjustments to the water vapor and cloud water fields are then applied during an intermittent data assimilation period. The assimilation of radar reflectivity had a large positive impact on the simulation of a squall line that occurred in the VORTEX (The Verification of the Onset of Rotation in Tornadoes EXperiment, Rasmussen et al. 1994)'95 period. Others have used the model-produced cloud water field during a pre-forecast integration period (Huang and Sundqvist 1993; Raymond et al. 1995). All studies have shown significant improvement of model forecasts in the intensity and location of precipitation by initializing the cloud water field.

1.2.7 Adjoint initializations

The concept of physical initialization is essentially a simplified adjoint approach. There have been a few efforts on developing more complex adjoint models in recent years (e.g., Verlinde and Cotton 1993; Zou et al. 1993; Vukicevic and Errico 1993; Zupanski and Mesinger 1995). Verlinde and Cotton (1993) derived the adjoint for 1D and 2D kinematic microphysical models and retrieved the initial state variables for the models. A series of identical-twin experiments showed that the proper scaling between the variables in the cost function, a sufficient amount of observations, and a good first guess were important to the convergence of the algorithm. Their results demonstrated that the adjoint algorithm did not converge when a first order discontinuity in the tendency function for one of the variables was included. To alleviate this problem

a spline over a wide interval spanning the discontinuity was constructed in their study. In a recent work by Zupanski and Mesinger (1995), an effort has been made to develop the full-physics adjoint of the ETA model. In their study, a modified, more continuous version of the Betts-Miller cumulus convection scheme (Betts 1986; Betts and Miller 1986) was incorporated in the full-physics NMC (National Meteorological Center) ETA model, and a "full-physical" adjoint model (with exclusion of surface processes, turbulence and radiation) was developed. Then a set of four-dimensional variational (4DVAR) assimilation experiments are performed using the full-physics ETA model and the adjoint model with the conventional data and the precipitation data. A summer synoptic case with a large area of convection and precipitation over the United States is used to assess the impact of the 4DVAR assimilation. It is demonstrated that the 4DVAR method with assimilation of precipitation data can result in a more realistic precipitation forecast than from the optimal interpolation method. The advantage of the adjoint method is its potential ability to use complex physical constraints and to assimilate the actual observed quantities (e.g., satellite radiance, radar reflectivity) which are general functions of the model variables. However, an adjoint model can not be defined in a mathematically correct way if the first derivative of the nonlinear forecast model does not exist. Physical processes in the atmosphere (such as condensation, convection, turbulence, etc.) are highly nonlinear and often discontinuous, especially in the case of cumulus parameterization. How best to resolve this conflict remains an open question.

The high computational expense is another disadvantage of the adjoint method, which makes it unrealistic to use full-physics adjoint models operationally in the near future.

1.2.8 OSSEs on cloud-scale numerical weather predictions

The previous studies on moisture/diabatic initialization were mostly for synoptic- or meso-α-scale numerical weather prediction. Some recent studies on the wind and/or thermal initialization for very high resolution (~1km) numerical simulations have been done by using Doppler radar data (e.g., Lin et al. 1993; Crook 1994, Crook and Tuttle 1994; Shapiro and Lazarus 1993; Lazarus 1996; Weygandt et al. 1990, 1993, 1998). There are a few studies using observing system simulation experiments (OSSEs) to assess the impact of moisture initialization in storm-scale models (Weygandt et al. 1990; Lazarus 1993; Park 1996). Weygandt et al.(1990) tested the sensitivity of a 2D cloud-scale model to initial wind, temperature and moisture fields. Their results indicated that successful numerical simulations of convective storms could be made in a moist, stratified atmosphere by knowing only the wind field perfectly at high temporal frequency. This may due to the fact that the mass field can be induced from the wind field through the dynamical constraints in the model equations. They also found that the initial moisture field is important in maintaining the induced mass field. Lazarus (1993) carried out a set of 3D thermal bubble simulations using the Advanced Regional Prediction System (ARPS, Xue et al., 1995). His results

indicated that the insertion of moisture (i.e., water vapor, cloud and rain water) information had a positive impact on the model forecasts of the wind and thermal fields, although the extent of the impact is dependent on the quality of the initial wind field. For instance, it was suggested in Lazarus (1993) that the initial rainwater information had larger (positive) impact on the wind forecast than the initial water vapor information when all three Cartesian components of the initial wind field were known, but that the initial water vapor field was more important when the initial wind field is not fully known (e.g., only one component is specified). Park (1996) and Park and Droegemeier (1998) investigated the sensitivity of a simulated convective storm to the perturbations in the initial water vapor field using a tangent linear model (TLM) of the ARPS. Experiments were done to test the sensitivity of the storm predictions to the initial water vapor errors inside and outside cloud/rain regions. It was shown that the in-cloud moisture is important for generating secondary storms and the environmental moisture is important in enhancing the main storm. They also showed that the cost function in their TLM is very sensitive to errors in the temperature field, either within or outside cloud/rain regions. These OSSEs have provided guidelines for future convective-scale data assimilation studies.

1.3 Outline of the present study

As mentioned above, most of the previous real-data diabatic initialization studies were carried out using meso-α or larger- scale numerical weather

prediction models. Little has been done for meso-β and smaller scale models, although spinup problems exist in these models as well (Xue et al 1998; Carpenter et al. 1998). This is mostly due to the resolution limitations in the conventional weather observation systems such as radiosondes. There were few high-resolution weather observations (comparable to convective-scale) available until the early 1990's when the Next Generation Weather Radar (NEXRAD) network started to be established. As a result over 160 10-cm wavelength Weather Surveillance Radar-1988 Doppler (WSR-88D) radars are deployed over the United States (e.g., Crum and Alberty 1993). At the same time, more channels have been added to the sensors/sounders on new GOES systems and better quality and resolution of imagery data are available. It is also noteworthy that the rapid development in computing power and data transmission has made the dissemination of high resolution data much more efficient than before. The GOES satellite data can provide imagery data with resolutions of 2 km in space and 15 minutes in time. The NEXRAD data can provide observations of cloud and precipitation systems with resolutions as high as 1 km in space and 6 minutes in time. All these developments have provided necessary resources for convective-scale data assimilation and numerical weather prediction. Our research is based on this premise and the goal is to develop and test a diabatic initialization tool for convective-scale numerical weather prediction using the ARPS.

The research required four steps:

1) to develop a cloud analysis system for moisture, cloud liquid/ice water and precipitate (including rain, snow, and hail) fields using multi-sensor observations;
2) to develop a moisture and diabatic initialization scheme in which moisture and thermal fields are adjusted based on the cloud and precipitation analyses;
3) to test the moisture and diabatic initialization scheme using simulated storms;
4) to test the moisture and diabatic initialization scheme with real storms.

For the first step, I developed a cloud analysis system in the ARPS Data Analysis System (ADAS, Brewster 1996) based on the LAPS (Local Analysis and Prediction System, Albers et al., 1996) cloud analysis. It was mentioned that the latest weather observing systems like radar and satellite are more advanced than the conventional observing networks. But there are limitations in these systems as well. The resolution of satellite imagery data is very poor in the vertical. Radar data resolution varies in space and the vertical resolution becomes poor at far ranges. Furthermore the Doppler radar can measure only the wind component which is along the radial direction rather than a full wind vector. The ADAS cloud analysis system synthesizes data obtained from surface, satellite, and radar observations and constructs three-dimensional cloud and precipitate fields. By using multi-sensor observations instead of just any individual source,

limitations to each individual observing system can be overcome and a more accurate analysis can be obtained.

In the second step, moisture and temperature fields are adjusted in correspondence with the analyzed cloud and precipitate distributions. Initial cloud and precipitation fields in the model are adjusted toward the analyses, with flexibility to account for possible analysis errors and imbalances between data and the numerical model. The thermal field is adjusted to compensate for the negative buoyancy introduced by the analyzed cloud and precipitation. Since numerical simulations show a close relationship between the thermal field and latent heat release due to cloud condensation, a thermal adjustment scheme that takes into account the latent heating effect is also developed in our diabatic initialization scheme. As mentioned before, numerical models started from conventional surface and radiosonde observations often under-predict precipitation due to the deficiencies in the initial moisture, latent heating, and vertical circulation fields. Through the moisture and diabatic adjustments, vertical circulations can be forced to develop and the associated divergence patterns should then induce precipitation with a realistic spatial and temporal distribution given that these adjustments are based on the analyzed cloud distribution.

After the thermal adjustment, the background water vapor field is moistened in the analyzed cloud regions. The moisture adjustment is important

for stimulating cloud condensation and retaining the vertical circulations induced by diabatic initializations.

The major difference between the present diabatic initialization and previous ones is that it is based on a three-dimensional cloud analysis that uses surface, satellite and radar data, rather than using two-dimensional precipitation estimations. Therefore there is no need to make major assumptions about vertical distributions of latent heating rate. The present initialization scheme depends mainly on the analysis of observations and is independent of model microphysical parameterization schemes. Therefore it can be applied to different models.

In the third step, the data assimilation system is tested using a set of observing system simulation experiments. A simulated storm is created using the ARPS. Cloud and precipitation fields are produced from the simulated storm and new simulations initialized from the analyses are carried out. Sensitivities of the model simulations to different moisture and diabatic initialization strategies are examined. Through these experiments, we investigated the merits and flaws of the assimilation system and obtained guidelines on real data applications.

In the last step, we applied the cloud analysis and diabatic initialization scheme to a real convective precipitation event. Through this set of experiments, the hypothesis behind the present research, i.e., that the new data assimilation system can improve convective-scale numerical weather predictions, is tested.

In Chapter 2, the components of the cloud analysis are described in detail. The moisture and diabatic initialization scheme is presented in Chapter 3. The OSSEs for the sensitivity tests are presented in Chapter 4 and real data assimilation and simulation tests are presented in Chapter 5. Conclusions and an outlook for future work are given in Chapter 6.

Chapter 2
ADAS Cloud Analysis

2.1 Introduction

In order to provide detailed initial conditions for the Advanced Regional Prediction System (ARPS, Xue et al., 1995) moisture variables and to serve as the basis for moisture data assimilation, a cloud analysis scheme has been developed in the ARPS Data Analysis System (ADAS, Brewster, 1996; Zhang et al., 1998). It incorporates cloud information from surface stations reporting World Meteorological Organization (WMO) standard Aviation Routine Weather Reports (METARs), satellite infrared and visible imagery data, and radar reflectivity to construct three-dimensional cloud and precipitate fields. The products of the analysis package include three-dimensional volumetric cloud fraction, cloud liquid- and ice-water mixing ratios, cloud and precipitate types, in-cloud vertical velocity, and the mixing ratios of rain, snow, and hail. Cloud base, cloud top and cloud ceiling fields are also derived. A schematic illustration of the ADAS cloud analysis system is shown in Fig. 2.1.

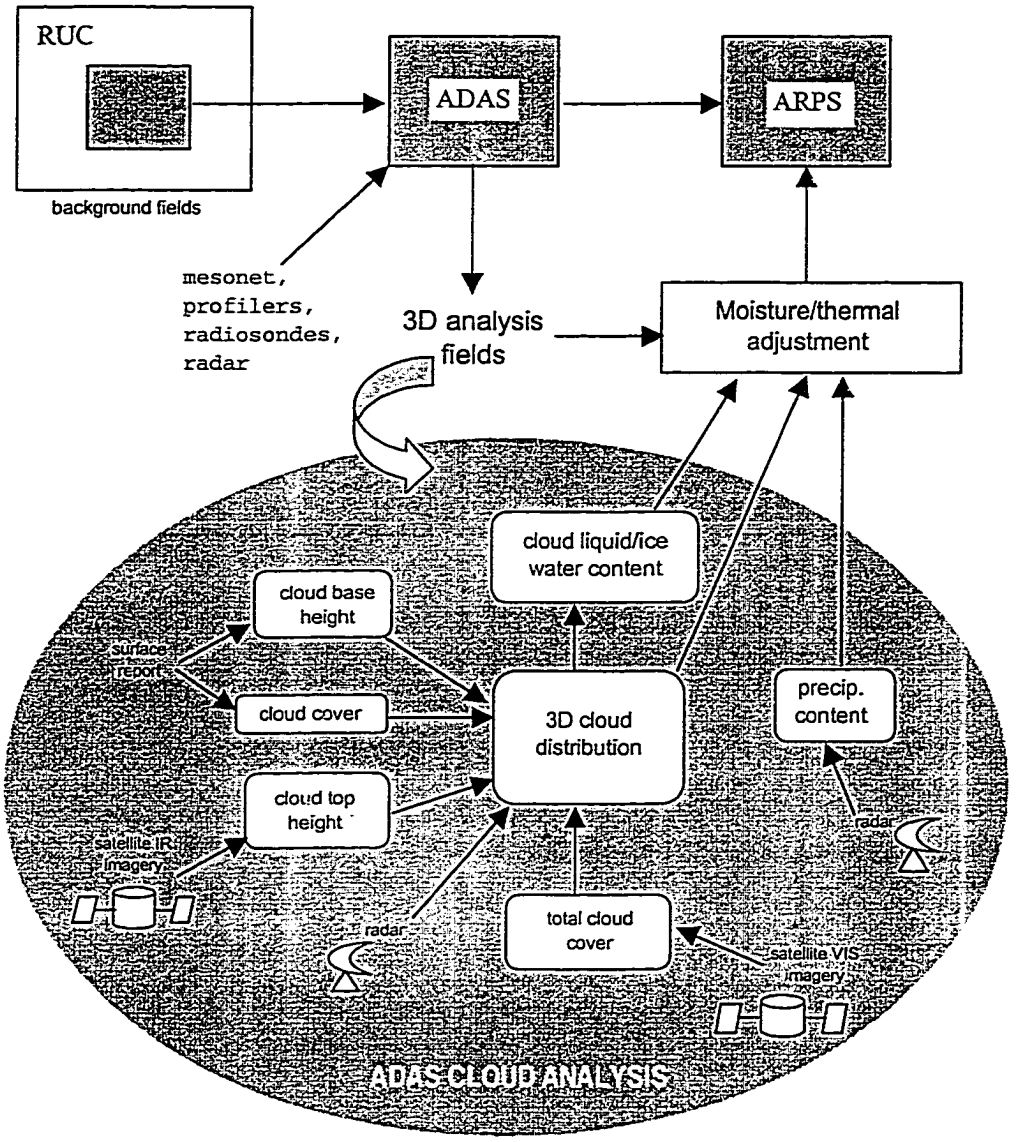

Fig. 2.1 Schematic diagram of the ADAS cloud analysis system.

The ADAS cloud analysis system is based on the LAPS (Local Analysis and Prediction System, Albers et al., 1996) cloud analysis with some modifications. The differences in the ADAS from the LAPS cloud analysis

include: 1) improved background cloud fraction field, 2) improved Barnes interpolation scheme, 3) improved cloud top analysis from satellite infrared data, 4) usage of lifting condensation level, 5) quality check on cloud type analysis, 6) improved in-cloud vertical velocity profile, and 7) more flexibility in the control of empirical parameters. The detailed analysis procedures are presented in this chapter.

2.2 Three-dimensional volumetric cloud fraction (VCF) analysis

The volumetric cloud fraction analysis scheme utilizes surface cloud reports to provide cloud base and cloud fraction (CF) information in the lower atmosphere. Cloud top is determined from satellite infrared data, while radar reflectivity is used primarily to add cloud information in the middle troposphere. Visible satellite imagery is used to evaluate the total cloud coverage and correct for overestimations of cloudiness. A flowchart of the volumetric cloud fraction analysis scheme is shown in Fig. 2.2.

2.2.1 Background volumetric cloud fraction field

In the ADAS volumetric cloud fraction (VCF) analysis, a three-dimensional background VCF field is derived from the ADAS relative humidity analysis using an empirical power relationship similar to the one used in Koch et al. (1997):

$$VCF = \left(\frac{RH - RH0}{1.0 - RH0} \right)^b \tag{2.1}$$

Here VCF has a value that ranges from 0.0 to 1.0, RH is the relative humidity, RH0 is a relative humidity threshold whose value is dependent on height, and b is an empirical constant. In the ADAS cloud analysis, b is set to 2.

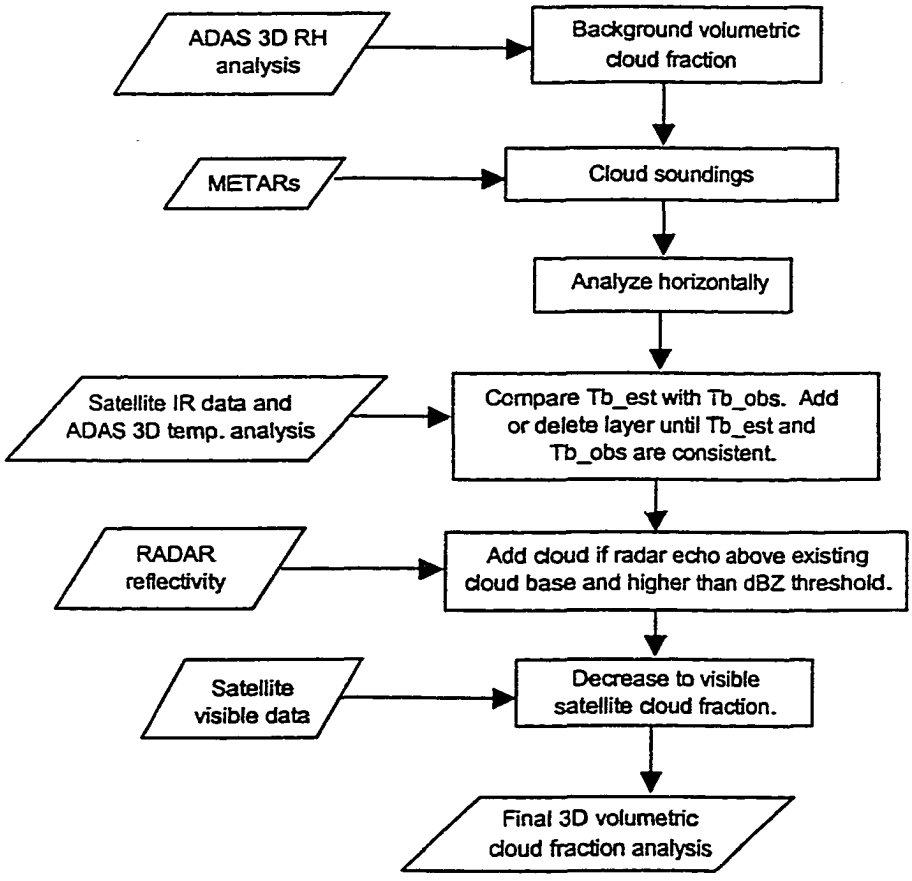

Fig. 2.2 Flowchart of the ADAS volumetric cloud fraction analysis.

The relationships between VCF and RH in the ADAS cloud analysis are depicted in Fig. 2.3. An example of the background VCF field derived from the ADAS relative humidity analysis on 18Z May 7, 1995 and a satellite visible image valid around the same time are shown in Fig. 2.4 and Fig. 2.5. The ADAS relative humidity analysis used the RUC (Rapid Update Cycle, Benjamin et al. 1994) analysis at 18Z as the background and the observations are mainly from the Oklahoma mesonet. It can be seen that the large cloudy region over Oklahoma and north-central Texas was successfully captured in the background VCF field. The narrow convective cloud band over the Texas panhandle was missed because of the sparse RH observations in that area and the failure of the RUC analysis to capture it as well.

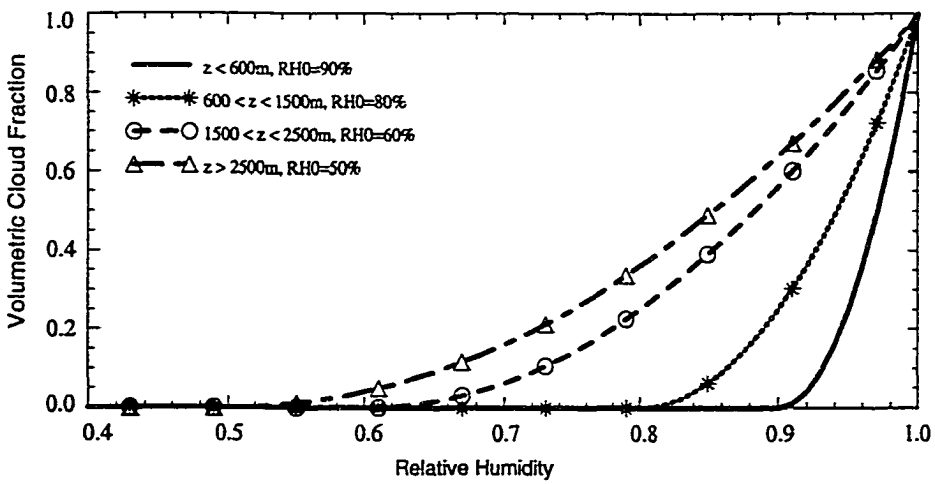

Fig. 2.3 Relationships between volumetric cloud fraction and relative humidity at different height levels [see Eq. (2.1) in the text].

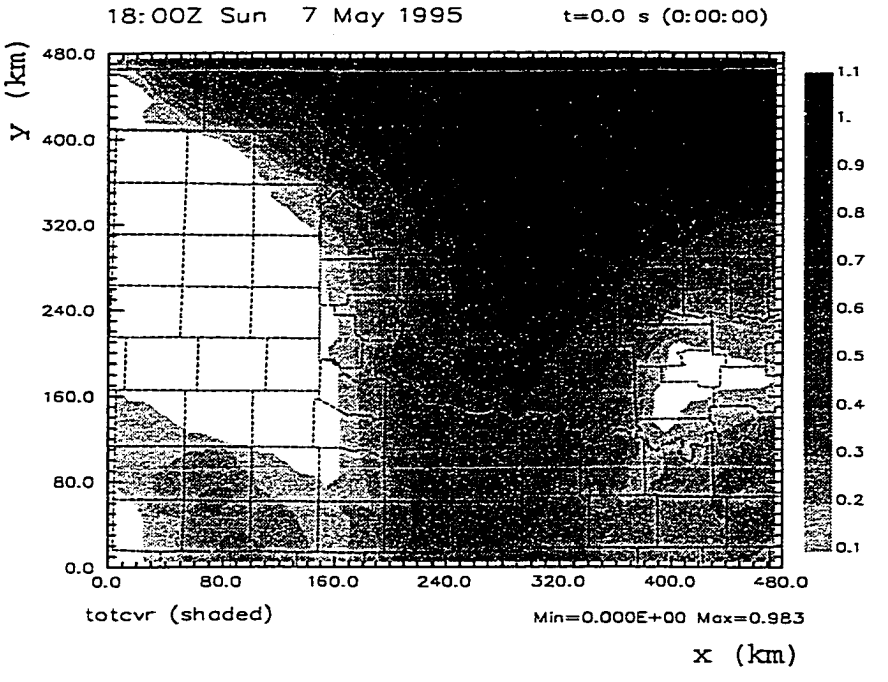

Fig. 2.4 Cloud cover derived from the ADAS relative humidity analysis at 18Z May 7, 1995.

2.2.2 Insertion of the cloud reports from METARs

The cloud reports from each METAR station provide cloud base and cloud fraction information. The cloud fraction information is quantified according to Table 2.1 (from the LAPS cloud analysis software). Using an assumed cloud thickness, the cloud top height is specified and a cloud sounding is generated. The assumed thickness is a function of the reported cloud base height and cloud fraction. When the reported cloud base is lower than 1 km, the cloud layer depth is set to the same as the cloud base height. When the reported cloud base is

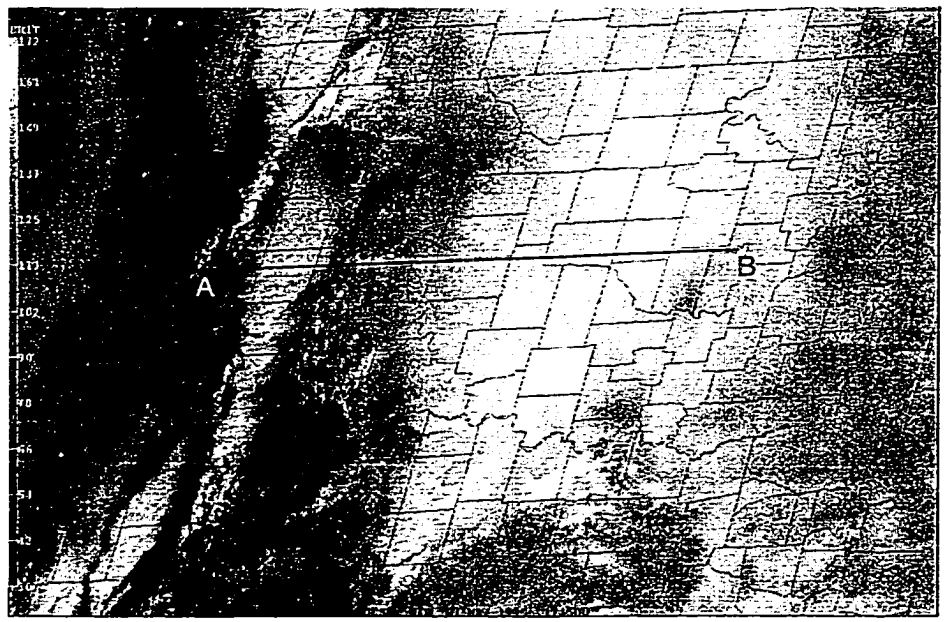

Fig. 2.5 Satellite visible image at 1745Z May 7, 1995. The line AB indicates the location where vertical cross sections of various fields are taken.

higher than 7 km, the cloud layer depth is set to 1.5 km. A linear variation of cloud depths between 1 km and 1.5 km is used for the clouds that have reported bases between 1 km and 7 km. If the reported cloud fraction is less than 0.5 the cloud depth is set to 500 m. The METAR-derived cloud soundings are horizontally interpolated to the analysis grid through a Barnes scheme. In a departure from LAPS, influence radius limits in the ADAS cloud analysis are applied in the objective analysis procedure. We found that without the influence radius limits, the interpolation tends to overestimate cloud coverage.

Table 2.1 Volumetric cloud fractions associated with the METAR cloud reports.

report	CLR	-SCT	SCT	aBKN	BKN	OVC	OVC	X
cover	0.01	0.15	0.25	0.40	0.70	0.60	1.00	1.00

2.2.3 Insertion of satellite infrared (IR) imagery data

To utilize satellite IR imagery data, an expected brightness temperature (T_{b_e}) field is computed from the three-dimensional METAR cloud fraction analysis and the ADAS temperature analysis. Clouds are then added or deleted depending upon the difference between the expected brightness temperature and the observed satellite brightness temperature T_{b_o}. The observed brightness temperature is obtained from the 11.24μm channel for GOES-6/7 and the 10.7μm channel for GOES-8/9.

If T_{b_o} is warmer than T_{b_e} the METAR clouds are reduced by lowering the top of the solid clouds (i.e., VCF=1.0) and by diluting the partial clouds (i.e., $0 < VCF < 1$). This IR based deletion procedure does not apply to low warm clouds so that erroneous clearing of very low cloud decks can be prevented.

If, on the other hand, T_{b_o} is colder than T_{b_e}, cloud top is determined from T_{b_o} and a layer of solid cloud is inserted. The IR cloud layer is usually 1.5 km thick and is constrained to not be lower than the METAR cloud base. The IR cloud top height can be obtained by two schemes. When the observed brightness

temperature is below a threshold (-20°C), cloud top is determined by scanning the ADAS temperature profile at a grid point for a temperature that matches the satellite brightness temperature. When the observed brightness temperature is above that threshold, a second cloud-top analysis algorithm following that described in MacPherson et al. (1996) is used. This algorithm assumes an idealized profile of temperature and humidity through a stratocumulus layer. A lifting condensation level is found and is taken as the cloud base. Then from the cloud base the air is allowed to ascend moist adiabatically until it reaches the satellite brightness temperature and the cloud top level is found. This scheme can provide a more reliable cloud top height analysis than the scan-and-matching method in the situations when cloud tops are associated with temperature inversions, e.g., for persistent stratocumulus clouds. When the inversion is not well resolved by the gridded temperature analysis, the matched temperature will not correspond to the cloud top but to some point much higher where the cloud-free environment temperature has dropped to the value of T_{b_o}. An example of such situation is illustrated in Fig. 2.6. The thick solid line in the figure represents the true atmospheric temperature profile and the thick dashed line represents the temperature analysis profile on the model grid. T_s and T_d are the air temperature and dewpoint at the surface, respectively. T_t indicates the cloud top temperature, which is approximately the air temperature at the bottom of the inversion layer. The thin dot-dashed lines represent dry- and moist-adiabatic lines. The real cloud top height is located at point A. However, the scan-and-matching method will

give a cloud top height corresponding to the point B (Fig. 2.6) since the model temperature analysis did not resolve the inversion at T_1. Using the conceptual model a cloud top height at point C is obtained, which is more realistic than the cloud top B.

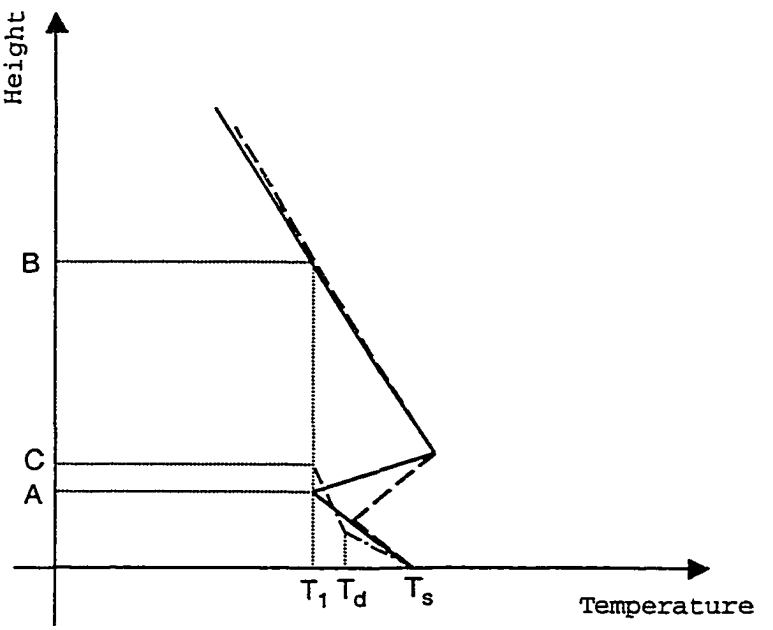

Fig. 2.6 Illustration of a conceptual model for determing the cloud top height for stratocumulus. The thick solid line represents the real atmospheric temperature profile, and the long dashed-line represents the temperature profile resolved by the model grid. T_s, T_d, and T_1 are the surface temperature, surface dewpoint, and the cloud top temperature, respectively. The dot-dashed lines indicate the dry- and moist-adiabatic temperature lapse rates. Points A, B, and C represent the cloud top height of the real cloud, and that derived from the scan-and-matching method and from the conceptual model, respectively.

Figs. 2.7a, b show vertical cross sections of the VCF analysis at 18Z May 7, 1995 after inserting METARs and satellite IR data, respectively. The location of the vertical cross section is indicated by the line AB shown in Fig. 2.5. It can be seen that high cloud decks were added over the top of the METAR-derived clouds at $x \approx 60$ km and $x > 160$ km. A small amount of METAR-derived mid-level cloud at $x \approx 120$ km and $z \approx 3$ km was removed after inserting the satellite IR data.

2.2.4 Insertion of radar reflectivity data

Radar reflectivities observed by multiple radars are remapped on to the ADAS grid and are combined to produce a single three-dimensional radar reflectivity analysis (Brewster 1996). At each grid point, reflectivity values from multiple radars are averaged together using a simple inverse-distance weighted average. The resulting reflectivity field is then bilinearly interpolated in space to fill in the gaps between radar beams. Clouds with VCF of 1.0 are inserted in the radar echo region if the radar echo is above the lowest METAR cloud base and if the reflectivity exceeds a threshold. In cases when there are no METARs available, the lifting condensation level determined from the ADAS temperature and humidity analyses is used as the cloud base. Without the lifting condensation level, clouds can only be inserted in the radar echo region above the satellite IR cloud base, which can be much higher than the actual cloud base (see Fig. 2.7b). This can result in underestimation of cloudiness. The radar echo threshold used in

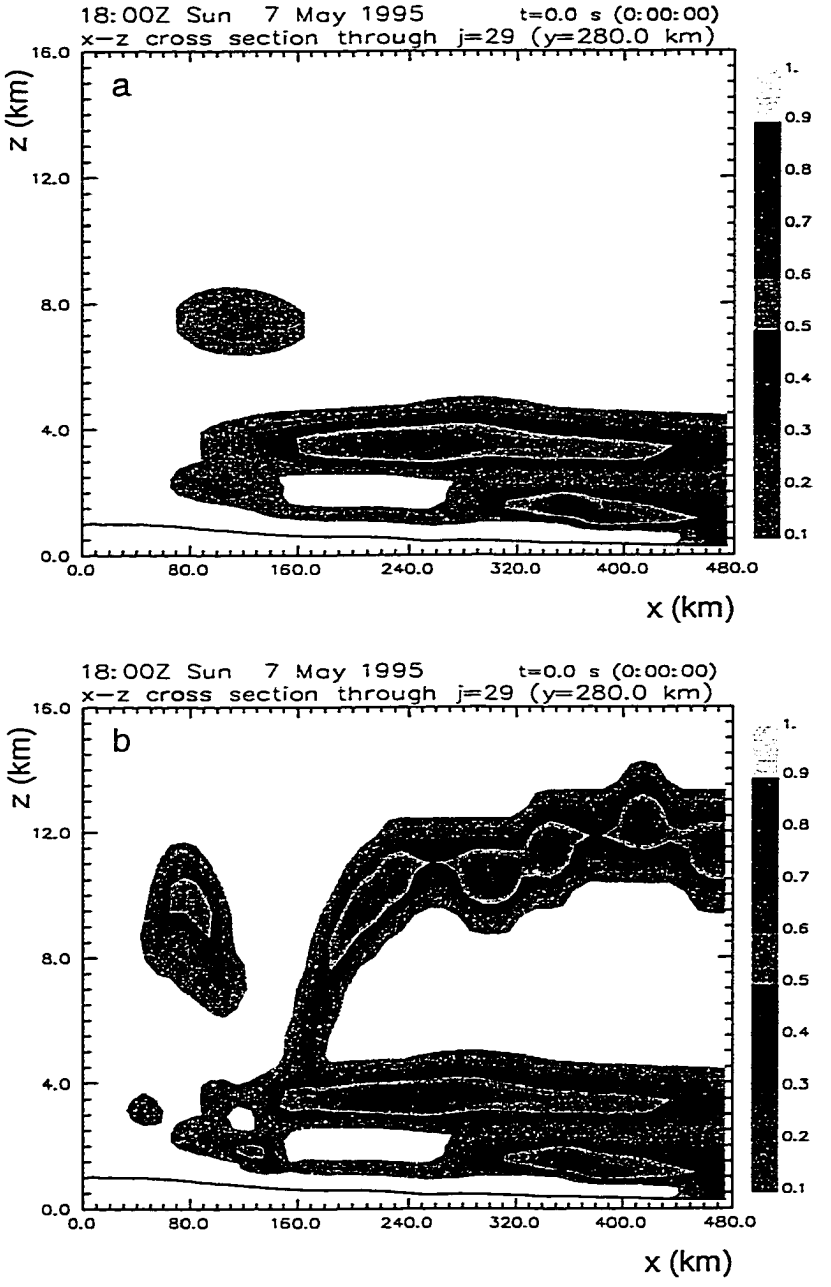

Fig. 2.7 Vertical cross section of the ADAS VCF analysis at 18Z May 7, 1995 after inserting the METARs (a) and the satellite IR imagery data (b). The location of the cross sections is indicated by the line AB in Fig. 2.5.

the ADAS cloud analysis is 20 dBZ for points below 1500 m above ground level (AGL) and 10 dBZ for points above 1500 m AGL. The two reflectivity thresholds and the two related height parameters are adaptive factors. These thresholds are used as simple quality control criteria for removing ground clutters and other non-precipitation radar echoes. Shown in Fig. 2.8a is the vertical cross section of the analyzed radar reflectivity field from two radars, one at Amarillo and the other at Oklahoma City. The VCF analysis after inserting the radar reflectivity is shown in Fig. 2.8b.

2.2.5 Insertion of satellite visible imagery data

A cloud albedo field is derived from the satellite visible imagery data and then a column total cloud fractional cover field is calculated from the albedo. The three-dimensional ADAS VCF analysis is integrated vertically and compared to the visible satellite cloud cover. If the ADAS cloud cover is significantly more than that derived from the visible data, the gridded volumetric cloud fraction is reduced iteratively for the total cover to be consistent with the satellite-derived cloud cover. Fig. 2.9 shows the vertical cross section of the VCF after inserting the satellite visible data. Comparing Fig. 2.9 with Fig. 2.8b we can see that a small amount of low clouds near $x \approx 125$ km and $z \approx 1.5$ km was removed according to the satellite visible data. Fig. 2.10a shows the column total cloud coverage before and after inserting the visible satellite data. The overestimation of cloud coverage in the area south-east of the Texas panhandle (Fig. 2.10a) is

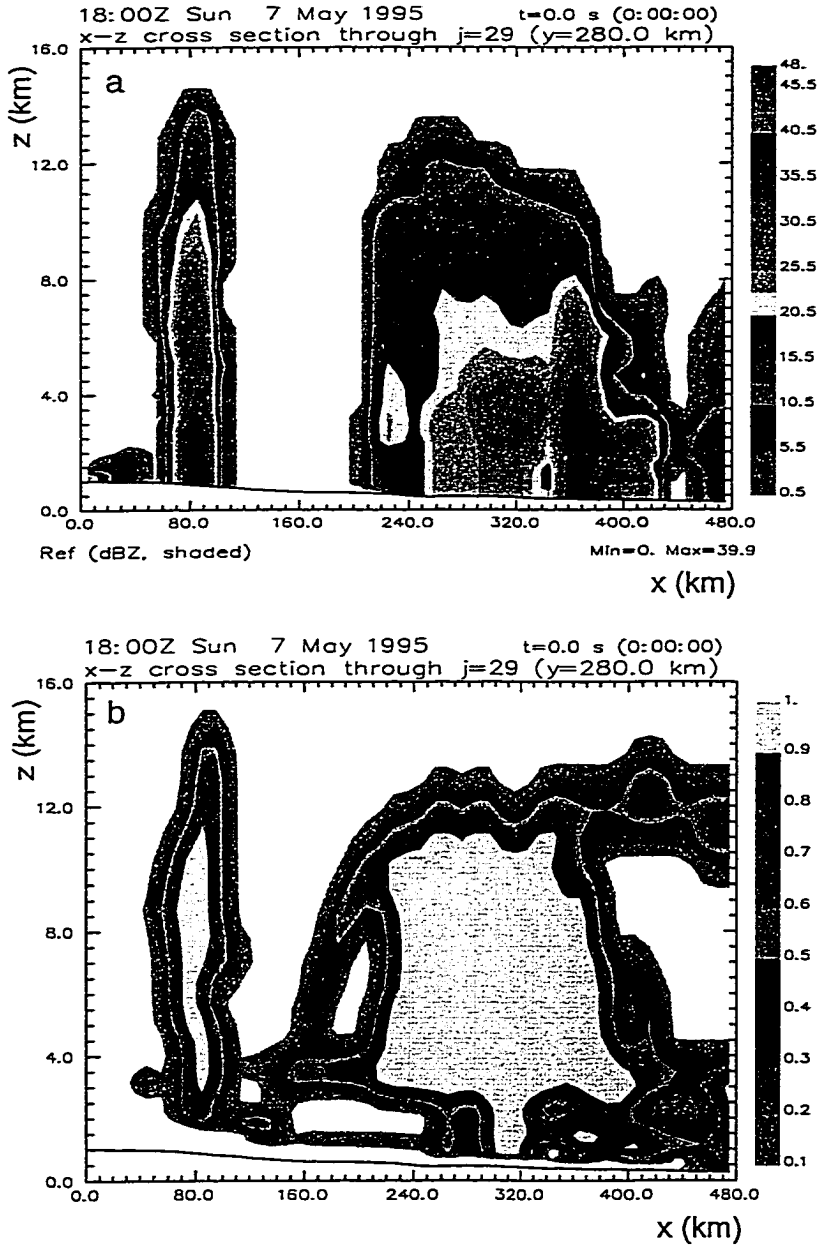

Fig. 2.8 Same cross section as in Fig. 2.7 except for the observed radar reflectivity (a) and the VCF analysis after inserting the reflectivity (b).

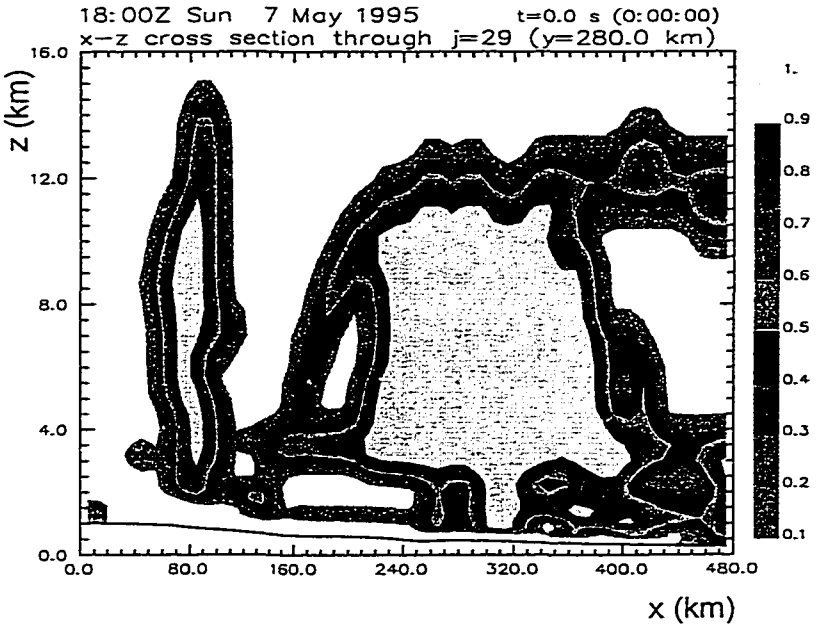

Fig. 2.9 Same cross section as in Fig. 2.7 except for the VCF analysis after inserting the satellite visible imagery data.

successfully corrected by the visible satellite data (Fig. 2.10b, Fig. 2.5). An Y-shaped low cloud coverage region in the north-eastern Texas panhandle (Fig. 2.5) was defined better in the cloud field after inserting the visible satellite data than that before the insertion.

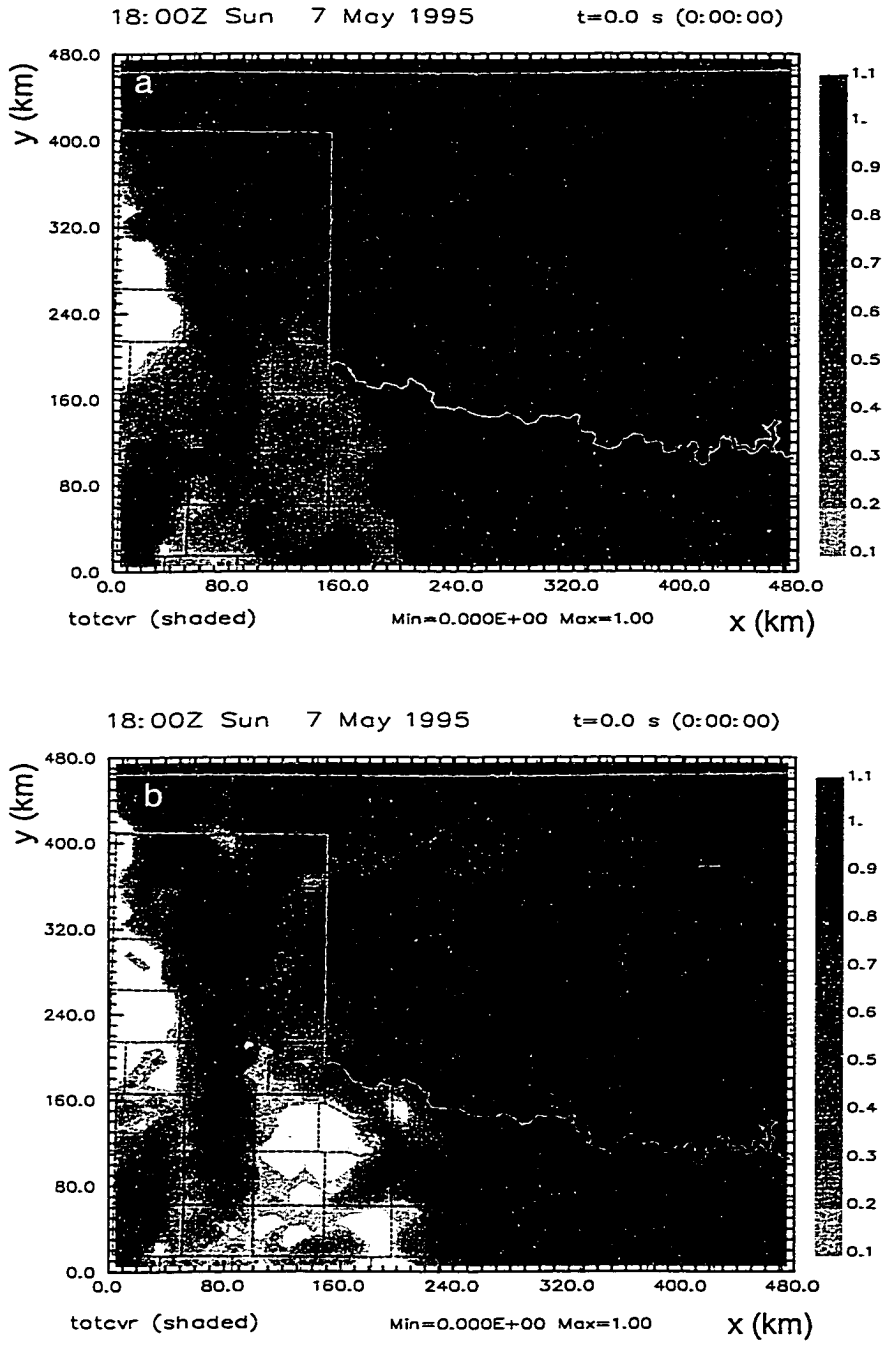

Fig. 2.10 Column total cloud cover before (a) and after (b) inserting the satellite visible data.

2.3 Cloud liquid- and ice-water mixing ratio analysis

After the three-dimensional volumetric cloud fraction distribution is obtained, cloud liquid- and ice-water content fields are calculated using a one-dimensional Smith-Feddes model (Albers et al., 1996; Haines et al., 1989) for regions where the cloud fraction exceeds a threshold (an adaptive parameter). A flowchart of the ADAS cloud liquid- and ice-water content analysis is shown in Fig. 2.11. The adiabatic liquid water content (*ALWC*) is estimated by assuming

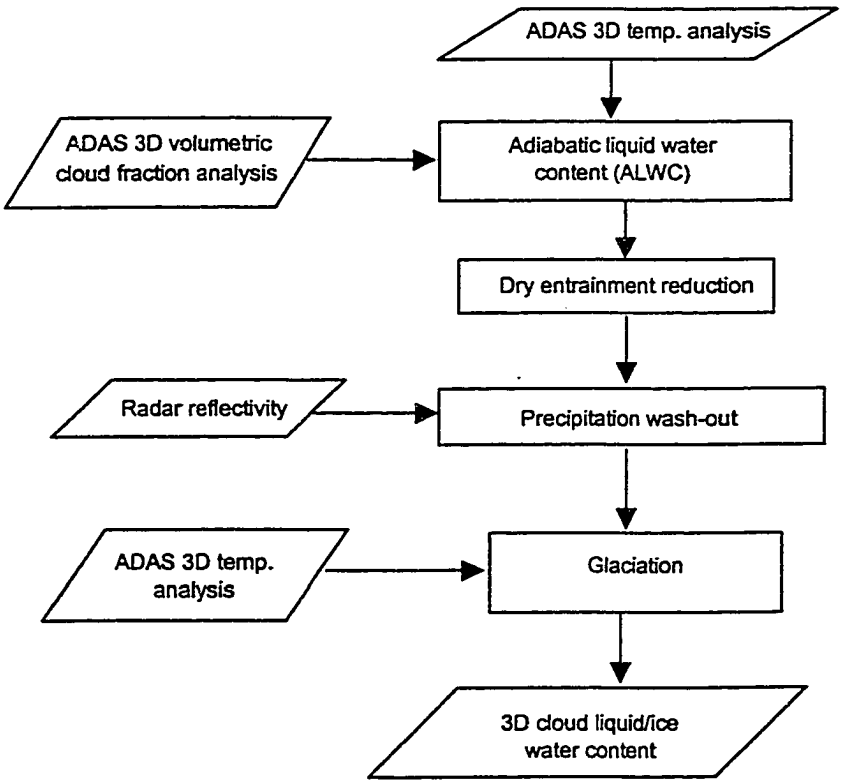

Fig. 2.11 Flowchart of the ADAS cloud liquid/ice water content analysis.

moist adiabatic ascent from cloud base to cloud top. The algorithm for *ALWC* is the following:

$$ALWC_k = ALWC_{k-1} + q_{vs_k-1} - q_{vs_k} \tag{2.2}$$

where q_{vs} is saturation water vapor mixing ratio and k is the vertical grid index. A reduction is then applied to *ALWC* to account for entrainment (Fig. 2.12). The resulting *ALWC* is parameterized as all liquid water for temperatures warmer than –10°C, as all ice for temperatures colder than –30°C, and as a linear variation between these extremes for temperatures between –10°C and –30°C. The ADAS temperature analysis and the analyzed cloud liquid and cloud ice mixing ratio fields for 18Z May 7, 1995 are shown in Figs. 2.13 and 2.14, respectively.

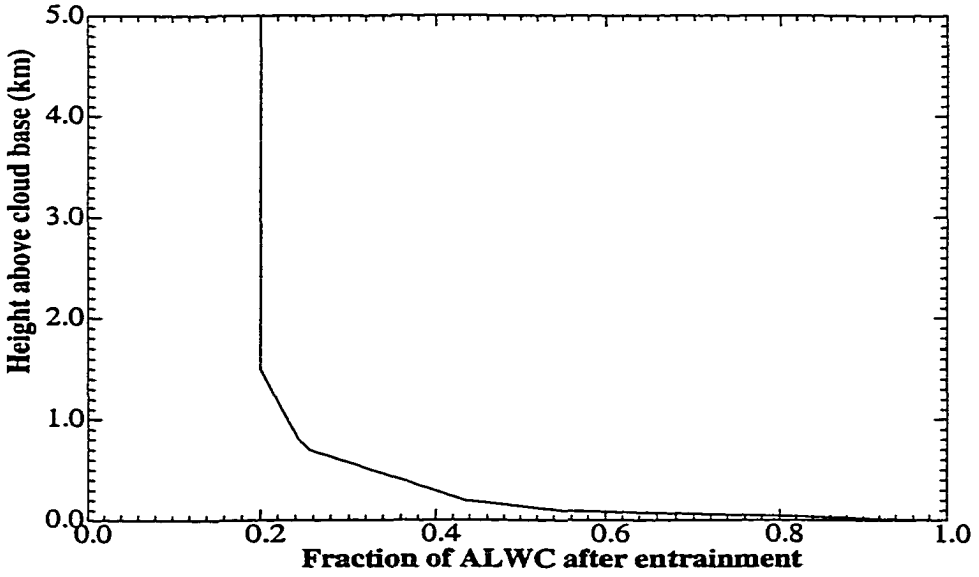

Fig. 2.12 Entrainment reduction curve.

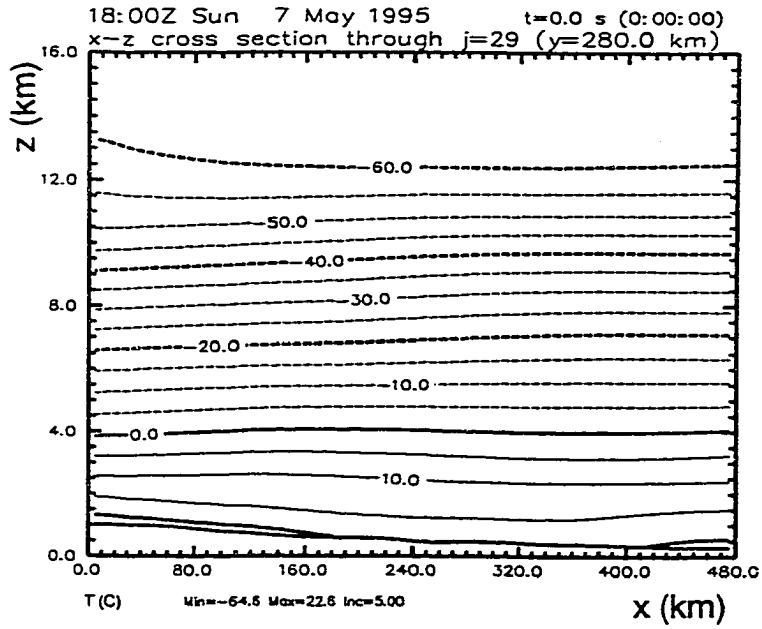

Fig. 2.13 Vertical cross section of the temperature analyses at 18Z May 7, 1995. The cross section is taken along the line AB as indicated in Fig. 2.5.

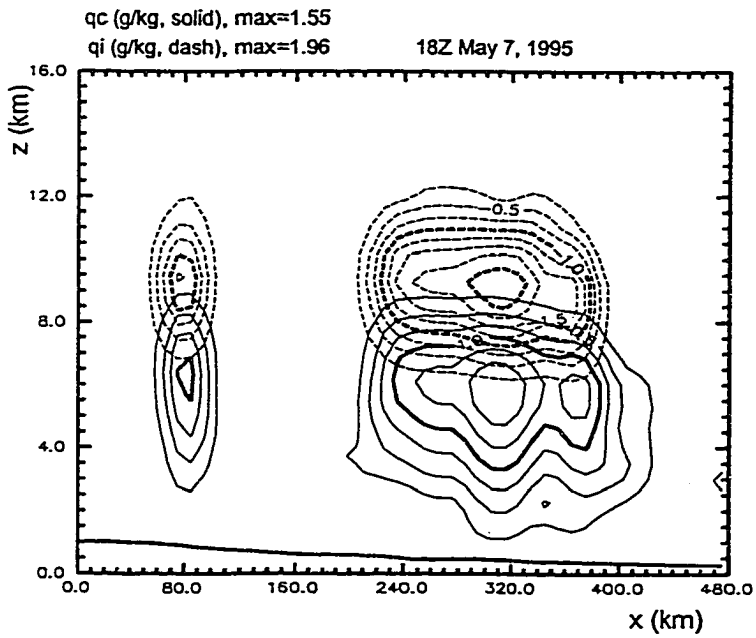

Fig. 2.14 Same cross section as in Fig. 2.13 except for the cloud liquid (solid line) and cloud ice (dashed line) water mixing ratio (unit: g/kg) analyses at 18Z May 7, 1995. The contour interval is 0.25g/kg.

2.4 Cloud type and in-cloud vertical velocity analysis

Cloud type is defined as a function of cloud depth, ambient air temperature, and static stability (see Table 2.2). In the ADAS cloud analysis, cloud type at each grid point is compared to those in the neighboring area. Nearby "blocky" cumulonimbus clouds are patched together to create a spatially continuous cumulonimbus tower (x = 80 km in Figs. 2.15a, b). The two cumulonimbus systems were clearly shown in the satellite image (Fig. 2.5) and the vertical cross section of the radar reflectivity (Fig. 2.8a). It is apparent that the cumulonimbus tower near x = 80 km is narrower yet more intense than the other one at $x = 320 - 400$ km. Therefore, the cloud type field after the quality check looks more consistent and more reasonable than that before the quality check (Figs. 2.15a, b).

In the LAPS cloud analysis, a cloud bogus vertical velocity field is produced in grid columns where clouds exist. The cloud bogus-vertical velocity field is determined by using prespecified profiles for different cloud types and cloud depths. The purpose of the cloud w-field diagnosis is to provide an approximate estimate for updrafts in the cloud and precipitation systems, given the fact that conventional upper air observations are deficient for providing meso-or

Table 2.2 Cloud types as a function of cloud depth H (km) and stability σ (K/km) for temperatures warmer than -10°C (a), for temperatures between -20°C and -10°C (b), and for temperatures colder than -20°C (c).

a) $T \geq -10^{o}C$

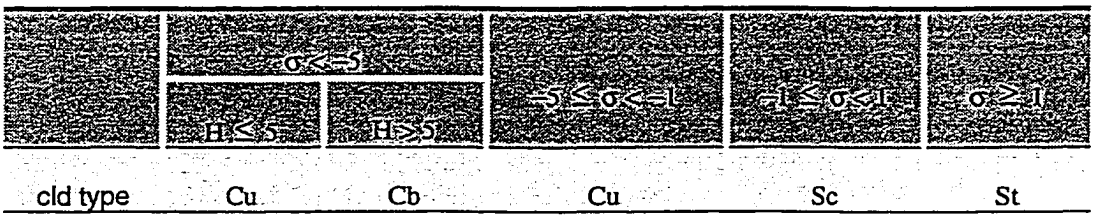

b) $-20^{o}C \leq T < -10^{o}C$

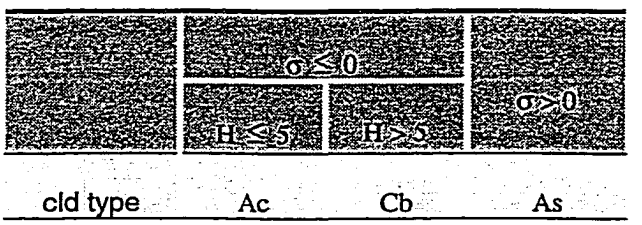

c) $T < -20^{o}C$

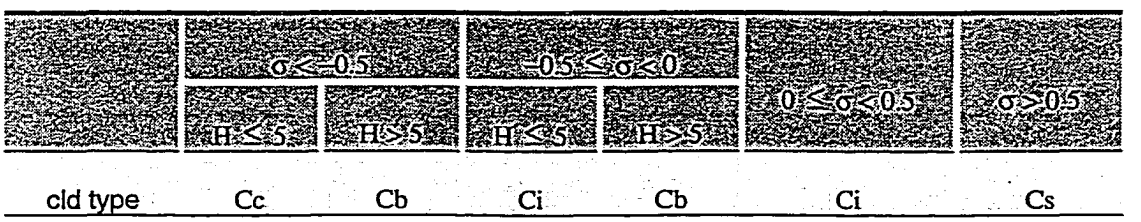

Note: T = temperature (K)

$\sigma = \partial\theta_e/\partial z$, static stability (K/km)

H = cloud depth (km)

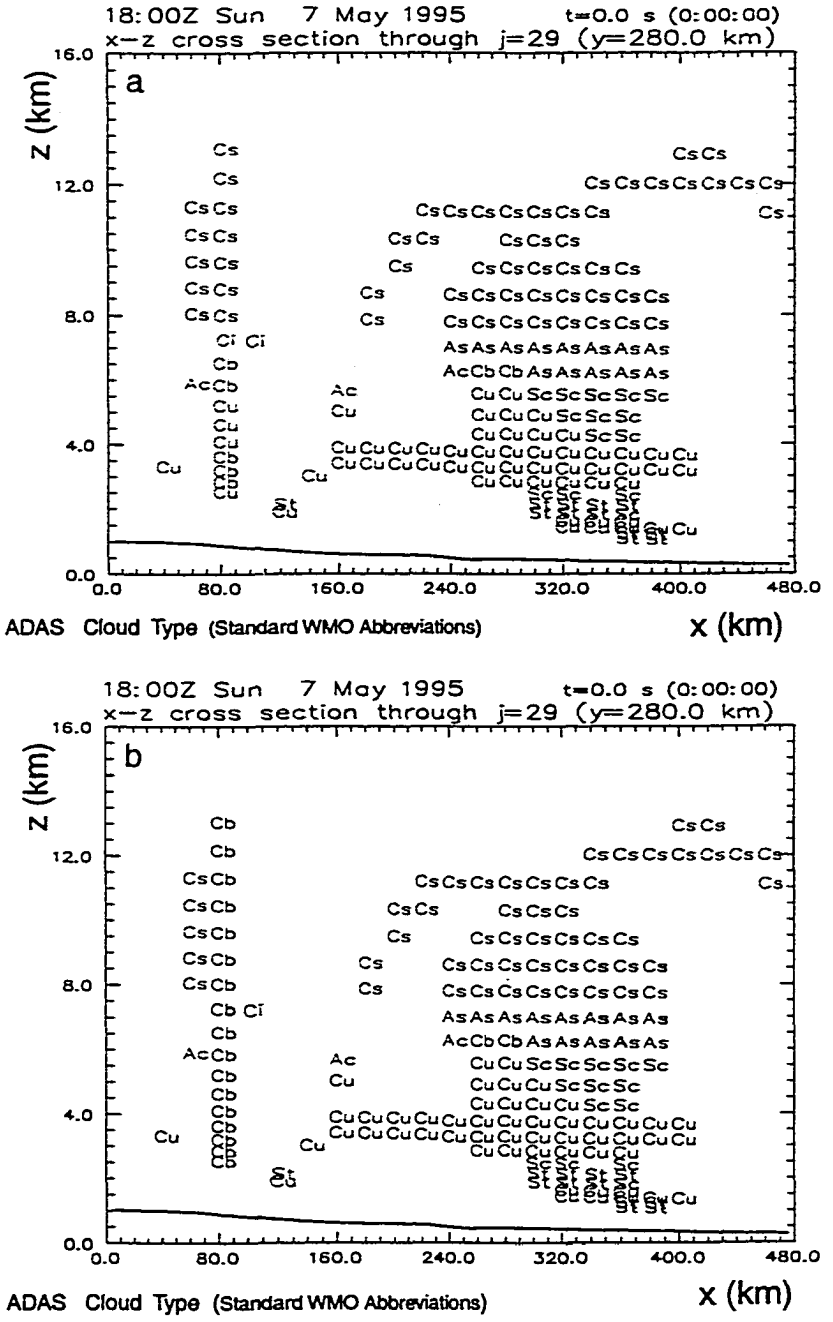

Fig. 2.15 Vertical cross sections of the cloud type field at 18Z May 7, 1995 before (a) and after (b) the quality check. The cross sections are taken along the line AB as indicated in Fig. 2.5.

convective scale vertical velocity measurements. This cloud w-field could be used to initialize numerical models when there were developing convective precipitation systems at the initial time. However, such an initial cloud-w field may not be retained because it is not balanced, in the sense of the mass continuity, by a consistent horizontal divergence field. It is also important to point out that there may be downdrafts in cloud/precipitation systems, especially during the decaying stages of the systems. More sophisticated methods have been developed for obtaining high resolution three-dimensional velocity fields from WSR-88D observations, e.g., single Doppler velocity retrievals (SDVR, Shapiro et al., 1995; Xu et al., 1995; Zhang and Gal-Chen, 1996). For the completeness of the ADAS cloud analysis system, however, the cloud w-field diagnosis scheme is described below.

For a cumuliform cloud the vertical velocity profile is a parabolic curve with the maximum located at the one-third of the cloud depth above the cloud base. The cloud base and cloud depth are determined from the ADAS three-dimensional cloud fraction analysis. The parabolic function for the cloud w-field is

$$w = w_{\max}\left[1 - \left(\frac{z - z_m}{\frac{2}{3}H}\right)^2\right] \tag{2.3}$$

$$H = z_t - z_b \tag{2.4a}$$

$$z_m = z_b + \frac{H}{3} \tag{2.4b}$$

$$w_{\max} = w_0 \cdot H \tag{2.4c}$$

Here w represents the in-cloud vertical velocity and z is the height coordinate. z_t and z_b represent the cloud top and base heights, respectively and H is the cloud depth. The maximum vertical velocity, w_{max}, is proportional to the cloud depth. Note that the location for w_{max} is defined at the one-third rather than one-half of the cloud depth above the cloud base, because vertical velocity is not necessarily zero at cloud base. In the LAPS cloud analysis, the maximum vertical velocity w_0 is a fixed value of 0.5 $ms^{-1}km^{-1}$ for cumulus (and cumulonimbus) and 0.05 ($ms^{-1}km^{-1}$) for stratocumulus clouds. Since this factor defines the intensity of the in-cloud updrafts, it should be a function of the model's grid spacing. To account for the variation, w_0 is designed as an adaptive user-input parameter in the ADAS cloud analysis. Fig. 2.16 shows an example of vertical velocity profiles using w_0 = 0.5 $ms^{-1}km^{-1}$ for a cumulus cloud of 6 km deep extending from 1 km AGL to 7 km AGL. The maximum w is 3 ms^{-1} located at 3 km. It is noticed that the parabolic w-profile in the LAPS is symmetric to the maximum. This may produce non-zero vertical velocity at the surface (Fig. 2.16) which violates the lower boundary condition. The problem occurs when the height of the maximum vertical velocity, z_m, is smaller than $\frac{2}{3}H$. To avoid this problem, the parabolic profile is modified in the ADAS cloud analysis using the following formula:

$$w = w_{\max}\left[1-\left(\frac{z-z_m}{z_m}\right)^2\right]; \quad \text{for } z_m < \tfrac{2}{3}H \text{ and } z < z_m \tag{2.5}$$

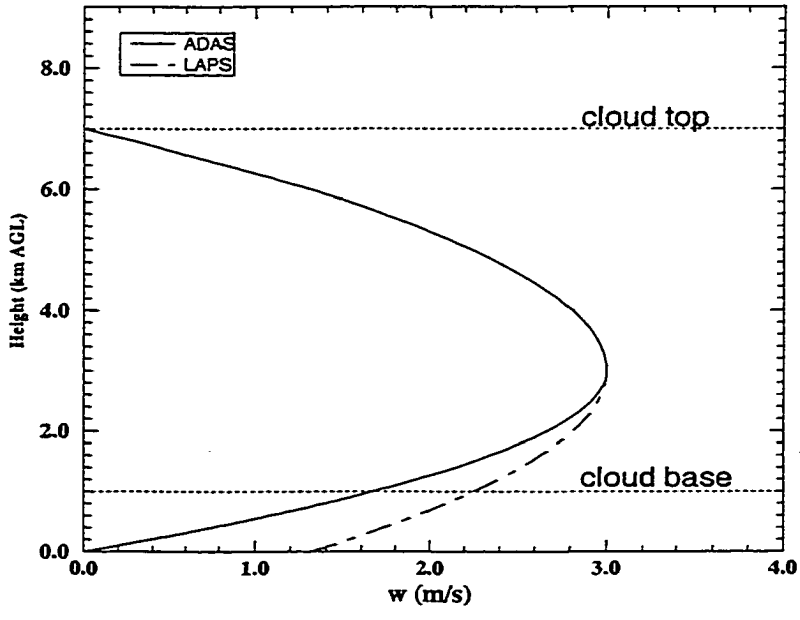

Fig. 2.16 Profiles of the in-cloud vertical velocity in the LAPS cloud analysis (dashed line) and in the ADAS cloud analysis (solid line).

For a stratiform cloud the vertical velocity is a constant (0.05 ms^{-1} in the LAPS cloud analysis) throughout the cloud. In the ADAS cloud analysis, this parameter is again a user-defined value. An example of the in-cloud w-field is shown in Fig. 2.17.

2.5 Precipitate type and mixing ratio analysis

A three-dimensional precipitate type field is diagnosed using the analyzed radar reflectivity and temperature fields. The diagnosis procedure begins from the

echo top in each grid column. Precipitate starts as snow if the wet bulb temperature (T_w) at the echo top is below 0°C and as rain if otherwise. Snow

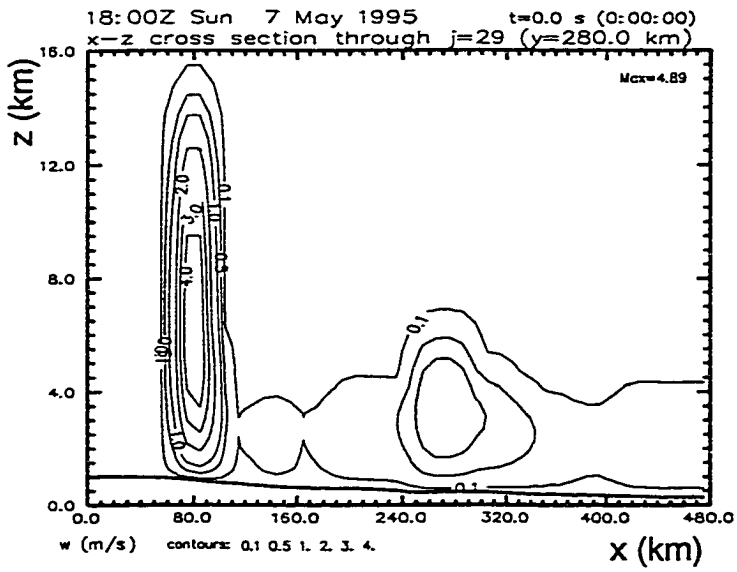

Fig. 2.17 Same cross section as in Fig. 2.14 except for the analyzed in-cloud vertical velocity field at 18Z May 7, 1995.

melts to rain when it falls into a region where T_w is higher than 1.3°C. Rain become freezing rain when it falls into a region where T_w is lower than 0°C. Freezing rain become sleet when it falls through a layer between pressure levels p1 and p2 where $\int_{p1}^{p2} T|dp| < -250$mb°C. Hail is diagnosed when radar reflectivity is higher than a threshold that is dependent on grid resolution. Precipitate mixing ratios (rain, freezing rain, snow, sleet, and hail) are derived directly from radar reflectivities. Rain and freezing rain water mixing ratios are computed from the following empirical relationship (Kessler, 1969):

$$Z = a \bullet (\rho \bullet q_r)^b \tag{2.6}$$

For snow, sleet, and hail mixing ratios, an empirical relationship defined in Rogers and Yau (1989) is used:

$$Z = c \bullet (\rho \bullet q_s)^d \tag{2.7}$$

Here ρ is the air density in kgm^{-3}; Z is the reflectivity factor in $mm^6\ m^{-3}$; q_r and q_s represent the rain (or freezing rain) and snow (or hail) mixing ratios, respectively; a, b, c, and d are empirical constants whose values are defined as the following:

$$a = 17300.0; \quad b = 1.75 \tag{2.8}$$

$$c = 38000.0; \quad d = 2.2 \tag{2.9}$$

The analyzed mixing ratios of rainwater, snow, and hail at 18Z May 7, 1995 are shown in Fig. 2.18.

2.6 Summary

The ADAS cloud analysis system is described in this chapter. The analysis provides a unique tool for incorporating multiple sensor observations from in situ and remote sensing platforms that are available in the operational forecasting environment. It combines METARs, infrared satellite, radar reflectivity, and visible satellite data to construct three-dimensional cloud and

precipitate distributions. The METARs cloud reports provide cloud base and cloud amount information for the lower atmosphere. Cloud top height is inferred from infrared satellite brightness temperature. Radar reflectivity adds detailed

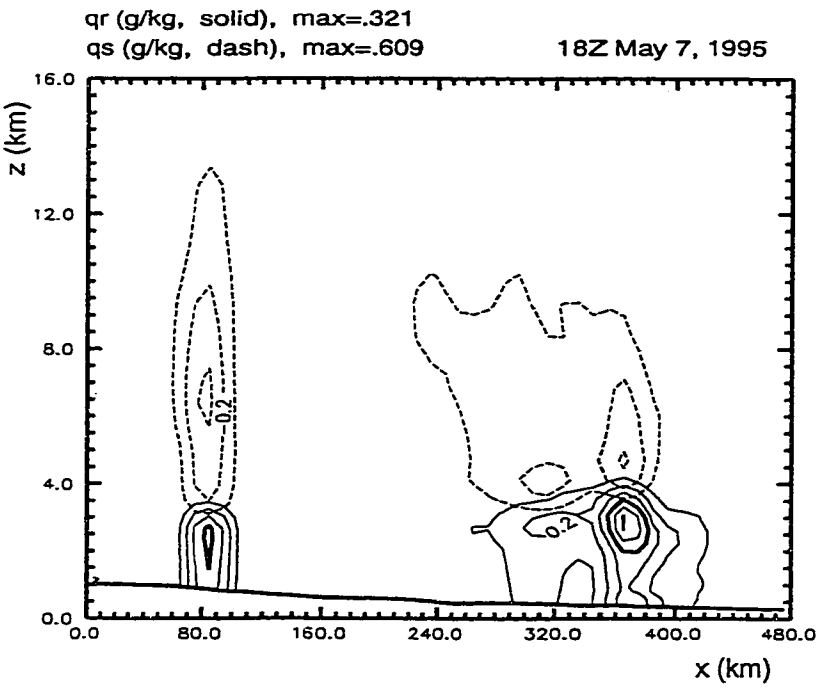

Fig. 2.18 Same cross section as in Fig. 2.16 except for the analyzed rainwater (solid line) and snow (dash line) mixing ratios (unit: g/kg) at 18Z May 7, 1995. The contour interval is 0.1 g/kg.

information about cloud and precipitate structure throughout the troposphere. Cloud liquid/ice water mixing ratios are diagnosed based on the cloud fraction distribution and the ADAS temperature analysis using a 1D moist adiabatic ascent model. Cloud type is diagnosed based on temperature, cloud depth, and static stability at each grid point. The three-dimensional vertical velocity field in clouds

is derived using pre-specified vertical profiles that are dependent on cloud type and cloud depth. Precipitate type is analyzed in the radar echo region using a simple 1D model based on wet bulb temperature. And mixing ratios of rainwater, snow and hail are calculated from empirical relationships. Although it is difficult to verify quantitatively the cloud analysis products due to the lack of appropriate observations, the analysis results have shown good agreement qualitatively with satellite cloud observations (Manobianco and Case 1998). Preliminary experiments have shown positive impact of the ADAS cloud analysis on storm-scale numerical weather prediction (Carpenter et al. 1998). Future work will use new and more advanced data sources, e.g., the column total cloud water content measured by the Advanced Microwave Sounding Unit (AMSU) on the NOAA-KLM series of polar-orbiting satellites and the vertical distribution of precipitation observed by the first spaceborne precipitation radar on the Tropical Rainfall Measuring Mission (TRMM) satellite, to perform quantitative verifications and to further improve the ADAS cloud analysis.

The ADAS cloud analysis products will be used to initialize the ARPS condensate fields. They also serve as the base for a moisture and diabatic initialization scheme. The initialization scheme will be presented in the next chapter.

Chapter 3
Moisture and Diabatic Initialization

3.1 Introduction

The ADAS cloud analysis system can be used as a convenient diagnostic tool for forecasters. The three-dimensional gridded analyses of clouds and precipitation, together with the ADAS temperature and wind analyses, can provide a direct and comprehensive view of interesting weather systems. They can also provide better initial conditions for convective-scale numerical models than conventional analyses. The cloud liquid/ice water, rainwater, snow, and hail mixing ratio analyses can readily be used to initialize the ARPS since they are prognostic variables in the model's microphysical processes. Conventional surface and radiosonde observations do not provide these condensate fields, which may cause a delay in precipitation formation when they are used for the initialization of numerical weather models under cloudy/precipitating conditions. The purpose of initializing cloud and precipitation fields is to speed up microphysical processes and to produce accurate precipitation amounts at the right time and at the right locations. However, such initialization is not complete

because the other model variables, i.e., water vapor, temperature and wind fields may not be consistent with the cloud and precipitate analyses. One reason for this is that these latter fields may not contain the same high-resolution information as in the cloud analysis. To alleviate this problem, moisture and diabatic initialization schemes are developed based on the cloud and precipitation analyses. A diabatic initialization seeks to provide a latent heat forcing in the thermodynamic equation, and to force vertical circulations and the associated divergence that are consistent with the observed precipitation. The purpose of a moisture initialization is to compensate for deficiencies in the conventional radiosonde moisture observations, to provide sources for cloud condensation, and to retain vertical circulations that are induced by a diabatic initialization. In our schemes, the initial temperature field is adjusted in cloud and rain regions to account for latent heat release from cloud condensation. The amount of latent heat is related to the amount of cloud water content that is inserted in the model initial conditions. Relative humidity is adjusted to assure saturated conditions in the analyzed cloudy regions. The moisture adjustment is especially important for producing realistic precipitation forecasts in data sparse areas. The initialization schemes are presented in the following sections.

3.2 Initialization of the ARPS cloud and precipitation fields

In the moisture initialization scheme, the initial cloud liquid (q_c) and cloud ice (q_i) water mixing ratios are simply set to the analyzed values. The

purpose of inserting q_c- and q_i-fields is to speedup microphysical processes and to produce appropriate precipitation amounts at the beginning of the model forecast. Since the conventional radiosonde network does not provide cloud condensate fields, it usually takes a certain time for a forecast started from conventional initial conditions to produce clouds and precipitation. Therefore the cloud analysis is very useful for short-term forecasting.

There are options for using the total or a fraction of the analyzed amount when initializing the rainwater, snow, or hail mixing ratios. When using the partial option, the residual amount of the analyzed rainwater, snow or hail mixing ratios can be neglected or converted into initial cloud liquid or cloud ice. The reason for not using the total amount of the analyzed rain or snow amount is that the water-drag caused by falling precipitate particles can hinder updrafts or even produce downward motions. Adding precipitates at the initial time can delay the spinup process of a model when cloud-scale vertical circulations are not initialized. Cloud particles are very small and induce little downward dragging force. By converting part of the rainwater (snow, hail) into cloud liquid (ice) water, the vertical circulations are allowed to develop before the falling rain becomes significant. On the other hand, the full amount of the analyzed rainwater, snow, and hail may be used to initialize the model if the storm has reached its peak intensity. Under this situation, an initial precipitate load is helpful for producing realistic precipitation and cold outflows at the surface. The outflows are important for the generation of second-generation storms.

3.3 A diabatic initialization

When using non-zero initial cloud and/or precipitate mixing ratios, negative buoyancy is introduced in cloud and rain regions due to the weight of the cloud and precipitate particles. In the real atmosphere, the negative buoyancy is balanced by upward accelerations due to latent heat release in the developing storms. However, latent heating effects may not be resolved by conventional data due to the sparsity of the observations. To mitigate this problem, a thermal adjustment was proposed and used in Xue et al. (1998a) to compensate for the changes made to buoyancy by the diagnosed cloud and precipitation fields.

Buoyancy is a source term in the vertical momentum equation. In the ARPS, the vertical momentum equation is

$$\frac{\partial w}{\partial t}+u\frac{\partial w}{\partial x}+v\frac{\partial w}{\partial y}+w\frac{\partial w}{\partial z}-\tilde{f}u=-\frac{1}{\rho}\frac{\partial p}{\partial z}+B+D_w \tag{3.1}$$

where u, v, and w are the three Cartesian components of the wind vector, $\tilde{f}=2\Omega\cos(\phi)$ is the Coriolis coefficient (Ω is the angular velocity of the earth's rotation and ϕ is latitude), ρ is the air density, p is pressure, B is the buoyancy term, and D_w contains the sub-grid scale turbulence and computational mixing terms (Xue et al., 1995). The buoyancy term is

$$B=g\left[\frac{\theta'}{\overline{\theta}}-\frac{p'}{\overline{\rho}c_s^2}+\frac{q_v'}{\varepsilon+\overline{q}_v}-\frac{q_v'+q_w}{1+\overline{q}_v}\right] \tag{3.2}$$

where g is the gravitational acceleration of the earth, θ is potential temperature, c_s is the sound speed, q_v is water vapor mixing ratio, ε=0.622, q_w includes all liquid or ice water content. In the ARPS the liquid and ice water categories include cloud liquid (q_c) and ice (q_i) water, rain water (q_r), snow (q_s), and hail (q_h). Thus we have:

$$q_w = q_c + q_i + q_r + q_s + q_h \tag{3.3}$$

Note that the terms in Eq. (3.2) with a bar represent the base state in the ARPS, which are the horizontal mean values of the model variables, and the terms with a prime represent the perturbations with respect to the base state.

To preserve the buoyancy before and after the insertion of the analyzed cloud and precipitate content, the following condition should be satisfied:

$$\left[\frac{\theta'}{\bar{\theta}} - \frac{p'}{\bar{\rho}c_s^2} + \frac{q_v'}{\varepsilon + \bar{q}_v} - \frac{q_v' + q_w}{1 + \bar{q}_v}\right]_{before} = \left[\frac{\theta'}{\bar{\theta}} - \frac{p'}{\bar{\rho}c_s^2} + \frac{q_v'}{\varepsilon + \bar{q}_v} - \frac{q_v' + q_w}{1 + \bar{q}_v}\right]_{after} \tag{3.4}$$

The background pressure and air density fields are assumed to be accurate and they are not changed in this initialization. Thus we have:

$$\left[\frac{\theta'}{\bar{\theta}} + \frac{q_v'}{\varepsilon + \bar{q}_v} - \frac{q_v' + q_w}{1 + \bar{q}_v}\right]_{before} = \left[\frac{\theta'}{\bar{\theta}} + \frac{q_v'}{\varepsilon + \bar{q}_v} - \frac{q_v' + q_w}{1 + \bar{q}_v}\right]_{after} \tag{3.5}$$

or,

$$\frac{\Delta\theta'}{\bar{\theta}} + \frac{\Delta q_v'}{\varepsilon + \bar{q}_v} - \frac{\Delta q_v' + \Delta q_w}{1 + \bar{q}_v} = 0 \tag{3.6}$$

where $\Delta\theta'$, $\Delta q_v'$, and $\Delta q_w'$ are the differences between the perturbation potential temperature, the water vapor mixing ratio, and the total liquid and ice water mixing ratios before and after the moisture and thermal adjustments, respectively. $\Delta q_w'$ is generally non-negative because the background cloud and precipitate fields are usually zero. Solving Eq. (3.6) for $\Delta\theta'$, we get:

$$\Delta\theta' = \bar{\theta} \bullet \left[(\Delta q_v' + \Delta q_w)/(1+\bar{q}_v) - \Delta q_v'/(0.622+\bar{q}_v) \right] \tag{3.7}$$

An example of the thermal adjustment based on preserving the buoyancy field is shown in Fig. 3.1. The vertical cross sections show the perturbation potential temperature fields before (Fig. 3.1a) and after (Fig. 3.1b) the thermal adjustment using the cloud liquid/ice and rainwater/snow mixing ratio analyses shown in Figs. 2.14 and 2.18. The change made to the perturbation potential temperature field is relatively small. The maximum adjustment to the potential temperature field is about ±0.7 K (Fig. 3.1c). We used the buoyancy adjustment in a simulation for a heavy convective precipitation case and found that the adjustment did not have a significant impact on reducing the spinup time for the precipitation.

In the real atmosphere, the physical mechanism for a positive buoyancy in storms is latent heat release from cloud condensation. The latent heating term is the connection between microphysical and thermodynamic processes. In a convective system, latent heat release provides a positive feedback mechanism (Bluestein, 1993): heating in upper levels induces upward motion and low level

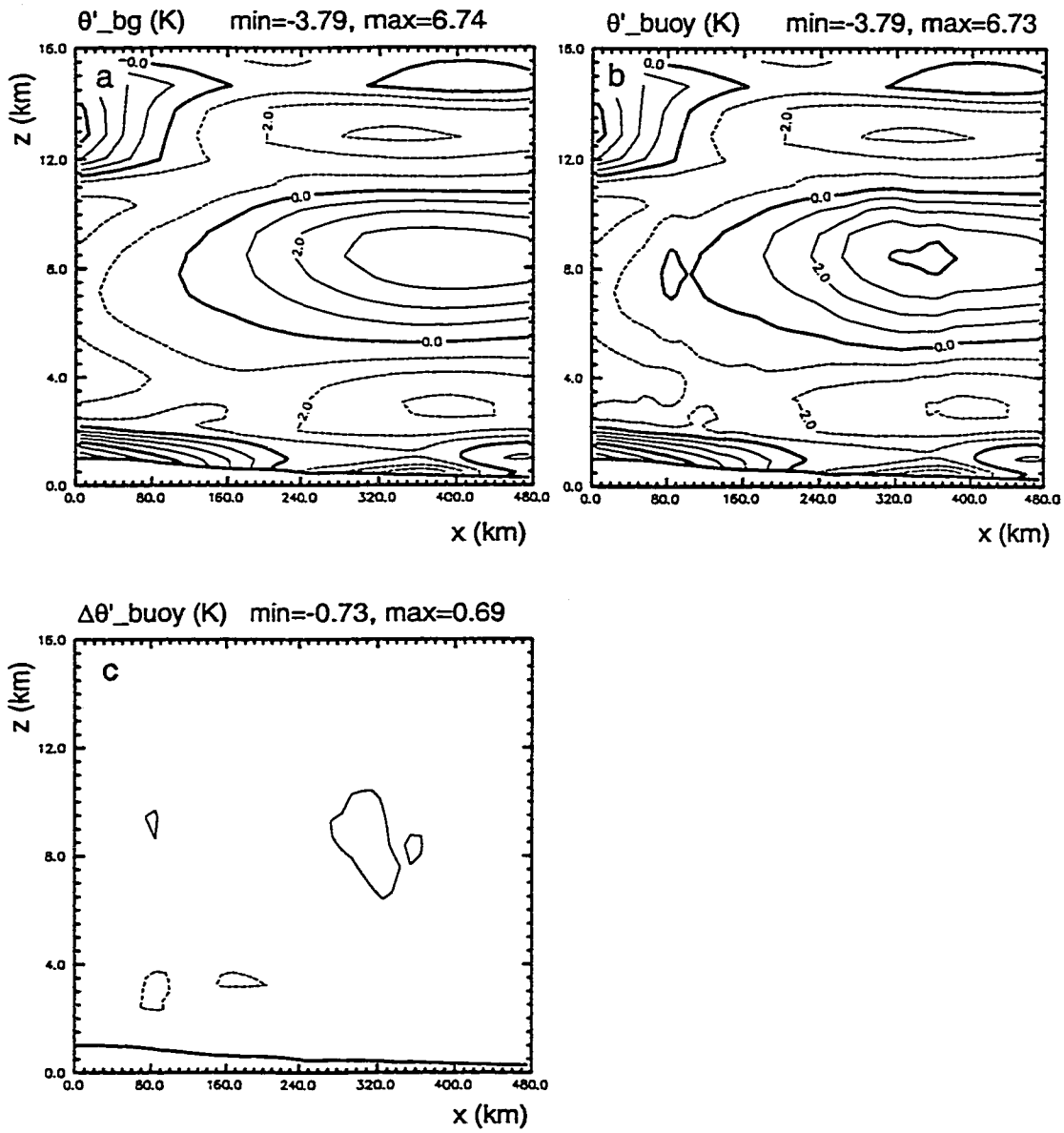

Fig. 3.1 An example of the buoyancy adjustment. Panel a shows the background θ′-field (unit: K) and the θ′-field after the buoyancy adjustment (b). The difference between (a) and (b) is shown in panel c. The contour intervals are 1K in panels a and b, and 0.5K in panel c.

convergence. Upward motion brings moist air from the surface layer and allows continuing condensation and more latent heat release. Therefore it is important to include latent heating in model initial conditions to assist the spinup of convective precipitation in models.

Latent heating rates are the source terms in the thermodynamic equation of a forecast model. The thermodynamic equation in the ARPS is

$$\frac{\partial \theta'}{\partial t} = -\left[u\frac{\partial \theta'}{\partial x} + v\frac{\partial \theta'}{\partial y} + w\frac{\partial \theta'}{\partial z} \right] - w\frac{\partial \bar{\theta}}{\partial z} + S_{\theta_{mcrp}} + S_{\theta_{other}} \tag{3.8}$$

where $S_{\theta_{mcrp}}$ represents the latent heating term due to cloud microphysical processes and $S_{\theta_{other}}$ are the heating rates due to radiation and other diabatic processes. $S_{\theta_{mcrp}}$ is defined by

$$S_{\theta mcrp} = \frac{L_v}{c_p}(P_{COND} - P_{CEVAP} - P_{REVAP}) \tag{3.9}$$

Here L_v is the latent heat of vaporization/condensation of water, c_p is the specific heat of dry air at constant pressure, P_{COND}, P_{CEVAP} and P_{REVAP} are changing rates of the water substances due to cloud condensation, cloud evaporation, and rain evaporation processes, respectively.

Fig. 3.2 shows vertical cross sections of the $S_{\theta_{mcrp}}$ fields at different times during a cloud-scale numerical simulation. The three-dimensional simulation was carried out using the ARPS. The grid resolution for the simulation was 1 km x 1

km x 500 m. The model was initialized using a single sounding and a warm bubble and was integrated forward for 120 minutes. The Kessler (1969) warm rain microphysical parameterization was used in the simulation. The vertical cross sections were taken through the cores of the simulated storms. Simulated perturbation potential temperature (θ') fields on the same cross sections as in Fig. 3.2 are shown in Fig. 3.3. It is seen that patterns of the two fields are very similar in the core regions of the simulated storm. The warm cores aloft are associated with regions of positive LH, and the cool pools near surface are associated with regions of the negative LH. Equation (3.9) indicates that positive LH is related to the cloud condensation (P_{COND}) and negative LH is related to the cloud and rain evaporation (P_{CEVAP} and P_{REVAP}). The cool pools near the surface are mainly related to the rain evaporation.

In most previous diabatic initialization studies, latent heating rates were determined from precipitation at the ground. Pre-specified profiles, e.g., climatological latent heating profiles (Puri and Miller 1990) or parabolic functions (Carr 1977; Wang and Warner 1988; Takano and Segami 1993; Wu et al. 1995), were then used to distribute the rainfall-derived latent heating rate vertically. Other investigators (Turpeinen et al. 1990; Manobianco et al. 1994; Raymond et al. 1995) have used model-generated profiles during pre-forecast integrations.

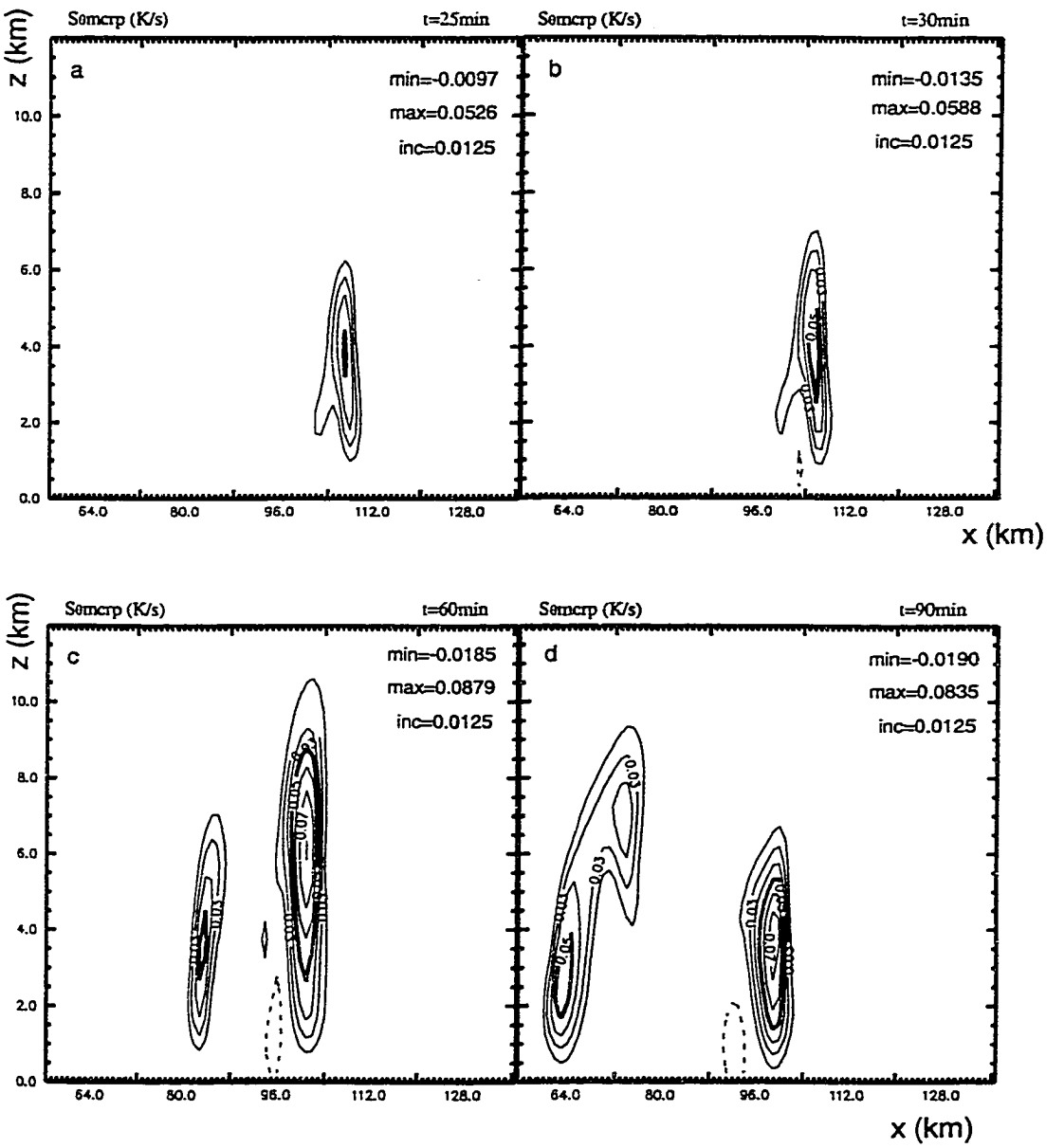

Fig. 3.2 Control latent heating rate fields (unit: K/s) produced by the control simulation at 25 (a), 30 (b), 60 (c) and 90 minutes (d) of the simulation time. The vertical cross sections were taken through the cores of the simulated storms.

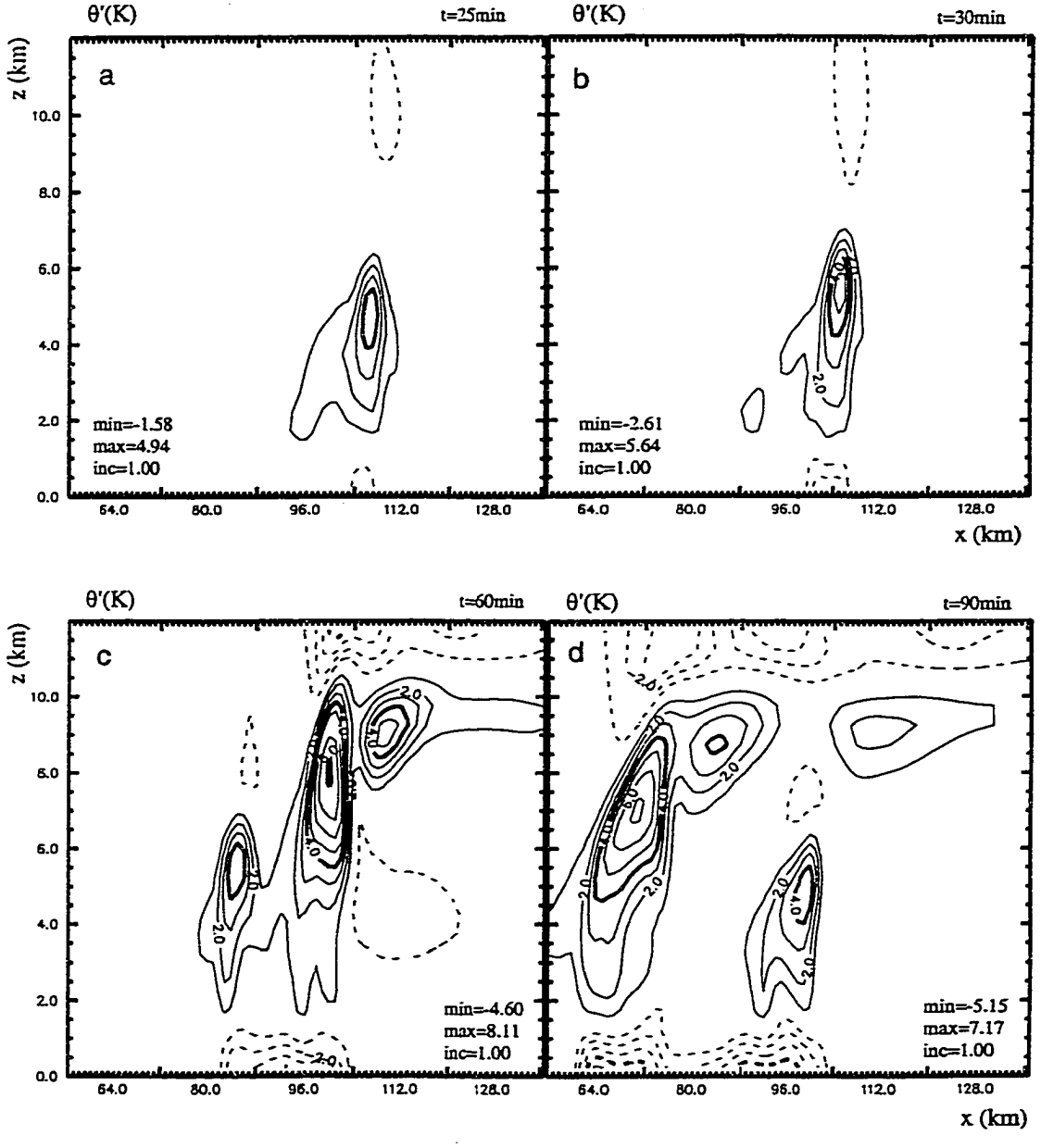

Fig. 3.3 The simulated perturbation potential temperature fields (unit: K) in the same cross sections as in Fig. 3.2 at 25 (a), 30 (b), 60 (c), and 90 minutes (d) of the simulation time.

To evaluate the techniques that use surface precipitation rates and parabolic LH profiles, we used a similar scheme to derive LH rates from the precipitation fields obtained during the storm simulation. Parabolic profiles are used in the scheme for distributing the LH. The LH distribution is defined by

$$\dot{Q} = \dot{Q}_{\max} \cdot \left[1 - 4\left(\frac{z - z_m}{z_2 - z_1} \right)^2 \right] \tag{3.10}$$

$$z_m = \frac{z_1 + z_2}{2} \tag{3.11}$$

where $\dot{Q}$ is the LH rate at a height z in a given grid column, and $\dot{Q}_{\max}$ is the maximum LH rate. The bottom and top of the parabolic profile, z_1 and z_2, are simply determined from the model's LH profile at the same grid column. $\dot{Q}_{\max}$ is determined such that the total LH rate in the grid column is equivalent to the amount of the latent heat released by condensing the "observed" amount of precipitation. That is,

$$\int_{z_1}^{z_2} \dot{Q} \cdot \rho dx dy dz = L_v \rho_w R dx dy \tag{3.12}$$

Here R represents rainfall rate, ρ and ρ_w are the air and water densities, dx and dy represent the size of a model grid box. Substituting Eq. (3.10) into Eq. (3.12) and solving for $\dot{Q}_{\max}$, we have

$$\dot{Q}_{\max} = \frac{3}{2} \cdot \frac{L_v \rho_w R}{\rho (z_2 - z_1)} \tag{3.13}$$

The LH rate fields that are derived using the simulated precipitation are shown in Fig. 3.4. The precipitation fields are the accumulated rainfall fields during the 30 minutes ending at the times when the LH rates are calculated (25 minutes for Fig. 3.4a). It is seen by comparing Fig. 3.4 with Fig. 3.2 that the derived LH fields are significantly smaller than the simulated fields, especially during the early stages of the storms. The reason for this is that cloud condensation at these times have resulted in significant LH in the control field while there is little or no precipitation produced at the ground. Consequently, the precipitation-derived LH rate fields are very small. At 25 and 30 minutes of the simulation time, the maximum control LH rate was over 0.05K/s because of the cloud condensation (Figs. 3.2a, b). However, the maximum LH derived from the precipitation was less than 0.01K/s (Figs. 3.4a, b) because no significant rainfall had developed at these times (Figs. 3.4a, b). At 60 minutes, a LH maxima located at $x \approx 83$ km and $z \approx 3.5$ km in the control field (Fig. 3.2c) was missing in the derived LH field (Fig. 3.4c) since the rainfall had not reached the ground in that region (Fig. 3.5c). It was found that the positions of the maximum LH centers in the derived fields were displaced from those in the simulated fields. The simulated maximum LH centers at 30 and 60 minutes were located at $x \approx 101$ km and $x \approx 99$ km (Figs. 3.2c, d), respectively. However, the corresponding maximum LH centers in the simulated fields were located at $x \approx 96$ km and $x \approx 93$ km (Figs. 3.4c, d), respectively. The underestimation and phase shifts in the derived LH fields were even larger when only hourly precipitation fields were used (not shown).

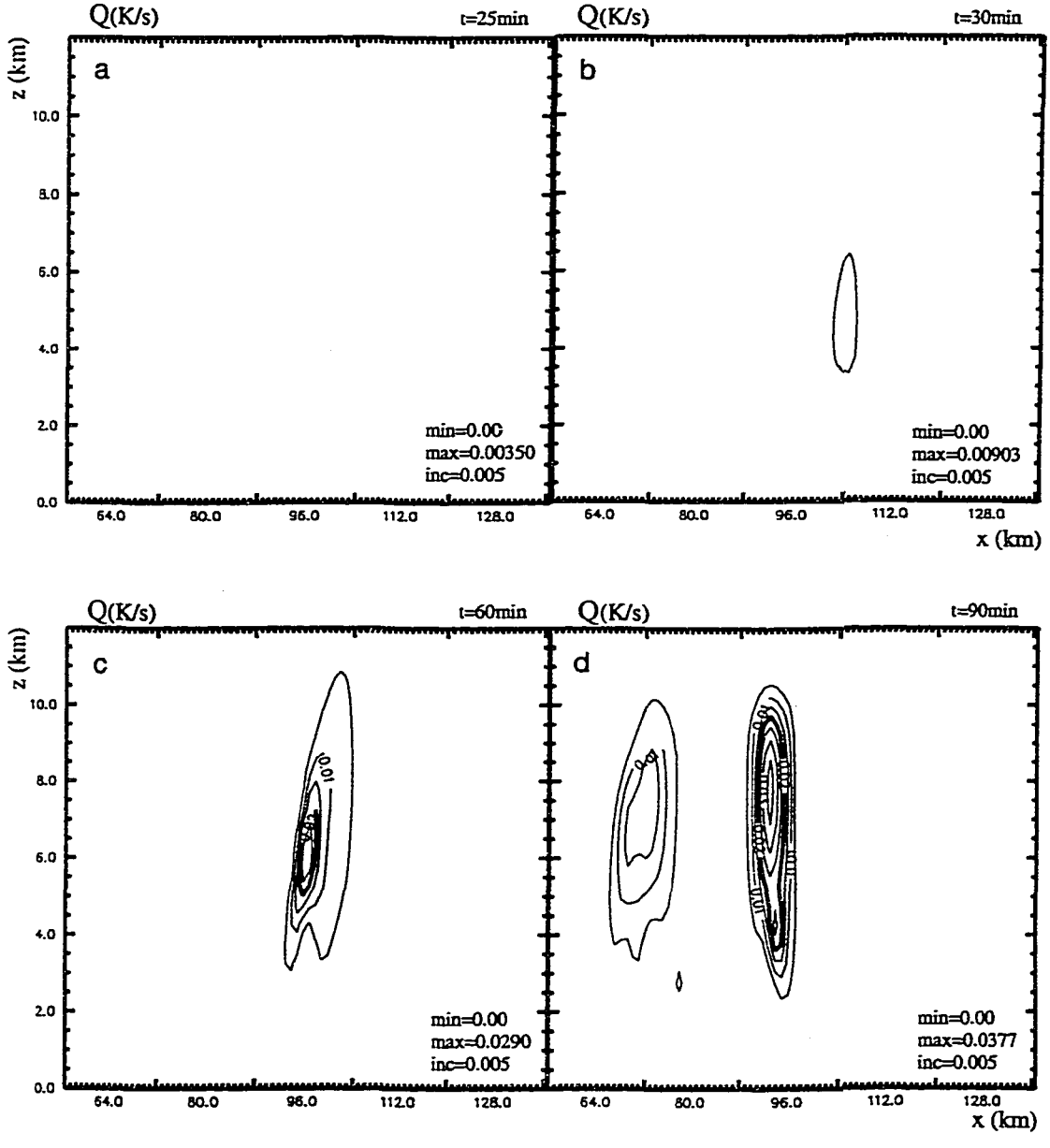

Fig. 3.4 The precipitation-derived latent heating rate fields (unit: K/s) in the same cross sections as in Fig. 3.2 at 25 (a), 30 (b), 60 (c), and 90 minutes (d) of the simulation time. Half-hour precipitation fields in the control run and parabolic profiles are used to derived the latent heating rates.

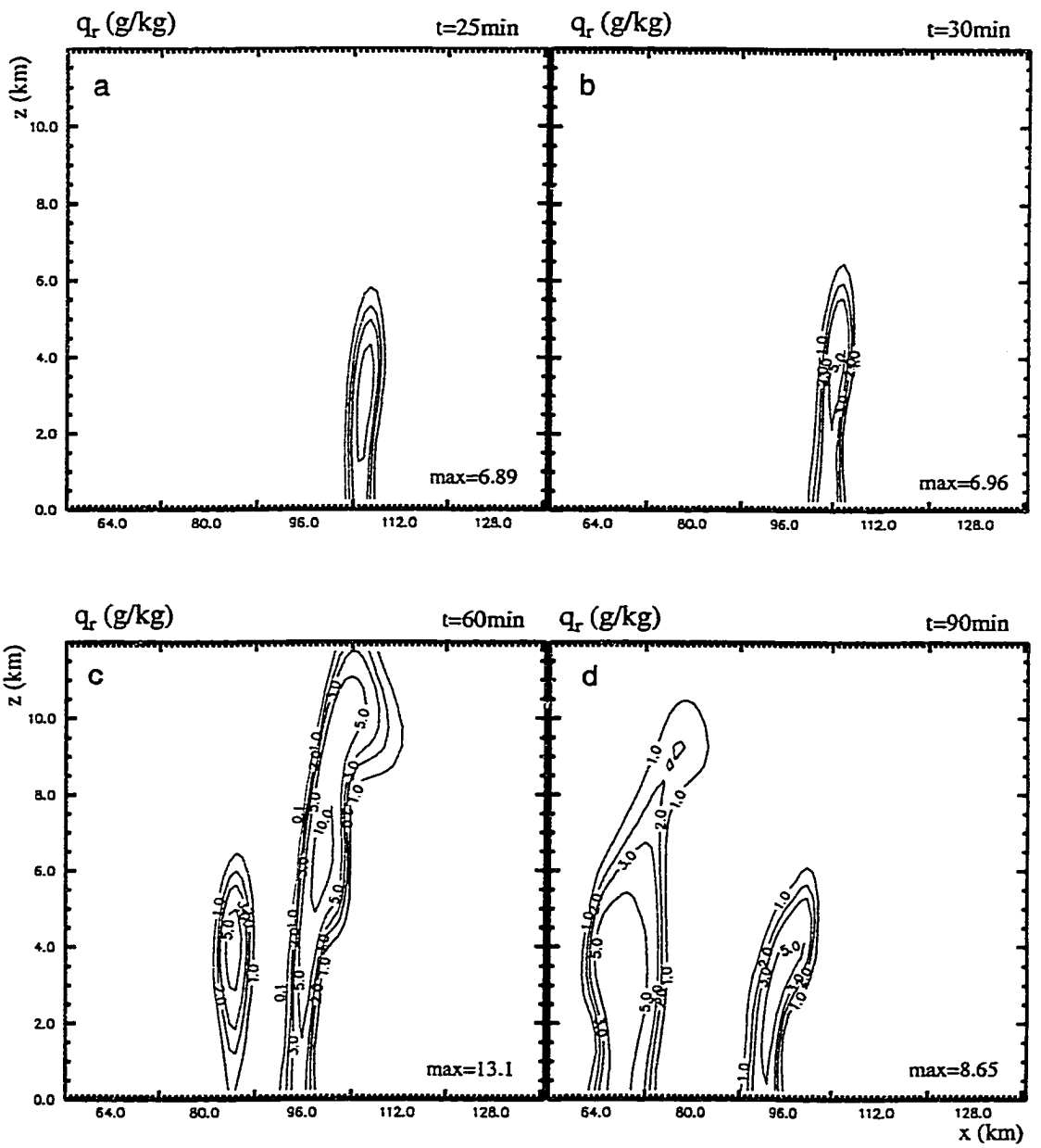

Fig. 3.5 Control q_r fields (unit: g/kg) in the same cross sections as in Fig. 3.2 at 25 (a), 30 (b), 60 (c), and 90 minutes (d) of the simulation time.

The inaccuracies in the derived LH fields were due to the indirect relationship between the LH field and the surface precipitation field. For this warm rain case, precipitation is the final product of microphysical processes that include cloud condensation, auto-conversion of cloud liquid water to rainwater, accretion of cloud liquid water by rainwater, and rain fallout. However, latent heat is released when clouds form and in places where clouds form. Therefore the (positive) LH field should be more closely related to the cloud field than to the surface precipitation field. The plots shown in Fig. 3.6 confirm that the structure of the cloud liquid water mixing ratio field is very similar to the structure of the control LH field (Fig. 3.2).

Based on the above results, a simple latent heat adjustment is proposed for the initial thermal field. The adjustment is defined by:

$$\Delta\theta' = \beta_\theta \cdot L_v(\Delta q_c + \Delta q_i)/(c_p\pi) \tag{3.14}$$

Here Δq_c and Δq_i represent the increments in q_c and q_i during the initialization of cloud and precipitation fields, respectively. β_θ is a weighting factor that ranges from 0 to 1. The weighting factor should be small in regions where high-resolution temperature observations can be obtained. In those regions latent heating effects have been reflected in the observed thermal field and an additional LH adjustment would be inappropriate. Future work will incorporate the latent

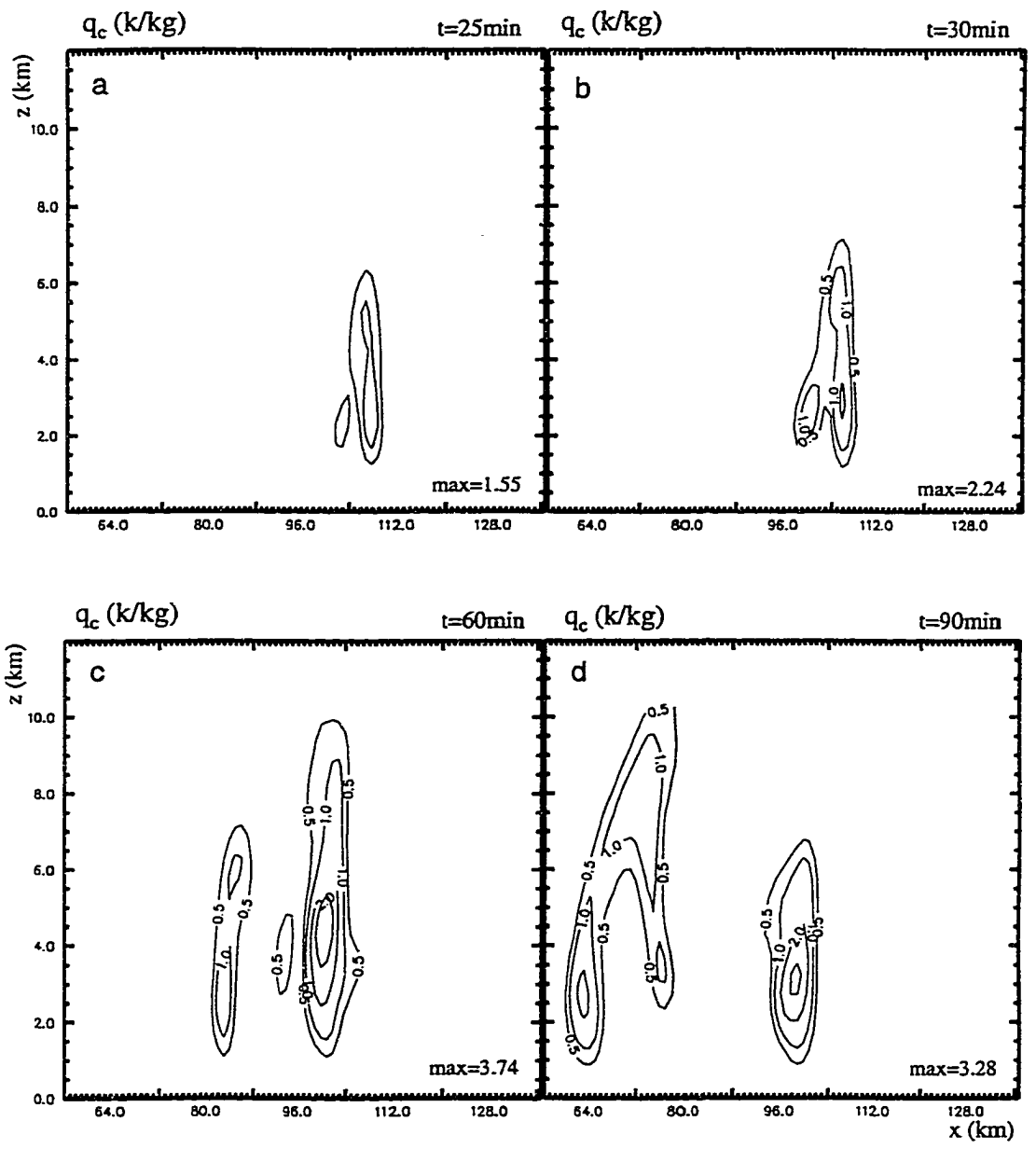

Fig. 3.6 Control q_c fields (unit: g/kg) in the same cross sections as in Fig. 3.2 at 25 (a), 30 (b), 60 (c), and 90 minutes (d) of the simulation time.

heating adjustment in an objective analysis scheme, in which the thermal increments obtained from Eq. (3.14) are treated as supplemental observations.

Fig. 3.7 shows the $\Delta\theta'$-field derived from Eq. (3.14) using an analyzed cloud liquid water mixing ratio (q_c) field (Fig. 3.8). The q_c-field is derived using the Smith-Feddes model in the ADAS cloud analysis (see Chapter 2, section *2.3*). The structure and magnitude of the derived $\Delta\theta'$-field is very similar to that of the simulated θ' fields (Fig. 3.3). There are smaller phase errors in time and space in the $\Delta\theta'$-fields than in the precipitation-derived LH fields. Therefore, using the LH adjustment based on the 3D cloud analysis is more appropriate for convective-scale diabatic initialization since convective weather systems have time scales that are comparable to those of the microphysical processes. The time scales of synoptic weather systems are much larger than that for microphysical processes, thus using precipitation-derived latent heating in diabatic initialization for large scale numerical weather prediction is a reasonable approximation.

More sophisticated diabatic initialization methods involve the retrieval of latent heating rates by reversing the microphysical processes in a forecast model or using the adjoint of a forecast model. The major advantage of such methods is that the balance between the retrieved latent heating fields and the forecast model is assured. The disadvantages of these schemes include the irreversibility of the microphysical processes and the high computational expense. A preliminary investigation of the former type of approach has been undertaken (Zhang and Carr, 1998). A simple retrieval scheme was developed based on the Kessler

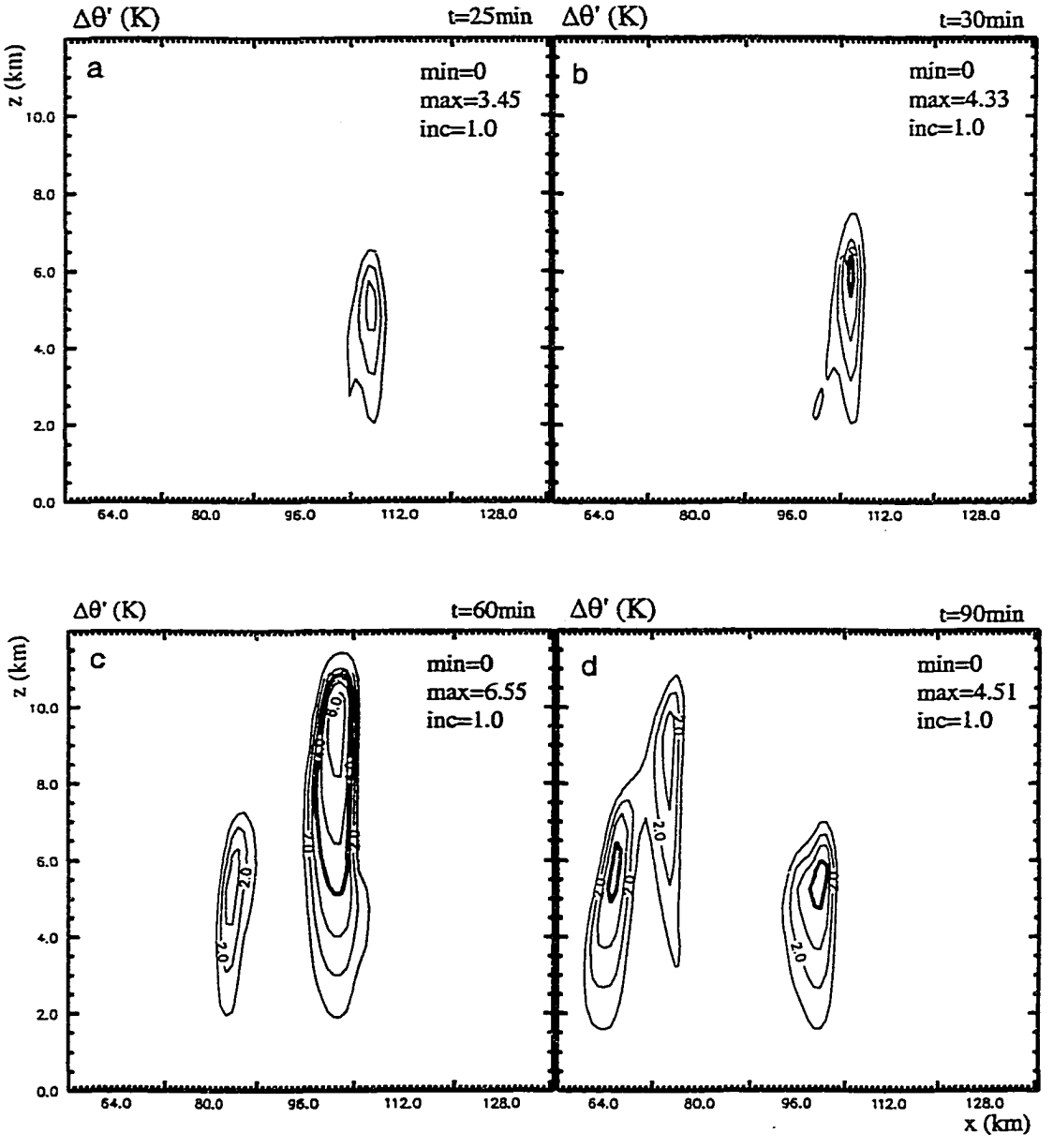

Fig. 3.7 Temperature adjustment fields (unit: K) based on latent heat release in the same cross sections as in Fig. 3.2 at 25 (a), 30 (b), 60 (c), and 90 minutes (d) of the simulation time. The amount of the latent heat is related to the q_c-field that is derived using the Smith-Feddes model.

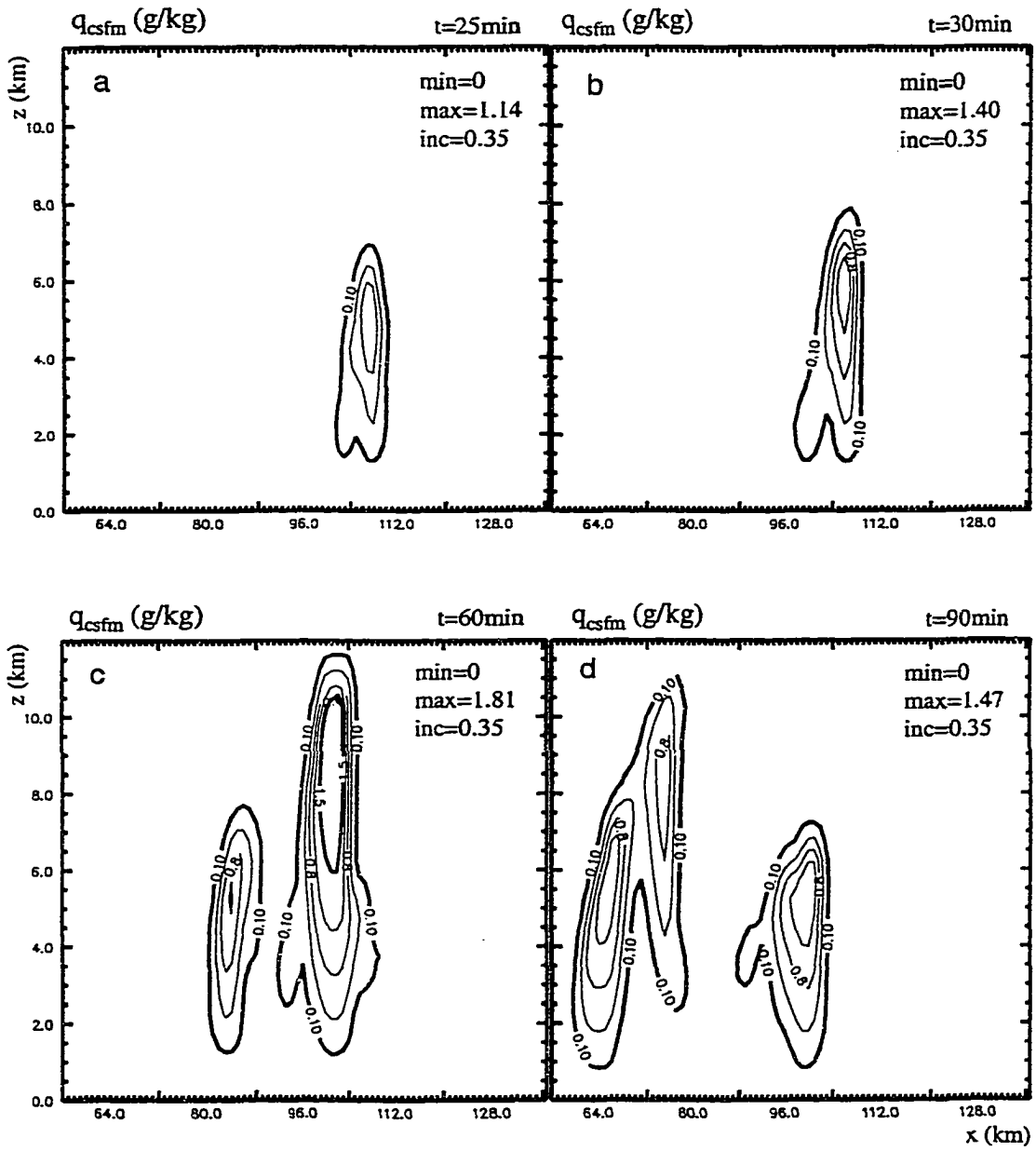

Fig. 3.8 Smith-Feddes model-derived q_c fields (unit: g/kg) in the same cross sections as in Fig. 3.2 at 25 (a), 30 (b), 60 (c), and 90 minutes (d) of the simulation time.

warm rain microphysical parameterization. Latent heating rates as well as moisture fields including water vapor, cloud liquid, and rainwater fields were derived from simulated high-resolution radar reflectivity data using a reverse-Kessler scheme. The reverse-Kessler scheme is presented in Appendix A.

3.4 Moisture Adjustment

Thermal adjustments can make the vertical temperature distribution more conductive to convection. Vertical circulations can be induced due to a less stable atmospheric condition in the cloud and rain regions than that without the thermal adjustments. However, the vertical circulations can not be retained if consistent condensation processes are absent. If the environment is not humid enough, the upward motion associated with the initialized divergence field will not be sustained by latent heat release (Wolcott and Warner, 1981). Turpeinen (1990) showed that diabatic NNMI had little effect on the duration of the spinup time unless the humidity field was enhanced. Thus a realistic initial moisture field is needed to assure sustained cloud condensation.

While moisture plays an important role in cloud condensation, conventional moisture observations are very limited in space and time. The three-dimensional ADAS cloud analysis contains information from radar and satellite and provides a good indication of moisture-abundant areas. Based on the cloud analysis the following moisture enhancement scheme has been developed. In the

diagnosed cloudy regions, minimum relative humidity (RH) values are imposed and the q_v-field is adjusted accordingly. The minimum relative humidity is determined from the analyzed cloud cover field using a linear function (Fig. 3.9). Based on the values in Fig. 3.9 relative humidity is adjusted to 50% if it is lower in the regions of 50% cloud cover. In regions of 100% cloud cover, relative humidity is adjusted to 95% if it is lower. The cloud cover and RH values at the two ends of the linear relationship are adjustable.

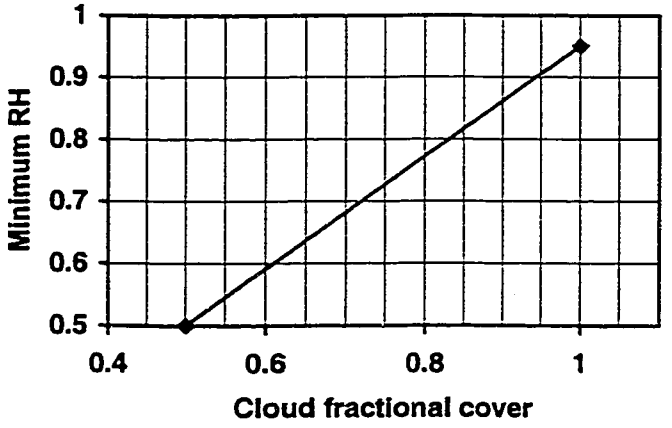

Fig. 3.9 Relationship between the minimum relative humidity and cloud cover.

Fig. 3.10 shows an example of the moisture adjustment. The example is the May 7, 1995 case that has been discussed in Chapter 2. Two RH fields on the same vertical cross section as in Fig. 2.18, one is before the moisture adjustment and the other is after, are shown in Figs. 3.10a and b, respectively. It can be seen that the adjustment moistened the two convective regions, one near x = 80 km

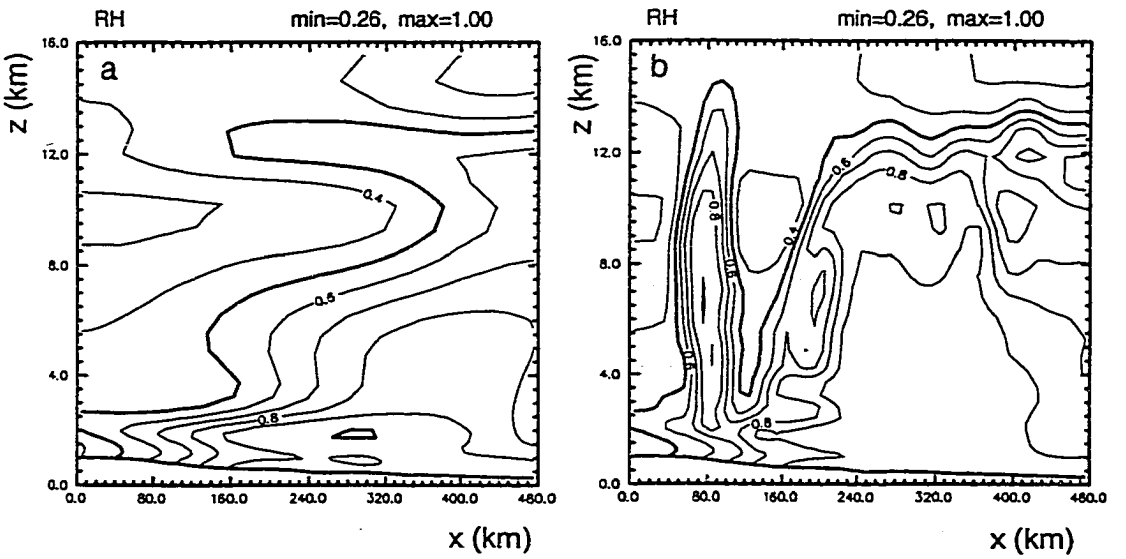

Fig. 3.10 Relative humidity fields before (a) and after (b) the moisture adjustment.

and the other near x = 320 km, especially in the one near x = 80 km. RH values in that region were below 50% before the adjustment, which was unrealistically dry for a cloudy and precipitating environment. After the adjustment, the RH value was brought up to above 90%. As a result of the moisture adjustment, the precipitable water increased about 2~4mm in the two precipitation areas (Fig. 3.11).

In the present moisture and diabatic initialization schemes, the moisture adjustment is always performed after the thermal adjustment so that the pre-specified minimum relative humidity is assured in clouds.

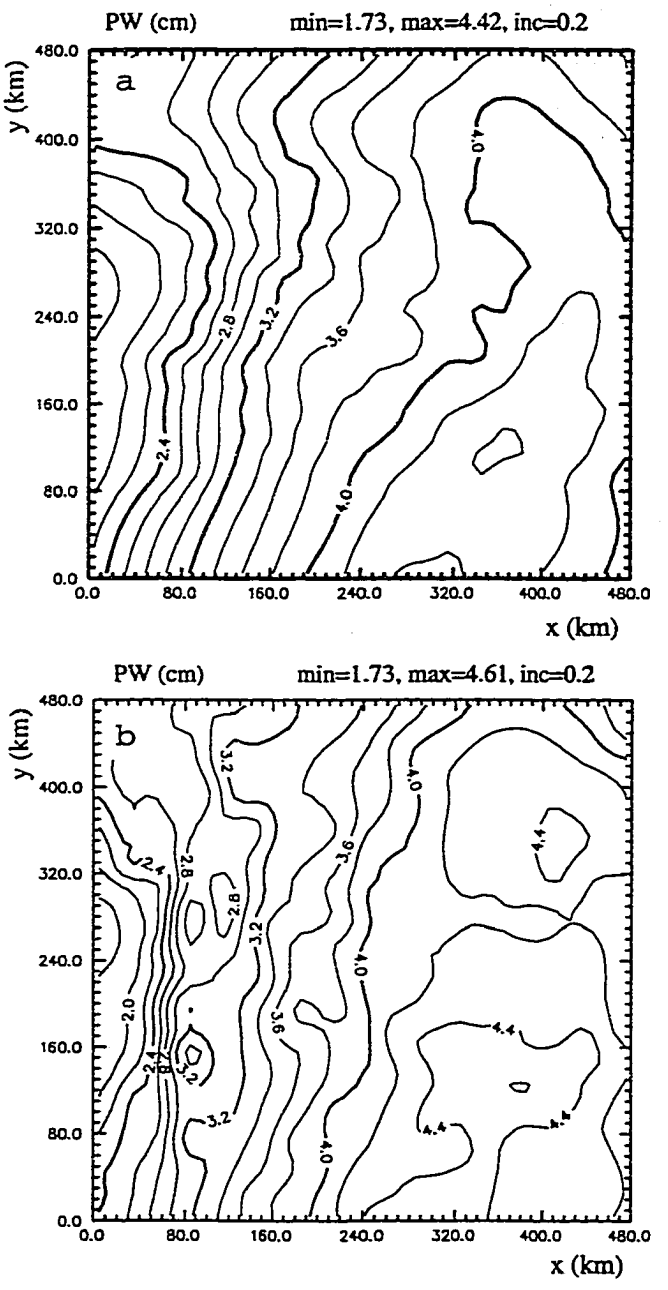

Fig. 3.11 Precipitable water before (a) and after (b) the moisture adjustment.

3.5 Summary

Moisture and diabatic initialization schemes based on the three-dimensional ADAS cloud and precipitation analyses were presented in this chapter. In the initialization schemes, the moisture and temperature analyses obtained from conventional observations are adjusted based on surface, radar, and satellite observations in order to get more realistic initial conditions during cloudy and/or precipitating atmospheric conditions, and to reduce the model spinup time for precipitation forecasts.

The cloud liquid and ice mixing ratio fields in the model are initialized using the analysis values, but the model's initial rainwater, snow, and hail mixing ratios are usually kept smaller than "observed". The reason for not inserting the total amount of precipitate at the initial time is that their mass may cause downward motions. These can prohibit development of cloud updrafts and delay the spinup of model precipitation. After the model cloud and precipitate fields are initialized, the thermal field is adjusted with two options to account for the latent heating associated with the inserted cloud content. After the thermal adjustment, the relative humidity field is modified and cloudy regions are moistened.

The present moisture and diabatic initialization schemes have two advantages over previous diabatic initializations:

(1) Instead of using two-dimensional precipitation estimates they are based on three-dimensional cloud analyses that use surface, satellite and radar data. The analyzed cloud base and top heights can provide relatively more objective information about the cloud distribution than simply using pre-specified sigma-levels.

(2) It is demonstrated that there are phase differences in time and space between latent heat release and precipitation. On the other hand, latent heating distribution is shown to be closely related to cloud distributions. Thus the 3D cloud analysis is more suited for initializing latent heating fields than is a 2D surface precipitation analysis.

The present schemes are based on observations and analysis procedures, and are independent of the forecast model's microphysical parameterization schemes. Therefore, they can be applied readily to different models. However, a drawback of such schemes is that a balance between the initial fields and the forecast model is not assured.

It is difficult to directly verify the moisture and diabatic initialization schemes based on observations because there are no appropriate data sources available. Performing Observing System Simulation Experiments (OSSEs) poses an efficient and feasible way of evaluating different initialization procedures. In order to examine systematically the impact of the moisture and diabatic initializations on convective-scale numerical weather forecasts, a series of OSSEs have been carried out. The results of the OSSEs are presented in the next chapter.

Chapter 4
Sensitivity of Convective-scale Numerical Simulations to Moisture /Diabatic Initialization

4.1 Introduction

It is recognized that conventional surface and radiosonde observation systems are not sufficient for solving spinup problems in mesoscale or cloud-scale numerical weather prediction models. The moisture and diabatic initialization scheme presented in the previous chapter that makes use of radar and satellite observations provides a new tool for initializing these models. How will the new initialization scheme affect convective-scale numerical weather forecasts? What are the merits and drawbacks of the new initialization scheme? To answer these questions, we carried out a set of observing system simulation experiments (OSSEs).

OSSEs consist of two basic elements: a control (benchmark) simulation and a set of perturbed simulations. The control simulation is a model forecast

started from a specific initial condition. Then the initial condition is altered, or, "perturbed", based on the scientific purposes of the experiments. Forecasts are then carried out from the perturbed initial conditions and results from each perturbed simulation are compared with those from the control simulation. Responses in the simulations to the different initial perturbations are studied. OSSEs have the advantage of having complete verification data sets, and with them we can assess the impact of the moisture and diabatic initialization scheme on convective-scale numerical weather simulations in great detail. With OSSEs we can also test the sensitivities of the forecast model to different moisture/diabatic initialization strategies. The OSSEs in the present study are different from previous approaches by Weygandt et al. (1990, 1993), Lazarus (1993), Park (1996), and Park and Droegemeier (1998). The major differences are (1) the focus of the problem and (2) the way of creating new initial conditions. The focus of our experiments is on moisture and diabatic initialization, while previous studies have been focused on wind initialization (Weygandt et al. 1990, Lazarus 1993), the relative importance of different fields (Weygandt et al. 1990, Lazarus 1993), and the relative importance of the same field in different regions (Weygandt et al., 1993, Park 1996). The initial fields in our experiments were created using the ADAS cloud analysis and the diabatic initialization scheme presented in Chapter 3, while in the previous experiments they were created using the simulated fields with some idealized operations. The operations included withholding data in certain regions (Weygandt et al. 1990; Lazarus

1993; Park 1996), applying smoothing (Weygandt et al. 1993), and adding random errors (Weygandt et al. 1993; Park 1996). Through those idealized approaches, useful and general knowledge has been obtained about the most optimistic results that one could get with the data and the data assimilation techniques being tested (Weygandt et al. 1990). The goal of our experiments is to evaluate the impact of a specific initialization scheme on convective-scale numerical weather prediction.

4.2 The model

The control run of the observing system simulation experiments was produced using the Advanced Regional Prediction System (Xue et al., 1995). The ARPS is a mesoscale and convective-scale atmospheric model with non-hydrostatic and fully compressible dynamics. The coordinate system in the ARPS is a generalized terrain-following coordinate with equal spacing in the x- and y-directions and grid stretching in the vertical. The Arakawa C-grid (Arakawa and Lamb 1977) is used in the spatial discretization. Second-order quadratically-conservative and fourth-order quadratically-conservative finite differences are used for advection terms and second-order differencing for other terms. A second-order leapfrog scheme is used in temporal differencing for large time steps with an Asselin temporal filter option. First-order forward-backward explicit temporal differencing with a second-order centered implicit option is used for small time steps. Options for the sub-grid scale turbulence calculation include

Smagorinsky-Lilly diagnostic first-order closure, 1.5-order turbulent kinetic energy formulation, and Germano (Germano et al., 1991) dynamic closure. Both second- and fourth-order schemes are available for spatial computational mixing terms in the ARPS. Cloud microphysics algorithms include: (1) Kessler warm-rain microphysics parameterization (Kessler, 1969, Klemp and Wilhelmson, 1978, Soong and Ogura, 1973), (2) 3-category ice microphysics parameterization by Lin et al. (Lin et al. 1983, Tao et al., 1989), and (3) Schultz's (1995) ice microphysics scheme which contains equations for water vapor, cloud water, rainwater, ice, snow, and hail. The model also includes Kuo (Kuo, 1965, Kuo, 1974) and Kain-Fritsch (Kain and Fritsch, 1993) cumulus parameterizations. The surface layer physics includes surface momentum, heat, and moisture fluxes from bulk aerodynamic drag laws as well as from stability-dependent formulations.

4.3 The control run

The important model features in the control run include a 4th-order advective scheme, a 1.5 order turbulent kinetic energy (TKE) closure, and Kessler-type warm-rain microphysics.

The horizontal resolution of the control run was 1 km and the vertical resolution was 500 m. The model domain was 65x65 km^2 in the horizontal and 16.5 km deep in the vertical. A single sounding (Fig. 4.1) was used to create the

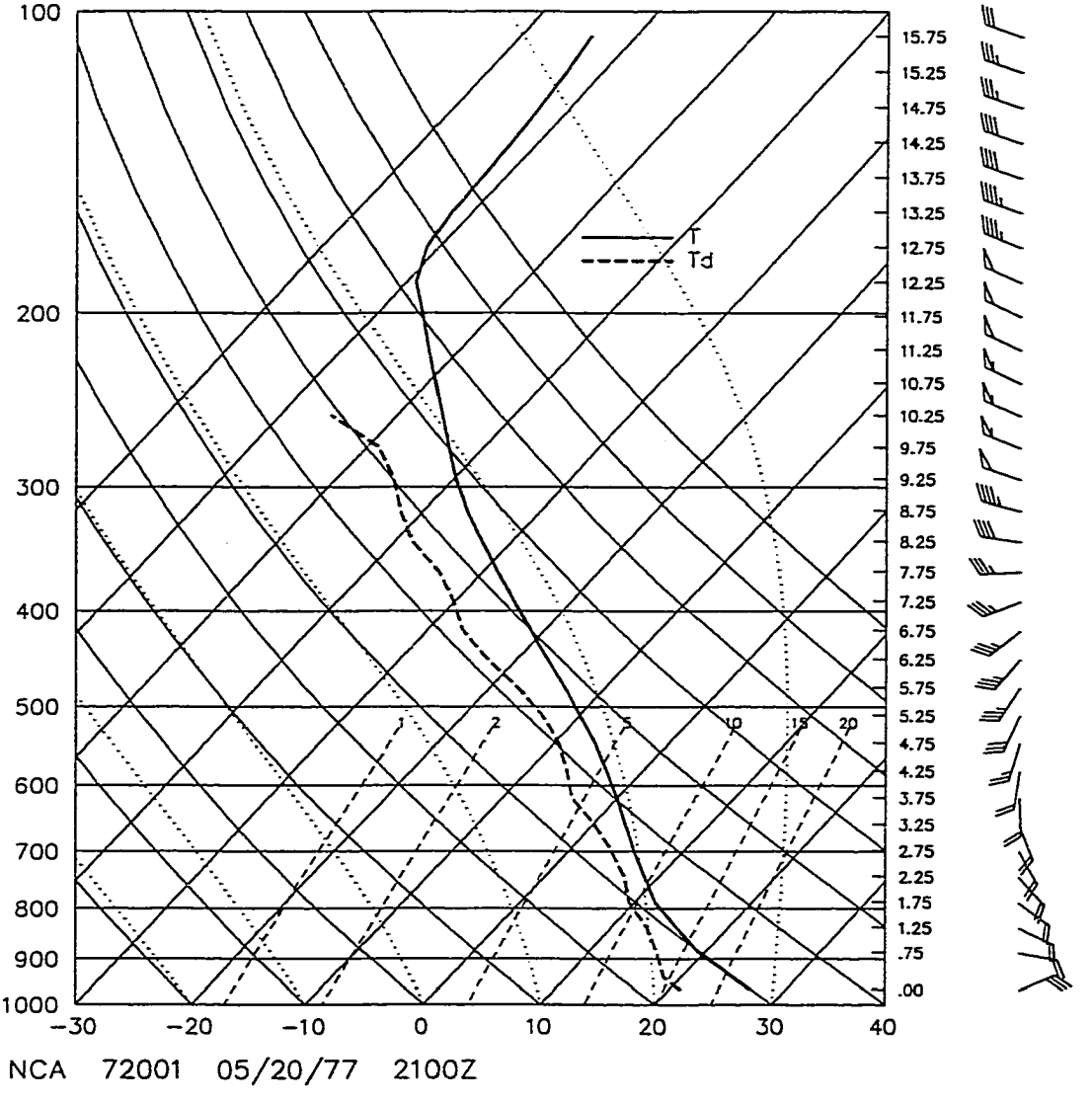

Fig. 4.1 The sounding that was used to create the base state model fields in the control run.

base state temperature, wind, and water vapor fields for the model. The sounding was taken at Ft. Sill, Oklahoma at 15 CST (Central Standard Time) on

May 20, 1977. Convection was triggered by a warm bubble in the initial potential temperature field. The bubble was an ellipsoid with 20-km diameters in both x- and y-directions and a 3-km diameter in the z-direction (Fig. 4.2). The magnitude of the temperature perturbation was 4 degrees Kelvin (3.69 K is shown in the plot because of the grid staggering). The control run was initialized using the sounding and the warm bubble and was integrated forward for two hours. Time series of the simulated domain maximum cloud (q_c) and rain water (q_r) mixing ratios are plotted in Fig. 4.3. Fig. 4.4 shows the 5-minute accumulated rainfall at 30 minutes and the half-hour accumulated rainfalls at 60, 90, and 120 minutes. The reason for choosing a 5-minute rainfall is that the OSSEs were started at 25 minutes. Only 5-minute accumulated rainfall is available at 30 min for the OSSEs.

Fig. 4.3 shows that clouds formed during the first 15 min of the control simulation and precipitation started soon after. The q_c-max decreased around 20 min due to accretion of cloud droplets by raindrops. A second fast growing period for q_C-max and q_r-max can be found around 35 minutes. A second cell developed to the northwest of the first storm and produced rainfall by the end of 1 hr (Fig. 4.4b). A brief drop in q_r-max around 95 minutes was related to the decay of the first storm and the intensification of the second storm, which had moved to the northwest corner of the domain (Fig. 4.4c).

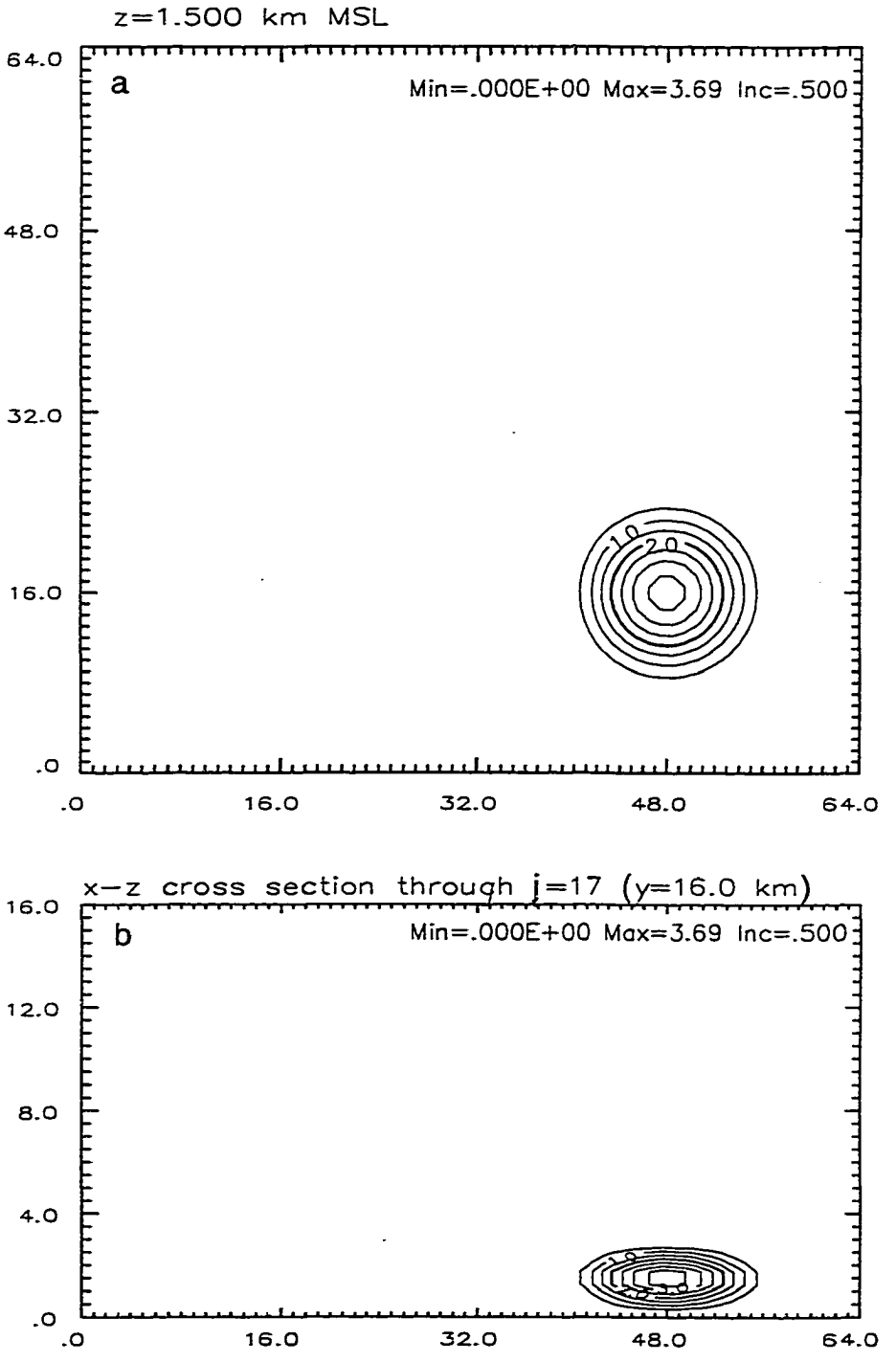

Fig. 4.2 X-y (a) and x-z (b) cross sections of the warm bubble that was used to create the initial perturbation temperature field in the control run. The cross sections are through the center of the bubble.

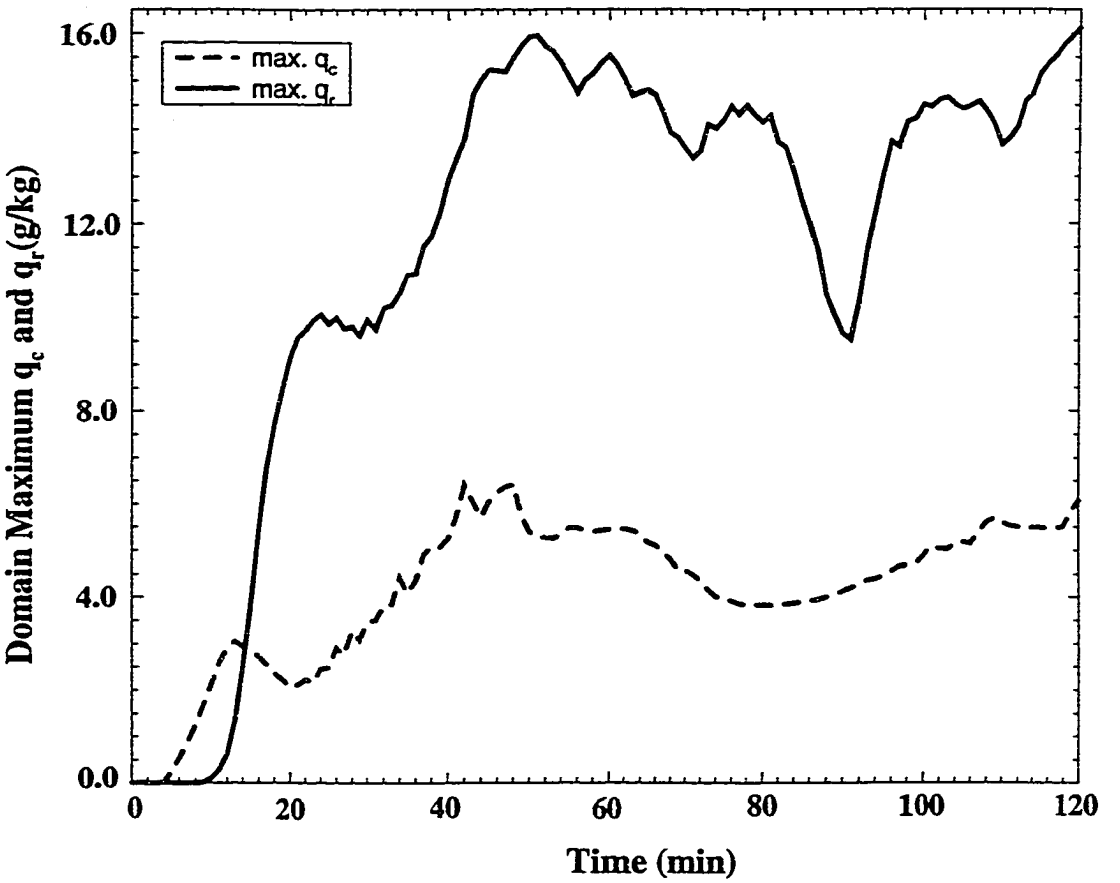

Fig. 4.3 Time series of the domain maximum qc and qr in the control run.

4.4. Experimental design

As mentioned above, the focus of our OSSEs is on the impact of different moisture/diabatic initialization strategies on convective-scale numerical weather prediction. To do this, a time is chosen in the control simulation when clouds and rain have already developed (25 min in Fig. 4.3). The simulated cloud

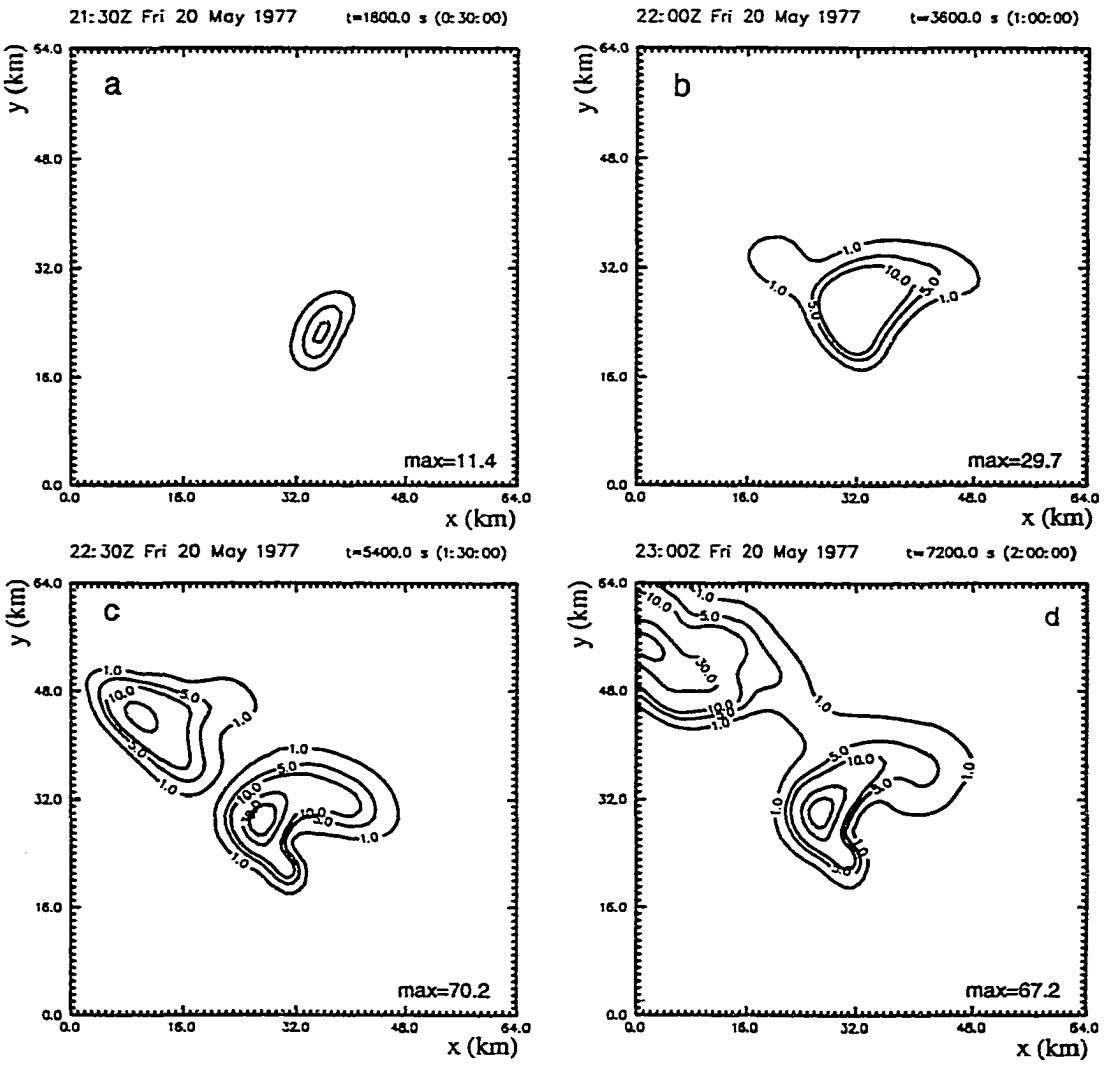

Fig. 4.4 The accumulated rainfall (mm) at 30 (a), 60 (b), 90 (c), and 120 (d) minutes in the control run. The accumulation periods were 30 min except for that in panel (a), which was accumulated from 25 to 30 minutes. The contour values are 1 mm, 5 mm, 10 mm, 30 mm, and 50 mm, respectivelly.

liquid water and rainwater mixing ratio fields at this time served as the source of the radar reflectivity and satellite cloud "observations". The ADAS cloud analysis and different moisture and diabatic initializations were performed to initialize the model at t = 25min. Then the model was restarted and subsequent simulations were carried out.

The model base state was used as the background atmospheric state for the cloud analysis. This is equivalent to the situation where the background fields come from conventional radiosonde observations. Since the average distance between radiosonde stations is about 300km, there would be only one sounding available in our 65x65km^2 domain. Cloud base and top height fields were determined using the control q_c-field at 25 minutes (Note: All times in this chapter refer to the time in the control run). Then a cloud liquid water mixing ratio field (no cloud ice is presented here since a warm rain microphysical parameterization was used in all OSSEs) was calculated using the Smith-Feddes model (Chapter 2, section *2.3*) and the base state temperature field. By doing this the author assumed that the three-dimensional volumetric cloud fraction analysis (Chapter 2, section *2.2*) could provide accurate estimates of cloud base and cloud top heights, while cloud liquid water amounts were not observed and needed to be determined using the ADAS cloud analysis. The control rainwater mixing ratio field at t = 25min was used in the initial conditions for several experiments. No efforts were made to emulate the radar sampling errors or errors in the

empirical relationship between radar reflectivity and rainwater mixing ratio. Temperature and water vapor fields are adjusted using the procedures described in Chapter 3 (sections *3.3* and *3.4*). Then the model was initialized at 25 min using different combinations of these fields and was integrated forward to the ending time of the control simulation, i.e., 2 hours. Thus the integration time for all OSSEs are 95 minutes long.

A list of all the OSSEs is shown in Table 4.1. The experiments are divided into four groups. Each group consists of three experiments. The three experiments in each group were initialized using different moisture initialization strategies so that the impact of each moisture component (water vapor, cloud, and rain) can be tested. The water vapor (q_v), cloud (q_c), and rainwater (q_r) fields in each three experiments were initialized using, respectively, (a) a moistened q_v field obtained from the RH adjustment that was described in Chapter 3 (section *3.4*), zero q_c and zero q_r; (b) the moistened q_v, analyzed q_c and zero q_r; and (c) the moistened q_v, analyzed q_c and analyzed q_r.

The purpose of the first and the second groups of experiments is to test the impact of the moisture initialization alone without the thermal adjustment. The base state wind field was used in the first group to mimic the condition when only conventional radiosonde observations are available. In the second group of experiments, the initial wind field was set to the base state in regions without any rainfall. The wind in rain regions was kept the same as in the control run. This is

emulating the case when we have a perfect Doppler wind retrieval (Shapiro et al., 1995; Xu et al., 1995; Zhang and Gal-Chen, 1996) using radar reflectivity and radial velocity observations. The first and second groups of experiments provide a preliminary test on the impact of the wind field on moisture and diabatic initialization. Testing the effects of the errors in wind retrievals is beyond the scope of this work. Studies related to the impact of the initial wind field on convective-scale numerical simulations have been done by Lazarus (1993), Weygandt et al. (1990, 1993), Weygandt (1998), and Levit and Droegemeier (1998, personal communication).

Table 4.1 List of the moisture and diabatic initialization experiments.

EXP.	Temp.	Wind	qv	qc	qr
1a	Base state	Base state	RH adjustment within clouds, base state outside	zero	zero
1b				Smith-Feddes	zero
1c				Smith-Feddes	analyzed
2a		Base state outside rain region, perfect inside		zero	zero
2b				Smith-Feddes	zero
2c				Smith-Feddes	analyzed
3a	Base state with the latent heating adjustment	Base state	RH adjustment within clouds, base state outside	zero	zero
3b				Smith-Feddes	zero
3c				Smith-Feddes	analyzed
4a		Base state outside rain region, perfect inside		zero	zero
4b				Smith-Feddes	zero
4c				Smith-Feddes	analyzed

Diabatic initialization of the temperature field, together with the moisture initialization, were used in the third and fourth groups of experiments. The initial thermal fields were adjusted based on the latent heating adjustment described in section *3.3*, Chapter 3. The initial wind fields in the third and fourth groups of experiments were the same as in the first and second ones, respectively.

4.5 Criteria for verification and comparisons

All the OSSEs were started at 25 min and were integrated forward for 95 min. Simulation results are compared with the control run using quantitative as well as qualitative measures. The quantitative criteria include two error statistics: 1) a multiplicative mean bias error, and 2) the traditional threat score. The multiplicative bias and threat score were calculated for 15 minute rainfall amount fields. The bias score is defined by

$$Bias = \frac{\sum_{i,j} R_{OSSE}(i,j)}{\sum_{i,j} R_{CTRL}(i,j)} \tag{4.1}$$

where R_{OSSE} and R_{CTRL} represent the rainfall amount every 15 minutes in the OSSEs and in the control run, respectively; i and j are grid indices. The summation in Eq. (4.1) is over the whole model domain. This bias score is a commonly used score in quantitative precipitation estimation and forecast. A value of greater than 1 indicates overestimated precipitation in a forecast and a value of less than 1

indicates an underestimation in a forecast. A bias score of 1 indicates an accurate forecast for the domain total precipitation amount. An alternative bias score, which has been widely used in statistics, is defined by

$$Bias^{1} = \frac{\sum_{i,j} R_{OSSE}(i,j) - \sum_{i,j} R_{CTRL}(i,j)}{\sum_{i,j} R_{CTRL}(i,j)} \tag{4.2}$$

It is seen from Eq. (4.2) that an overestimation (underestimation) in precipitation forecasts is implied by a $Bias^{1}$ value of greater (less) than 0. A value of $Bias^{1}= 0$ (instead 1) suggests an accurate forecast of precipitation amount in the model domain. The second bias score ($Bias^{1}$) is not used in this dissertation, although it can be derived from the first one using the following formula:

$$Bias^{1} = Bias - 1 \tag{4.3}$$

The threat score (TS) is a measure of the skill in predicting the area of precipitation amounts over any given threshold. It is defined by

$$TS = \frac{C}{F + R - C} \tag{4.4}$$

where F is the number of grid points where the model precipitation forecast is above a given threshold, C is the number of points where the forecasts are correct, and R is the number of grid points observing the rainfall over the threshold. In our case the "observation" is the simulated rainfall in the control run. The precipitation threshold used in the threat score calculations was 1 mm.

The traditional threat score is not very suited for verification of convective-scale precipitation forecasts, as it will be shown later in this chapter. Miller and Kalnay (1998, personal communication) have been developing a new set of criteria which are more appropriate for evaluating small scale precipitation forecasts as well as for general verification of numerical weather forecasts. Here we used two very simple alternative scores: maximum threat score with shifting (MTSS) and the shifting distance associated with the maximum threat score (d_MTSS). The "MTSS" is the threat score calculated by horizontally shifting the forecast precipitation field around its original location within a certain distance (in our case, within 15 km in each direction) until a maximum threat score is obtained.

Qualitative examinations were made by comparing individual fields. Cross sections of moisture, perturbation potential temperature, and wind fields were taken at interesting locations and at different times of the model simulations. The evolution of the storm systems in different experiments were compared with the control run and against each other. Detailed discussions are provided in the following sections.

4.6 Results and discussion

4.6.1 Conventional wind experiments without diabatic initialization

The time series of the bias and the traditional threat scores for experiments 1a, 1b, and 1c are shown in Figs. 4.5a, b, respectively. It can be seen that Exp. 1a and 1b failed to produce any significant precipitation. In Exp. 1c, a non-zero rainwater mixing ratio field was inserted at the initial time. The rainwater fell out much too quickly after the simulation started and the storm completely disappeared after 1 hour (Fig. 4.6). The initial rain evaporated and produced a cool pool at the surface at 30 min (Fig. 4.7a). The cold outflows pushed outward and stimulated development of a second precipitation system to the northwest of the first storm (Fig. 4.7b, c). The small peaks at ~ 100 min in the bias and threat scores (Fig. 4.5a, b) correspond to this weak precipitation system.

The failure for producing realistic amounts of precipitation in the first set of experiments is due to the insufficient moisture and diabatic initialization. Without the thermal adjustment, the initial temperature in the rain regions in Exps. 1a, 1b, and 1c was cooler than the control temperature field. The warm storm core in the control run (Fig. 4.8) did not exist in the OSSEs' initial thermal field because the base state temperature was used for the latter. Since saturation vapor pressure is dependent on temperature, moistening in clouds was limited and insufficient. It is shown in Fig. 4.9 that the initial precipitable water for Exps.

1a, 1b, and 1c is significantly less than in the control run, especially in the region of the storm core (Fig. 4.9c). The relatively cool and dry initial conditions prevented condensation and vertical circulations from developing.

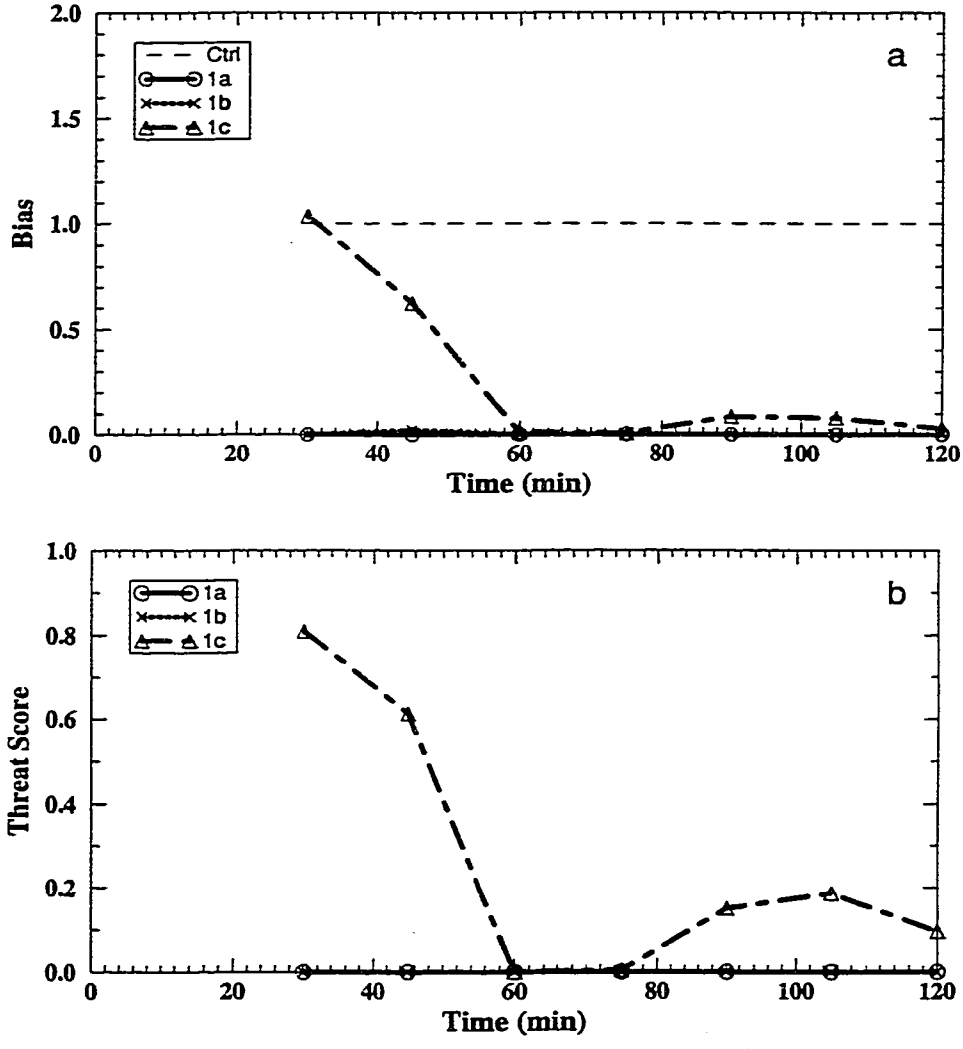

Fig. 4.5 Time series of the bias (a) and threat scores (b) for Exps. 1a, 1b, and 1c.

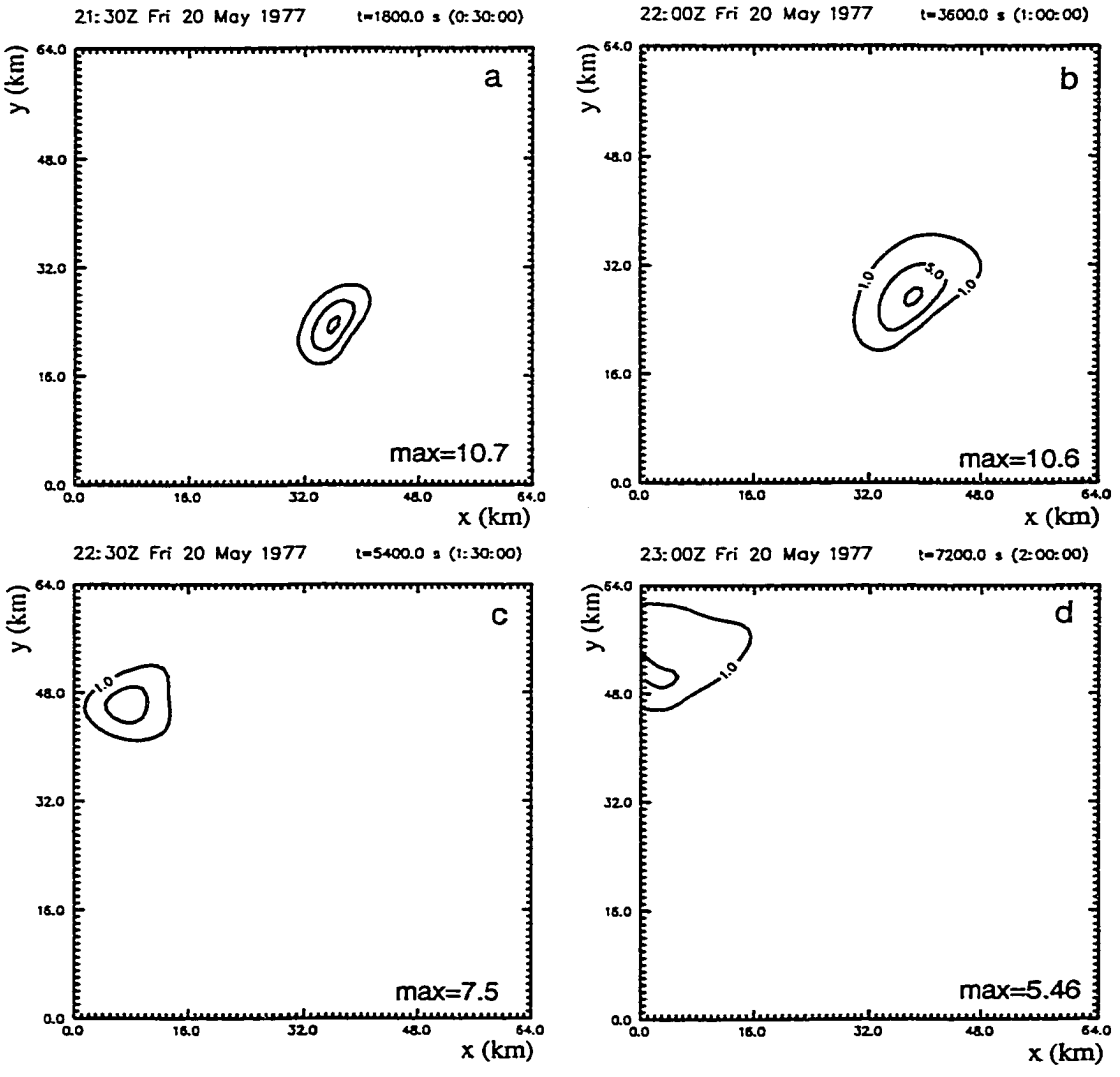

Fig. 4.6 The 5 min accumulated rainfall valid at 30 min (a) and the half-hour accumulated rainfall valid at 60 min (b), 90 min (c), and 120 min (d) in Exp. 1c. The contour values are 1 mm, 5 mm, and 10 mm, respectivelly.

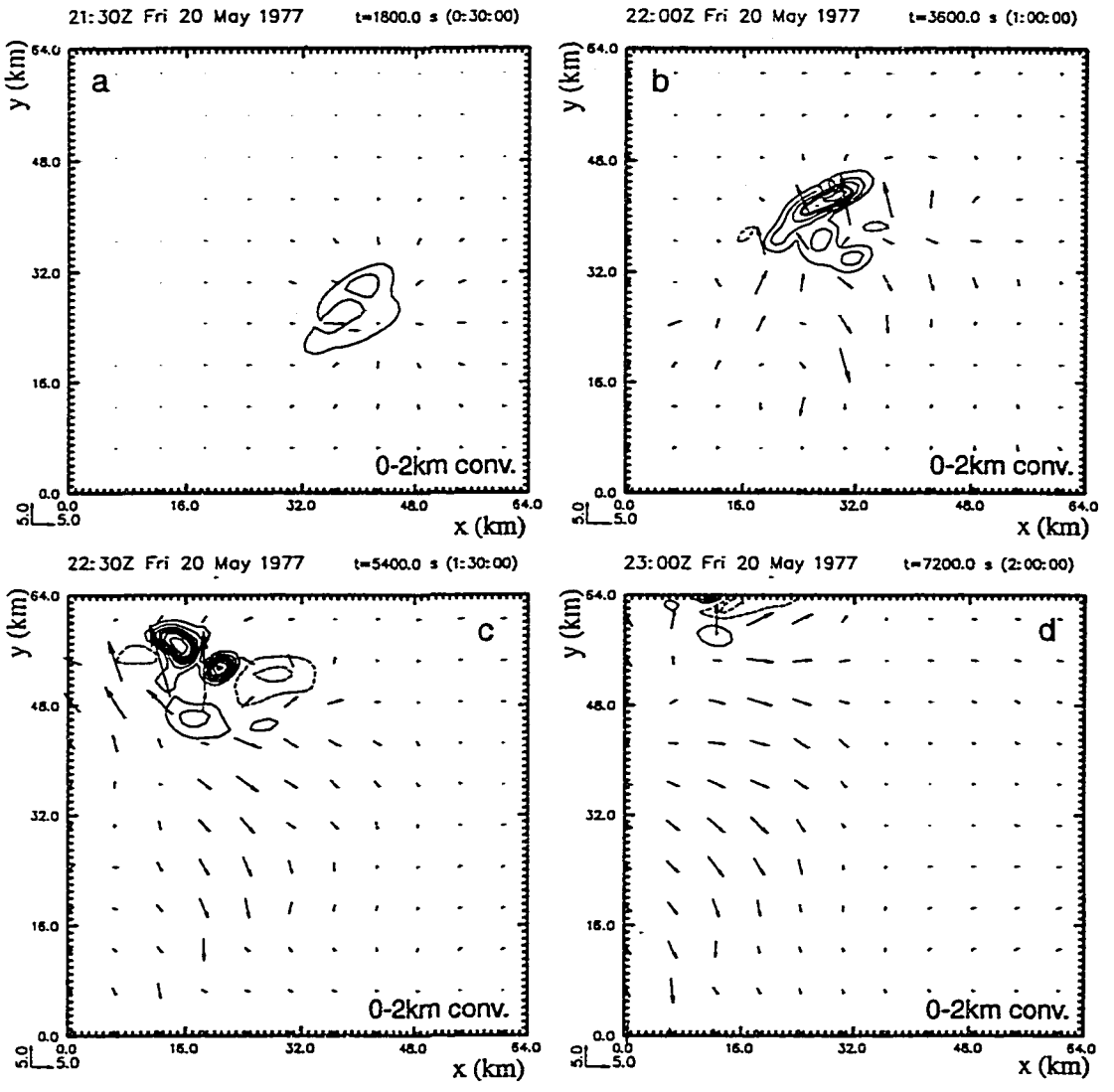

Fig. 4.7 The surface potential temperature perturbation (K, contour) and the wind vector (m/s) fields at 30min (a), 60 min (b), 90 min (c), and 120 min (d) in Exp. 1c. The contour interval is 0.5K.

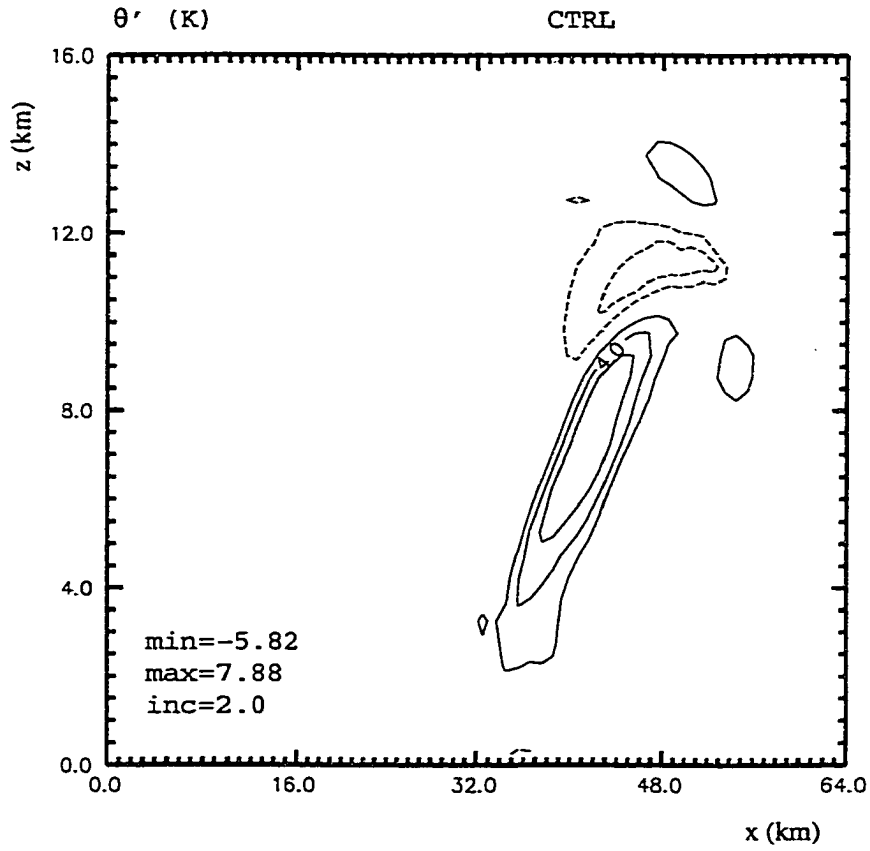

Fig. 4.8 X-Z cross section of the perturbation potential temperature field (unit: K) through y = 22 km at 25 min in the control run. The contour interval is 2K.

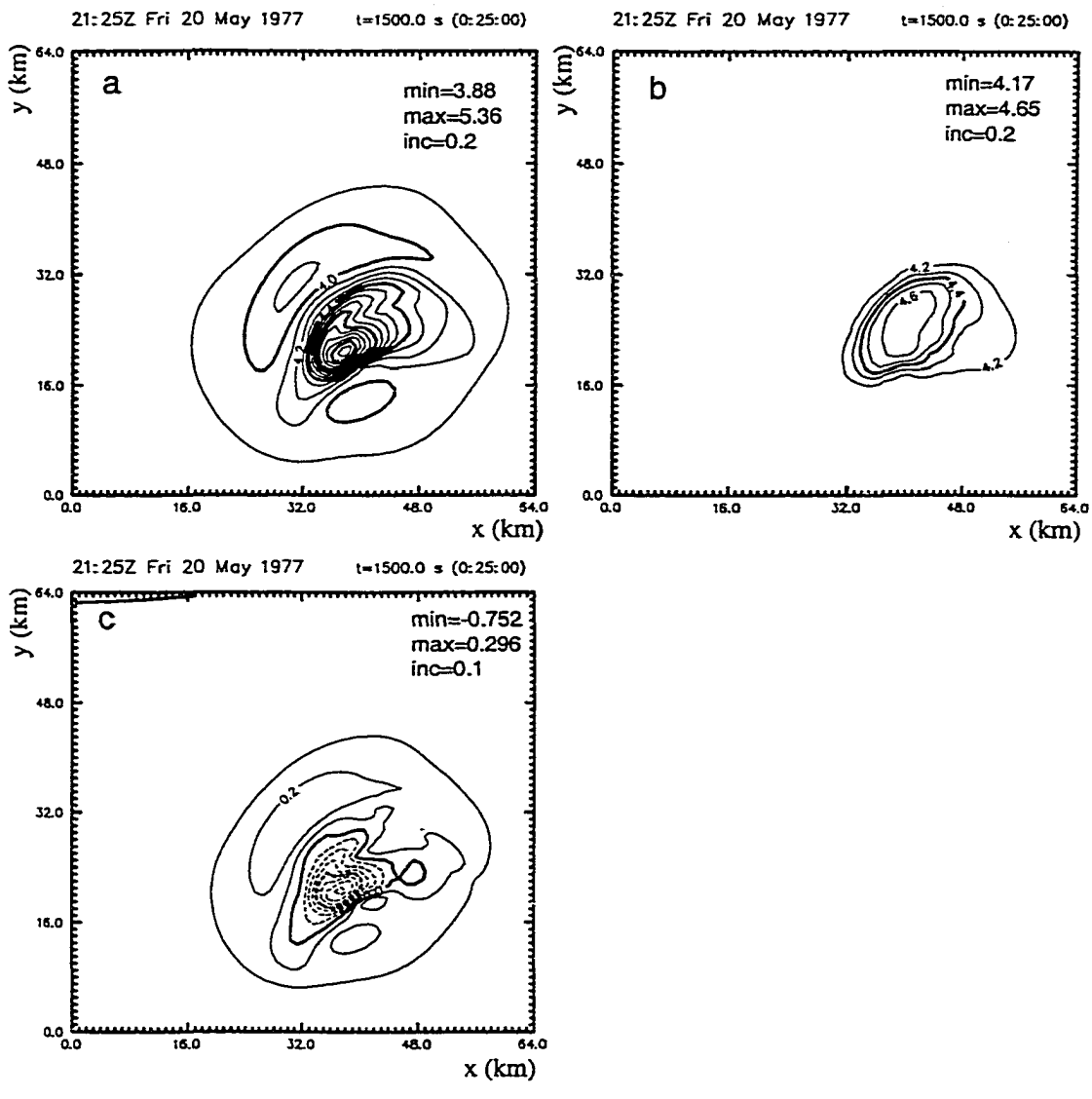

Fig. 4.9 The precipitable water fields (unit: cm) at 25 min in the control run (a), in the Exps. 1a, 1b, and 1c (b), and the difference between the two (c). The contour intervals are 0.2 cm in panels a and b, and 0.1 cm in panel c.

4.6.2 Retrieved wind experiments without diabatic initialization

The results from experiments 2a, 2b, and 2c are very similar to those from experiments 1a, 1b, and 1c (Fig. 4.10). Despite the fact that the initial wind field is "perfect" in the rain regions, the simulations failed to produce the

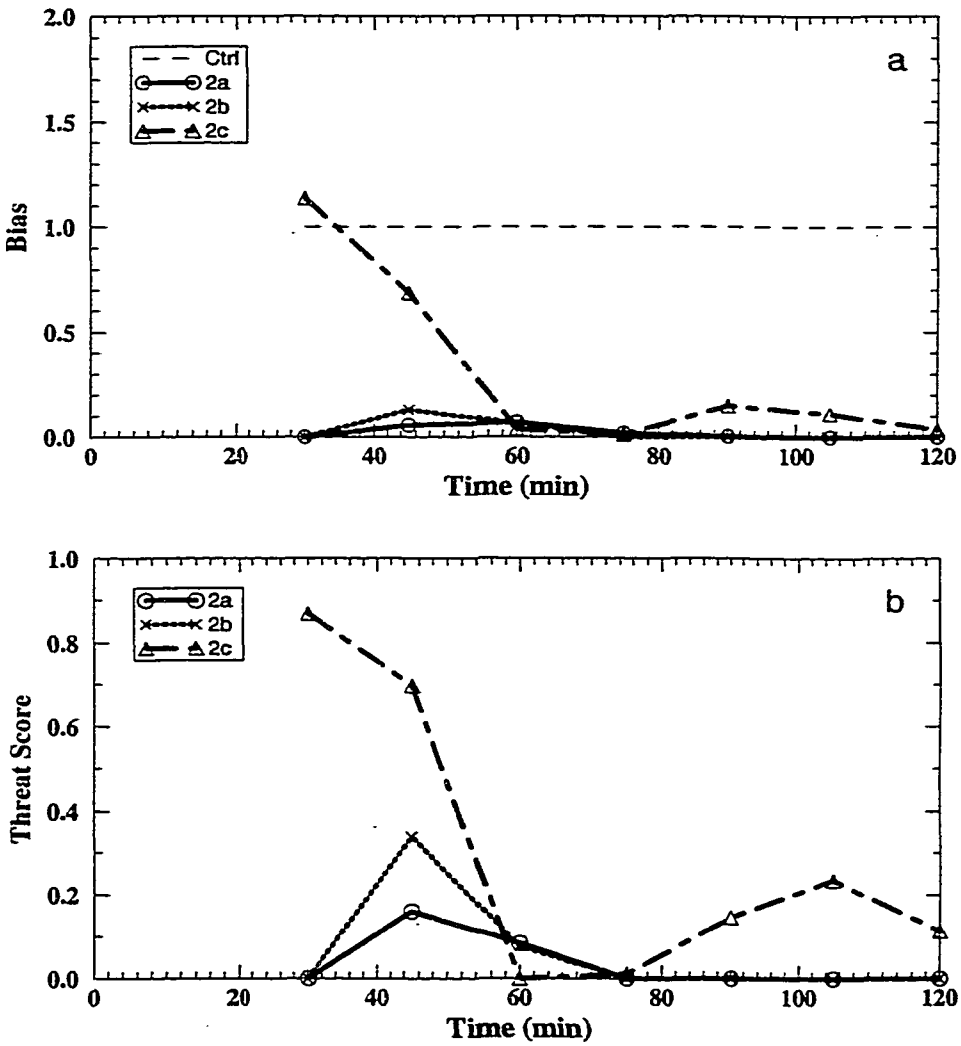

Fig. 4.10 Time series of the bias (a) and threat scores (b) for Exps. 2a, 2b, and 2c.

appropriate amount and areal coverage of precipitation. From Fig. 4.11 we can see that the initial vertical circulation in Exps. 2a, 2b, and 2c collapsed in less than 10 minutes. There are two reasons that the experiments failed to develop strong convection. One reason is the relatively dry and cool initial conditions as the author mentioned in section *4.6.1*. In the control run, continuing condensation warmed the air aloft and kept the updraft going. In Exps. 2a, 2b, and 2c, on the other hand, cloud condensation was weaker despite the initially correct updraft because the model was started from a drier and cooler initial condition. As a result, latent heating was small and the initial updraft was not

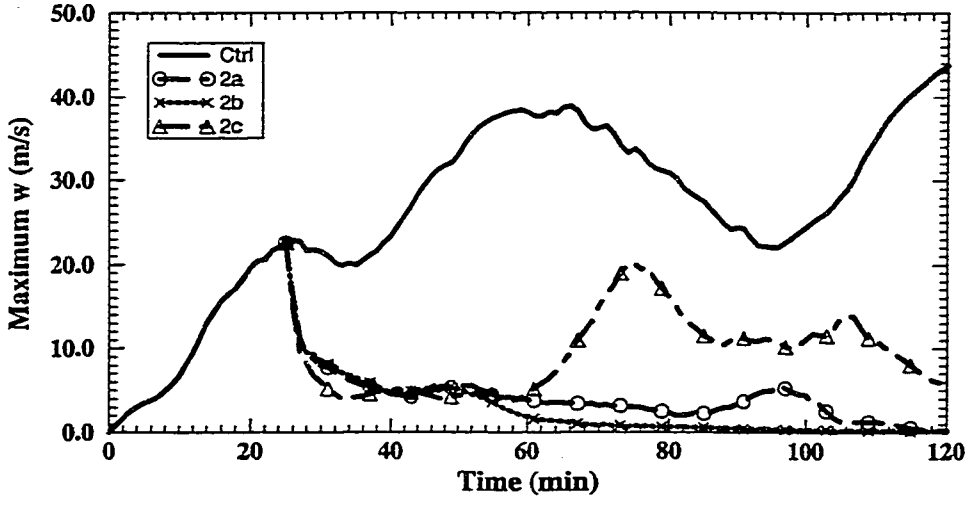

Fig. 4.11 Time series of the domain maximum updraft (unit: m/s) in the control run and in Exps. 2a, 2b, and 2c.

retained. Similar results were obtained by Turpeinen (1990) who found, on the large scale, that vertical circulations initialized by nonlinear normal mode

initialization could not be sustained when the initial moisture field was not properly initialized. Another reason is the lack of large-scale horizontal divergent fields that are needed to support the initial updrafts in the rain regions. An experiment (not shown) initialized with the perfect wind field in the whole domain (and everything else kept the same as in the base state) produced reasonable precipitation for the existing storm at the initial time, given the fact that the environment fields for this case are relatively moist and unstable. Therefore an accurate wind initialization can be helpful in cases where moisture observations are sufficient. Single Doppler velocity retrieval (Shapiro et al., 1995; Xu et al., 1995; Zhang and Gal-Chen, 1996) and three-dimensional wind adjustment with insertion/ removal of vertical circulations based on the cloud and precipitation analysis ("storm-surgery") (Fiedler 1998, http://cmrp.ou.edu/~bfiedler/cmrp/surgery), among others, may provide high resolution wind initializations that are suitable for convective-scale NWPs.

4.6.3 Conventional wind experiments with diabatic initialization

The bias and threat scores for experiments 3a, 3b, and 3c are shown in Figs. 4.12a, b. Fig. 4.13 shows the 30-min. accumulated rainfall fields valid at 60 and 120 minutes for the control run and for the three experiments. With diabatic initialization, all three experiments successfully spun up the storm precipitation at 60 minutes. The positions of the simulated storm precipitation agreed well with the control precipitation field. However, the first storm dissipated too quickly in

Exp. 3c (Figs. 4.13g, h) and the bias score (Fig. 4.12a) shows overestimation of the precipitation during the early simulation period and underestimation during the late simulation period in all three experiments.

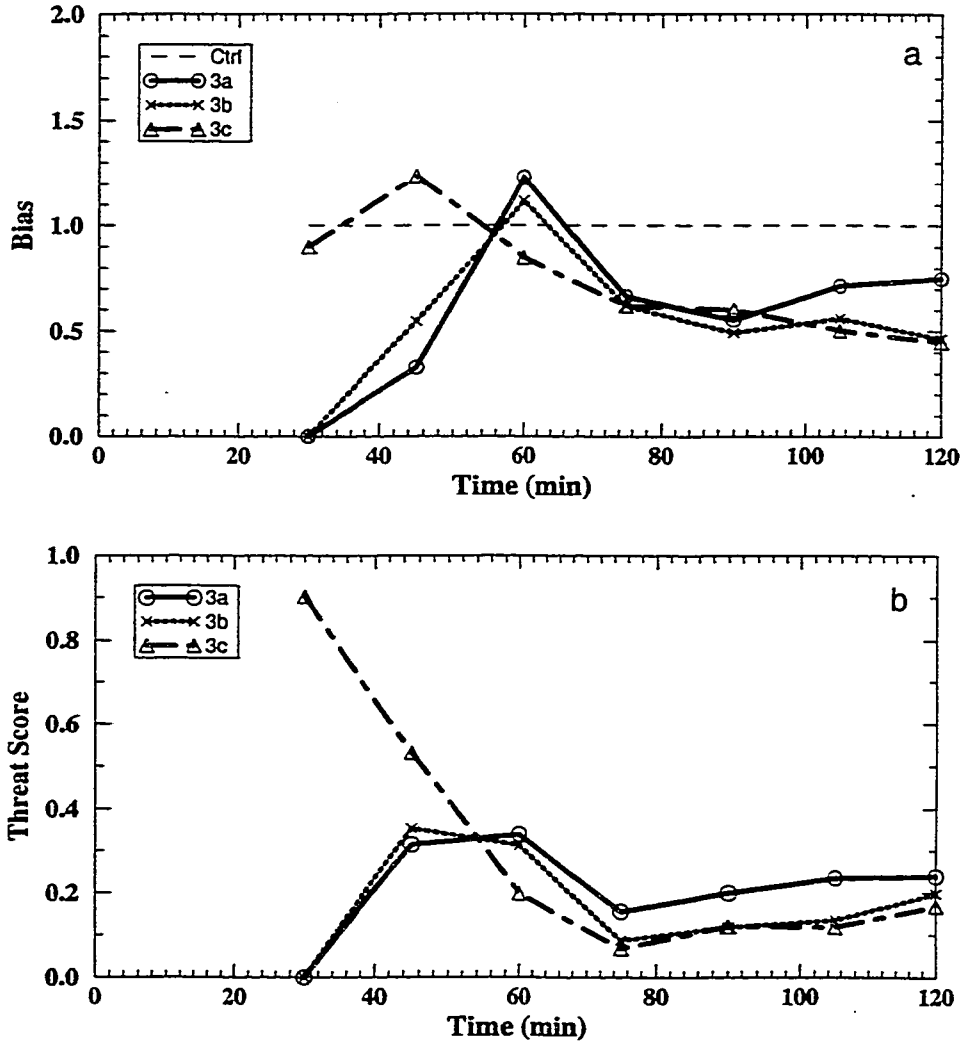

Fig. 4.12 Time series of the bias (a) and threat scores (b) for Exps. 3a, 3b, and 3c.

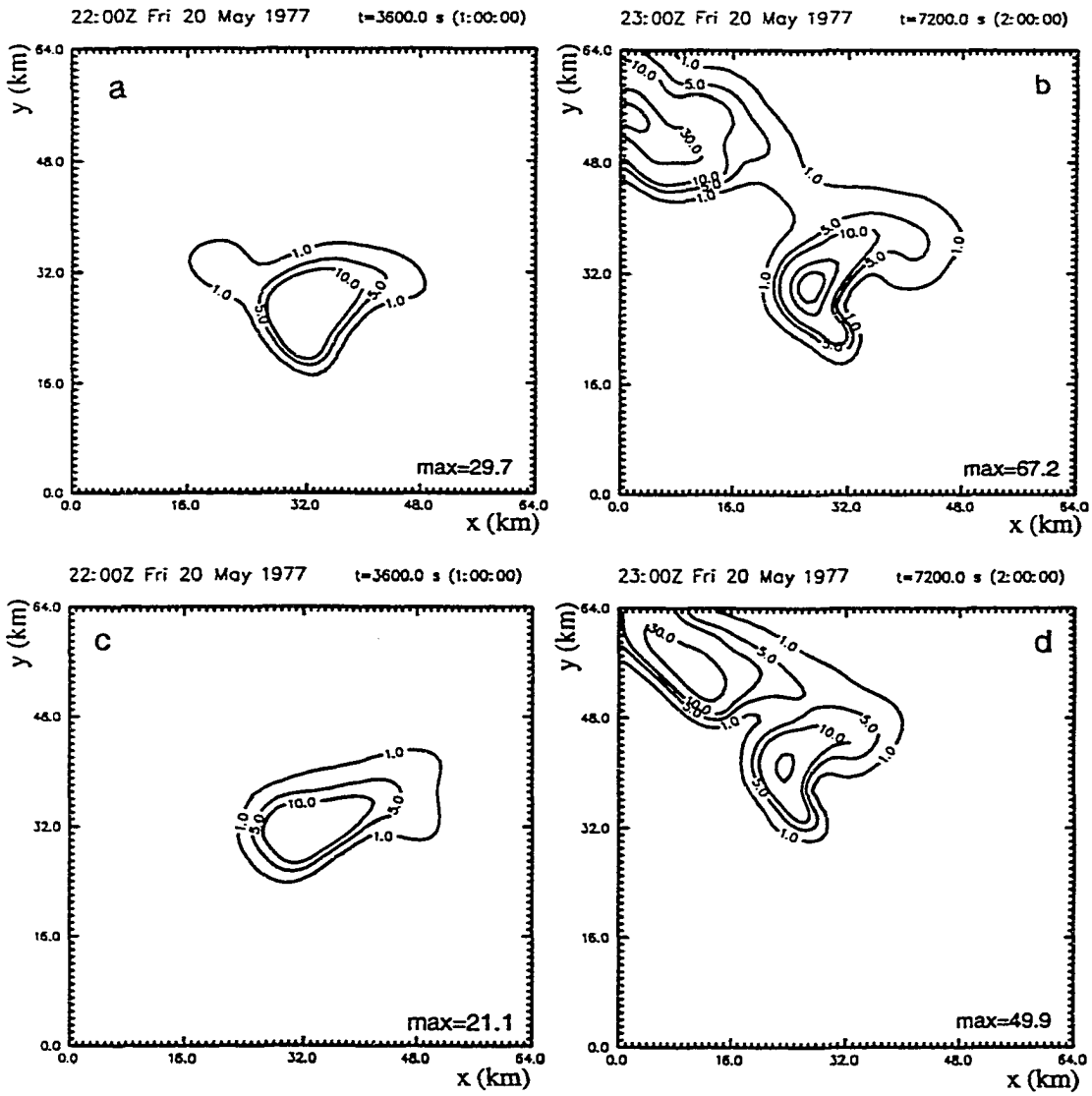

Fig. 4.13 The 30 min accumulated rainfall valid at 60 min (left panels) and 120min (right panels) in the control run (panels a and b) and in Exps. 3a (panels c and d), 3b (panels e and f), and 3c (panels g and h). The unit is mm, and the contour values are 1 mm, 5 mm, 10 mm, 30 mm, and 50 mm.

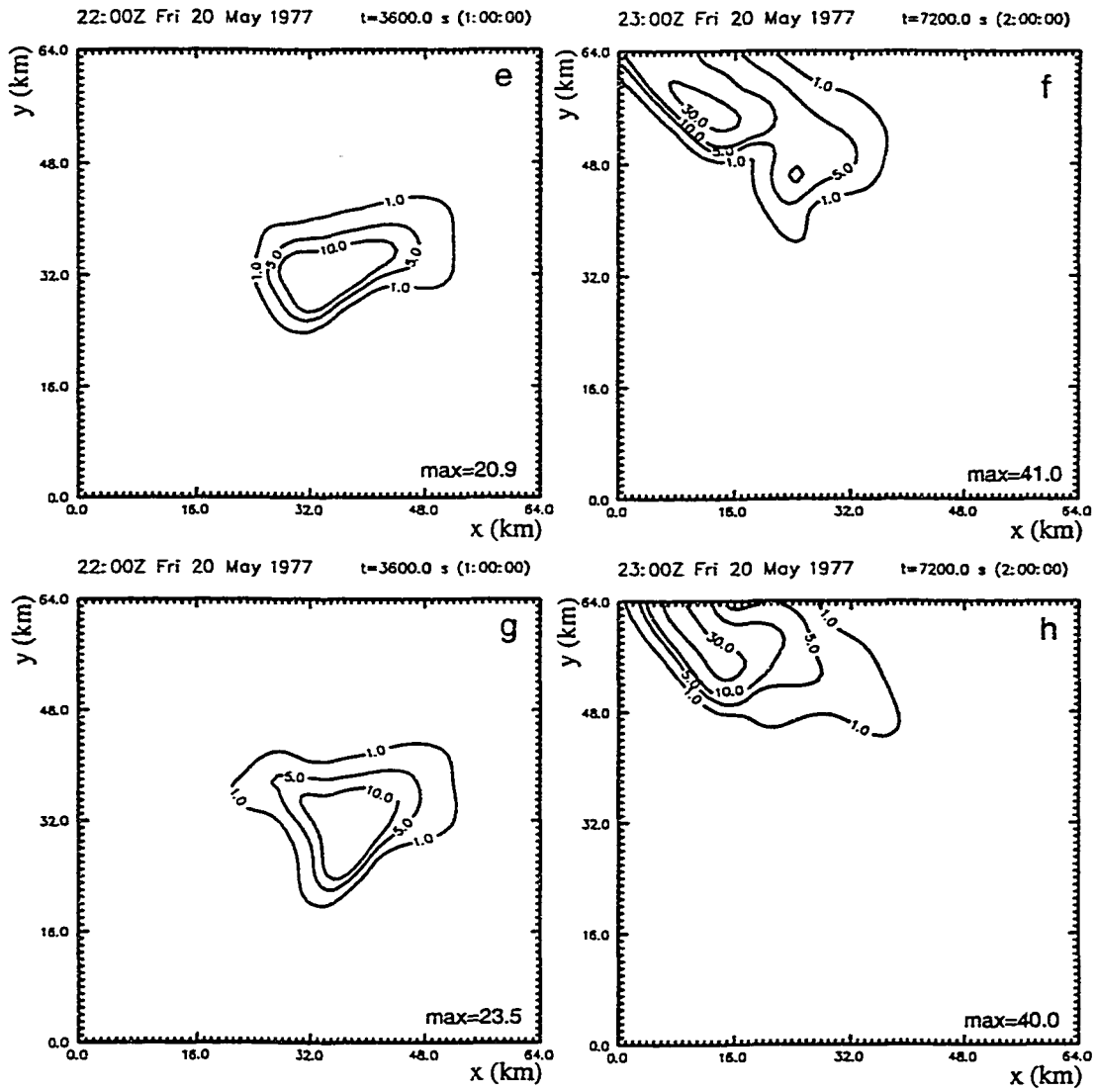

Fig. 4.13 (Continued)

The overestimation occurred because there were more initial water vapor and cloud water in the three experiments than in the control run due to an overestimation in the cloud liquid water analysis by the Smith-Feddes model. A greater amount of initial cloud water resulted in a warmer initial thermal field

than in the control run through the LH adjustment. Subsequently, the initial water vapor field is more moist because the RH adjustment is dependent on the temperature field. Figs. 4. 14a, b, and c show the precipitable water (PW) field at 25 min in the control run, in Exps. 3a, 3b, and 3c, which were all the same, and the difference between the two, respectively. In a large part of the storm region, the initial PW for the three experiments is 2mm or more than that in the control run (Fig. 4.14c). The overestimated initial moisture condensed into cloud water soon after the simulations started because the storm regions are saturated initially. The cloud water auto-converted into rain according to the following formula:

$$\partial q_r/\partial t\big|_{auto} = \alpha_{auto} \bullet (q_c - q_{c0}) \tag{4.5}$$

where $\partial q_r/\partial t\big|_{auto}$ represents the increase rate of the rainwater mixing ratio due to auto-conversion of cloud water into rainwater, α_{auto} is the autoconversion rate, q_{c0} is a threshold value for the auto-conversion process to activate. In our simulations α_{auto} was $0.001s^{-1}$ and q_{c0} was 1g/kg. Equation (4.5) indicates that any cloud water content, when exceeding 1g/kg, will gradually convert into rainwater in about 1000 seconds (~17 minutes). Once there is rainwater, the accretion process will take effect and rainwater content increases at the following rate:

$$\partial q_r/\partial t\big|_{accr} = \alpha_{accr} \bullet (q_c q_r)^{0.875} \tag{4.6}$$

Here $\partial q_r/\partial t\big|_{accr}$ represents the increase rate of the rainwater mixing ratio due to accretion of cloud droplets by raindrops and α_{accr} is the accretion rate. Accretion

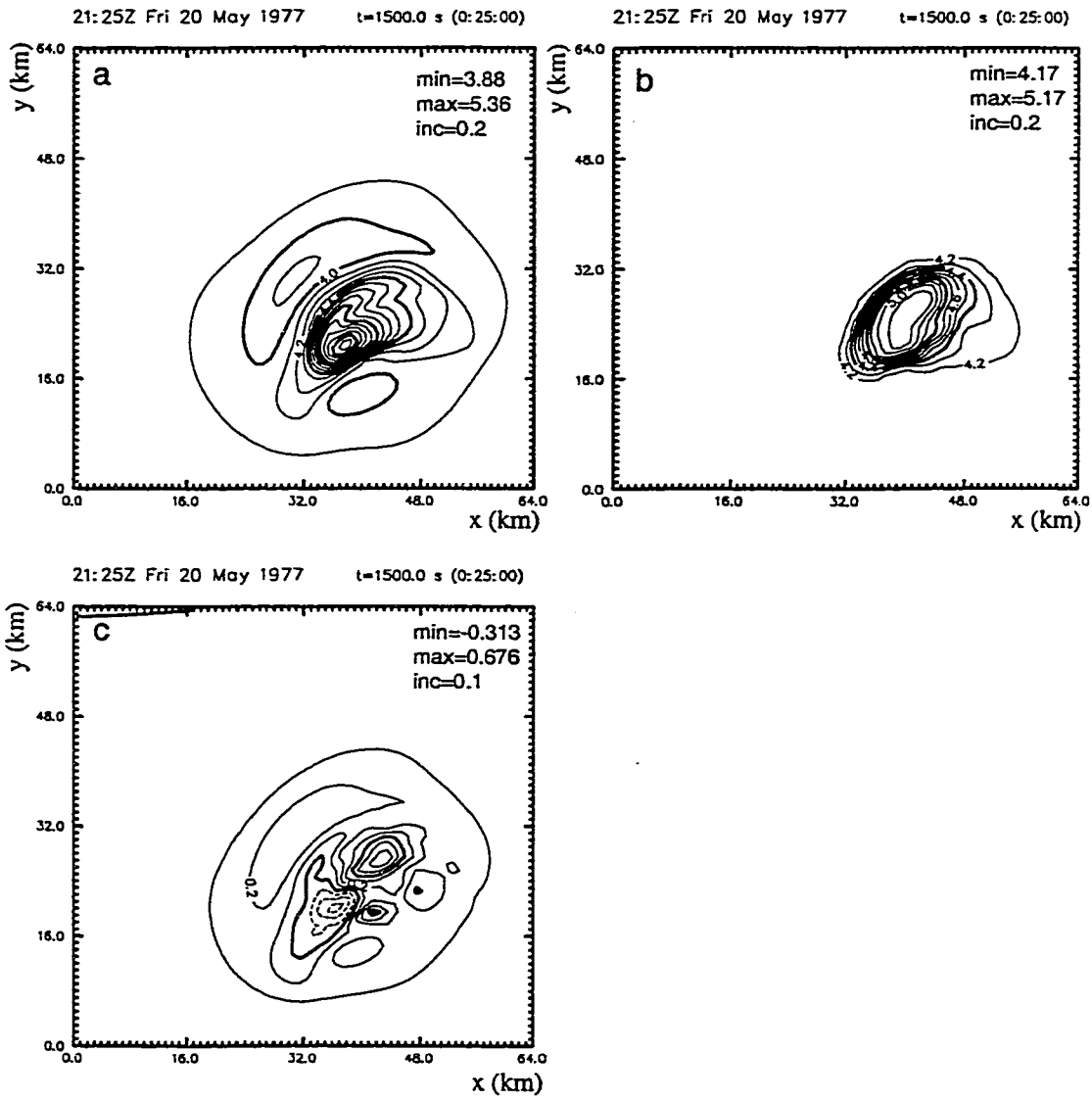

Fig. 4.14 The precipitable water fields (unit: cm) at 25 min in the control run (a), in the Exps. 3a, 3b, and 3c (b), and the difference between the two (c). The contour intervals are 0.2 cm in panels a and b, and 0.1 cm in panel c.

is a very efficient and important mechanism for raindrop growth. A bias score plot (Fig. 4.15) for 5-minute accumulated rainfall shows that the rainfall amount in Exp. 3a remained small before 40 min. After 40 min (i.e., 15 – 20 min from the beginning time of the simulation) the bias score increased rapidly, corresponding to the end of an auto-conversion cycle and the onset of the accretion process.

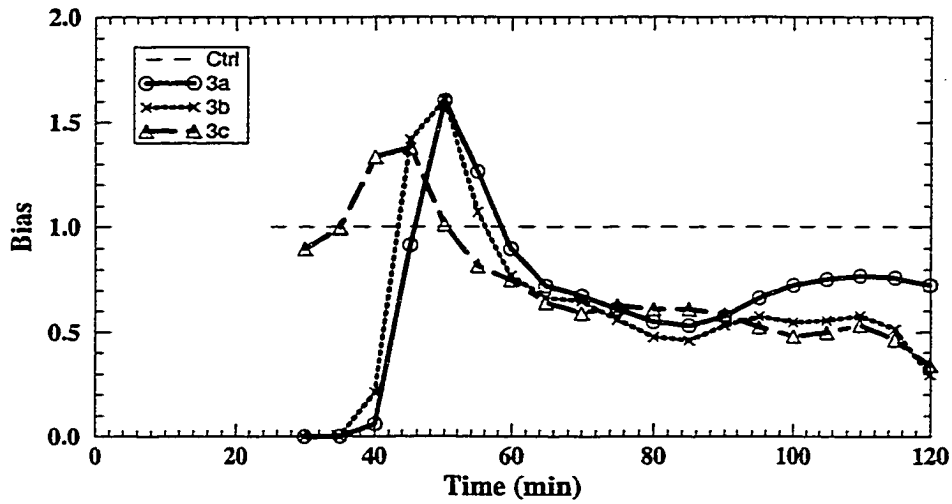

Fig. 4.15 Time series of bias scores for the 5 minute-accumulated rainfall in Exps. 3a, 3b, and 3c.

The peak bias score for Exp. 3b is very similar to that for Exp. 3a except for a small lead in time. The small lead was due to the nonzero initial q_c field in Exp. 3b, which reduced the time for accretion to become significant. In Exp. 3c, nonzero rainwater was inserted at the initial time. The initial rainwater fell out and produced rainfall that was similar to the control field. The initial q_r also

induced the accretion process quickly, and resulted in a 5 min temporal lead in the bias score peak (Fig. 4.15) with respect to the peaks for Exps. 3a and 3b.

It is noticed that the threat scores (Fig. 4.12b) are poor, even though the areal coverage of the simulated rainfall fields agreed reasonably well with the control (Fig. 4.13). After examining the results we found that small errors in the positions of the simulated storms (i.e., phase errors) caused the low threat scores. To evaluate the phase errors, a maximum threat score with shifting (MTSS) and the shifting distance (d_MTSS) at which the MTSS is obtained are calculated. Fig. 4.16a shows significant increases in the threat scores after the simulated rainfall fields are "optimally" displaced from their original position. Comparison between Fig. 4.16 and Fig. 4.12 indicates that the low threat scores (Fig. 4.12b) are largely due to the phase errors (Fig. 4.16b) in the simulated precipitation fields. These results show that the MTSS and d_MTSS can provide useful additional information for verification of convective-scale precipitation forecasts.

Time series of the shifting distances corresponding to the maximum threat scores are plotted in Fig. 4.16b. It is seen that the phase errors generally grow with time. The large phase errors for Exp. 3c from 80 min to 110 min are due to the unrealistic quick dissipation of the first storm. Fig. 4.17 shows that at 90 min there were two distinct storm systems in the control run. Exps. 3a and 3b captured the two-cell structure (Figs. 4.17b, c). However, there was only one storm cell in Exp. 3c (Fig. 4.17d). In the control run there was a vertical

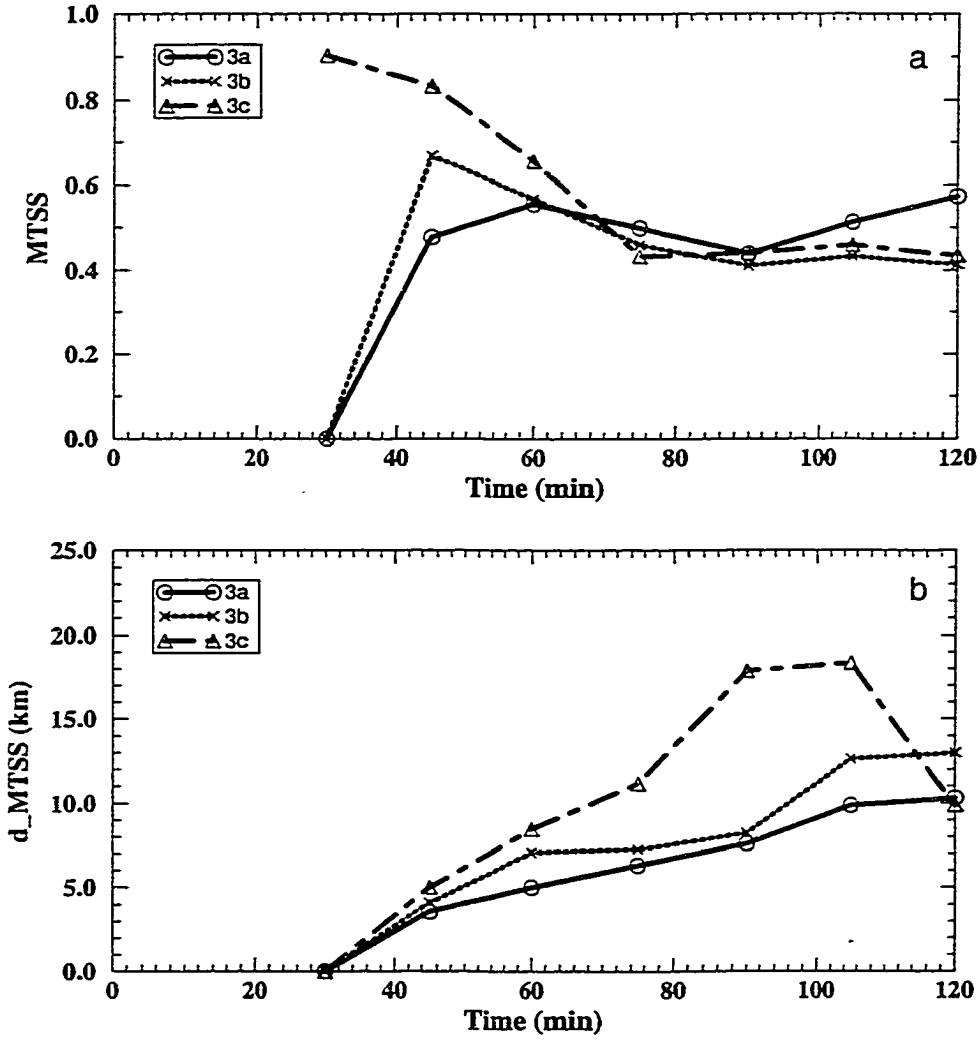

Fig. 4.16 Time series of the maximum threat score with shifting (MTSS, panel a) and the shifting distance corresponding to the maximum threat score (d_MTSS, panel b) for Exps. 3a, 3b, and 3c.

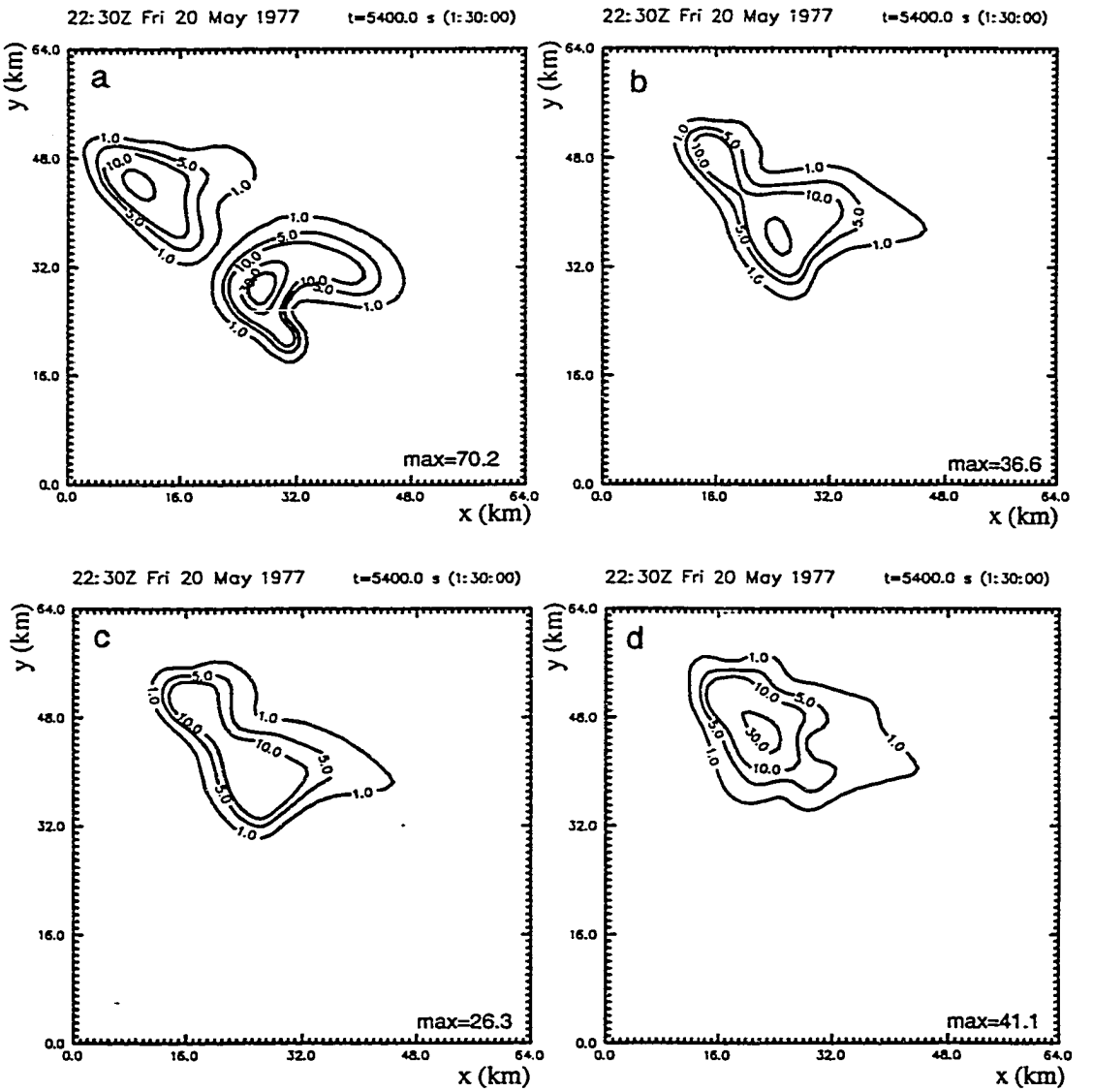

Fig. 4.17 The half-hour accumulated rainfall valid at 90 min in the control run (a) and in Exps. 3a (b), 3b (c), and 3c (d). The unit is mm, and the contour values are 1 mm, 5 mm, 10 mm, 30 mm, and 50 mm.

circulation in the simulated thunderstorm existing at 25 min (not shown). The associated low-level convergence region was centered at x ≈ 36km and y ≈ 21.5km at 30 min (Fig. 4.18a). The storm precipitation generated cold outflows at the surface (Fig. 4.18b) and a second convective region began to the northwest of the first storm half an hour later (Figs. 4.18c, d). As the second storm grew stronger with time, the first storm retained its intensity (Figs. 4.18e, f, g, and h). On the other hand, there was no vertical circulation at the initial time in Exps. 3a, 3b, and 3c because the base state wind field was used. The moisture and diabatic initialization helped to induce vertical circulations at 30 min (Figs. 4.19a, 4.20a) although they were weaker than in the control run. The circulation in Exp. 3a grew quickly and generated cold outflows and stimulated the development of the second storm, as did the control run (Figs. 4.19b, c). The storm intensities were comparable to those in the control run, although the positions were displaced (Figs. 4.19c, d). In Exp. 3c the circulation at 30 min was much weaker than in Exp. 3a and in the control run (Fig. 4.20a), because the initially inserted rainwater was falling and hampering the developing updraft. As a result, the first storm weakened and died before 90 min (Figs. 4.20b, c). The early evolution of the vertical circulations in Exp. 3b was similar to those in Exp. 3a (not shown). But the initial cloud water load hindered the development of the first storm and the storm dissipated shortly before 2 hours.

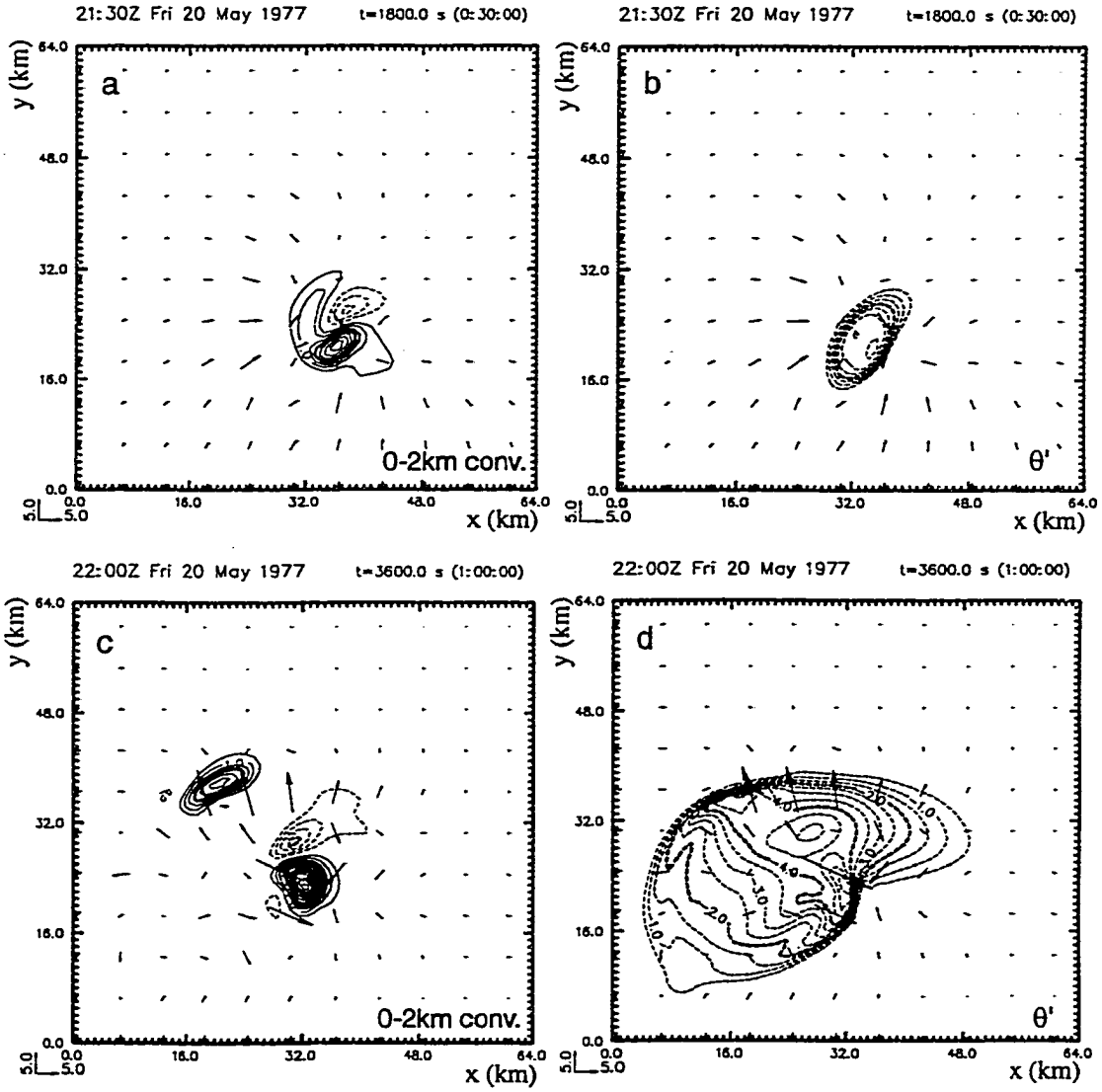

Fig. 4.18 Low-level (0-2 km) convergence (contours in left panels, unit: $10^{-3}s^{-1}$) and the surface perturbation potential temperature (contours in right panels, unit: K) overlapped with the surface wind vector fields at 30 min (panels a, and b), 60 min (panels c and d), 90 min (panels e and f), and 120 min (panels g and h) in the control run. The contour intervals for the low-level convergence and perturbation potential temperature fields are $0.5x10^{-3}s^{-1}$ and 0.5 K, respectively.

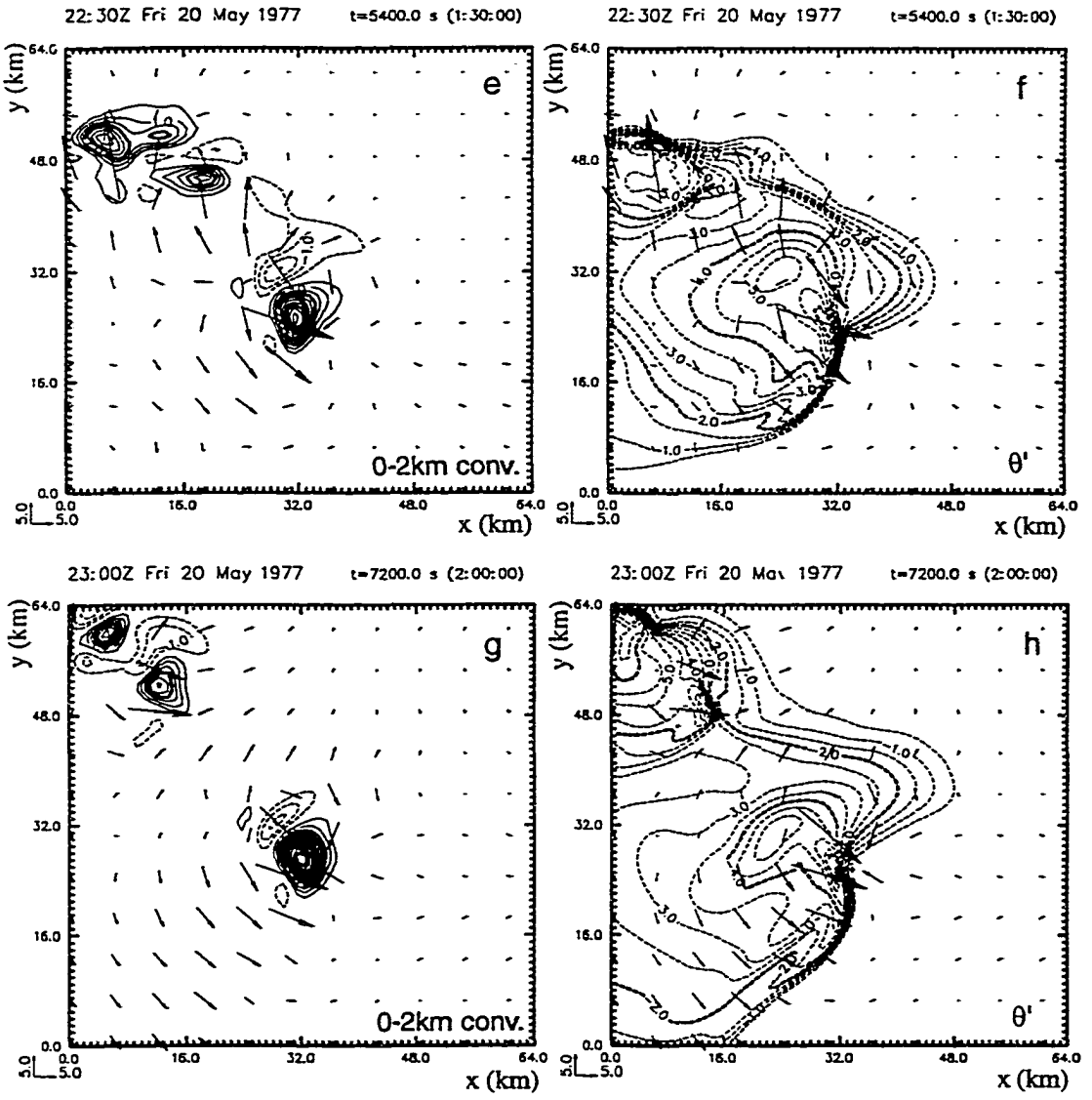

Fig. 4.18 (Continued)

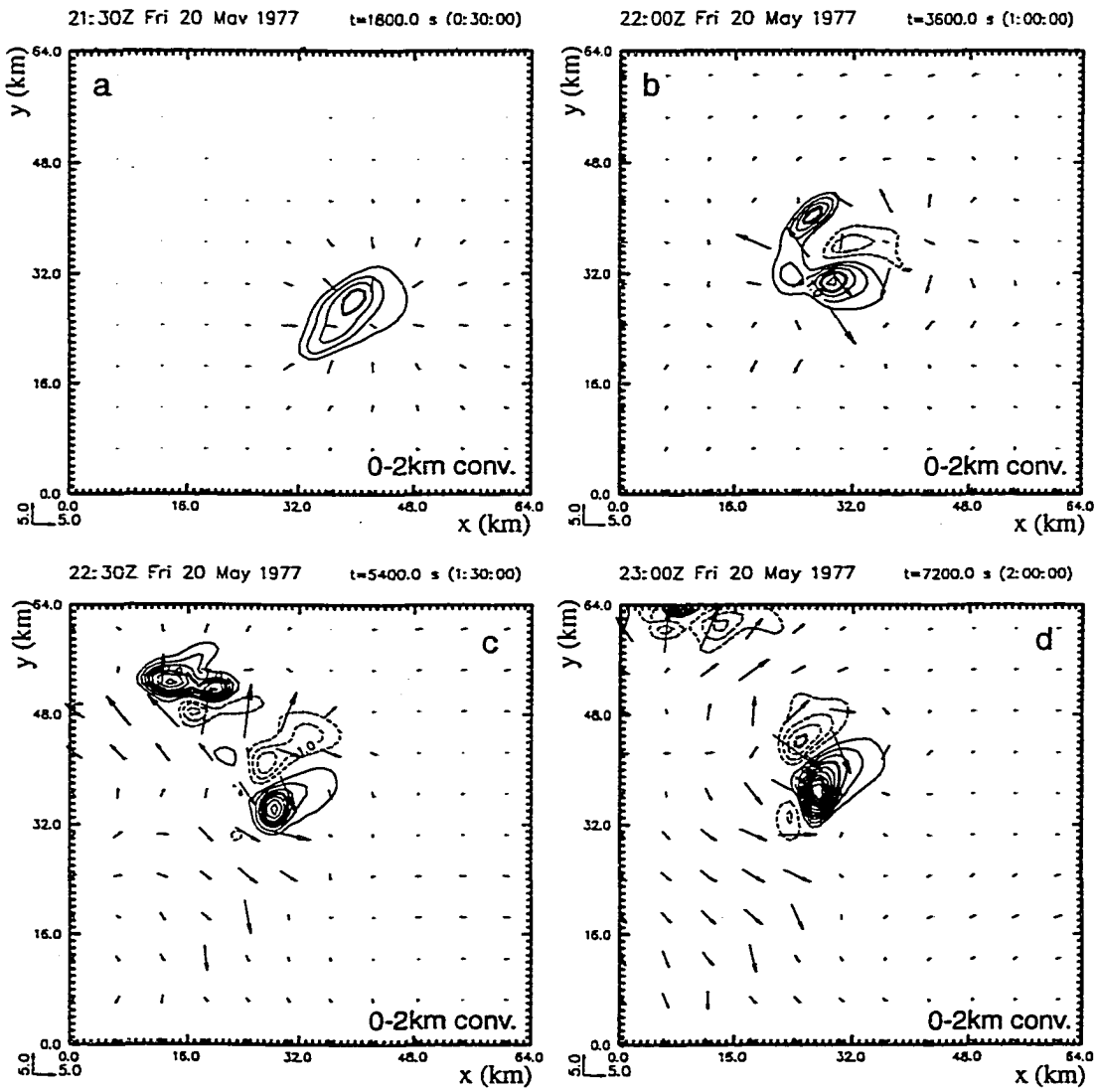

Fig. 4.19 Low-level (0-2 km) convergence (contours in unit of $10^{-3}s^{-1}$) and the surface wind vector fields at 30 min (a), 60 min (b), 90 min (c), and 120 min (d) in Exp. 3a. The contour interval is $0.5x10^{-3}s^{-1}$.

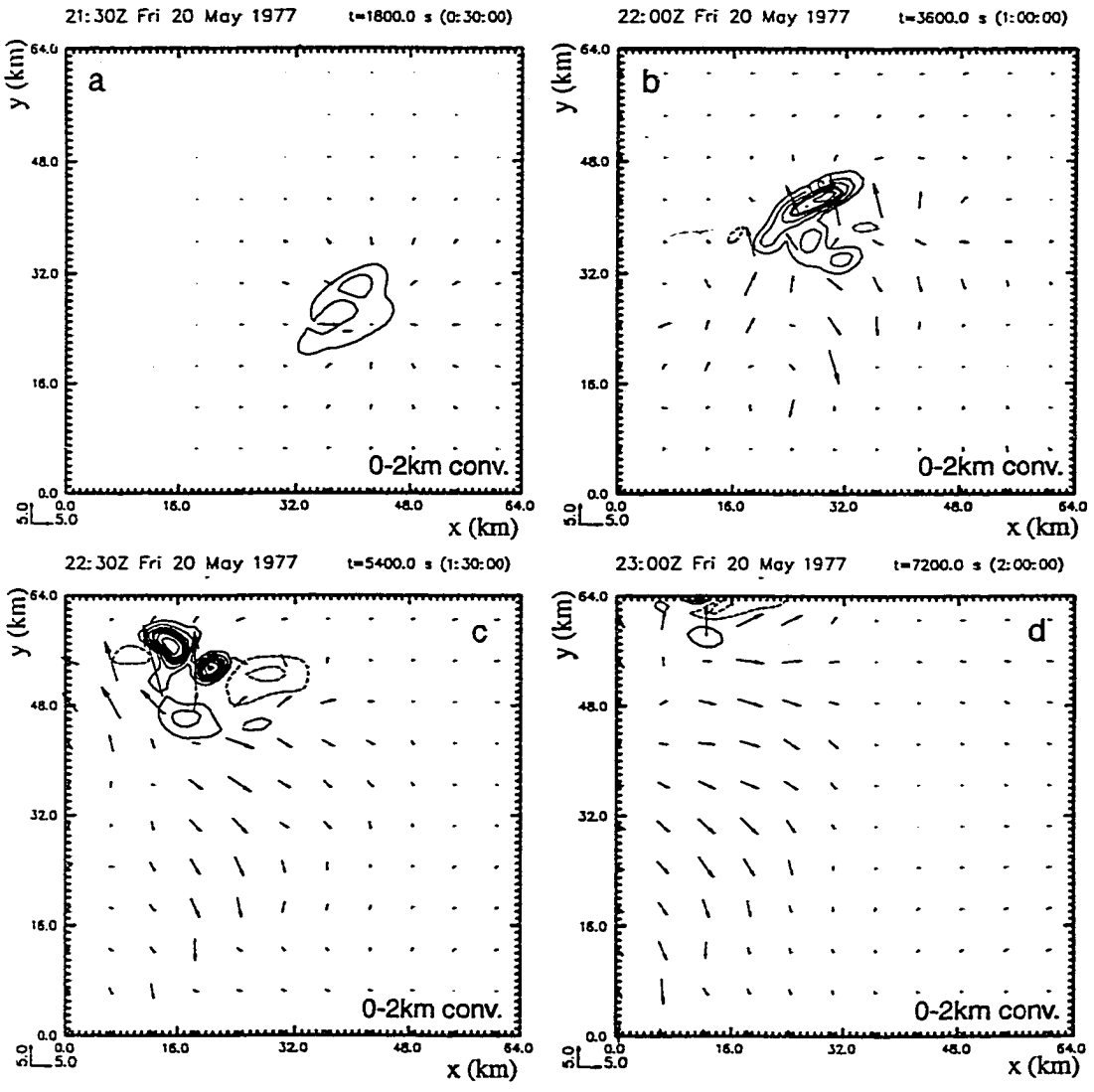

Fig. 4.20 Low-level (0-2 km) convergence (contours in unit of $10^{-3}s^{-1}$) and the surface wind vector fields at 30 min (a), 60 min (b), 90 min (c), and 120 min (d) in Exp. 3c. The contour interval is $0.5x10^{-3}s^{-1}$.

4.6.4 Retrieved wind experiments with diabatic initialization

The bias and traditional threat scores for experiments 4a, 4b, and 4c are shown in Figs. 4.21a, b, respectively. Figs. 4.22a, b show the MTSS and the d_MTSS for the three experiments. The evolution of the bias scores are similar to the three conventional wind experiments with the diabatic initialization, although the intensities of the precipitation are stronger and more realistic in the experiments with the retrieved wind (Fig. 4.21a vs. Fig. 4.12a). There are significant improvements in the traditional threat scores comparing the two sets of experiments (Fig. 4.21b vs. Fig. 4.12b). Shifting also improves the threat scores, but not as much as in Exps. 3a, 3b, and 3c (Fig. 4.22a vs. Fig. 4.16a). This indicates that the phase errors in the retrieved wind experiments are not as large as in the conventional wind experiments. The d_MTSS plot in Fig. 4.22b confirms this. For example, the position errors at 120 min are 1.4 km, 3.6 km, and 4.4 km for Exps. 4a, 4b, and 4c, respectively. They are substantially smaller than their counterparts in the conventional wind experiments, which were 10.0 km, 13.0 km, and 10.0 km, respectively (Fig. 4.16b). A more remarkable improvement is the decrease of the phase errors in Exp. 4c with respect to Exp. 3c between 80 to 110 min. Recall that the large phase errors in Exp. 3c were due to the unrealistic disappearance of the first storm. In Exp. 4c, the initial wind field in the rain region was the same as that in the control run and an updraft was existing at the time (Fig. 4.23). The initial updraft provided a balancing

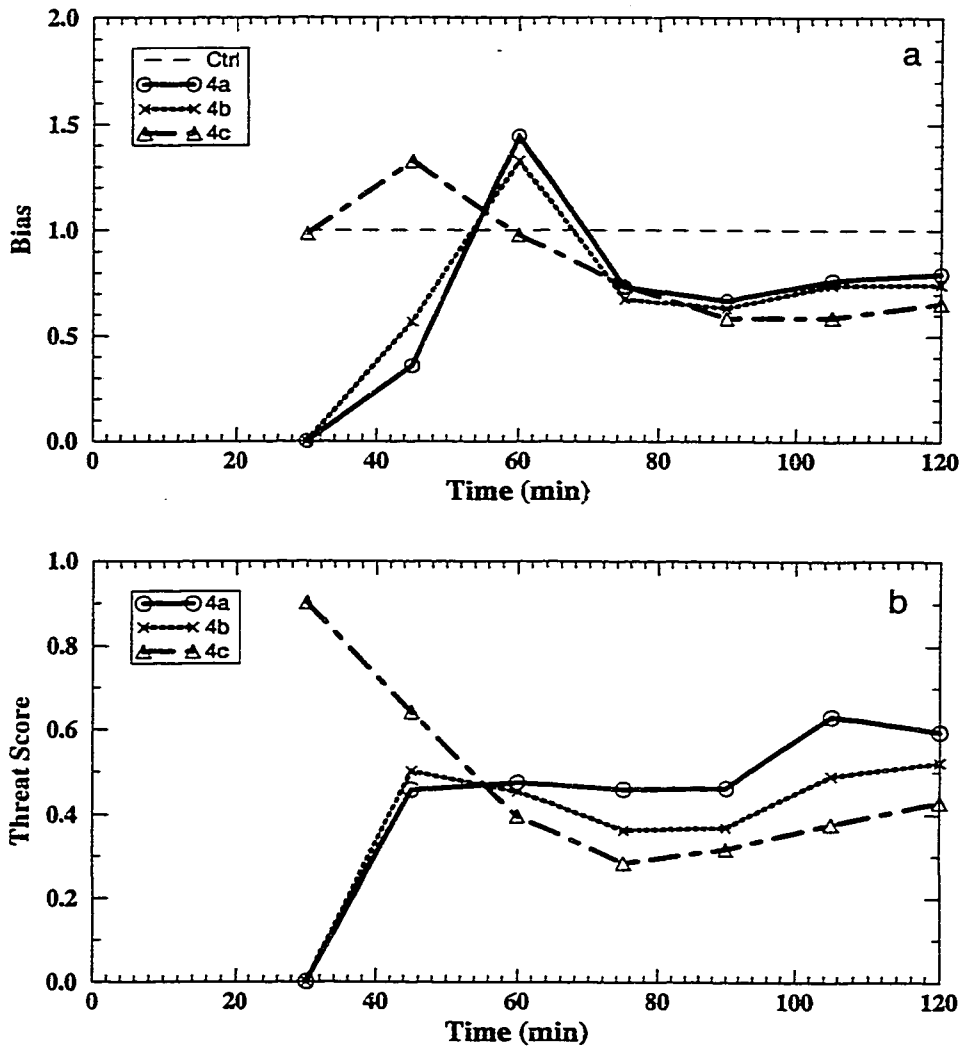

Fig. 4.21 Time series of the bias (a) and threat scores (b) for Exps. 4a, 4b, and 4c.

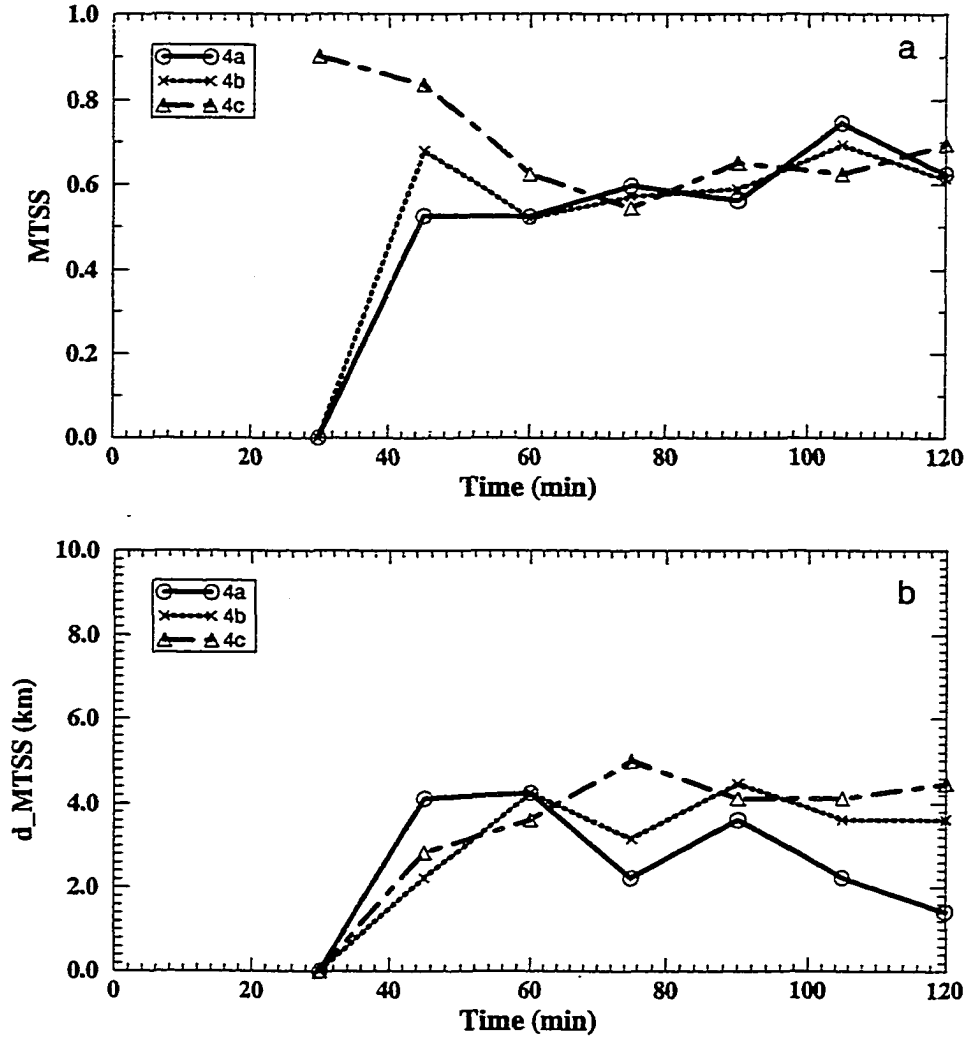

Fig. 4.22 Time series of the maximum threat score with shifting (MTSS, panel a) and the shifting distance corresponding to the maximum threat score (d_MTSS, panel b) for Exps. 4a, 4b, and 4c.

mechanism for the falling rain and avoided the detrimental effect of the initial rainfall on the development of the first storm. The low level convergence associated with the first storm is stronger at 30 min in Exp. 4c (Fig. 4.24a) than it is in Exp. 3c (Fig. 4.20a). The storm was retained for a longer time, and its intensity as well as the position are much more accurate than in Exp. 3c (Fig. 4.24 vs. Fig. 4.18).

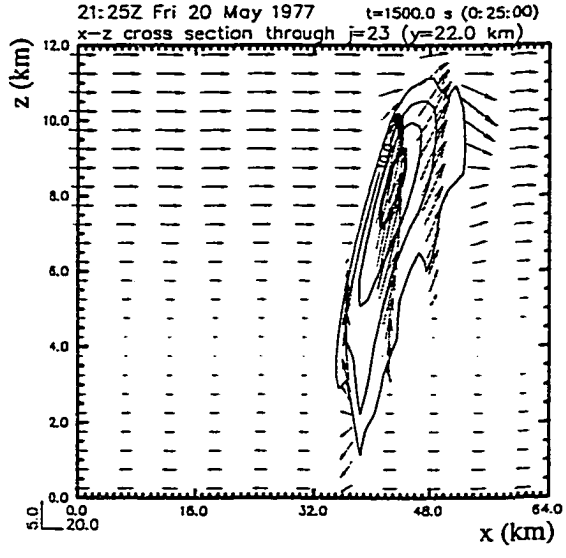

Fig. 4.23 X-z cross section of the vertical velocity field (unit: m/s) through y = 22 km at 25 min in Exp. 4c. The contour interval is 5 m/s.

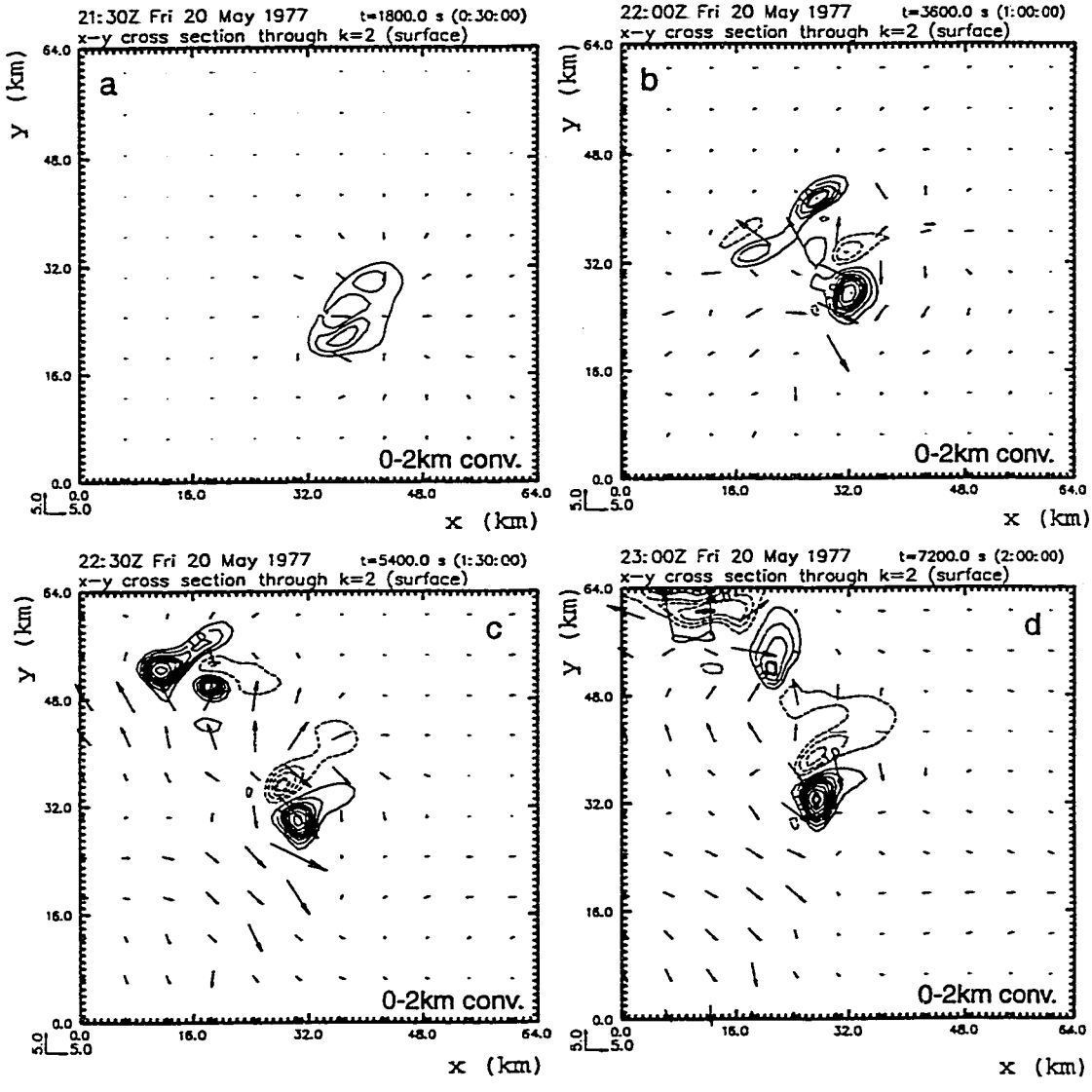

Fig. 4.24 Low-level (0-2 km) convergence (contours in unit of $10^{-3}s^{-1}$) and the surface wind vector fields at 30 min (a), 60 min (b), 90 min (c), and 120 min (d) in Exp. 4c. The contour interval is $0.5x10^{-3}s^{-1}$.

4.7 Summary

Observing system simulation experiments (OSSEs) have been carried out to assess the impact of the new moisture and diabatic initialization scheme on convective-scale numerical weather forecasts. Sensitivities of the forecast model to different moisture/diabatic initialization strategies and to different wind initializations were also tested.

The OSSEs were divided into 4 groups. The first two groups of experiments were initialized using different moisture initialization strategies without the diabatic initialization. Among the two groups, one was initialized using a smooth background wind field, which emulates the conventional radiosonde observations, and the other was initialized using a detailed wind field within the rain region to emulate a Doppler wind retrieval. Both sets of experiments failed to produce realistic amounts and areal coverage of precipitation. The results indicate that conventional observing systems are insufficient for resolving the warm and moist regions in clouds. As a result, the initial condition was too cool and dry compared to "reality" and was unfavorable for convection to develop. We found that moisture initialization and diabatic initialization should be performed consistently. Without diabatic initialization, the moisture adjustment is limited and insufficient. We also found that inserting detailed wind information within the rain regions did not help the precipitation

simulations when there was no diabatic initialization. The inserted divergent circulations were not retained due to (1) the absence of cloud condensation and latent heat release and (2) the absence of a consistent large-scale horizontal divergence field to support the initial updrafts in the rain regions. A three-dimensional wind adjustment as proposed by Fiedler (1998, personal communication) may provide a solution for obtaining a consistent horizontal divergence field. A continuous data assimilation can also help sustain the initial updrafts in the rain regions. These techniques will be investigated in future work. It was shown that inserting a rainwater field at the initial time had a positive impact in producing cool pools near the surface and generating new storms.

The second two groups of experiments were initialized using both moisture and diabatic initializations. The results show that the diabatic initialization has successfully reduced the model spinup time and produced precipitation with reasonably good intensity and areal coverage. It was found that the initial water load, especially rainwater, when not balanced by consistent updrafts, can hinder the development of existing storms at the initial time. It was also found that an accurate initial wind field in the rain region had a significant positive impact on reducing the phase errors in precipitation simulations.

The simulation results also showed the impact of inaccuracies in the moisture and diabatic initialization on precipitation forecasts. Overestimation of precipitation was found in the early period of the model simulations with diabatic

initialization, which was due to the overestimation of water vapor and cloud water in the initialization. An improvement to this might be obtained through assimilation of satellite-derived precipitable water and vertically integrated cloud liquid water fields. In the meantime, it was shown that the present moisture and diabatic initialization scheme can provide significant improvement in convective-scale precipitation forecasts with the aid of radar and satellite observations. We now need to determine if application of the moisture and diabatic initialization scheme to a real data case will also show similar improvement. The real data experiments are presented in the next chapter.

Chapter 5
A Case Study

5.1 Introduction

In the previous chapter, the impact of a new moisture and diabatic initialization procedure on convective-scale numerical weather prediction was tested using OSSEs. It was found that the moisture and diabatic initialization had a significant positive impact on reducing the model's spinup time for the precipitation forecasts. The OSSEs were a set of simplified scenarios for moisture and diabatic initialization of the real atmosphere. The model was perfect with respect to the reference atmosphere. The "retrieved" wind fields in the rain regions were error free. These conditions are never satisfied in real-time data assimilation and numerical weather prediction. To further test the generality of the sensitivities obtained from the OSSEs, we carried out a set of real data experiments.

5.2 The case

The case chosen for the tests was a widespread convective precipitation event that occurred on 7 May 1995. The synoptic background for the event is illustrated in Figs. 5.1, 5.2, and 5.3. Figure 5.1 shows the RUC (Rapid Update Cycle, Benjamin et al. 1994) analysis of the 500 mb geopotential height and wind fields valid at 1200 and 1800 Z on 7 May and 0000 Z on 8 May of 1995. At 1200 Z a deep extratropical cyclone was centered over Arizona (Fig. 5.1a). The cyclone moved northeastward and slowly weakened over the next 12 hours (Figs. 5.1b, c). The 3-hourly surface dew point and wind vector fields are shown in Fig. 5.2. A north-south oriented dryline was located in eastern New Mexico at 1200 Z (Fig. 5.2a). The dry line moved eastward across the western Texas border and reached the middle of the Texas panhandle at 1800 Z (Fig. 5.2b). After 1800 Z the dryline moved much slower and remained in the Texas panhandle area (Fig. 5.2c). A strong southerly low-level jet with windspeeds of more than 25 m/s was located on the east side of the dryline (Fig. 5.3). The strong winds brought moist air from the south into the southwestern Oklahoma region. The fields shown in Figs. 5.2 and 5.3 are the RUC 60 km analyses interpolated onto a 20 km ARPS grid.

Strong convective systems developed and passed over the Great Plains during the day. Fig. 5.4 shows a sequence of the composite radar reflectivities over the Oklahoma and adjacent regions. At 1200 Z on 7 May a broad region of

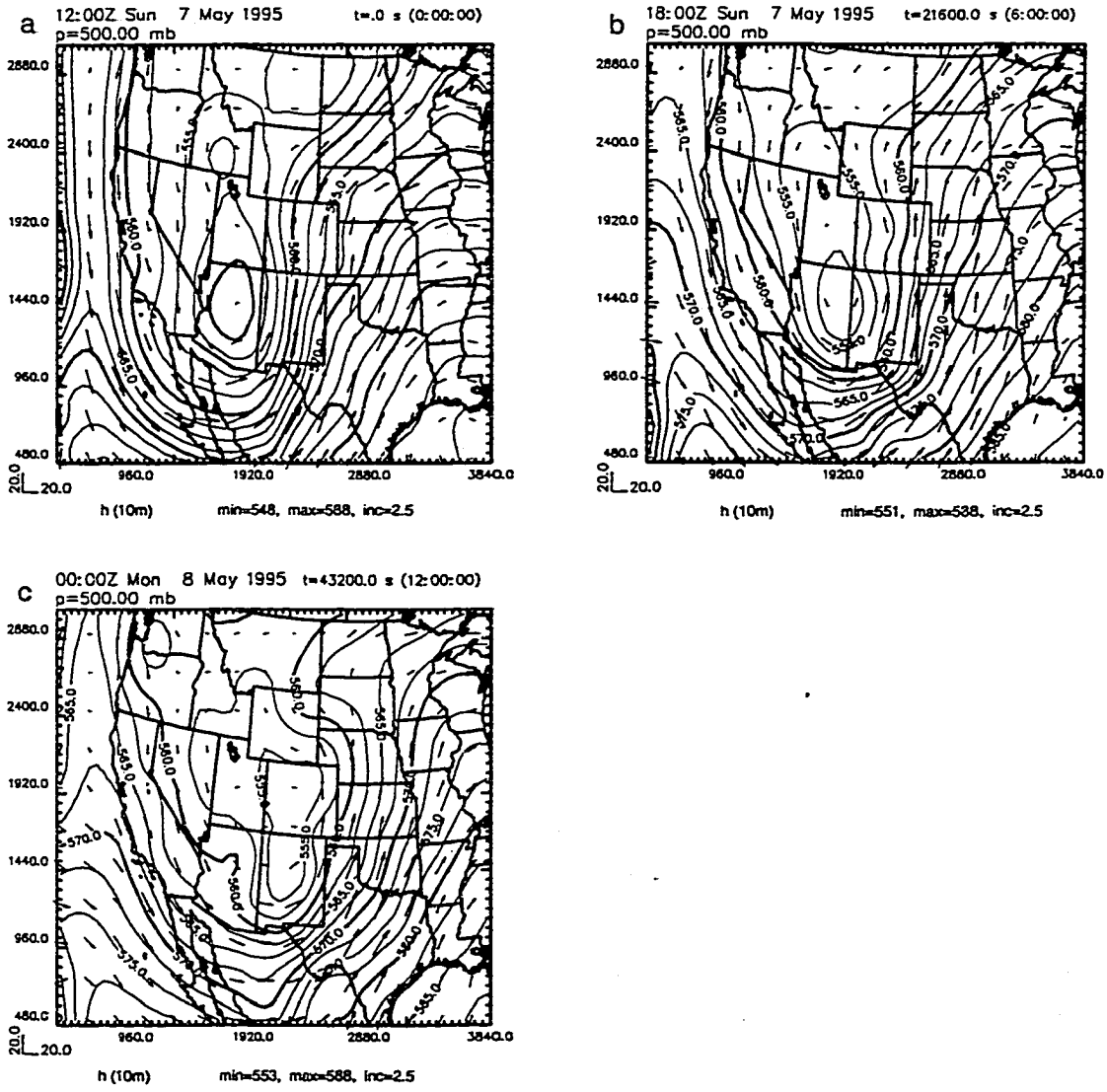

Fig. 5.1 RUC analysis of the 500 mb geopotential height (unit: 10 m) and wind fields at 1200 (a) and 1800 Z (b) on 7 May and 0000 Z (c) on 8 May, 1995. The contour intervals are 25 m.

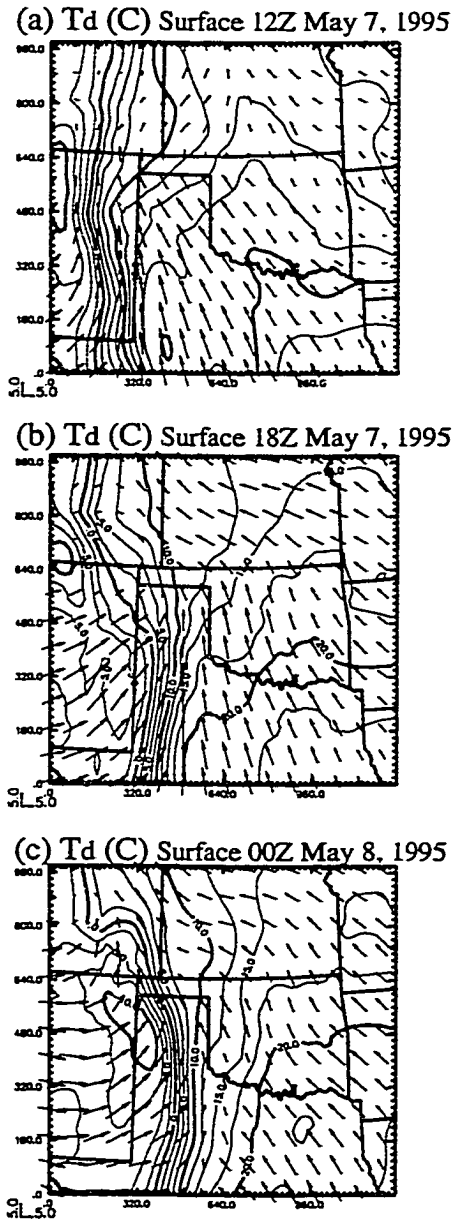

Fig. 5.2 RUC analysis of the surface dewpoint (unit: °C) and wind vector (unit: m/s) fields valid at 1200 (a) and 1800 (b) Z on 7 May and 0000 (c) Z on 8 May, 1995. The contour intervals are 2.5 °C.

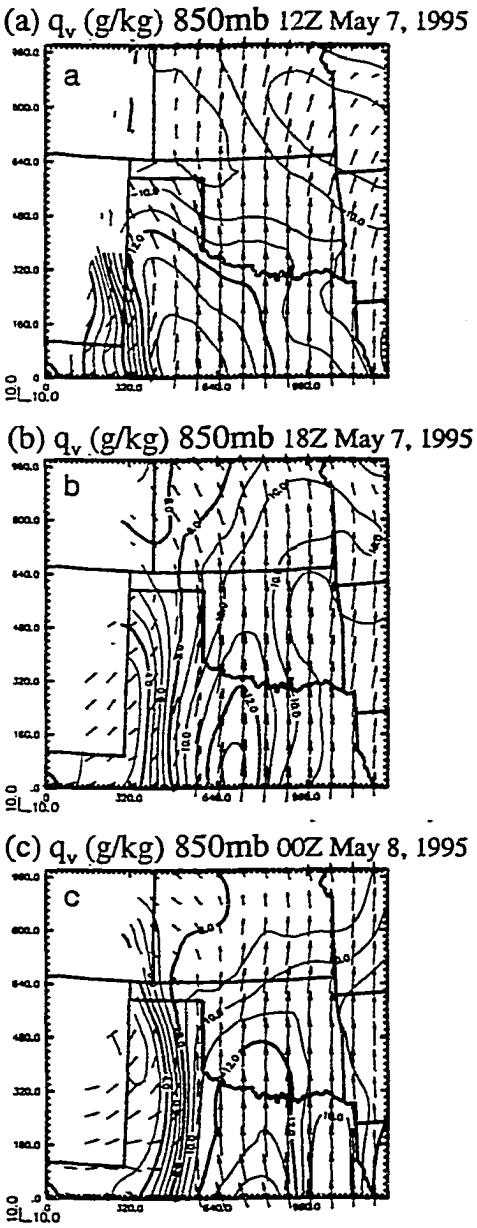

Fig. 5.3 RUC analysis of the 850 mb water vapor mixing ratio (unit: g/kg) and wind vector (unit: m/s) fields valid at 1200 (a) and 1800 Z (b) on 7 May and 0000 Z (c) on 8 May, 1995. Note that the data near the west boundary of the model domain were missing because the 850 mb level was below the surface. The contour intervals are 1g/kg.

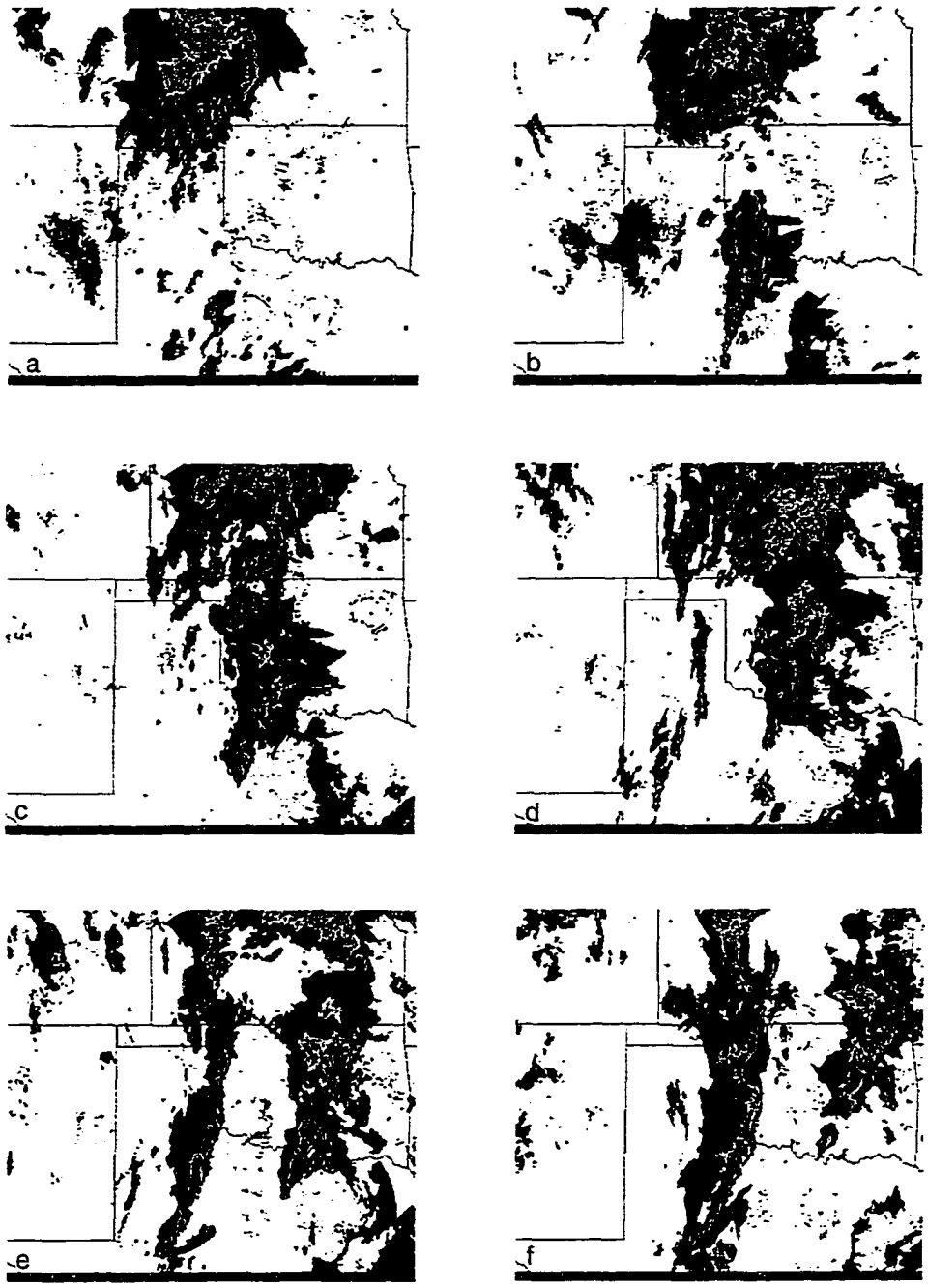

Fig. 5.4 Composite reflectivities valid at 1200 (a), 1430 (b), 1600 (c), 1800 (d), 2000 (e), and 2200 (f) Z 7 May, 1995.

convective precipitation was located in western Kansas and the Oklahoma panhandle, and isolated cells appeared in central Texas (Fig. 5.4a). The isolated cells later organized and formed a solid convective complex and moved north- and northeastward into southwest Oklahoma (Fig. 5.4b). At 1600 Z, a large part of this convective system was within western Oklahoma, with the northern end of the system joined together with the Kansas storms (Fig. 5.4c). This large precipitation complex then moved east-northeast across central Oklahoma and eventually dissipated after it moved into Missouri (Figs. 5.4d, e, and f). Severe thunderstorms from Texas moved into the southern end of the complex and produced tornadoes near Ardmore, OK around 2100 Z on 7 May. Another system was a narrow yet intensive band of convection that developed along the dryline. Isolated convection was initiated between 1600 and 1700 Z on 7 May and rapidly developed into a line of storms within 1 hour (Fig. 5.4d). The convective precipitation band intensified significantly and became a solid squall line at 2000 Z (Fig. 5.4e). This squall line further strengthened during the next several hours and slowly moved to the east (Figs. 5.4f). The system began to decay around 0600 Z on 8 May and moved out of Oklahoma into Arkansas after 1200 Z on 8 May.

This strong convective precipitation case has been studied extensively using the ARPS model (Wang et al. 1996, 1998; Xue et al. 1996, 1998a, 1998b). These studies have focused on the dynamical features of the dryline (Xue et al. 1996), the propagation and structure of the squall line (Wang et al. 1996, 1998),

and the convective initiation along the dryline (Xue et al. 1998b). In Xue et al. (1998a), radar reflectivities were inserted into the model through an intermittent data assimilation procedure. The assimilation of the radar data resulted in improvement of the squall line prediction. The patterns of the 6-hour accumulated rainfall ending at 0600 Z on 8 May, 1995 agreed well with the observations (Xue et al. 1998a). The present research is similar to the work of Xue et al. (1998a), although with different initialization schemes being used. The precipitation predictions during the early hours of the squall line and the impact of the moisture and diabatic initialization on the model's spinup process are the foci of the present study.

5.3 The Model Configurations

The ARPS model was also used in the real data experiments. The configuration of the model for the experiments included a 4th-order advection scheme, a 1.5 order TKE closure, the Kain-Fritsch cumulus parameterization, and an explicit ice microphysical parameterization based on the scheme developed by Lin et al. (1983). The explicit microphysical scheme takes into account condensation/evaporation and deposition/sublimation, autoconversions of cloud liquid (ice) water to rain (snow) and snow to graupel, accretion, riming, melting, freezing of cloud liquid droplets to cloud ice particles and of raindrops to graupel. There were 35 vertical levels in the model and the top of the model domain was ~16.5 km high. The horizontal resolution for the predictions was 10

km and the vertical resolution varied from 25 m near the surface to about 1 km at the top of the domain. A map of the model domain and the topography is shown in Fig. 5.5.

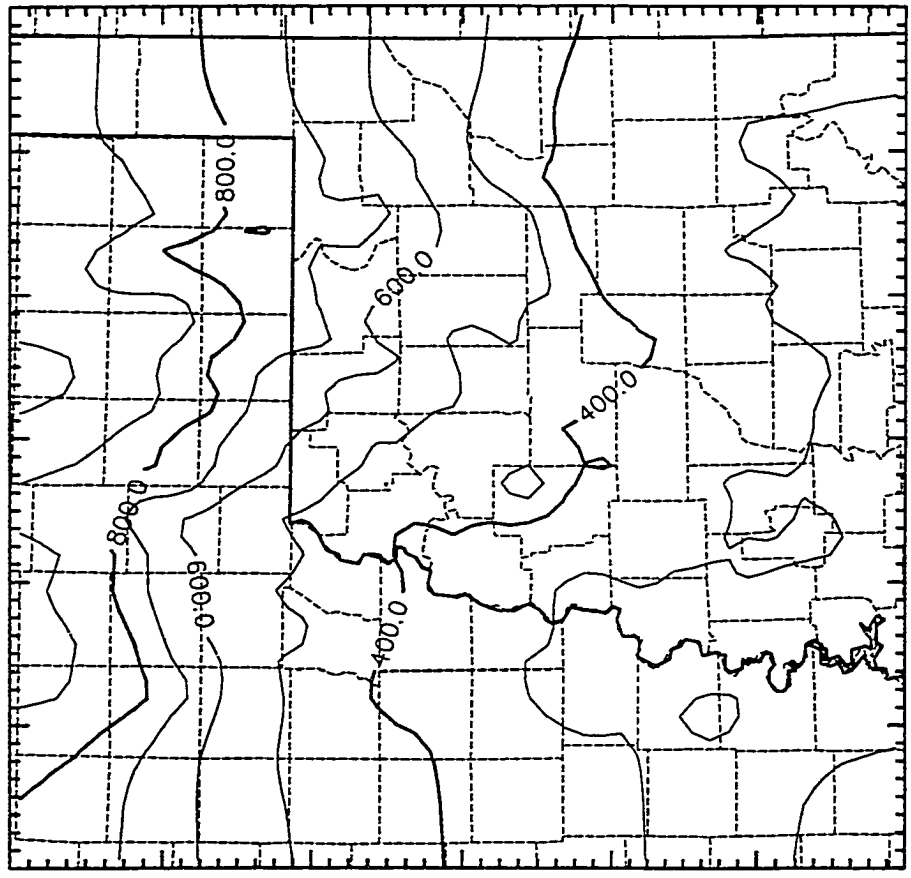

Fig. 5.5 A map of the model domain and the topography height field (unit: m) in the domain.

The background fields for the initial conditions were the 3-hourly RUC-I analyses. The 60 km analyses were interpolated to the ARPS 10 km grid, and additional observations were ingested using an objective analysis based on the

Bratseth scheme (Brewster, 1996) in the ADAS. The cloud analysis, described in Chapter 2, and different moisture and diabatic initializations were performed to obtain the initial conditions for the subsequent numerical prediction experiments.

During all forecasts, the model's lateral boundaries were forced by the same external boundary conditions. The external boundary conditions were obtained from the RUC 60 km forecasts. The forecast fields were obtained every hour and interpolated in space onto the 10 km ARPS model grid and linearly interpolated in time to every model time step. The model fields were relaxed towards the external boundary conditions using a technique similar to the one described by Davies (1983) (Xue et al. 1995).

5.4 Experimental Design

A list of the eight numerical forecasts of the 7 May event is given in Table 5.1. All forecasts were started at 1800 Z on 7 May 1995 and the length of the model integration was 6 hours. In the first experiment (CNVN, which roughly stands for the "conventional" surface and radiosonde data analysis), RUC 60 km analyses were used as the initial condition. This run provided a reference run which represented a forecast started from conventional surface and radiosonde weather observations. The initial conditions for the second experiment (MESO, which roughly stands for the analysis with local "mesonet" data) were obtained by

incorporating observations from the Oklahoma Mesonet (Crawford et al. 1992, Brock et al. 1995), wind profilers , and extra radiosondes through the ADAS while using the RUC analysis as the background. The distribution of the additional observations is depicted in Fig. 5.6.

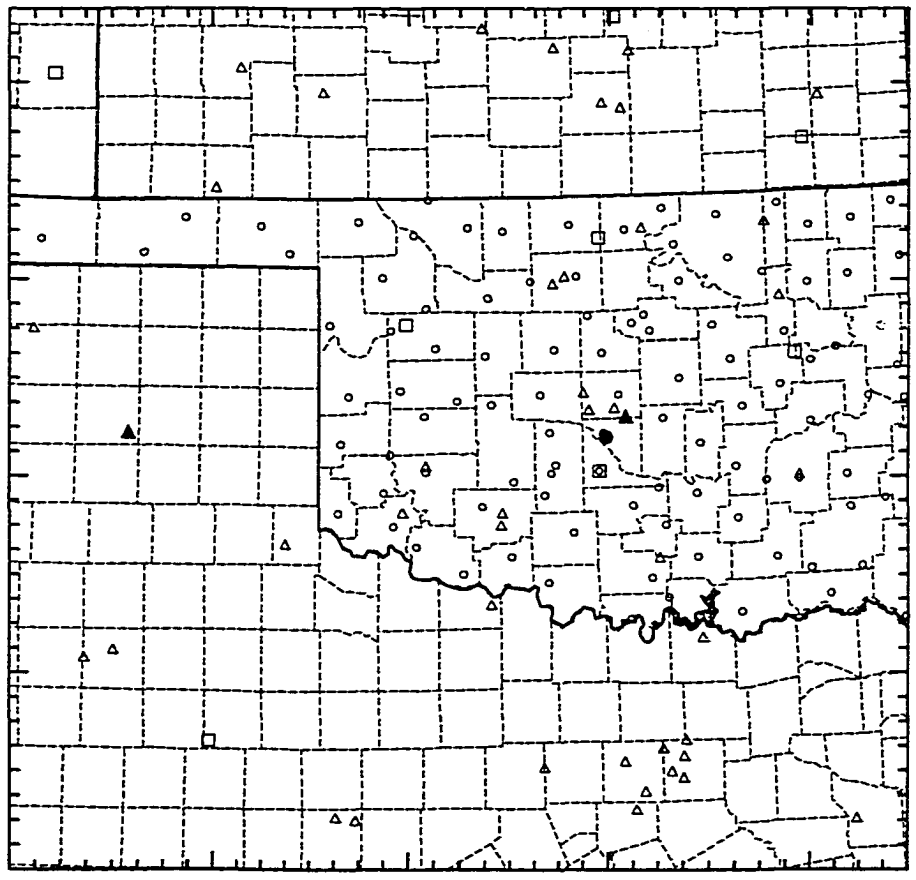

Fig. 5.6 Distribution of the Oklahoma Mesonet stations (circles), surface aviation observations (triangles), wind profilers (squares), WSR-88D radars (filled triangles), and radiosonde stations (filled circles).

The three experiments DIa, DIb, and DIc (see Table 5.1, where DI stands for "Diabatic Initialization") were initialized using different moisture initializations based on the ADAS cloud analysis. The additional data used in the cloud analysis included reflectivity data from two WSR-88D radars (KAMA and KTLX, Fig. 5.6), the imagery data from the visible and the infrared (11.0μm) channels on the GOES-8 satellite, and more than 30 surface aviation observations (SAOs, see Fig. 5.6). The initial water vapor fields for the three experiments were enhanced in the cloudy regions using the method described in Chapter 3. The analyzed rainwater (snow) as well as the cloud liquid/ice mixing ratio fields were inserted in Exp. DIc. In Exp. DIb, the analyzed cloud fields were inserted while the rainwater (snow) mixing ratios were zero at the initial time. No cloud liquid /ice or rainwater (snow) content was inserted in Exp. DIa. The initial thermal fields in the "DI" experiments were modified based on the latent heating adjustment method that was described in Chapter 3. The "DIW" experiments are similar to the "DI" experiments except that a different weight factor β_θ [see Eq. (3.14)] was used.

The initial temperature and dewpoint fields at different levels for Exp. CNVN are shown in Fig. 5.7. A cool region in the surface and 850 mb temperature fields in western Oklahoma corresponds to the precipitation in that region (Fig. 5.4d). The strong dewpoint gradient at the surface in the Texas panhandle indicates the location of the dryline. The dewpoint gradient is much weaker on the 850 mb level than that at the surface. The structure of the

dewpoint field at 500 mb is similar to that at 850 mb, yet the 500 mb temperature gradient is much weaker than that at the lower levels.

Table 5.1 List of the real data moisture and diabatic initialization experiments.

EXP.	Temp.	Wind	qv	qc	qr
CNVN	RUC analysis (conventional data)			zero	zero
MESO	ADAS analysis (mesonet, wind profilers, etc.)			zero	zero
DIa	LH adjustment with constant weights	ADAS analysis	RH adjustment within clouds	zero	zero
DIb				Smith-Feddes	zero
DIc				Smith-Feddes	Z-qr (qs)
DIWa	LH adjustment with varying weights	ADAS analysis		zero	zero
DIWb				Smith-Feddes	zero
DIWc				Smith-Feddes	Z-qr (qs)

Shown in Fig. 5.8 are the same fields as in Fig. 5.7 except for Exp. MESO. It can be seen that the surface cool pool is significantly stronger in the ADAS analysis than it is in the RUC analysis. The dryline in the ADAS analysis is stronger and deeper than in the RUC analysis and the northern end of the dryline is better defined. The differences were mainly due to the contributions from the Oklahoma Mesonet data. The RUC and ADAS temperature analyses at 500 mb are very similar, while the ADAS dewpoint analysis is more moist in central Oklahoma. The higher dewpoint in the ADAS analysis in central Oklahoma was due to an additional radiosonde observation at Norman, Oklahoma at 18 Z.

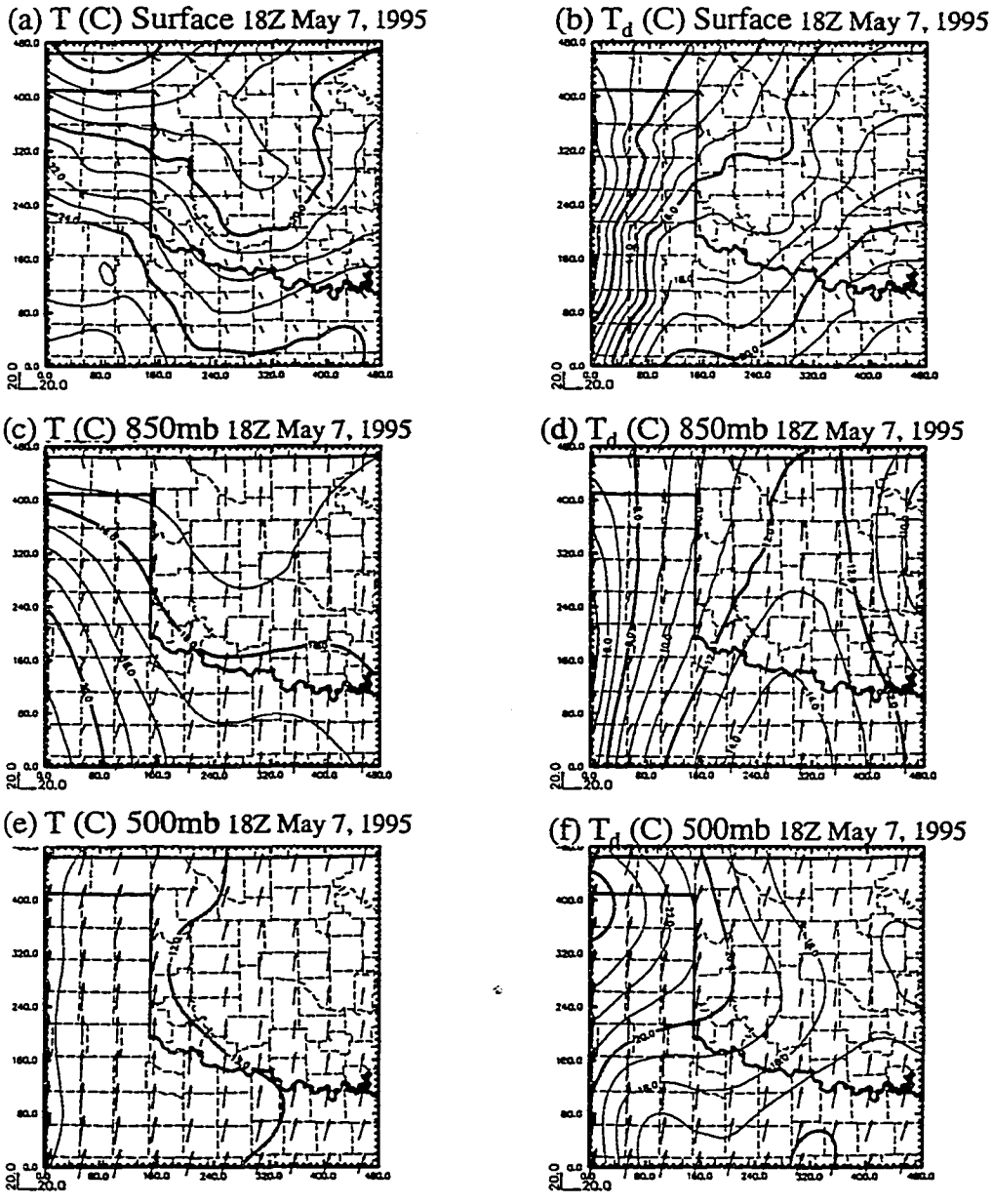

Fig. 5.7 RUC analysis of the temperature (T, unit: °C, left column) and the dewpoint (T_d, unit: °C, right column) fields on the surface (top row), 850 mb (middle row), and 500 mb (bottom row) levels valid at 1800 Z on 7 May 1995. The contour intervals are 1 °C.

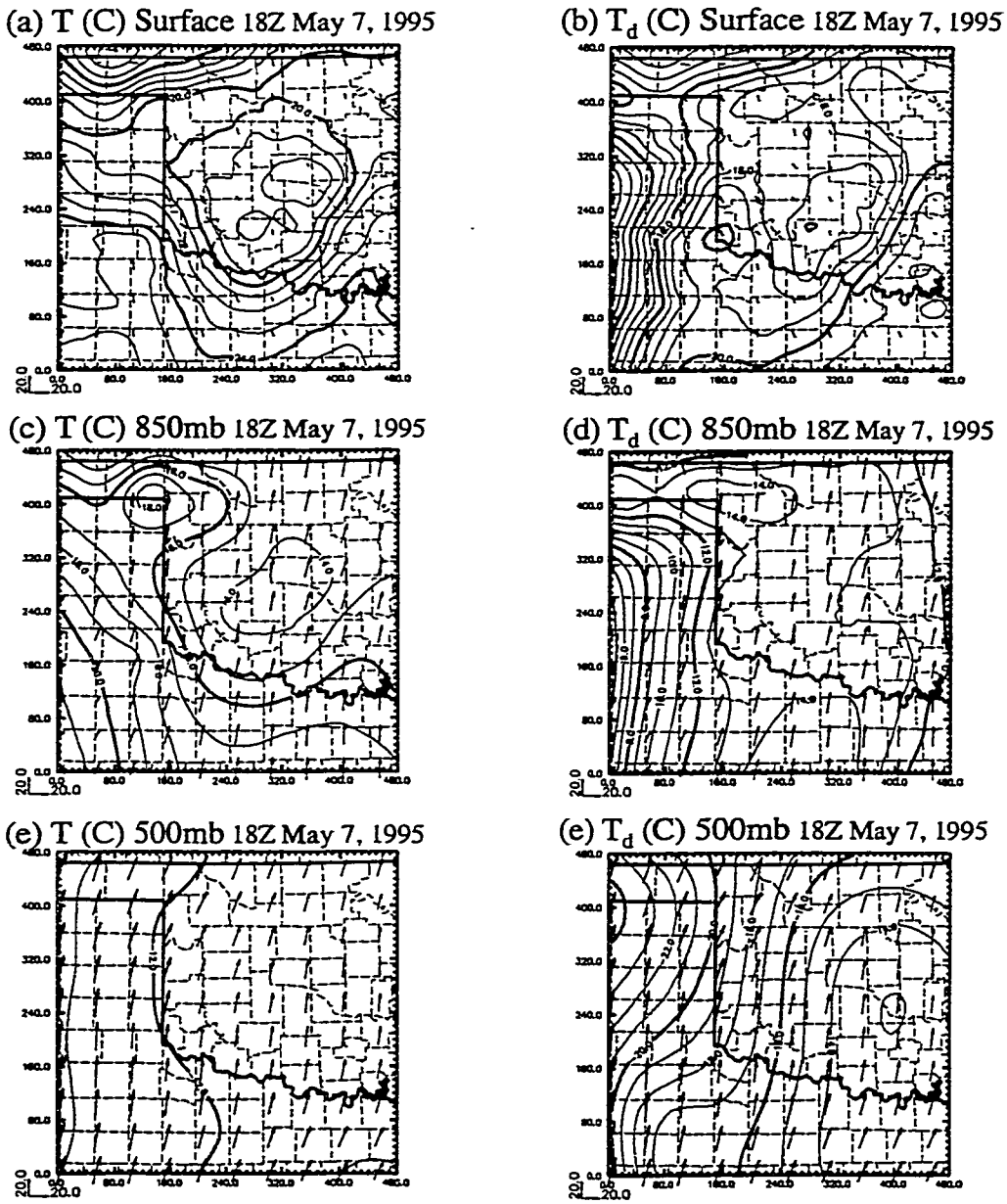

Fig. 5.8 ADAS analysis of the temperature (T, unit: °C, left column) and the dewpoint (T_d, unit: °C, right column) fields on the surface (top row), 850 mb (middle row), and 500 mb (bottom row) levels valid at 1800 Z on 7 May 1995. The contour intervals are 1 °C.

The initial cloud liquid/ice water and rainwater, snow and hail mixing ratio fields were zero in experiments CNVN and MESO. In the diabatic initialization experiments, the initial water vapor fields were adjusted in the cloud/rain regions and the analyzed cloud and precipitate mixing ratio fields were used to initialize the forecasts. Figures. 5.9 and 5.10 show vertical cross sections of the initial cloud liquid/ice, rainwater, snow, and hail mixing ratio fields, respectively. The cross sections were east-west oriented through Oklahoma City.

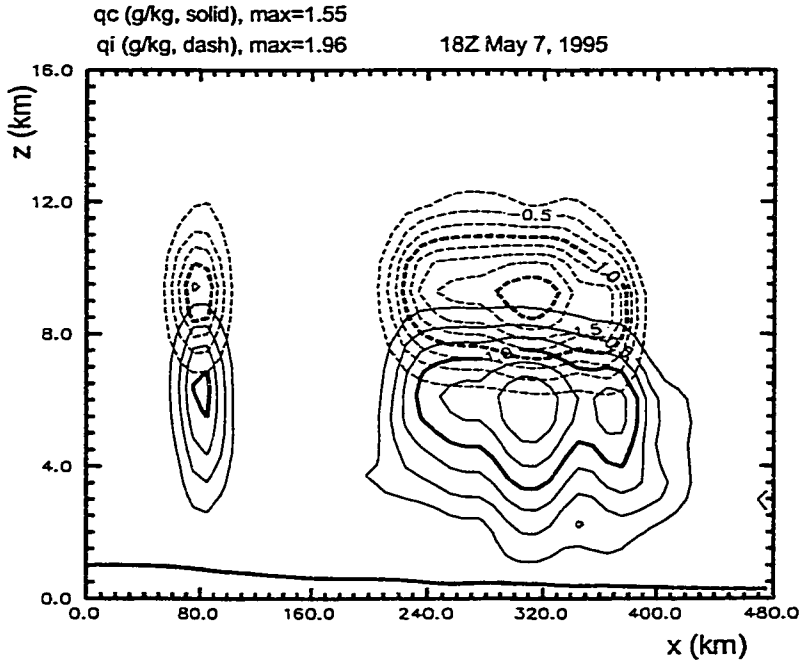

Fig. 5.9 A vertical cross section of the cloud liquid (solid line, unit: g/kg) and ice (dash line, unit: g/kg) mixing ratio fields from the ADAS cloud analysis valid at 1800 Z on 7 May 1995. The cross section was east-west through Oklahoma City. The contour intervals are 0.25g/kg.

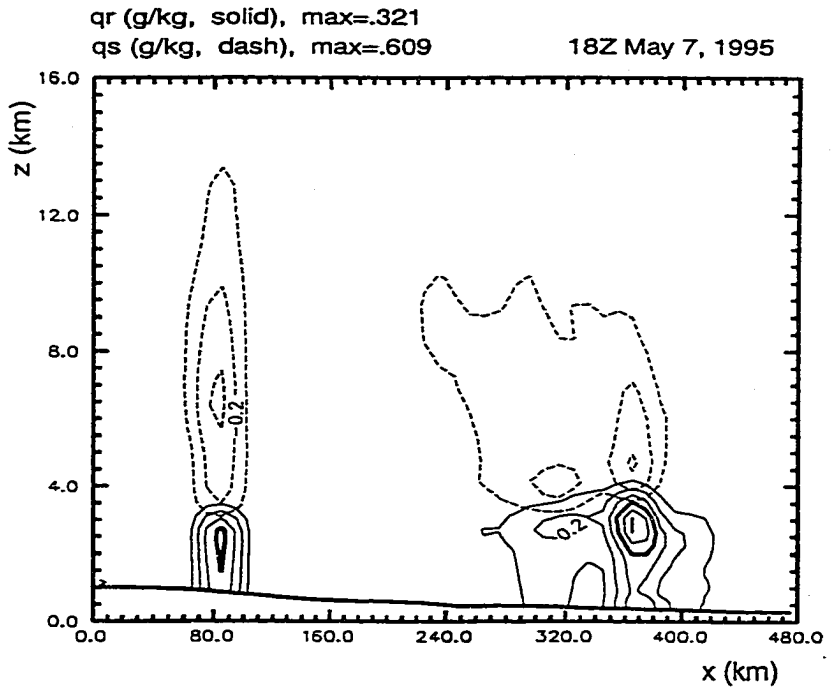

Fig. 5.10 A vertical cross section of the rainwater (solid line, unit: g/kg) and snow (dash line, unit: g/kg) mixing ratio fields from the ADAS cloud analysis valid at 1800 Z on 7 May 1995. The cross section was east-west through Oklahoma City. The contour intervals are 0.1g/kg.

The same cross sections of the initial relative humidity (RH) fields in Exp. CNVN, MESO and the diabatic initialization experiments are shown in Figs. 5.11a, b and c, respectively. The RUC RH analysis was substantially too dry given the fact that there were two deep convective precipitation systems at the time, one near x = 80 km and the other near x = 320 km (see Figs. 5.9 and 5.10). The ADAS RH analysis showed a higher humidities at the lower levels in the central Oklahoma region. However, little improvement was made in the Texas panhandle area due to the lack of observations. The RH field after the moisture

adjustment showed better consistency with the cloud and rainwater mixing ratio analyses.

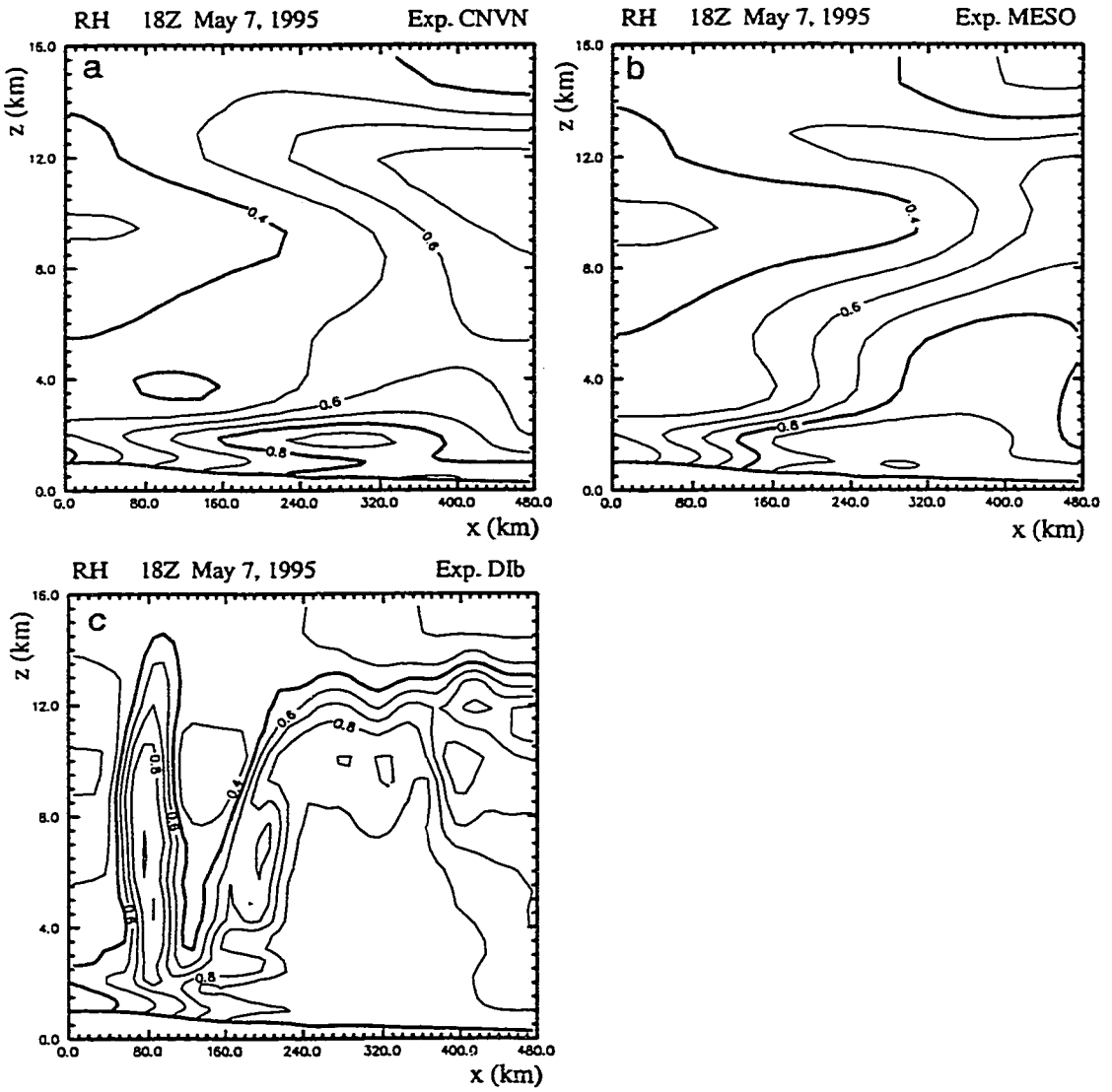

Fig. 5.11 Vertical cross sections of the initial relative humidity fields in Exp. CNVN (a), MESO (b), and DIb (c). The cross sections are the same as in Fig. 5.10. The contour intervals are 0.1.

The initial perturbation potential temperature fields for Exps. CNVN and MESO are shown in Figs. 5.12a and b. There is a weak warm core at ~ 8 km and a cold core at the surface in the eastern part of the domain (Fig. 5.12a), which are consistent with observed structures of mesoscale convective systems (MCSs, Houze, 1993). The warm core is significantly warmer in the ADAS analysis (Fig. 5.12b). This analysis is consistent with the numerical simulation results shown in Chapter 4, where it was found that warm cores are correlated with regions of high cloud concentrations. The thermal adjustment in the "DI" experiments produced a second warm core, which is related to the squall line in the Texas panhandle (Fig. 5.12c). In the meantime, the thermal adjustment further warmed the central Oklahoma region by more than 5 K (Fig. 5.12c). Forecast results presented later in this chapter will show that the latent heating adjustment in this region is redundant. In fact, the mid-troposphere warm anomaly was reflected in the ADAS analysis due to the temperature observations from a radiosonde located at Norman, OK (filled circle in Fig. 5.6). Thus the latent heating adjustment should be given a smaller weight in this region. To test the impact of the weighting factor, a set of experiments (DIWa, DIWb, and DIWc in Table 5.1) with spatially dependent weights for the LH adjustment was carried out. In this set of experiments, the weight for the LH adjustment was simply set to one in the region near storm system "A" ($x \leq 160$ km), and set to zero in the region of storm system "B" ($x > 160$ km, Fig. 5.12d). Future work will seek a more appropriate weighting function that takes into account the relative accuracy of the LH

adjustment with respect to other temperature data (e.g., radiosonde observations, thermodynamic retrievals, etc).

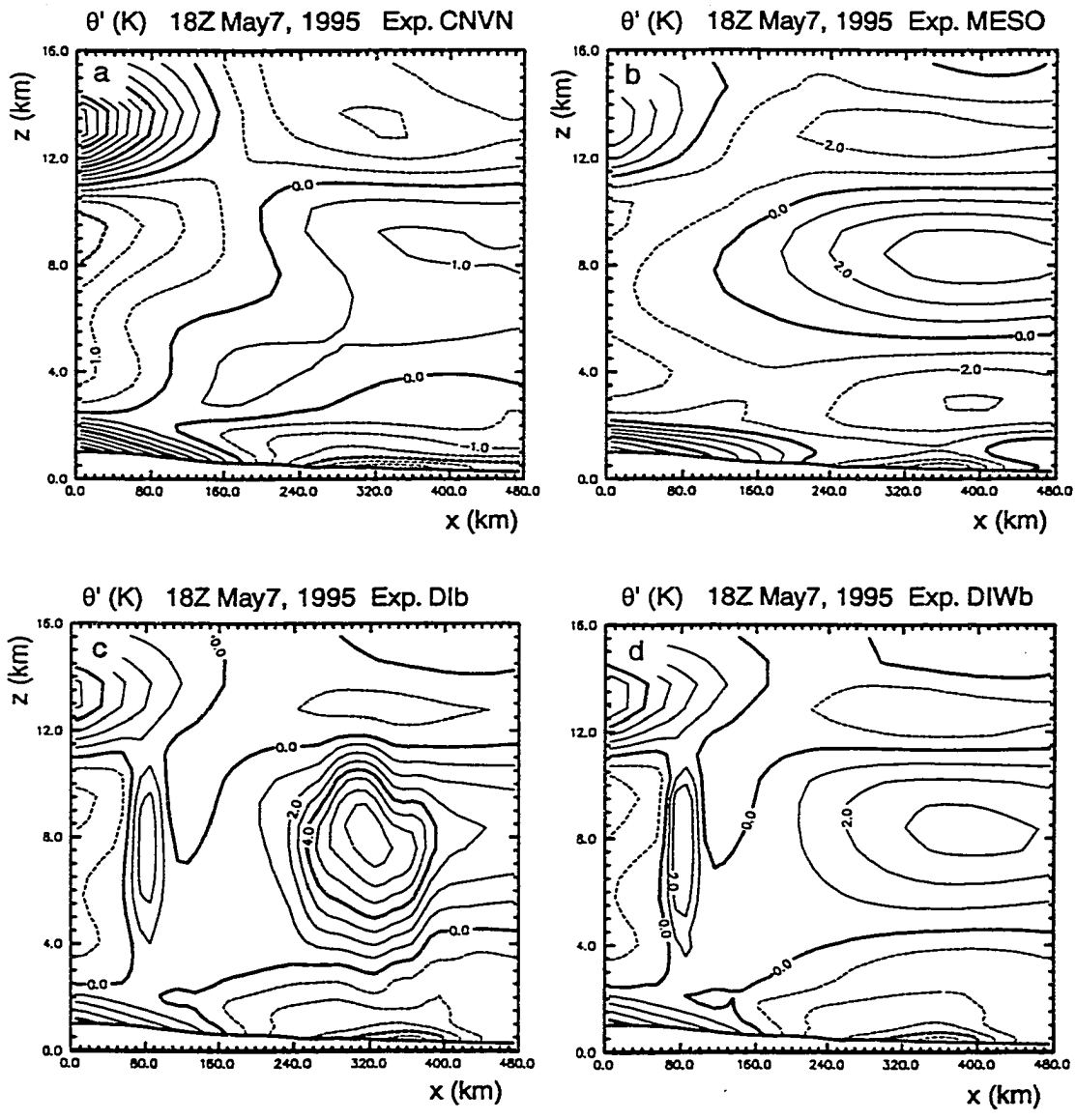

Fig. 5.12 Vertical cross sections of the initial perturbation potential temperature fields in Exps. CNVN (a), MESO (b), DIb (c) and DIWb (d). The cross sections were the same as in Fig. 5.10. The contour intervals are 0.5 K for panel *a* and 1 K for panels *b*, *c*, and *d*.

5.5 Results

5.5.1 Verification

The hourly rainfall fields derived from radar and rain gauge data at the Arkansas-Red Basin River Forecast Center (ABRFC) are shown in Fig. 5.13. Between 1800 and 1900 Z on 7 May scattered convective rain bands were seen along the dryline in the Texas panhandle and a large precipitation band resided in central Oklahoma (Fig. 5.13a). The scattered rain bands later organized and evolved into a strong squall line and slowly moved eastward from the Texas panhandle into western Oklahoma. The large precipitation complex moved northeastward and entered Missouri at 0000 Z 8 May 1995. For the convenience of the discussion, the convective rain band along the dryline will be referred to as 'storm system "A" ' in the following text and the large precipitation complex in central and northeast Oklahoma will be referred to as 'storm system "B" '. The traditional bias and threat scores are calculated for the predicted hourly rainfall fields for each experiment. The individual hourly rainfall fields from different forecasts are also examined and evaluated qualitatively.

5.5.2 Conventional data analysis experiments

The bias and threat scores for Exps. CNVN and MESO are shown in Fig. 5.14. The threat scores are calculated using a 1 mm threshold. In Exp. CNVN, it took the model more than three hours to spin up a significant amount of

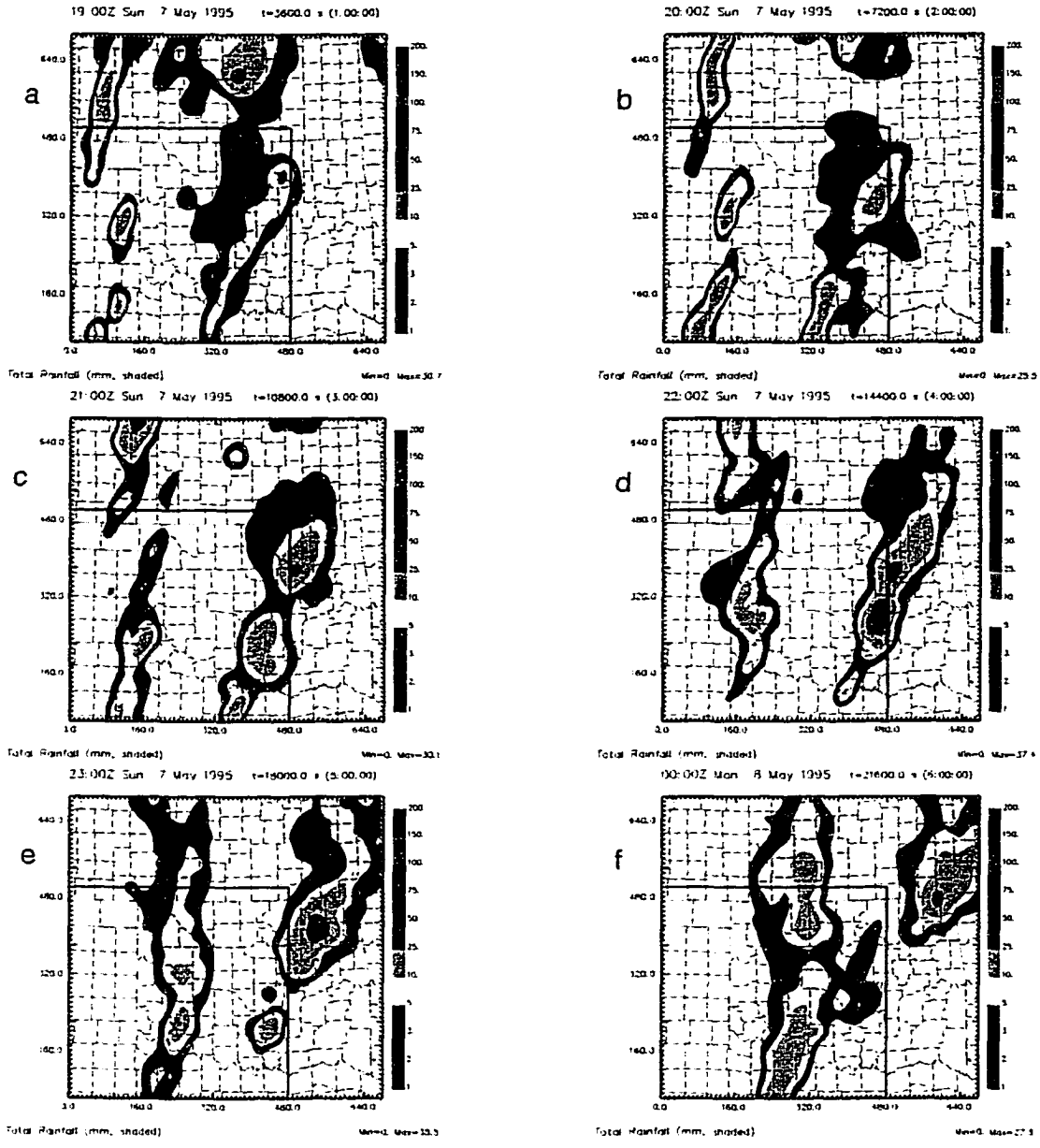

Fig. 5.13 Hourly precipitation (unit: mm) analyses from the ABRFC valid at 1900 (a), 2000 (b), 2100 (c), 2200 (d), and 2300 Z (e) on 7 May and 0000 (f) Z on 8 May, 1995. The box indicates the model domain for the numerical prediction experiments.

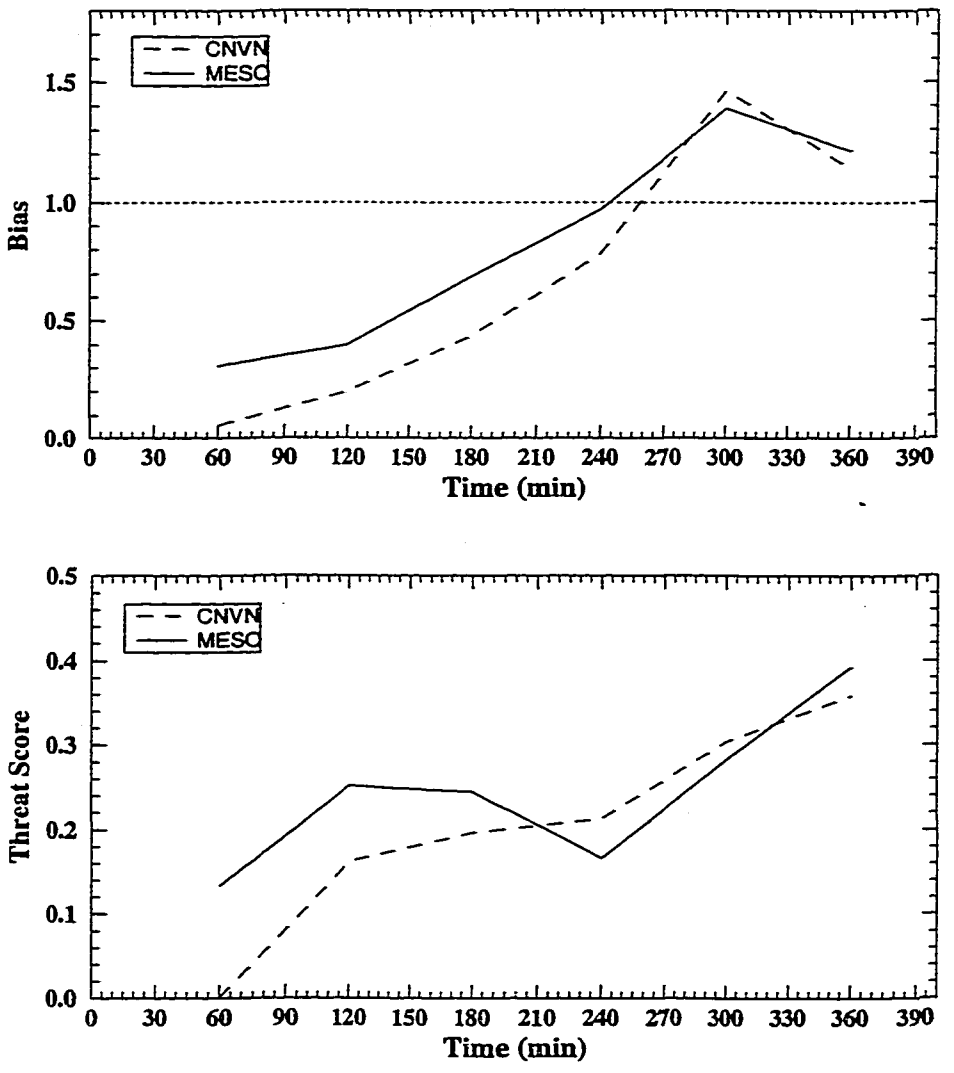

Fig. 5.14 The bias (a) and threat scores (b) for the hourly precipitation fields in the experiments CNVN and MESO.

precipitation. The hourly precipitation fields from Exp. CNVN (Fig. 5.15) show that there is little forecast precipitation until 2100 Z on 7 May. At 2100 Z, there are two separate rain bands in the observed precipitation field (Fig. 5.13c) while

in the rainfall forecast the two rain regions are much closer together (Fig. 5.15c). The predicted precipitation systems eventually evolved into a north-south oriented line at 2300 Z on 7 May, which resembled the observed squall line. However, the eastern part of the precipitation complex moved very little. A strong storm cell in the predicted field was located near northern boundary of the model domain ($x \approx 300$ km, $y \approx 420$km), while in the observed rainfall field, a strong cell was located outside of the eastern boundary of the model domain at $x \approx 540$ km, $y \approx 420$km. The quasi-stationary precipitation and the over-prediction of rainfall in the northern part of the system resulted in a positive bias error of nearly 50% for Exp. CNVN at this time (300 min in Fig. 5.14a). The predicted precipitation system slowly moved eastward similar to the observed squall line. However, the southern part of the line moved too slowly and lagged the observed squall line by about 100 km at 0000 Z on 8 May, 1995 (Fig. 5.15f vs. Fig. 5.13f). This resulted in an erroneous northeast-southwest orientation compared to the observed north-south orientation.

5.5.2 ADAS analysis experiment

The bias score for Exp. MESO (Fig. 5.14a) showed consistent improvement over Exp. CNVN for all six hours of the model forecast. Fig 5.16 shows a sequence of hourly precipitation fields from Exp. MESO. A small amount of precipitation was produced in the south-central Oklahoma early in the

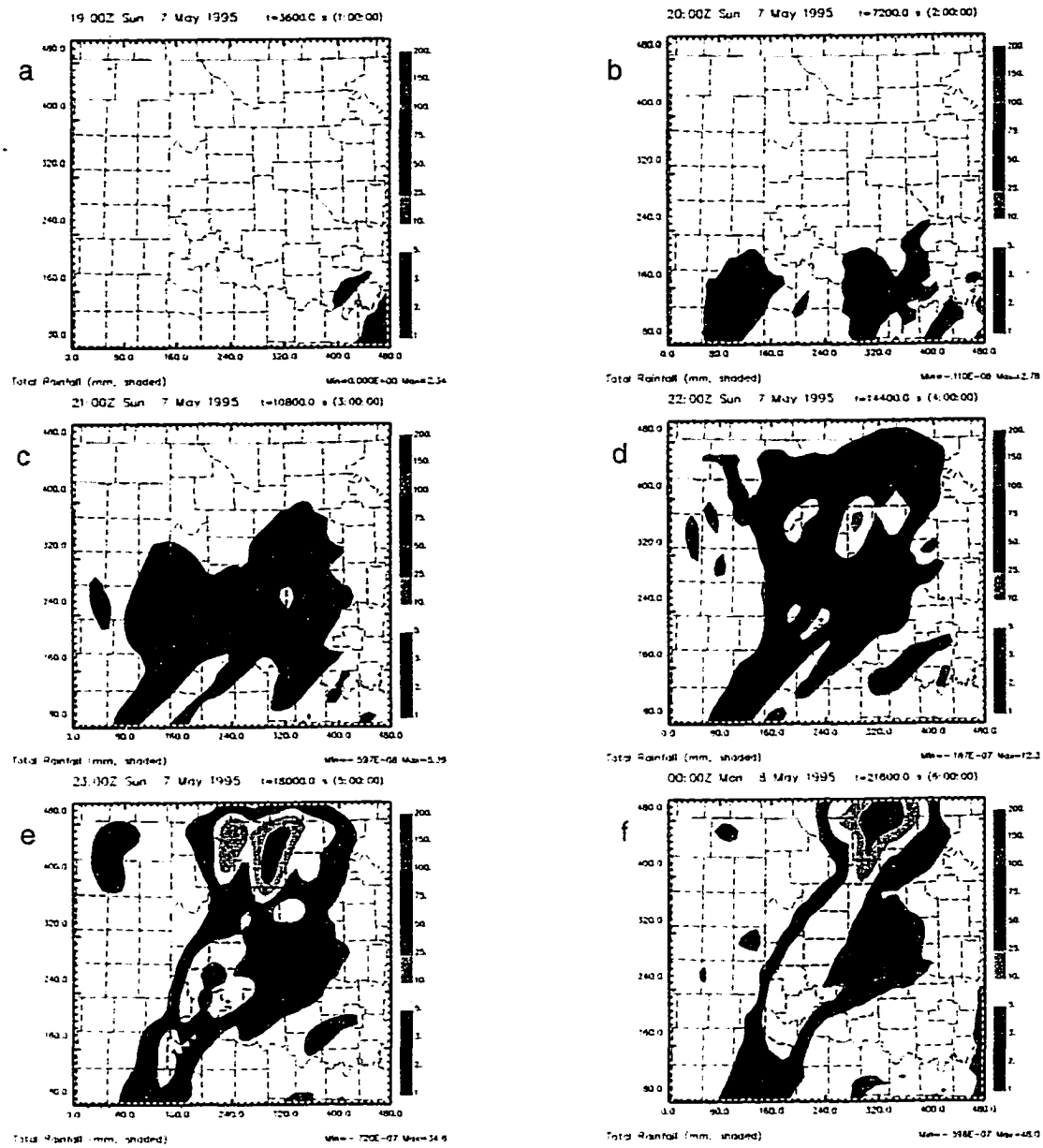

Fig. 5.15 The hourly precipitation (unit: mm) fields from Exp. CNVN valid at 1900 (a), 2000 (b), 2100 (c), 2200 (d), and 2300 Z (e) on 7 May and 0000 (f) Z on 8 May, 1995.

forecast and the intensity of this precipitation system increased during the first three to four hours. A second precipitation region developed during the third hour (Fig. 5.16c) and the location was close to the observed rain band in the Texas panhandle (Fig. 5.13c). The two-band structure is more realistic than the one precipitation complex predicted in Exp. CNVN (Fig. 5.15c). The improvement was probably due to the better representation of the dryline in the initial conditions for Exp. MESO than for Exp. CNVN. The improved analysis resulted in higher CAPE (Convective Available Potential Energy) and lower CIN (Convective Inhibition) near the leading edge of the dryline in the ADAS analysis than in the RUC analysis (Figs. 5.17 and 5.18). The north-south oriented high CAPE and low CIN bands were collocated, indicating a favorable condition for the development of convective storms. Yet both the intensity and the areal coverage of the dryline precipitation were underestimated in Exp. MESO. The northern part of the squall line was not predicted until 2300 Z on 7 May (Fig. 5.16e). The movement of precipitation system "B" was better predicted than in Exp. CNVN, yet the eastward motion was still too slow. At 2300 Z, the strong cell in the predicted rainfall field was still within the model domain ($x \approx 410$ km, $y \approx 400$ km). Nevertheless, the phase error in Exp. MESO ($\approx$ 130 km) for the heavy rainfall center was much smaller than that that in Exp. CNVN ($\approx$ 240 km).

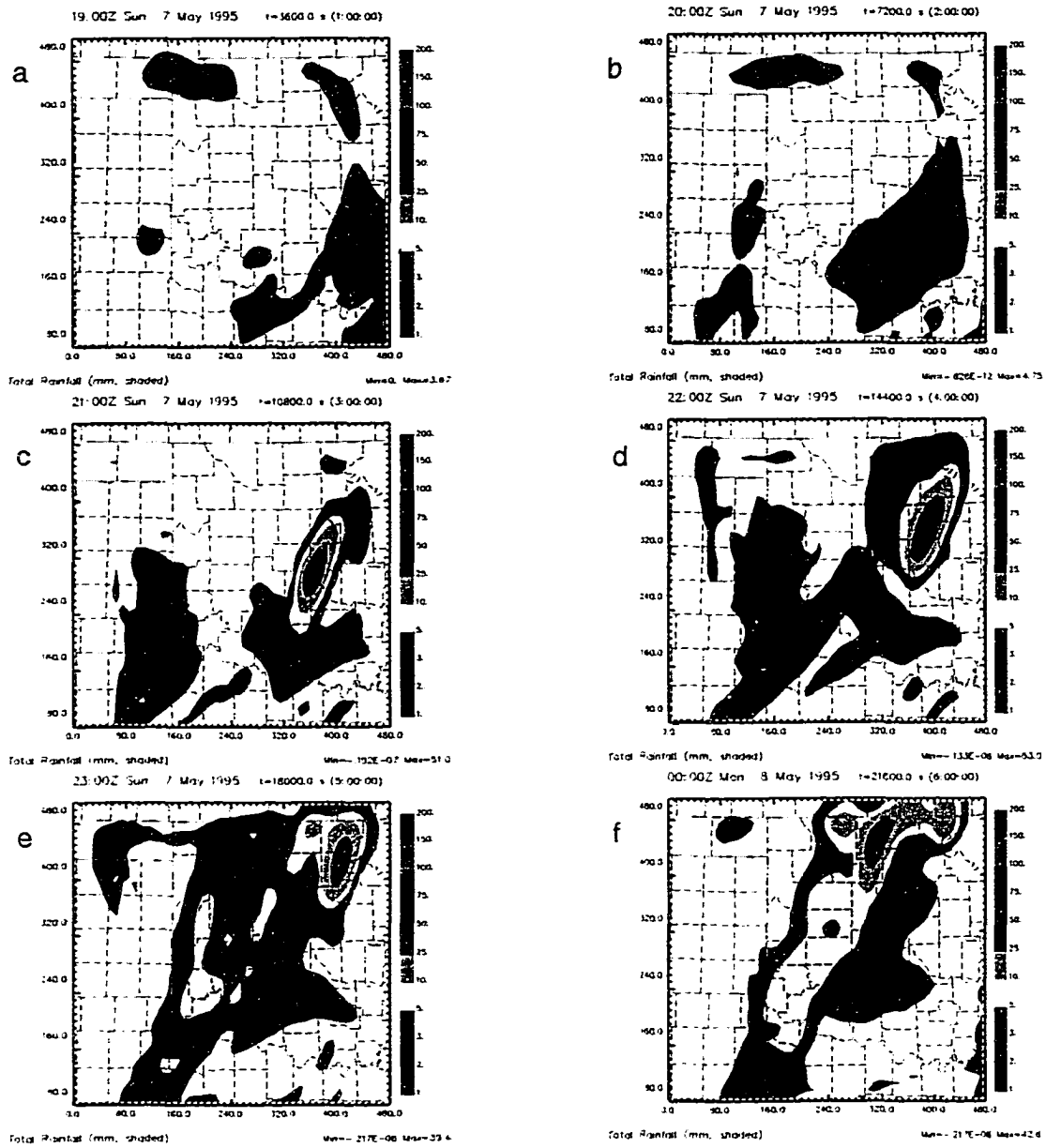

Fig. 5.16 The hourly precipitation (unit: mm) fields from Exp. MESO valid at 1900 (a), 2000 (b), 2100 (c), 2200 (d), and 2300 Z (e) on 7 May and 0000 (f) Z on 8 May, 1995.

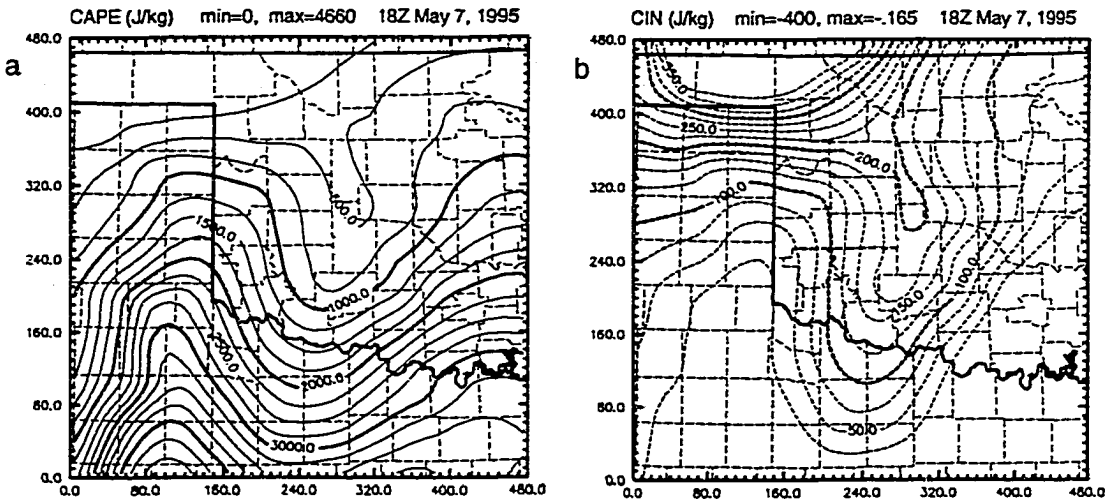

Fig. 5.17 The RUC analysis of the surface CAPE (panel a, unit: J/kg) and CIN (panel b, unit: J/kg) fields at 1800 Z on 7 May, 1995.

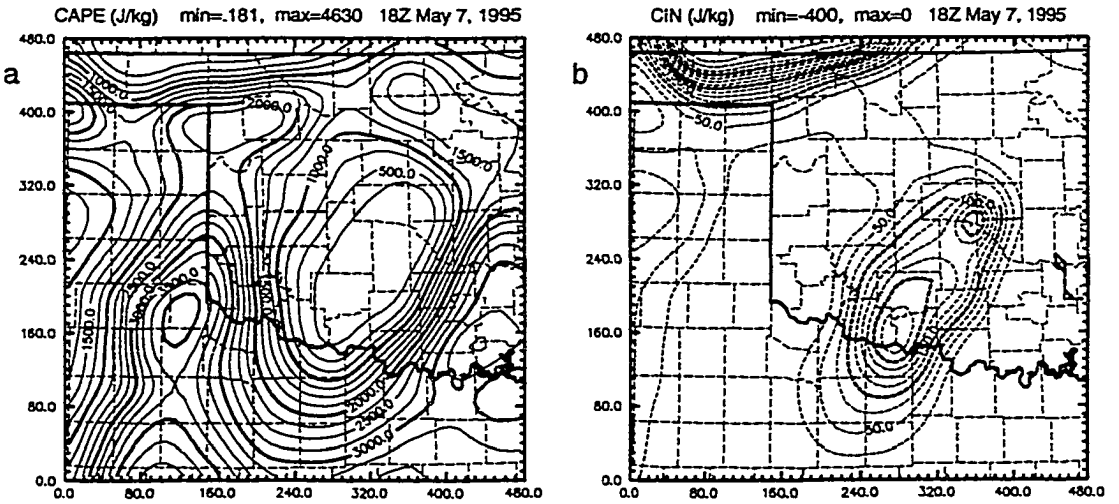

Fig. 5.18 The ADAS analysis of the surface CAPE (panel a, unit: J/kg) and CIN (panel b, unit: J/kg) fields at 1800 Z on 7 May, 1995.

Fig. 5.14b showed that the threat scores for the hourly precipitation fields in Exp. MESO are higher than the scores in Exp. CNVN except at 240 min (i.e. 2200 Z). After comparing the hourly rainfall fields at 2200 Z for the two experiments, we found that the threat scores were not very representative in evaluating the results. The rainfall patterns at this time in Exp. CNVN showed a large area of weak precipitation (Fig. 5.15d), while the analysis field showed two separate regions of precipitation (Fig. 5.13d). The system to the east (storm system "B") was relatively strong and contained intense storm cells. The system to the west (storm system "A") was relatively weak and the precipitation was more uniformly distributed. The rainfall in Exp. MESO showed a pattern similar to the observed fields. However, system "B" was displaced to the northwest compared to the observed one. This phase error resulted in a low threat score for Exp. MESO despite the fact that the overall precipitation patterns showed better consistency with the observations than those in Exp. CNVN. The results indicate that the threat score is an incomplete measure for the quantitative verification of convective-scale precipitation forecasts.

5.5.3 Diabatic initialization experiments

The time series of the bias and threat scores for Exps. DIa, DIb, and DIc are shown in Fig. 5.19. The thermal adjustment based on Eq. (3.14) with a constant weight of $\beta_\theta = 1$ over the whole model domain resulted in substantial overestimation of the hourly precipitation (Fig. 5.19). It was found that the

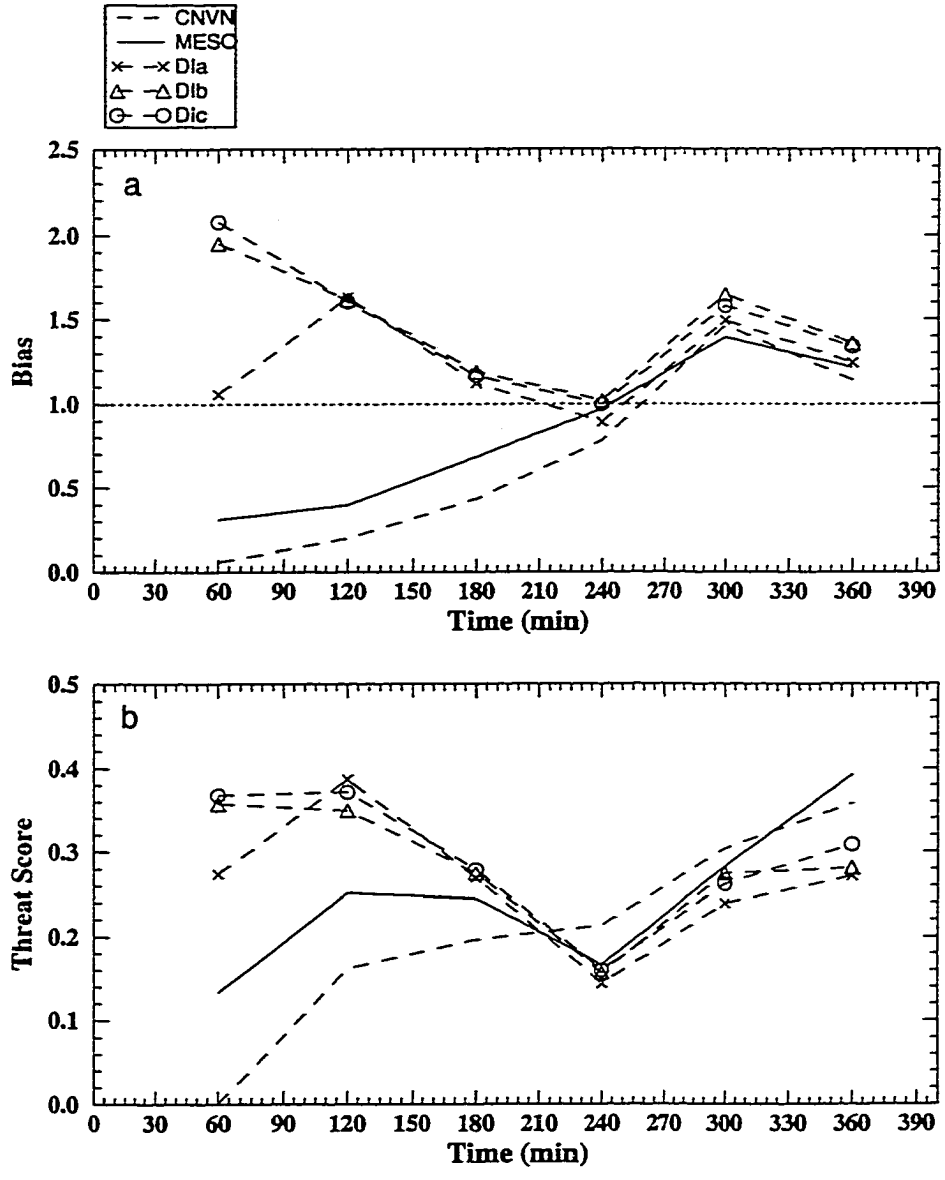

Fig. 5.19 The bias (a) and threat scores (b) for the hourly precipitation fields in Exps. CNVN, MESO, DIa, DIb, and DIc.

overestimation was solely for the precipitation in storm system "B". The plots of the rainfall in Exp. DIb (Fig. 5.20) showed that while the intensities of the predicted hourly rainfalls in storm system "A" were weaker than the observed ones, those in storm system "B" were much stronger. The patterns of the hourly rainfall fields in Exps. DIa and DIc (not shown) were very similar to those in Exp. DIb. Table 5.2 lists the maximum values of the hourly rainfall in storm system "B" for the three experiments. The heaviest rainfalls were consistently higher in

Table 5.2 Maximum hourly rainfall values at different times in the ABRFC rainfall analysis and in Exps. DIa, DIb, and DIc.

	19Z	20Z	21Z	22Z	23Z	00Z
ABRFC	33.8	41.3	32.5	40.1	39.9	28.9
DIa	25.5	68.4	84.9	59.2	50.5	93.2
DIb	28.2	54.1	54.1	57.4	58.3	84.9
DIc	29.0	53.1	50.1	53.4	56.4	62.8

the three experiments than they were in the analysis. A similar run with a Kessler warm rain microphysical parameterization (not shown) instead of ice microphysics showed very similar results. The overestimation was most likely due to the excess warming caused by the latent heating adjustment in the region near storm system "B". The thermal adjustment was redundant because a radiosonde observation in the same region measured the warm anomaly caused by the convective system. The OSSEs presented in Chapter 4 showed similar results

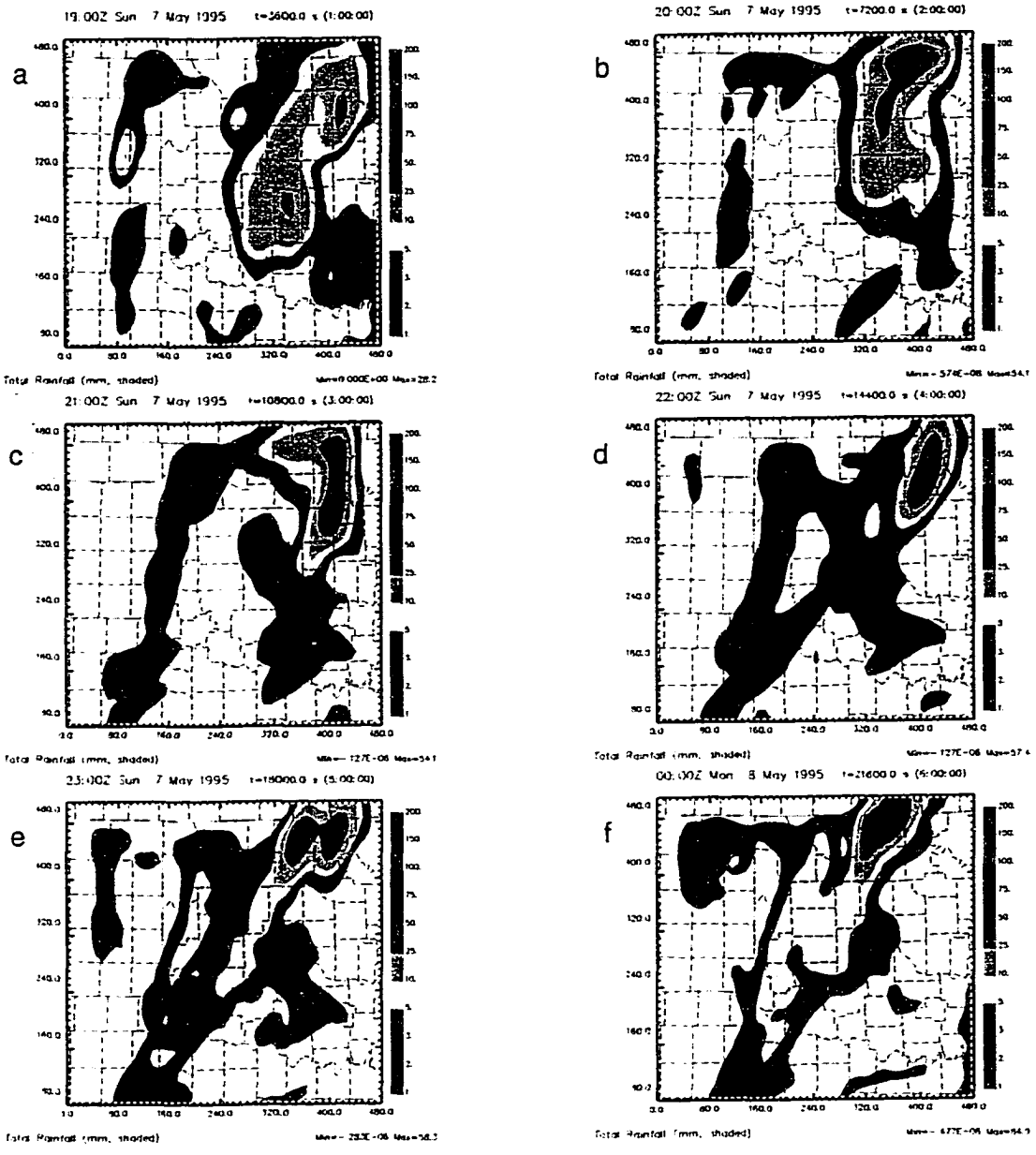

Fig. 5.20 The hourly precipitation (unit: mm) fields from Exp. DIb valid at 1900 (a), 2000 (b), 2100 (c), 2200 (d), and 2300 Z (e) on 7 May and 0000 (f) Z on 8 May, 1995.

where excess warming resulted in overestimation of the precipitable water and, in turn, the precipitation. The results suggest that a proper weighting of the latent heating adjustment is important.

The diabatic initialization in storm system "A" had a significant positive impact on the precipitation predictions. The threat score (Fig. 5.19b) was improved during the first three hours because of the improvement in the areal coverage of the precipitation resulting from the diabatic initialization (Fig. 5.20). The intensity and the orientation of the rain band were more comparable to observations than they were in Exp. MESO. Moreover, the northern end of the squall line was successfully forecast (Fig. 5.20). This may be due to the local maximum in the initial CAPE field near the northeast corner of the Texas panhandle (Fig. 5.17a). Convection did not develop in that region in Exps. CNVN and MESO despite the high CAPE, attesting to the value of including a diabatic initialization. However, there was little improvement in the diabatic initialization experiments of the orientation error of the squall line compared to Exps. CNVN and MESO. The phase and orientation errors have contributed to the low threat score at 240 min.

The results from Exps. DIa, DIb, and DIc suggested that a proper weighting is important when applying the latent heating (LH) adjustment to the thermal field. Thus three diabatic initialization experiments with a non-uniform weighting function were carried out. The bias and threat scores for the three

experiments are shown in Fig. 5.21. While the threat scores (Fig. 5.21b) are similar to those for Exps. DIa, DIb, and DIc, the bias scores for Exps. DIWa, DIWb and DIWc are closer to unity than those for Exps. DIa, DIb, and DIc, except that the initial bias score in Exp. DIWa was small. The heaviest hourly rainfall values (Table 5.3) are much more comparable to the observed ones after the first two hours of integration. It was found that there was also a small improvement in the precipitation forecast in storm system "A". Fig 5.22 shows that the rain band associated with storm system "A" was more solid and better organized than it was in the first five experiments. There are also small regions where the hourly rainfall exceeds 5 mm/hr at 2100 and 2200 Z (Figs. 5.22c, d), which were not observed in Exp. DIb (Figs. 5.20c, d).

Table 5.3 Maximum hourly rainfall values at different times in the ABRFC rainfall analysis and in the predictions of DIWa, DIWb, and DIWc.

	19Z	20Z	21Z	22Z	23Z	00Z
ABRFC	33.8	41.3	32.5	40.1	39.9	28.9
DIWa	9.49	13.9	24.3	39.0	33.8	26.7
DIWb	10.4	13.0	35.3	49.4	37.7	29.3
DIWc	10.6	14.9	35.8	44.4	36.0	25.1

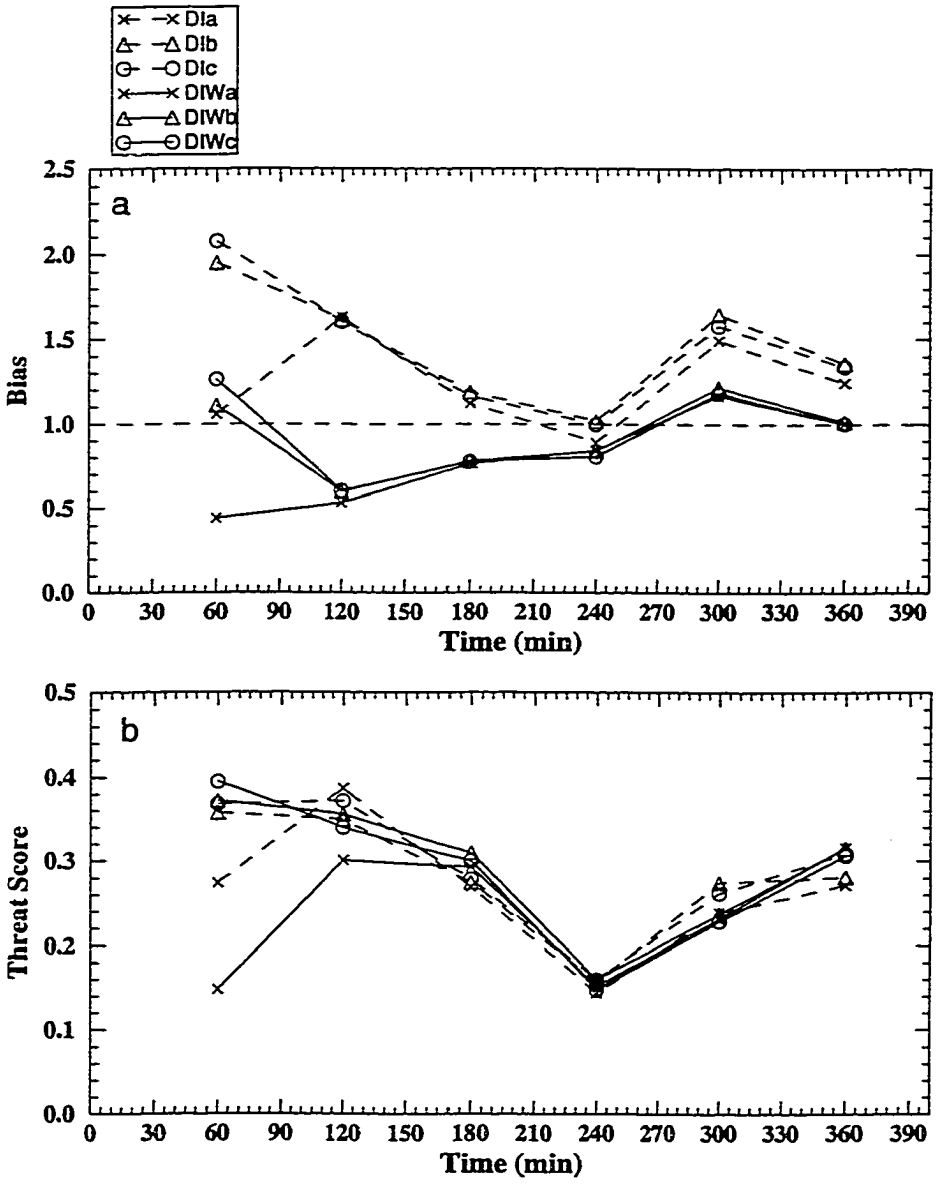

Fig. 5.21 The bias (a) and threat (b) scores for the hourly precipitation fields in Exps. DIa, DIb, DIc, DIWa, DIWb, and DIWc.

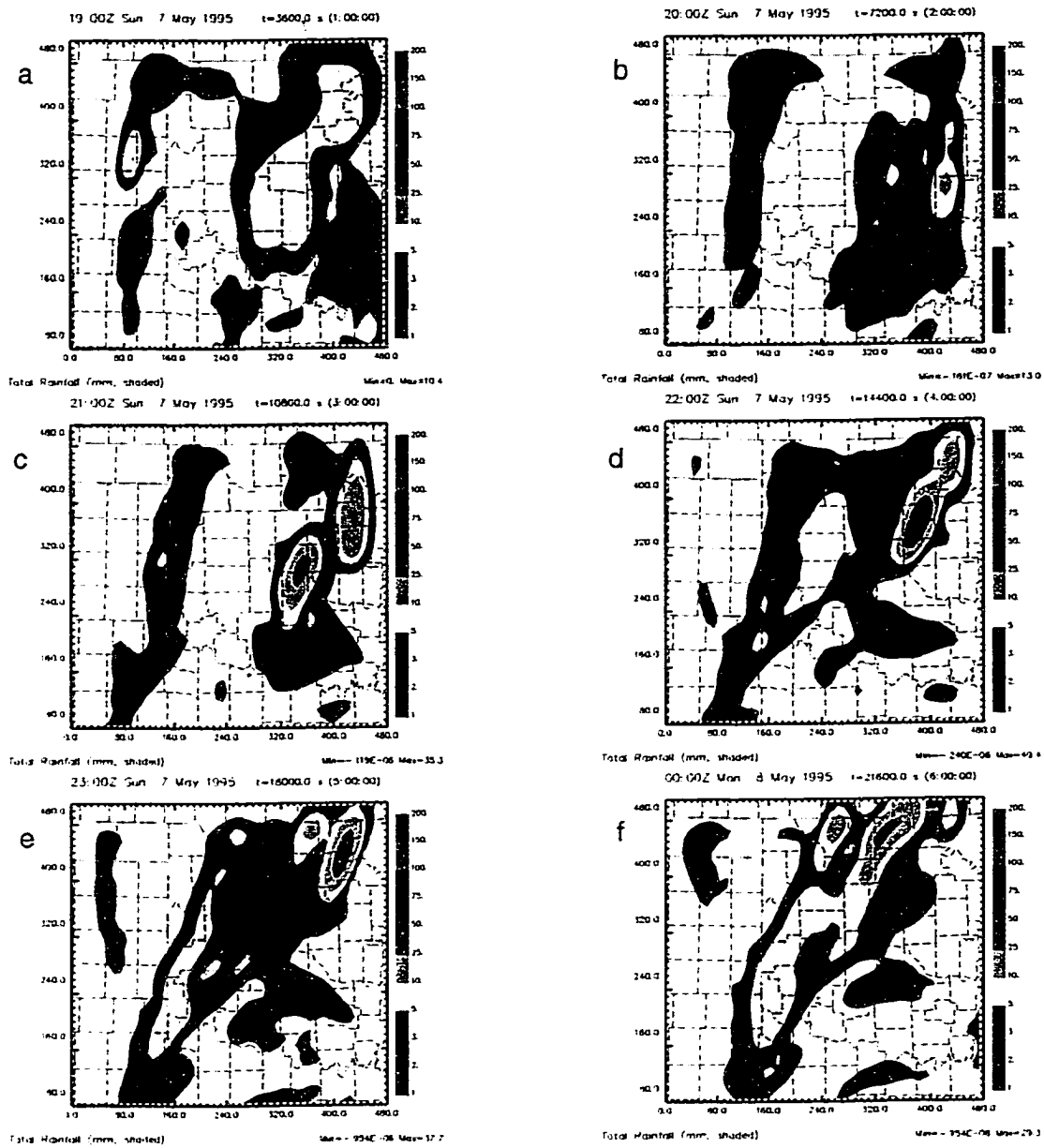

Fig. 5.22 The hourly precipitation fields from Exp. DIWb valid at 1900 (a), 2000 (b), 2100 (c), 2200 (d), and 2300 Z (e) on 7 May and 0000 (f) Z on 8 May, 1995.

5.6 Summary

The moisture and diabatic initialization schemes described in Chapter 3 were tested using a set of real atmospheric data. The case selected for the testing was a strong convective precipitation event that occurred on 7 and 8 May, 1995. The event was characterized by two major precipitation systems: one was a strong squall line that developed along a dryline (storm system "A"), and the other was a broad convective precipitation system that originated from two convective complexes that had merged together (storm system "B").

Eight experiments were carried out using the ARPS. The predictions were started from different initial conditions and lasted for six hours. The initial conditions for the eight experiments were obtained from four different schemes: (1) a conventional data analysis, (2) an ADAS data analysis, (3) a diabatic initialization using radar and satellite data and a constant weight for the LH adjustment, and (4) a diabatic initialization using spatially dependent weights for the LH adjustment.

A comparison of the bias and threat scores for four experiments (CNVN, MESO, DIb, and DIWb) that represent the four initialization schemes is shown in Fig. 5.23. The prediction started from the conventional analysis failed to capture the structure of the two separate precipitation systems. Both the intensity and areal coverage of the precipitation systems were significantly underestimated

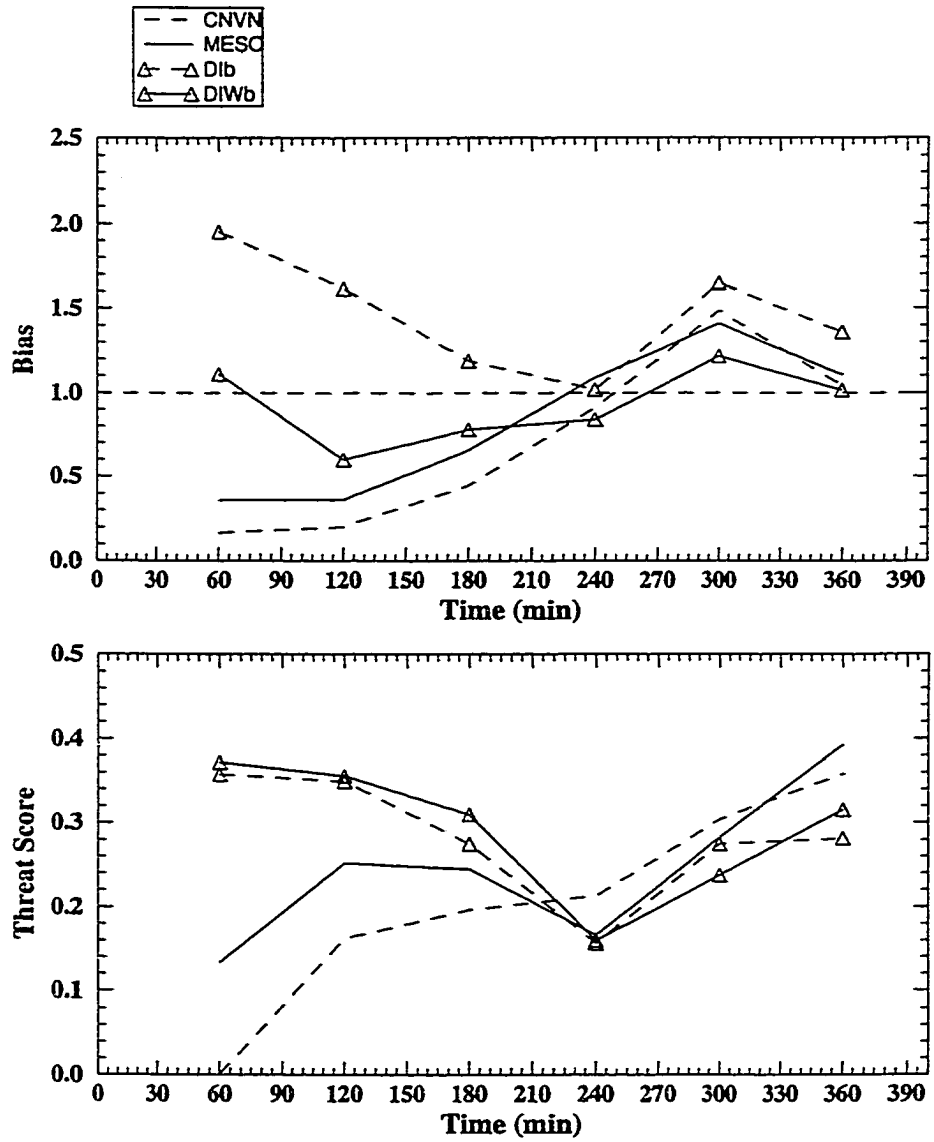

Fig. 5.23 The bias (a) and threat scores (b) for the hourly precipitation fields in Exps. CNVN, MESO, DIb, and DIWb.

during the first three to four hours. The prediction initialized with the ADAS analysis successfully forecast two distinct precipitation systems that resembled the observed ones. However, the intensity and the areal coverage of the

precipitation systems were still underestimated for the first three to four hours. A part of the rainfall coverage near the north end of the dryline was not forecast well, even though there was a local CAPE maximum in the same region.

Diabatic initialization with a constant weight for the LH adjustment improved the forecast of storm system "A" significantly. The areal coverage of the hourly precipitation was correctly predicted in less than an hour. This indicates that diabatic initialization helped trig the convection and the release of the large CAPE in the northern part of the dryline. However, the LH adjustment in storm system "B" was excessive because observations from a nearby sounding had already detected a warm core in the storm region before the LH adjustment. The LH adjustment caused a large overestimation of the precipitation in storm system "B". After setting the weight for the LH adjustment to zero in regions of storm system "B", more realistic hourly rainfall amounts were obtained. Using the non-uniform weighting also improved the intensity of the precipitation band associated with storm system "A". The weighting scheme in the current experiments is relatively crude. Future work will seek to incorporate the latent heating adjustment through an objective analysis.

It was demonstrated that diabatic initialization provided significant improvement for the precipitation spinup problem. Nevertheless, there were still deficiencies in the forecast movement of the precipitation systems. The eastward movement of precipitation system "B" as well as the southern part of

system "A" were too slow compared with the observed speeds. It was suggested by the OSSEs in the last chapter that the lack of detailed information in initial wind fields could result in large phase errors in the predicted precipitation fields. In experiments by Yu and Droegemeier (1999, personal communication) the movement of system "B" at 0000 Z May 8, 1995 were well predicted by starting the model 9 hours earlier than the present experiments (0900 Z May 7, 1995) and using a larger domain. This suggests that the phase errors in the present experiments may be due to spinup problems in the dynamic fields. Another possible cause for the slow movement of system "B" in our experiments might be the lateral boundary conditions that were forced by the RUC forecasts, which might not be compatible with the ARPS forecast fields. Experiments with a larger domain may alleviate this problem. In future work the capability of a wind initialization scheme to further improve the precipitation predictions will be investigated. Future study will also be conducted on a continuous data assimilation using nudging and/or digital filtering techniques.

Chapter 6
Summary and Conclusions

6.1 Summary

Precipitation is one of the most important variables for weather forecasting, yet quantitative precipitation forecasting remains one of the most difficult problems in numerical weather prediction. The "spinup" problem, i.e., the underestimation of the appropriate amount and areal coverage of precipitation during the early stages of numerical weather forecasts, is known to be related to deficiencies in the initial moisture, latent heating and divergent circulations. It is one of the most serious problems for short-range forecasting and constitutes a fundamental challenge in data assimilation. The motivation for our research is to mitigate the spinup problem for a convective-scale numerical prediction model by providing better initial conditions using radar and satellite data.

A three-dimensional cloud analysis system has been developed. It integrates data sources from METARs, GOES imagery, and WSR-88D radar and constructs three-dimensional cloud and precipitate fields. The METARs provide

information about cloud base and cloud amount for the lower atmosphere. Satellite infrared imagery data are used to determine cloud top height. Detailed cloud and precipitate structures in the middle troposphere are inferred from radar reflectivities. Based on these observations, a three-dimensional volumetric cloud fraction field can be obtained. Cloud liquid water and ice mixing ratio fields are computed using a simple one-dimensional cloud model, which assumes a moist-adiabatic ascent in clouds with an empirical entrainment correction. Precipitate mixing ratios are derived from radar reflectivity fields through empirical relationships. This cloud analysis provides a unique advanced tool for multi-sensor cloud and precipitation analyses. It is based on observations that are available in the operational forecast environment and it is independent of numerical weather forecast models. Although some of the analysis products (e.g., cloud liquid water) are approximate estimations based on simple physical models, they can be further improved by incorporating more advanced observational data [e.g., cloud content observations from microwave instruments on geostationary and polar-orbiting satellites, cloud and precipitation structures observed by the precipitation radar onboard the TRMM (Tropical Rainfall Measuring Mission) satellite, precipitable water fields derived from GOES as well as GPS (Global Positioning System) satellites, etc.]. The analysis system has great potential for providing a convenient and comprehensive diagnostic tool as well as a tool for diabatic data assimilation.

The ADAS cloud analysis has been used to initialize the ARPS cloud liquid, cloud ice, rainwater, snow, and hail mixing ratio fields. It also serves as the basis for a moisture and diabatic initialization scheme. In most previous studies, diabatic initializations were based on two-dimensional precipitation estimates. The precipitation estimates were obtained from raingages, radar, or satellite data and were used to determine a vertically-integrated latent heating rate. Prespecified profiles, e.g., climatological latent heating profiles (Puri and Miller 1990) or parabolic functions (Carr 1977; Wang and Warner 1988; Takano and Segami 1993; Wu et al. 1995), were then used to distribute the rainfall-derived latent heating rate vertically. Experiments show that such LH fields have phase errors in time and in space, since latent heating may occur in places where there is no rainfall at the ground. It is demonstrated that positive latent heating is more closely related to cloud water (ice) content than it is to surface rainfall. Therefore a moisture and diabatic initialization based on the three-dimensional cloud analysis system is proposed.

In the initialization scheme, the moisture and temperature analyses obtained from conventional radiosonde observations are adjusted based on the cloud analysis so that the model forecast can produce accurate precipitation amounts at the right time and at the right locations. The initial temperature field is adjusted in cloud and rain regions to account for latent heat release from cloud condensation and to induce vertical circulations that are consistent with the observed precipitation. Cloudy regions are moistened to compensate for

deficiencies in the moisture observations, to provide sources for cloud condensation, and to retain the vertical circulations induced by the diabatic initialization. One of the major advantages of the new moisture and diabatic initialization scheme is that it is based on a three-dimensional multi-sensor cloud analysis. Experiments have demonstrated that the latent heat adjustment based on the 3D cloud analysis results much smaller phase errors for initial diabatic forcing fields than that based on 2D surface precipitation fields. Another advantage is that the present moisture adjustment is based on the analyzed cloud base and top heights which are obtained from surface, radar and satellite observations, while previous studies (e.g., Turpeinen et al. 1990; Takano and Segami 1993) have used prespecified sigma levels for cloud base and top heights.

The impact of the moisture and diabatic initialization on convective-scale numerical weather prediction was examined through a set of OSSEs using the ARPS. Sensitivities of the forecast model to different moisture/diabatic initialization strategies and to different wind initialization were also tested. It was found that the diabatic initialization was important for improving the accuracy of the initial thermal as well as moisture fields in data sparse regions. The moisture adjustment could be insufficient if the background temperature field was too smooth. The diabatic initialization had a significant positive impact on reducing the model's spinup time for the precipitation forecasts. The results showed that inserting a cloud or rainwater field at the initial time could help produce cold outflows at the surface and generate new storms. However, the initial water load

also hindered the development of vertical circulations in the existing storms at the initial time because of the falling motion of precipitate particles and the negative buoyancy caused by the weight of cloud water and rainwater. A wind initialization within the rain regions was shown to be helpful in providing consistent updrafts that balanced the rainwater load and reduced the phase errors in precipitation forecasts.

Sensitivities of the ARPS to the new diabatic initialization scheme were further tested using a real data case. The event was characterized by two major precipitation systems: one was a strong squall line that developed along a dryline, and the other was a broad convective precipitation system formed from two convective complexes that had merged together.

The sensitivities of the real data forecasts to different moisture and diabatic initialization strategies were similar to those found in the OSSEs. The prediction started from a conventional data analysis failed to capture the separate structures of the observed precipitation systems. Both the intensity and areal coverage of the precipitation systems were significantly underestimated during the first three to four hours. Significant phase errors existed in the precipitation fields. The forecast initialized with the ADAS analysis, in which the observations from a surface mesonet system were included, successfully produced two distinct precipitation systems that resembled the observed ones. Phase errors in the simulated precipitation field were reduced significantly. However, the

intensity and the areal coverage of the precipitation systems were still underestimated during the first three to four hours. After applying the moisture and diabatic initialization, the spinup time for the model precipitation was reduced to less than one hour. The simulated intensity and areal coverage of the precipitation systems, especially the latter, were improved significantly. However, the diabatic initialization had little impact on the phase error in the simulated precipitation field.

The real data experiments showed that the thermal adjustment in the diabatic initialization should be applied only in regions that lack temperature observations. In vicinities of direct temperature observations, the latent heating adjustment can be excessive because the latent heating effect may already be reflected in the nearby temperature observations. Therefore, an appropriate weighting function for the LH adjustment is important in the diabatic initialization. The weighting function should be a function of the distribution of temperature observations and the accuracy of the observations.

6.2 Conclusions and future work

It is shown that conventional surface and radiosonde observation networks are insufficient for meso-β and smaller-scale numerical weather prediction. The ADAS cloud analysis, which makes use of the METARs, radar reflectivity, and satellite imagery data, can provide high-resolution three-dimensional cloud and

precipitate fields and compensate for the deficiencies in conventional observing systems. A moisture and diabatic initialization scheme was developed based on the cloud analysis and was shown to be successful for alleviating the spinup problem and improving convective-scale numerical precipitation forecasts.

Further improvements can be made to the cloud analysis by using additional observational data. The Advanced Microwave Sounding Unit (AMSU) on the NOAA-KLM series of polar-orbiting satellites can provide observations of column total cloud water content. The column total cloud water field could be used to constrain the cloud liquid/ice water content field derived from the Smith-Feddes model. The Tropical Rainfall Measuring Mission (TRMM) satellite, which carries the first low earth orbiting precipitation radar along with a 9-channel SSM/I like Microwave Imager (TMI), an AVHRR (Advanced Very High Resolution Radiometer) -like visible-infrared radiometer, a lighting sensor and a cloud sensor, can provide detailed, three-dimensional cloud and precipitation structures (http://trmm.jpl.nasa.gov; http://trmm.gsfc.nasa.gov). While the TRMM data are only available in tropical areas and at relatively low time frequency, they have high vertical resolution and can be used to validate and calibrate the cloud and precipitation analysis. Polarimetric radars that are under development at the National Severe Storm Laboratory (NSSL) have great potential for providing more accurate estimates of precipitation content as well as discriminations of cloud hydrometeor types (http://nssl.noaa.gov/srad/drarsr/). This information is extremely helpful for understanding microphysical processes

in the atmosphere, for improving precipitation estimates and for precipitation forecasts. More accurate moisture analyses can be obtained through assimilation of satellite-derived precipitable water fields, e.g., those retrieved from GOES-8 and GOES-10 sounders (http://cimss.ssec.wisc.edu/goes/ real-time/realtime.html) or those from the Global Positioning System (GPS). The capability of a wind initialization and a continuous data assimilation to further improve the precipitation forecasts, especially the position of the precipitation, should be investigated.

Appendix A Reverse-Kessler Scheme

A.1 Introduction

The spinup problem, an underestimation of the appropriate amount and areal coverage of precipitation during the early hours of integration, is a common deficiency in many numerical weather predictions. This problem is related to inaccuracies in the initial specification of divergence, moisture and thermal fields (Mohanty et al. 1986). Many previous studies have used raingauge measurements (Wang and Warner 1988) and the precipitation rates derived from satellite data (Puri and Miller 1990; Turpeinen et al. 1990) to improve the initial conditions of moisture and divergence fields. Recent studies have begun assimilating cloud water fields derived from satellite data (Zhao and Carr 1997; Wu et al. 1995) or produced by a model's pre-forecast integration (Raymond et al. 1995) into the model to improve the spinup process.

Although many previous studies have been successful to varying extents in alleviating the spinup problem, the lack of detailed information on initial moisture, cloud water and latent heating fields is still a key problem. The NEXt

Generation Weather Radar (NEXRAD) can provide three-dimensional precipitation fields with high spatial and temporal resolution. In this appendix, a simple scheme that uses high resolution radar reflectivity data to retrieve cloud water and latent heating distributions and to adjust the water vapor field is presented. The concept of the scheme is similar to that of "physical initialization" (Krishnamurti et al. 1984). In our case the model's precipitation parameterization is the Kessler warm rain microphysical parameterization (Kessler 1969). By reversing this explicit microphysical scheme, the water vapor, cloud water and latent heating fields are determined. Most of this material has been presented in Zhang and Carr (1998).

A.2 Reverse-Kessler scheme

The initialization of the moisture and diabatic fields should be closely related to the microphysical processes in the forecast model. In the Kessler (1969) scheme, explicit conservation equations for cloud liquid water and rainwater are defined as following (the diffusion terms are neglected here for simplicity):

$$\frac{dq_r}{dt} - \frac{1}{\rho}\frac{\partial(\rho V_t q_r)}{\partial z} = P_{AUTO} + P_{ACC} - P_{EVAP} \tag{A.1}$$

$$\frac{dq_c}{dt} = P_{COND} - P_{ACC} - P_{AUTO} \tag{A.2}$$

Here q_c and q_r are cloud water and rainwater mixing ratios. P_{AUTO}, P_{ACC}, P_{EVAP}, and P_{CON} are the changing rates of the water substances due to autoconversion, accretion, rain evaporation, and cloud condensation/evaporation mechanisms, respectively, V_t is the mean terminal velocity of the raindrops and ρ the air density. In cloudy regions, Eq. (A.1) can be further simplified by assuming that rain evaporation is small, i.e.:

$$\frac{dq_r}{dt} - \frac{1}{\rho}\frac{\partial(\rho V_t q_r)}{\partial z} = P_{AUTO} + P_{ACC} \tag{A.3}$$

The microphysical production terms in Eqs. (A.1) - (A.3) are parameterized as follows:

$$P_{AUTO} = k_1(q_c - q_{ccrit}) \tag{A.4}$$

$$P_{ACC} = k_2 q_c q_r^{0.875} \tag{A.5}$$

$$P_{EVAP} = \frac{1}{\bar{\rho}}\frac{C(1-q_v/q_{vs})(\bar{\rho}q_r)^{0.525}}{\alpha + \beta/(q_{vs}\bar{p})} \tag{A.6}$$

$$P_{CON} = \frac{(q_v - q_{vs})/\Delta t}{1 + \frac{a_w(273.15 - b_w)L_v}{(T - b_w)^2 c_p}} \tag{A.7}$$

and the terminal fall velocity V_t (m/s) for the mean-size raindrop is described by

$$V_t = V_0(\bar{\rho}q_r)^{0.1364}\sqrt{\frac{\rho_0}{\bar{\rho}}} \tag{A.8}$$

where k_1, k_2, q_{ccrit}, C, α, β, a_w, b_w, and V_0 are empirical constants, L_v is the latent heat of evaporation of the water, c_p the specific heat of dry air at constant pressure, p the pressure, T the temperature, q_v the water vapor mixing ratio, and Δt the time step for model integration.

In Eq. (A.3), q_r and V_t can be determined from radar reflectivities. Then q_c can be solved by substituting Eqs. (A.4), (A.5) and (A.8) into Eq. (A.3):

$$q_c = \left[\frac{dq_r}{dt} - \frac{1}{\rho} \frac{\partial(\rho V_t q_r)}{\partial z} + k_1 q_{ccrit} \right] \Big/ (k_1 + k_2 q_r^{0.875}) \tag{A.9}$$

After q_c is obtained, the condensation rate P_{CON} is calculated by rearranging Eq. (A.2):

$$P_{COND} = \frac{dq_c}{dt} - P_{ACC} - P_{AUTO} \tag{A.10}$$

Then q_v can be solved by using Eq. (A.7):

$$q_v = q_{vs} + \Delta t \cdot P_{COND} \left[1 + \gamma / (T - b_w)^2 \right] \tag{A.11}$$

where

$$\gamma = a_w (273.15 - b_w) L_v / c_p \tag{A.11a}$$

Outside the cloudy region, P_{EVAP} is calculated from Eq. (A.6) by using the background water vapor mixing ratio and temperature fields. The latent heating rate field $\dot{Q}$ is then determined from the condensation and evaporation rates P_{COND} and P_{EVAP}:

$$\dot{Q} = L_v (P_{COND} - P_{EVAP}) \tag{A.10}$$

The cloud water, water vapor, and latent heating fields derived from Eqs. (A.9), (A.11) and (A.12) are consistent with the model if the same microphysical scheme was used in the model. They are also consistent with the observed radar reflectivities. In most previous studies, latent heating field estimates were inferred from two-dimensional precipitation estimates, either from satellite or surface observations; thus certain assumptions concerning the vertical structure of those fields are required. With the reverse-Kessler scheme no assumptions about the vertical structures of moisture or latent heating fields are required.

A.3 Observational System Simulation Experiments (OSSEs)

A.3.1 The Control Run

A two-dimensional storm simulation is produced using the ARPS. The key model features in the simulation include non-hydrostatic, compressible dynamics, stretched vertical coordinate, 4th-order advective scheme, 1.5 order TKE sub-grid turbulence models, and Kessler-type warm rain microphysics. The

horizontal resolution of the simulation is 1 km, and the vertical resolution varies from 25 m near the surface to about 1 km at the top of the domain. The simulation was initialized by using a single sounding and a warm bubble and integrated forward for one hour.

A.3.2 Experimental Design

In the reverse-Kessler scheme, multiple time levels of radar reflectivity data are required in order to evaluate time tendency terms in the retrieval equations. In the current study, the model generated rainwater mixing ratio fields in the control run were extracted and the radar reflectivities were calculated from them. The time interval between two consecutive radar reflectivity data sets was 6 minutes to emulate the NEXRAD observations in precipitation mode. The wind and temperature fields used in the retrievals were also taken from the simulated data, but they were resampled in different resolutions to test the sensitivity of the retrieval scheme to errors in these fields.

A set of retrieval experiments using different wind and temperature fields is listed in Table A.1. The first three experiments were designed to test the sensitivities of the reverse-Kessler scheme to errors in wind and temperature fields, while the last two were used to test the sensitivity of the retrieval scheme to different stages of precipitation evolution. In experiment I, the wind and temperature fields were observed from a single sounding. The sounding was obtained by taking the horizontal mean of the simulated fields. In experiment II,

the wind field was taken as the same resolution in the simulation, while the temperature was treated as a single sounding. In experiment III, both the wind and temperature fields at the same resolution as in the control run were used for the retrieval. All three experiments were done with the radar reflectivities derived from the simulated rainwater mixing ratio fields at 27 and 33 minutes in the control run.

Table A.1 List of the OSSEs

	wind	temp	time
exp.I	sgl. snd	sgl. snd	27 min
exp.II	full resl.	sgl. snd	27 min
exp.III	full resl.	full resl.	27 min
exp.IV	full resl.	full resl.	21 min
exp.V	full resl.	full resl.	15 min

Experiments IV and V are the same as in experiment III except that the retrievals were done at different initial times. In Exp. IV the radar data at 21 and 27 min were used in the retrieval and in Exp. V the radar data at 15 and 21 min were used.

A.3.3 Results

The verification for the retrieval experiments was provided by the simulated moisture and latent heating fields in the control run. Table A.2 shows the error statistics for the retrieved fields in different experiments. Two error

statistics, bias and the correlation coefficient, were calculated. The bias is defined as the ratio of the mean value of the retrieved field to that of the simulated or "true" field in the cloud and rain region. The correlation coefficients were those between the retrieved and simulated fields in the cloud/rain region.

Table A.2 The error statistics of the retrieved fields

	q_c		q_v		$\dot{Q}$	
	Bias	**Corr**	**Bias**	**Corr**	**Bias**	**Corr**
exp.I	1.19	.86	1.06	.98	1.12	.72
exp.II	1.13	.88	1.06	.98	1.20	.77
exp.III	1.13	.88	1.08	.98	1.24	.77
exp.IV	.77	.85	1.07	.98	1.26	.73
exp.V	.84	.92	1.03	.99	.81	.60

From Table A.2 we can see that overall the retrieved moisture and latent heating fields agree well with the simulated ones. The accuracy of the retrieved cloud water is sensitive to errors in the wind field but not to those in the temperature field. It can be seen from Eq. (A.9) that the q_c retrieval depends on the accuracy of the advection term for the rain water mixing ratio field (in dq_r/dt), while no terms in the equation involve temperature. The latent heating retrieval is sensitive to errors in both the wind and temperature fields, with more sensitivity to the former. This is because the retrieved latent heating was determined by P_{COND} and P_{EVAP} [Eq. (A.12)]. Errors in the temperature field can cause errors in P_{EVAP} [Eq. (A.6)]. Errors in the wind field can cause errors in q_c fields and

thus in the P_{COND} calculations [Eq. (A.10)]. Since the cloud condensation /evaporation rate P_{COND} was determined by the changing rate of the cloud water mixing ratios between two time levels, the impact of the wind error can become large. The retrieved water vapor field is less sensitive to either wind or temperature errors than the previous two fields, because the cloud region was always saturated.

It is seen in Table A.2 that the retrieved cloud water fields have a wet bias in exp. III but dry biases in exp. IV and V. This was due to the nonlinearity in the growth (or decay) of the rainwater fields. In the retrieval scheme, the changing rates of the radar reflectivities were assumed to be linear during the 6-minute time period. Time series of the domain maximum rainwater mixing ratio and radar reflectivity fields (not shown) indicated that the growth process of the two quantities were nonlinear. The time tendencies of rainwater mixing ratio estimated by using the linear approximation (for reflectivity) were larger than the simulated value at 27 min and smaller than that at 15 and 21 min. Therefore the retrieved q_c-fields had a wet bias at 27 min and dry biases at 15 and 21 min because q_c is proportional to the time tendency of the q_r- field [Eq. (A.9)].

A.4. Summary

In this appendix, the reverse-Kessler retrieval scheme for retrieving moisture and latent heating fields from high resolution radar reflectivity data was

presented. The scheme was tested using simulated data. It is found that the retrieved cloud water mixing ratio field was sensitive to the errors in the wind field but not as sensitive to those in the temperature field. The retrieved latent heating fields was slightly sensitive to the errors in the temperature field and relatively more sensitive to those in the wind field. The nonlinear growth (decay) of the rainwater mixing ratio field caused the dry (wet) bias in the retrieved q_c-field. Overall the retrieved moisture and latent heating fields agree well with the simulated data.

The current reverse-Kessler scheme is preliminary and is tested using two-dimensional data sets. The scheme was not applied in our OSSEs and the real data experiments since those tests were intended to test the ADAS cloud analysis and the moisture and diabatic initialization scheme. In the future, the possibility of a variational diabatic initialization that combines the ADAS cloud analysis and the reverse-Kessler scheme will be investigated.

REFERENCES

Albers, S. C., J. A. McGinley, D. A. Birkenheuer, and J. R. Smart, 1996: The local analysis and prediction system (LAPS): Analyses of clouds, precipitation, and temperature. *Wea. Forecasting*, **11**, 273-287.

Andersen, J. H., 1977: A routine for normal mode initialization with nonlinear correction for a multilevel spectral model with triangular truncation. ECMWF Int. Rep. No. 15, 41pp. [ECMWF, Shinfield Park, Reading, Berkshire RG2 9AX, England.]

Aonashi, K., 1993: An initialization method to incorporate precipitation data into a mesoscale numerical weather prediction model. *J. Meteor. Soc. Japan*, **71**, 393-405.

Aonashi, K., and A. Shibata, 1996: The impact of Assimilating SSM/I precipitable water and rain flag data on humidity analysis and short-term precipitation forecasts. *J. Meteor. Soc. Japan*, **74**, 77-99.

Arakawa, A., and V. Lamb, 1977: Computational design of the basic dynamical processes of the UCLA general circulation model. *Methods in Computational Physics*, Vol. **17**, J. Chang, Ed., Academic Press, 173-265.

Baer, F., and J. Trbbia,.1977: On complete filtering of gravity wave modes through nonlinear initialization. *Mon. Wea. Rev.*, **105**, 1536-1539.

Barnes, S. L., 1973: Mesoscale objective analysis using weighted time-series observations. NOAA Tech. Memo. ERL NSSL-62, National Severe Storms Laboratory, Norman, OK 73069, 60pp. [NTIS COM-73-10781].

Benjamin, S. G., and N. L. Seaman, 1985: A simple scheme for objective analysis in curved flow. *Mon. Wea. Rev.*, **113**, 1184-1198.

—, and R. Bleck, 1993: Regional weather prediction with a model combining terrain-following and isentropic coordinates. Part I: Model description. *Mon. Wea. Rev.*, **121**, 1770-1785.

—, K. J. Brundage, and L. L. Morone, 1994: The Rapid Update Cycle. Part 1: Analysis/Model description. *Technical procedure Bulletin.* 416. NOAA/NWS, 16pp. [Available from the National Weather Service, Office of Meteorology, 1325 East-West highway, Silver Spring, MD 20910.]

Betts, A. K., 1986: A new convective adjustment scheme. Part I: Observational and theoretical basis. *Quart. J. Roy. Meteor. Soc.*, **112**, 677-691.

—, and M. J. Miller, 1986: A new convective adjustment scheme. Part II: Single column tests using GATE wave, BOMEX, ATEX and Arctic air-mass data sets. *Quart. J. Roy. Meteor. Soc.*, **112**, 693-709.

Bluestein, H. B., 1993: *Synoptic-Dynamics meteorology in midlatitudes. Volume II: Observations and theory of weather systems.* Oxford University Press. 594pp.

Bourke, W., and J. L. McGregor, 1983: A nonlinear vertical mode initialization scheme for a limited area prediction model. *Mon. Wea. Rev.*, **111**, 2285-2297.

Bratseth, A. M., 1986: Statistical interpolation by means of successive correction. *Tellus*, **38A**, 439-447.

Brewster, K., F. Carr, N. Lin, J. Straka, and J. Krause, 1994: A local analysis system for initializing real-time convective-scale models. Preprints, *10th Conf. on Numerical Wea. Prediction.* Portland, OR, *Amer. Meteor. Soc.*

—, 1996: Implementation of a Bratseth analysis scheme including Doppler radar. Preprints, *15th Conf. on Weather Analysis and Forecasting*, AMS, Boston, 92-95.

—, 1994: Assimilation of mesoscale data for the prediction of thunderstorm initiation. Submitted for the general examination for the Doctor's degree. School of Meteorology, University of Oklahoma.

Brière: Initialization of a modeled convective storm using Doppler radar-derived fields. *Mon. Wea. Rev.*, **121**, 2757-2775.

Brill, K. F., L. W. Uccellini, J. Manobianco, J. H. Homan, and P. J. Kocin, 1991: The use of successive dynamic initialization by nudging to simulate cyclonegenesis during GALE IOP I. *Meteorol. Atmos. Physi.*, **45**, 15-40.

Brock, F.V., K.C. Crawford, R. L. Elliott, G. W. Cuperus, S. J. Stadler, H. L. Johnson, and M. D. Eilts, 1995: The Oklahoma Mesonet: A technical overview. *J. Atmospheric and Oceanic Technology,* **12(1)**, 5-19.

Carpenter, R. L. Jr., K.K. Droegemeier, G.M. Bassett, K. Brewster, D.E. Jahn, J. Levit, M. Xue, W.L. Qualley, and R. Strauss, 1998: Storm-scale NWP for commercial aviation: results from real-time operational tests in 1996-1997. Preprints, *12th Conf. On Numerical Weather Prediction*, Phoenix, AZ., Amer. Meteor. Soc., 213-216.

Carr, F. H., 1977: Mid-tropospheric cyclones of the summer monsoon. *Pure and Applied Geophysics.* **115**, 1383-1412.

—, and M. Baldwin, 1991a: Incorporation of observed precipitation estimates during initialization of synoptic and mesoscale storms. Preprints, *First Int. Symp. On Winter Storms*. New Orleans, LA, Amer. Meteor. Soc., 71-75.

—, and —, 1991b: Assimilation of observed precipitation data using NMC's eta model. Preprints, *Ninth Conf. On Numerical Weather Prediction*, Denver, CO., Amer. Meteor. Soc., 422-425.

Chang, S. W., and T. R. Holt, 1994: Impact of assimilating SSM/I rainfall rates on numerical prediction of winter cyclones. *Mon. Wea. Rev.*, **122**, 151-164.

Crawford, K. C., F. V. Brock, R. L. Elliott, G. W. Cuperus, S. J. Stadler, H. L. Johnson, and C. A. Doswell, 1992: The Oklahoma Mesonet — A 21st century project. *8th International Conf. On Interactive Information and Processing Systems for Meteorology, Oceanography, and Hydrology.* Atlanta, Georgia. Amer. Meteor. Soc.

Crook, A., 1994: Numerical simulations initialized with radar-derived wind. Part I: Simulated data experiments. *Mon. Wea. Rev.*, 122, 1189-1203.

— and J. D. Tuttle, 1994: Numerical simulations initialized with radar-derived wind. Part II: Forecasts of three gust front cases. *Mon. Wea. Rev.*, 122, 1204-1217.

Crum, T. D., and R. L. Albert, 1993: The WSR-88D and the WSR-88D operational support facility. *Bull. Amer. Meteor. Soc.*, **74**, 1669-1687.

Daley, R.,1979: The application of nonlinear normal mode initialization to an operational forecast model. *Atmos.-Ocean,* **17**, 97-124.

Danard, M., 1985: On the use of satellite estimates of precipitation in initial analyses for numerical weather prediction. *Atmos.-Ocean*, 23, 23-42.Crook,

A., 1994: Numerical simulations initialized with radar-derived wind. Part I: Simulated data experiments. *Mon. Wea. Rev.*, **122**, 1189-1203.

Davies, H.,1983: Limitations of some common lateral boundary schemes used in regional NWP models. *Mon. Wea. Rev.*, **111**, 1002-1012.

—, and R. E. Turner, 1977: Updating prediction models by dynamical relaxation: an examination of the technique. *Quart. J. Roy. Meteor. Soc.*, **103**, 225-245.

Donner, L. J., 1988: An initialization for cumulus convection in numerical weather prediction models. *Mon. Wea. Rev.*, **116**, 377-385.

—, and P. J. Rasch, 1989: Cumulus initialization in a global model for numerical weather prediction. *Mon. Wea. Rev.*, **117**, 2654-2671.

Doviak, R. J., and D. S. Zrnic, 1984: *Doppler radar and weather observations.* Academic Press, 458pp.

Errico, R. M., and G. T. Bates, 1988: Implicit normal mode initialization of the PSU/NCAR mesoscale model. NCAR Tech. Note, NCAR/TN-312 + IA, 112pp.

—, and P. J. Rasch, 1988: A comparison of various normal-model initialization schemes and the inclusion of diabatic processes. *Tellus*, **40A**, 1-25.

Filiberti, M. A., L. Eymard, and B. Urban, 1994: Assimilation of satellite precipitable water in a meteorological forecast model. *Mon. Wea. Rev.*, **122**, 486-506.

Fox-Rabinovitz, M.S., 1996: Diabatic dynamic initialization with an iterative time integration scheme as a filter. *Mon. Wea. Rev.*, **124**, 1544-1557.

Germano, M., U. Piomelli, P. Moin, and W. H. Cabot, 1991: A dynamic subgrid-scale eddy viscosity model. *Phys. Fluids*, **A3**, 1760-1765.

Hoke, J. E., and R. A. Anthes, 1976: The initialization of numerical models by a dynamic-initialization technique. *Mon. Wea. Rev.*, **104**, 1551-1556.

Huang, X.-Y., P. Lynch, 1993: Diabatic digital-filtering initialization: Application to the HIRLAM model. *Mon. Wea. Rev.*, **121**, 589-603.

—, H. Sundqvist, 1993: Initialization of cloud water content and cloud cover for numerical prediction models. *Mon. Wea. Rev.*, **121**, 2719-2726.

—, A. Cederskow, and E. Kallen, 1994: A comparison between digital filtering initialization and nonlinear normal-mode initialization in a data assimilation system. *Mon. Wea. Rev.*, **122**, 1001-1015.

Jones, C.D., and B. Macpherson, 1997: A Latent Heat Nudging Scheme for the Assimilation of Precipitation into an Operational Mesoscale Model, *Meteor. Appl.*, **4**, 269-277.

Kain, J. S., and J. M. Fritsch, 1993: Convective parameterization for mesoscale models: The Kain-Fritsch scheme. *The Representation of Cumulus Convection in Numerical Models, Meteor. Monogr.*, **24**, 165-170.

Kasahara, A., R. C. Balgovind, and B. B. Katz, 1988: Use of satellite radiometric imagery data for improvement in the analysis of divergent wind in the tropics. *Mon. Wea. Rev.*, **116**, 866-883.

—, A. P. Mizzi., and L. J. Donner, 1992: Impact of cumulus parameterization on the spinup of precipitation forecasts in the tropics. *Mon. Wea. Rev.*, **120**, 1360-1380.

Kessler, E. 1969: On the distribution and continuity of water substance in atmospheric circulation. *Meteor. Monogr.*, **10**, No. 32, *Amer. Meteor. Soc.*

Klemp, J.B., and R.B. Wilhelmson, 1978: The simulation of three-dimensional convective storm dynamics. *J. Atmos. Sci.*, **35**, 1070-1096.

Koch, S. E., A. Aksakal, and J. T. Mcqueen, 1997: The influence of mesoscale humidity and evapotranspiration fields on a model forecast of a cold-frontal squall line. *Mon. Wea. Rev.*, **125**, 384-409.

Krishnamurti, K. Ingles, S. Cooke, T. Kitade and P. Pasch, 1984: Details of low-latitude, medium-range numerical weather prediction using a global spectral model. Part II: Effects of orography and physical initialization. *J. Meteor. Soc. Japan*, **62**, 613-648.

—, 1985: Numerical weather prediction in low latitudes. *Adv. Geophysics.*, **28b**, 283-333.

—, H. S. Bedi, , W. Heckley, and K. Ingles, 1988: Reduction of the spinup time for evaporation and precipitation in a spectral model. *Mon. Wea. Rev.*, **116**, 907-920.

—, J. Xue, H. S. Bedi, K. Ingles, and D. Oosterhof, 1991: Physical initialization for numerical weather prediction over the tropics. *Tellus*, **43AB**, 53-81.

—, S. K. Roy Bhowmik, D. Oosterhof, G. Rohaly, and N. Surgi, 1995: Mesoscale signatures within the tropics generated by physical initialization. *Mon. Wea. Rev.*, **123**, 2771-2790.

Kristjansson, J. E., 1991: Initialization of cloud water in a weather prediction model. Preprints, *9th Conf. on Numerical Weather Prediction*, Denver, CO, *Amer. Meteor. Soc.*, 823-824.

Kuo, H.L., 1965: On formation and intensification of tropical cyclones through latent heat release by cumulus convection. *J. Atmos. Sci..*, **22**, 40-63.

—, 1974: Further studies of the parameterization of the influence of cumulus convection on large scale flow. *J. Atmos. Sci..*, **31**, 1232-1240.

Kuo, Y.-H., and Y.-R. Guo, 1989: Dynamic initialization using observations from a network of profilers and its impact on short-range numerical weather prediction. *Mon. Wea. Rev.*, **117**, 1975-1998.

Lazarus, S., 1993: *Forward variational assimilation and prediction experiments of deep convection using simulated and observed single-Doppler data.* Submitted for the general examination for the Doctor's degree. School of Meteorology, University of Oklahoma.

—, 1996: *The assimilation and prediction of a Florida multicell storm using single-Doppler data.* Ph. D. dissertation. University of Oklahoma. 340pp.

Lin, Y., P. S. Ray, and K. W. Johnson, 1993: Initialization of a modeled convective storm using Doppler radar-derived fields. *Mon. Wea. Rev.*, **121**, 2757-2775.

—, R.D. Farley,, and H.D. Orville, 1983: Bulk parameterization of the snow field in a cloud model. *J. Clim. Appl. Meteor.*, **22**, 1065-1092.

Lynch, P., D. Giard, and V. Ivanovici, 1997: Improving the efficiency of a digital filtering scheme for diabatic initialization. Mon. Wea. Rev., 125, 1976-1982.

Machenhauer, B., 1977: On the dynamics of gravity oscillations in a shallow water model, with application to normal mode initialization. *Contrib. Atmos. Phys.*, **50**, 253-271.

Manobianco, J., S. Koch, V. M. Karyampudi, A.J. Negri, 1994: The impact of assimilating satellite-derived precipitation rates on numerical simulations of the ERICA IOP 4 cyclone. *Mon. Wea. Rev.*, **122**, 341-365.

— and J. Case, 1998: Final report on prototype local data integration system and central Florida data deficiency. NASA Contractor Report CR-1998-208540.

MacPherson, B., B. J. Wright, W. H. Hand, and A. J. Maycock, 1996: The impact of MOPS moisture data in the U.K. Meteorological Office mesoscale data assimilation scheme. *Mon. Wea. Rev.*, **124**, 1746-1766.

McGinlay, J. A., S. C. Albers, and P. A. Stamas, 1991: Validation of a composite convective index as defined by real-time local analysis system. *Wea. and Forecasting*, **6**, 337-356.

Molinari, J., 1982: Numerical hurricane prediction using assimilation of remotely-sensed rainfall rates. *Mon. Wea. Rev.*, **110**, 553-571.

Monhanty, U. C., A. Kasahara and R. Errico, 1986: The impact of diabatic heating on the initialization of a global forecast model. *J. Meteor Soc. Japan.*, **64**, 805-817.

National Weather Service and Oceanic and Atmospheric Research, 1994: Wind Profiler Assessment Report and Recommendations for Future Use. National Weather Service, Office of Meteorology W/OM22, 1325 East West Highway, Silver Spring, MD20910-3233, 141pp

Park, S. K., 1996: Sensitivity analysis of deep convective storms. Ph.D. dissertation, University of Oklahoma, 245pp.

—, and K.K. Droegemeier, 1998: Sensitivity analysis of a 3D convective storm: Implications for data assimilation, *Mon. Wea. Rev.*, submitted.

Puri, K., 1987: Some experiments on the use of tropical diabatic heating information for initial state specification. *Mon. Wea. Rev.*, **115**, 1394-1406.

—, and M. J. Miller, 1990: The use of satellite data in the specification of convective heating for diabatic initialization and moisture adjustment in numerical weather prediction models. Mon. *Wea. Rev.*, **118**, 67-93.

—, and N. E. Davidson, 1992: The use of infrared satellite cloud imagery as proxy data for moisture and diabatic heating in data assimilation. *Mon. Wea. Rev.*, **120**, 2329-2341.

Ramamurthy, M. K., and F. H. Carr, 1987: Four-dimensional data assimilation in the monsoon region. Part I: Experiments with wind data. *Mon. Wea. Rev.*, **115**, 1678-1706.

—, and —, 1988: Four-dimensional data assimilation in the monsoon region. Part II: Role of temperature and moisture data. *Mon. Wea. Rev.*, **116**, 1896-1913.

Rausmussen, E. A., J. M. Straka, R. P. Davies-Jones, C. E. Doswell III, F. Carr, M. D. Eilts, D. R. Mac Gorman, 1994: Verification of the Origins of Rotation in Tornadoes EXperiment: VORTEX, *Bull. Amer. Meteorological Soc.*, 995-1006.

Raymond, W. H., W. S. Olsen, and G. Callen, 1995: Diabatic forcing and initialization with assimilation of cloud water and rainwater in a forecast model. *Mon. Wea. Rev.*, **123**, 366-382.

Rogers, R. R., and M. K. Yau, 1989: *A Short Course In Cloud Physics.*, Pergamon Press, 293pp.

Shapiro, A. and S. Lazarus, 1993: A modified dynamic recovery technique for cloud-scale numerical models. Preprints, *17th Conf. on Severe Local Storms*, St. Louis, MO., *Amer. Meteor. Soc.*, 455-459.

—, S. Ellis, and J. Shaw, 1995: Single-Doppler velocity retrievals with Phoenix II data: Clear air and microburst wind retrievals in the planetary boundary layer. *J. Atmos. Sci.*, **52**, 1265-1287.

—, L. Zhao, S. Weygandt, K. Brewster, S. Lazarus, and K.K. Droegemeier, 1996: Initial forecast fields created from single-Doppler wind retrieval, thermodynamic retrieval and ADAS. Preprints, *11th Conf. On Numerical Weather Prediction*, Northfolk, VA., Amer. Meteor. Soc.

Schultz, P., 1995: An explicit cloud physics parameterization for operational numerical weather prediction. *Mon. Wea. Rev.*, **123**, 3331-3343.

Soong, S-T., and Y. Ogura, 1973: A comparison between axi-symmetric and slab-symmetric cumulus cloud models. *J. Atmos. Sci.*, **30**, 879-893.

Stauffer, D. R., and N. L. Seaman, 1994: Multiscale four-dimensional data assimilation. *J. Appl. Meteor.*, **33**, 416-434.

Takano, I., and A. Segami, 1993: Assimilation and initialization of a mesoscale model for improved spin-up of precipitation. *J. Meteor. Soc. Japan.*, **71**, 377-391.

Tao, W.K., J. Simpson, and M. McCumber, 1989: An ice-water saturation adjustment. *Mon. Wea. Rev.*, **117**, 231-235.

Temperton, C. and D. L. Williamson, 1981: Normal mode initialization for a multi-level grid point model. Part I: Linear aspects. *Mon. Wea. Rev.*, **109**, 729-743.

Turpeinen, O. M., T. L. Garand, R. Benoit, and M. Roch, 1990: Diabatic initialization of the Canadian regional finite-element (RFE) model using satellite data. Part I: Methodology and application to a winter storm. *Mon. Wea. Rev.*, **118**, 1381-1395.

—, 1990: Diabatic initialization of the Canadian regional finite-element (RFE) model using satellite data. Part II: Sensitivity to humidity enhancement, latent-heating profile and rainrates. *Mon. Wea. Rev.*, **118**, 1396-1407.

Verlinde, J., and W. R. Cotton, 1993: Fitting microphysical observations of nonsteady convective clouds to a numerical model: An application of the adjoint technique of data assimilation to a kinematic model. *Mon. Wea. Rev.*, **121**, 2776-2793.

Vukicevic, T., and R. M. Errico, 1993: Linearization and adjoint of parameterized moist diabatic processes. *Tellus.*, **45A**, 493-510.

Wang, D, M. Xue, V.C. Wong, and K. K. Droegemeier, 1996: Prediction and simulation of convective storms during VORTEX-95. Preprints, *11th Conf. On Numerical Weather Prediction*, Northfolk, VA., Amer. Meteor. Soc.,301-303.

—, M. Xue, D. Hou, and K. K. Droegemeier, 1998: Midlatitude squall line propagation and structure as simulated by a 3-D non-hydrostatic storm-scale model. Preprints, *12th Conf. On Numerical Weather Prediction*, Phoenix, AZ., Amer. Meteor. Soc., 209-212.

Wang, W., and T. T. Warner, 1988: Use of four-dimensional data assimilation by Newtonian relaxation and latent-heat forcing to improve a mesoscale-model precipitation forecast: A case study. *Mon. Wea. Rev.*, **116**, 2593-2613.

Weygandt, S. S., J. M. Straka, and K. K. Droegemeier, 1993: Sensitivity of storm-scale predictions to initialization with simulated Doppler radar data. Preprints, *26th Conf. on radar Meteor.*, Norman, OK, Amer. Meteor. Soc., 193-195

—, K. K. Droegemeier, C. E. Hane, and C. L. Ziegler, 1990: Data assimilation experiments using a two dimensional cloud model.

—, 1993: Initialization of deep convective storm models using real and simulated Doppler-radar data. Submitted for the general examination for the Doctor's degree. School of Meteorology, University of Oklahoma.

—, 1998: *The Retrieval of initial forecast fields from single-Doppler observations of a supercell thunderstorm.* Ph. D. dissertation. University of Oklahoma. 257pp.

Wolcott, S. W., and T. T. Warner, 1981: A humidity initialization utilizing surface and satellite data. *Mon. Wea. Rev.*, **109**, 1989-1998.

Wu, X., G. R. Diak, C. M. Hayden, and J. A. Young, 1995: Short-range precipitation forecasts using assimilation of simulated satellite water vapor profiles and column liquid water amounts. *Mon. Wea. Rev.*, **123**, 347-365.

Xu, Q., C.-J. Qiu, H.-D. Gu, and J.-X. Yu, 1995: Simple adjoint retrievals of microburst winds from single-Doppler radar data. *Mon. Wea. Rev.*, **123**, 1822-1833.

Xue, M., K. K. Droegemeier, V. Wong, A. Shapiro, K. Brewster, 1995: *ARPS Version 4.0 User's Guide.* 380pp. [Center for Analysis and Prediction of Storms, University of Oklahoma, Norman, OK 73019, U.S.A.]

—, K. K. Droegemeier, D. Wang, and K. Brewster, 1996: Prediction and simulation of a squall line case during VORTEX-95. Preprints, *18th Conf. On Severe Local Storms*, San Francisco, CA., Amer. Meteor. Soc., 169-173.

—, D. Wang, D. Hou, K. Brewster, and K. K. Droegemeier, 1998a: Prediction of the 7 May 1995 squall lines over the central U.S. with intermittent data assimilation. Preprints, *12th Conf. On Numerical Weather Prediction*, Phoenix, AZ., Amer. Meteor. Soc., 191-194.

—, D. Hou, D. Wang, and K. K. Droegemeier, 1998b: Analysis and prediction of convective initiation along a dryline. Preprints, *12th Conf. On Numerical Weather Prediction*, Phoenix, AZ., Amer. Meteor. Soc., 161-163.

Zhang, J., and T. Gal-Chen, 1996: Single-Doppler wind retrieval in the moving frame of reference. *J. Atmos. Sci.*, **53**, 2609-2623.

—, F. H. Carr, and K. Brewster, 1998: ADAS cloud analysis. *12th Conf. On Numerical Weather Prediction*, Phoenix, AZ., Amer. Meteor. Soc., 185-188.

—, and F. H. Carr, 1998: Moisture and latent heating rate retrieval from radar data. *12th Conf. On Numerical Weather Prediction*, Phoenix, AZ., Amer. Meteor. Soc., 205-208.

Zhao, Q., 1993: *The incorporation and initialization of cloud water/ice in an operational forecast model.* Ph. D. dissertation, University of Oklahoma, 187pp.

— and F. H. Carr, 1997: A prognostic cloud scheme for operational NWP models. *Mon. Wea. Rev.*, **125,** 1931-1953.

Zou, X., I. M. Navon, and J. G. Sela, 1993: Variational data assimilation with moist threshold processes using the NMC spectral model. *Tellus*, **45A**, 370-387.

Zupanski, D., and F. Mesinger, 1995: Four-dimensional variational assimilation of precipitation data. *Mon. Wea. Rev.*, **123**, 1113-1127.

IMAGE EVALUATION
TEST TARGET (QA–3)

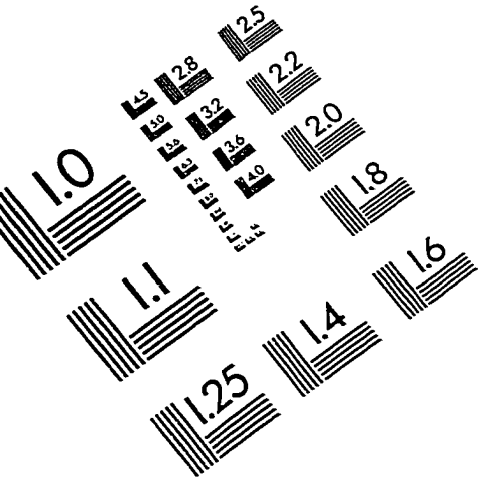

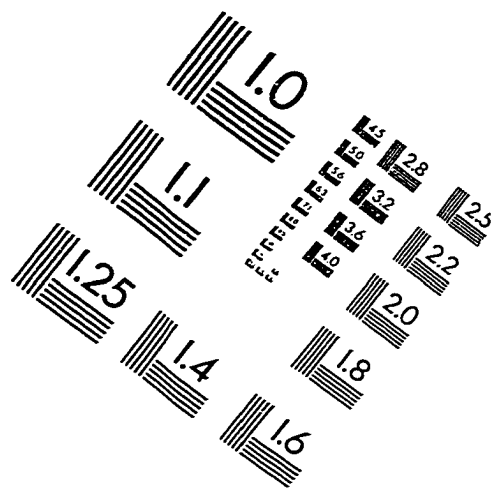

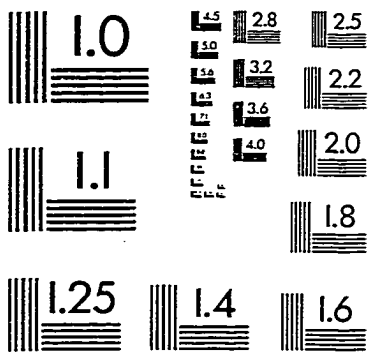

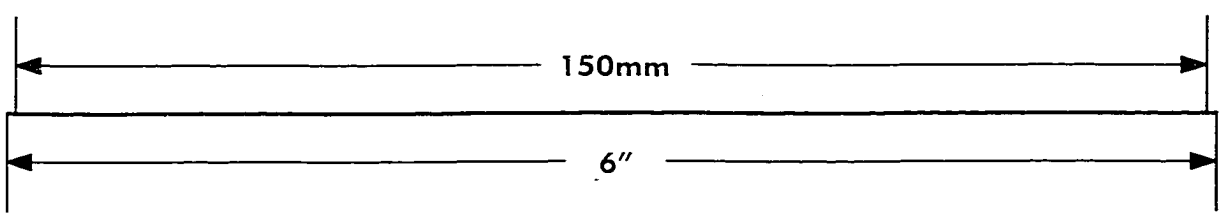

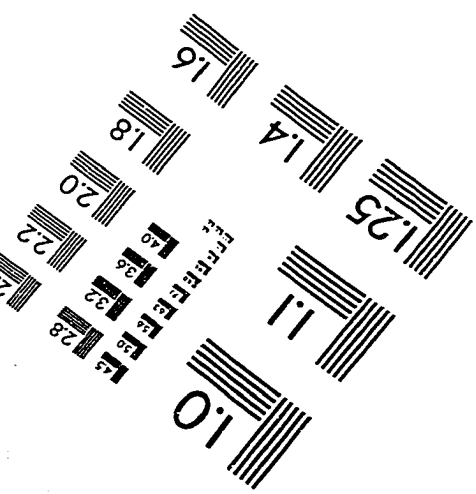

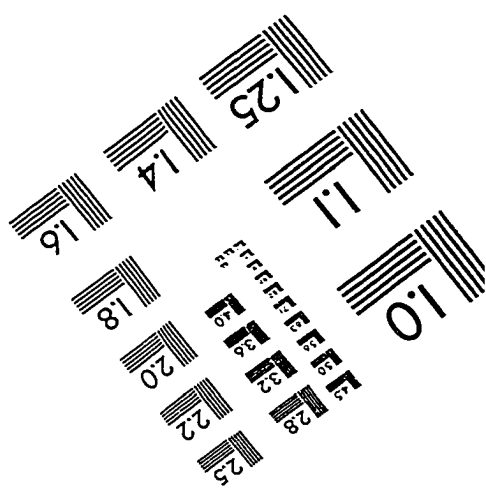

APPLIED IMAGE, Inc
1653 East Main Street
Rochester, NY 14609 USA
Phone: 716/482-0300
Fax: 716/288-5989

© 1993, Applied Image, Inc., All Rights Reserved